Numerical Simulation of Liquid Oxygen Droplet Combustion in Hydrogen under Microgravity Conditions

Benjamin Lu Davis

A dissertation submitted in partial fulfillment of the requirements for the degree of

Doctor of Philosophy

University of Washington

2025

Reading Committee:

James C. Hermanson, Chair

John Raiti, Chair

John C. Kramlich

Program Authorized to Offer Degree:

Electrical and Computer Engineering

University of Washington

Abstract

Numerical Simulation of Liquid Oxygen Droplet Combustion in Hydrogen under Microgravity Conditions

Benjamin Lu Davis

Chairs of the Supervisory Committee:

Jamer C. Hermanson and John Raiti

Department of Aeronautics and Astronautics

Department of Electrical and Computer Engineering

This work presents an efficiently lean, custom-built numerical simulator developed to study the combustion of a liquid oxygen (LOX) droplet combusting in Hydrogen gas (H_2) under microgravity conditions. Motivated by drop-tower tests conducted at ZARM (The Center for Applied Space Research and Microgravitation) in Bremen, Germany, the quasi-static evaporation framework reproduces key coupled processes– flame dynamics, Stefan flow, droplet regression, and surface ice formation– within a computationally minimalist yet physically faithful model. The governing reaction-diffusion equations were solved using finite-difference methods incorporating time-dependent, spatially homogeneous Stefan velocity fields generated by real-time evaporative feedback from the flame. The simulation achieves strong quantitative agreement with experimental and computational benchmarks, reproducing flame stand-off ratios ($F/D \approx 2$–3.5) and peak adiabatic flame temperatures ($T_{\text{peak}} \approx 3000$ K) consistent with previous work. Diffusive heat transfer dominates the total energetic flux, contributing 80–85% of the total heat input ($Q_{\max} \approx 0.3$–0.5 W), while radiative effects remain secondary, in accordance with previous estimates. Parametric sweeps over surface ice coverage fraction ψ reveal compensating feedback between evaporative impedance and geometric flame shape contraction. A single predominant global reaction mechanism, augmented by equilibrium radical generation at the reactive flame front, suffices to reproduce thin flame-sheet behavior within the high-Damköhler limit. The resulting simulator balances interpretability, stability, and physical fidelity, requiring no HPC infrastructure and running interactively accessibly in Google Colab. Beyond LOX–H_2 combustion, this framework offers a transparent, extensible platform for general coupled parabolic PDEs, bridging the gap between high-overhead CFD and simplistic static equilibrium tools.

Following the doctrine of philosophy: Dedicated to fellow inventive thinkers also inspired by passion and ingenuity, and to those who aspire to provide everlasting gifts to humankind, through the purposeful creation of innovative original ideas that promote well-being and serve the human experience.

Acknowledgments

I would like to express my deepest gratitude to my advisors Jim Hermanson and John Raiti for their incredible help, endless support, and unwavering encouragement throughout my adventurous journey at UW. I tremendously appreciate all their monumental efforts in facilitating my growth, nurturing my personal development, and guiding me in my scholarly endeavors among my academic pursuits. I'll always admire their unwavering drive for promoting the best research experience here at UW, and their full-hearted commitment to fostering the most successfully pristine environment for the UW scientific research community. I am so grateful and fortunate beyond belief to have had such devoted and amazing mentors along the way, whose roles substantially made my experience at UW thoroughly delightful, engaging, and memorable.

I would like to thank all the faculty who served on my academic committees along the way–John Kramlich, Ian Schnee, Dana Dabiri, and Carl Knowlen– for providing valuable feedback, and engendering interdisciplinary collaborative involvement to serve the broader UW intellectual community.

As Prof. Hermanson has mentioned at lab meetings, "Breakthroughs are always welcome, and even appreciated. Break-downs, on the other hand, are also always accepted." This quote characterizes the lab's mutually supportive environment and optimistic atmosphere. I would like to laud and thank my lab-mates– Andrew Janson, Shuba Murthy, Andrew Jacob, Lui Tsumura, Nathan Alexander, Jon Frydman, Mukund Gupta, and Phani Ponduri– for all our gregarious discussions and enjoyable teamwork. While sharing in both disappointment and elation along the way, it's been a pleasure and honor celebrating our successes together, while persistently maintaining a sense of curiosity and excitement for scientific experimentation and exploration.

I would like to extend my deepest thanks to our collaborators at University of Bremen's ZARM in Germany and at Kyushu University in Japan– Florian Meyer, Noelia Martinez Figueira, and Shion Ando– for accommodating three disparate time zones for our international teleconference Hydra-Con gatherings, and for consistently engaging in interesting discussions, always sharing illuminating investigative insights along the way, to connect together our various endeavors to share with the scientific community.

I would like to express my sincerest gratitude to my family, especially my preciously dear wife (Kristina) Shenger Wang– also a UW alum whom I met at UW while we were both students– for her incredible enlightening wisdom for my personal guidance, scientific planning and brainstorming for motivation, and steadfast patience throughout navigating my arduous UW journey. I absolutely could not have made it this far without her by my side.

I would like to express my kind thanks to Jennifer Huberman, Mack Carter, Stephanie Swanson, and Anant Anantram from the Department of Electrical and Computer Engineering for the incredible administrative support behind the scenes, as well as Akshay Gadre and Dinuka Sabahandu for the amazingly successful and enjoyable teaching assistant experiences while providing insightful pedagogical

advice and career guidance. I would also like to thank my all mentors at Wibotic, and fellow UW ECE alumni, especially– Ben Waters, Alex Huttinen, Timo Lahtinen, Jasmine Callon, Genki Marshall, Noel Hosking– for providing a fantastic opportunity to experience and learn about the engineering and robotics industry, expanding my horizons beyond the microcosm of the academic world.

Throughout my almost six years at UW in the EE program, I have had the privilege of participating in both student life and engaging with various other interdisciplinary departments outside of the direct immediate engineering school, contributing to my continued learning for my academic endeavors, shaping my formative educational growth, and fulfilling my intellectual zealous fervor. During my time at UW, while pursuing and completing my concurrent masters degrees in statistics and in applied mathematics, and simultaneously passing a significant portion of the graduate economics curriculum, and teaching for the Philosophy department, I've had the good fortune of encountering and getting to know the following fellow classmates and colleagues, including (in no particular order and not limited to):

Husky Math Club: James Zheng Cao, William Dudarov, Jerry Jiayi Gao, Ziying (Zoe) Huang, Logan Garwood, Kerenor Inger, Hannah Swoffer, Omzin Wunkaew, Xinyu (Xiyah) Chang, Alex Albors Juez, Tengis Batbold, Celine Sachi

Fellow UW Economics Classmates: Lucy Hong, Terrence Dai, Cheng Chen, Mahtab Karimi, Reuben Narad, Jinwei Zhang, Claire Jun Xu, Pengyu Wang

Fellow UW EE Classmates, EE Teaching Assistants, and IEEE Colleagues: Jordan Hsu, Jason Xie, Hubert Huang, Gen Sakura, Lucas Wang, Lucas Bucci, Viswa Virinchi Muppirala, Felix Schwock, Amber Chou, Ember Chow, William Livernois, Xinghua Sun, Winston Sun, Zijie Jin, Jayita Dutta, Sitong Zhou, Nicklaus Thompson, Deeksha Prabu, Dylan Jones

UW Interdisciplinary Engineering School Colleagues and Classmates: Rachel Hsu, Gantcho Dimitrov, Allison Gu, Mitsuki Shimomura, Jason Ginos, Collins Davis, Spencer Kraisler, Amy Sprague

UW Fellow Applied Math and Statistics Classmates: Hamza Golubovic, Federico Chung, Francie McQuarrie, Thayer Fisher, Steven Wilkins-Reeves, Claire Jun Xu, Pengyu Wang, Caelan Ritter

UW Philosophy Scholars and Colleagues: Kade Kichella, John Lesanne Ketema, Erica Bigelow, Brittney High, Kai Milanovich, Jesus Raya, Gary Zhou, Andrew Spier, Selina Liu, Hanbyul Kang, Chance Hoppenrath, Cloe Cha, Noga Rahat, Dylan Jones

Husky Electronic Music Producers: Songjae Kim, Gary Zhou, Jon

UW Japanese Language Exchange Kaiwa Table Clubmates: Mitsuki Shimomura, Lui Tsumura, Octi Zhang, Cameron McWilliams, Alice Che, Bryce Matsuda, Emi Nakashima, Mia Chon

Reflecting upon my years 2020-2025 at UW specifically, I would like to thank my close friends and jovial companion intellectual thinkers– especially those who are also fellow Seattle Huskies and affiliated University of Washington classmates and alumni, even if our time enrolled at UW may not have overlapped– for sharing in the ongoing joy of the journey's progression, investment in my personal devel-

opment by listening to my story and helping me reflect, providing diverse perspectives for emotional and creative support throughout the tough and challenging moments; and spending time listening to my ideas with shared interest and enthusiasm, whether at research showcases, exams and defenses, and various other gatherings over the years. Among these include (in no specific order and are not limited to): Max Bright, Ben Guyer, Trevor Hedges, Linda Hedges, Dan Hedges, Casey Gooch, Brandon Spicer, Spencer Peters, Fielder Gall, Meera Unadkat, Sam Oakes, Marco van Hilst, Dylan Thibault, A.C., Shawn Jullens, Bri Robertson, Griffin Donnelly, Frank Liu, Joe Lollo, Kayla Fisher, Michael Nisenzon, Kentaro Hoffman, Elda Mengisto, Alex Denova, John Crutcher, Peter Ballmer, Cooper Vincent, Burgess Malarkey, Brad Fitch, Whit Jamieson, Michael Omori, Nick Xing, Hongtai Yang, Justin Harjanto, David Zhai, Tang Song, Michael Hosford, Leo Stefurak, David Wyde, Jacob Mayer, Siva Sankrithi, Lauren Bricker, Quaint & Tom Doelger, Tom Butler, Caryn Abrey, Adam Ross, Helena Cohen, Vanya Cohen, Mark Steinbach, Chris Rose, Ethan Solomon, Sangeeta Dinghra, Bryan Yue, Chrissa da Gomez, Michael Rodney, Pete Holmes, Brian Fukuda, Allan Lau, Matthew Song, Thayer Fisher, Xander Abajian, Zihan Chen, Aman Thukral, Hannah Downs, Phyllicia Tjandra, Erica Guo, Hanshu Xu, Whitney Su, Kelvin Ng, Yann Huynh, Dave Fetterman, Amit Mital, Rebecca Norlander, David Lien, Stefan Ball, Cole Holland, James Myles, Benjamin Salman, Jonathan Salman, Jessica Luo, Slava Naprienko, Gustavo Berho, Brad Hawkins, Leo Zucker, Quentin Chi, Stefan Jones, Shen Hao, Siming Wang, Archer Xiaoxue Wu, Eric Liu, Chris Tapley, Matthew Coopersmith

I would also like to thank anybody else whom I have not yet mentioned. The culminating aggregate synthesis of all the cordial interactions throughout my life experiences thus far, have shaped my growth and mindset to be implicitly integrated into the following ideas to be shared.

Contents

Contents **7**

HYDRA Overarching Perspective **13**

1 Introduction **13**

2 Background **14**

2.1 LOX–H2 Fuel System 14

2.2 Problem Setup: Fundamental Chemical Physics Context 15

2.3 Experimental and Computational Approaches 16

2.4 Motivation for a New Approach 17

3 Literature Review **18**

3.1 Classical Foundations (1920–1960) 19

3.2 Modern Droplet-Combustion Theory (1960 – 1980) 20

3.3 Flame-Structure and Stability Analyses (1980–2000) 25

3.4 Modern Stability Analyses in Hydrogen Flames (2000–Present) 26

3.5 Experimental and Microgravity Developments (1980 – Present) 27

3.6 Numerical Approaches: Supercritical and Cryogenic Droplet Modeling (2000–Present) . . 29

3.6.1 Ice Formation in LOX Droplet Systems 29

3.7 Hydrogen-Oxygen Combustion Kinetics in the Heat and Mass Transport Context 30

3.7.1 Historical Background and Canonical Frameworks 30

3.8 Textbook Frameworks and Analytical Formulations 32

3.9 Hydrogen–Oxygen Chemical Kinetics 33

3.9.1 Foundational Kinetic Mechanisms 33

3.9.2 Validation Heritage 34

3.9.3 Modern Detailed Mechanisms 35

3.9.4 Refinements and Low-Temperature Pathways 35

3.9.5 Integration of Kinetics within the Transport Framework 36

3.9.6 Chemical Kinetics of H2-O2 Combustion in the Numerical Heat and Mass Transport Context 39

3.10 University of Washington LOX-H2 Numerical Modelling Lineage 48

3.10.1 Early OpenFOAM Exploration: Frydman (2018) 48

3.10.2 Incorporating Cryogenic Effects via Dilution: Gupta (2021) 49

3.10.3 Solver Enhancement via Variable Diffusion: Ponduri (2023) 53

3.10.4 Thematic Synthesis of the UW LOX-H2 Lineage . . . 56
3.10.5 Transition to Present Work . . . 57
3.11 Experimental Benchmark Basis: Meyer et al. (ZARM) LOx-H_2 Droplet Combustion Under Microgravity . . . 58
3.11.1 Context and Purpose of the Reference Experiment . . . 58
3.11.2 Novelty and Scientific Contribution . . . 58
3.11.3 Experimental Platform and Methodology . . . 58
3.11.4 Diagnostics and Measurement Techniques . . . 59
3.11.5 Operating Conditions and Parameter Space . . . 59
3.11.6 Observed Phenomena: Qualitative Experimental Outcomes . . . 60
3.11.7 Quantitative Data and Derived Parameters for Numerical Simulation . . . 62
3.11.8 Experimental Figures and Interpretation for Modeling . . . 63
3.11.9 Summary of Experimental Insights for Model Validation . . . 65
3.11.10 Key Physical Insights and Carryover Principles . . . 65
3.11.11 Experimental Correlations for Model Validation . . . 66
3.11.12 Numerical Modeling Alignment and Justification . . . 67
3.11.13 Validation Metrics and Performance Criteria . . . 68
3.11.14 Computational Simplification and Comparative Advantage . . . 68
3.11.15 Summary of Carryover Data and Modeling Relevance . . . 69
3.12 Computational Framework and Tools of the Trade . . . 70
3.13 Synthesis and Research Gap . . . 72

4 Interdisciplinary Contributions of the Original Simulator's Novel Methods to Combustion Science, Computational Physics, and Applied Mathematics 72

4.1 Establishing Model Assumptions: . . . 72
4.2 Original Simulator . . . 75
4.3 Analytical Theory's Foundational Framework . . . 76
4.3.1 Intuition Conveyed by Pure Mathematical Physics: . . . 78
4.3.2 Progressively Invoking Simplifying Assumptions . . . 80
4.3.3 Causal System Assumption . . . 80
4.3.4 Memoryless Property Assumption . . . 80
4.3.5 $\vec{Y}$'s Uniqueness in Generalized Dynamical System . . . 81
4.3.6 One Dimensionality Assumption . . . 81
4.3.7 Canonical-Form Fundamental Equation of Motion in 1D . . . 82
4.3.8 Novel Extension and Original Universal Generalization . . . 84
4.4 PDE Solutions: Single Species . . . 98

4.4.1 Diffusion without Source, Infinite Domain . . . 99
4.4.2 Diffusion without Source, One-Sided Reflecting Boundary, Semi-Infinite Domain . 100
4.4.3 Diffusion without Source, One-Sided Absorbing Boundary, Semi-Infinite Domain . 101
4.4.4 Source-less Diffusion upon Finite Domain between Two Insulating Walls: Neumann Boundary Conditions . . . 104
4.4.5 Source-less Diffusion upon Finite Domain between Two Insulating Walls: Neumann Boundary Conditions . . . 106
4.4.6 Source-less Diffusion upon Finite Region between Two Absorbing Walls: Dirichlet Boundary Conditions . . . 106
4.4.7 Diffusion without Source upon Finite Strip with Mixed Boundary Conditions . . . 113
4.4.8 Heating the Expanse from One End, Semi-Infinite Domain . . . 115
4.4.9 Heating Insulated Room from One Side . . . 118
4.4.10 Heating Room with Absorbing Barrier . . . 121
4.4.11 Extension: Heat Baths of Different Heights . . . 124
4.4.12 Sourced Diffusion, Infinite Domain: "Flame Heat Kernel" . . . 125
4.4.13 Flame Family solutions . . . 131
4.4.14 Diffusion with Source, One-Sided Reflecting Boundary . . . 131
4.4.15 Diffusion with Source, Absorbing Boundary . . . 132
4.4.16 Diffusion with Source, Neumann Boundary Conditions . . . 134
4.4.17 Diffusion with Source, Dirichlet Boundary Conditions . . . 136
4.4.18 Diffusion with Source, Mixed Boundary Conditions . . . 138
4.4.19 Drift Diffusion and Moving Source Cases . . . 139
4.4.20 Direct Spherical Transformation Invertible Mapping . . . 140
4.4.21 ODE when PDE too Complicated . . . 148
4.5 Multiple Species Scenario . . . 151
4.5.1 LOX Lever Rule: Novel Mathematical Result . . . 151
4.6 Numerical Analysis Theory . . . 153
4.6.1 Process of Converting to Numerical Scheme . . . 154
4.6.2 Derivation of Finite Difference Scheme . . . 155
4.6.3 Defining Numerical Parameters . . . 156
4.6.4 Meaning of Numerical Parameters and Interpretation of Coefficients . . . 157
4.6.5 Time-Weighting v/w Hyper-parameters . . . 157
4.6.6 Spatial-Weighting $g/q/s$ Hyper-parameters . . . 158
4.6.7 Arranging to Appropriate Mathematical Form . . . 159
4.7 Numerical Methods Computational Implementation . . . 160

4.7.1 Computational Complexity Theory . . . 160
4.7.2 Solving Linear Systems expressed as Matrix Equations . . . 162
4.7.3 Sparse Matrix Solutions . . . 162
4.7.4 Thomas Tridiagonal Matrix Algorithm . . . 163
4.7.5 Python Implementation . . . 165
4.7.6 Python Code Structure . . . 165
4.7.7 Handling Boundary Conditions . . . 167
4.7.8 Steady State ODE: Tridiagonal Algorithm Numerically Unstable . . . 169
4.8 Testing Code against Theory: Results . . . 169
4.8.1 One Species Case . . . 170
4.8.2 Single Species PDE Solution Comparison Testing . . . 170
4.8.3 Handling PDE Time Dynamics without Analytical Solution . . . 172
4.8.4 Multiple Species Case . . . 173

5 Methods **174**

5.1 Transport Properties and Diffusivities . . . 174
5.1.1 Underlying Physics and Theoretical Framework . . . 174
5.1.2 Binary Mass Diffusivity . . . 180
5.1.3 Numerical Implementation of Heat Diffusivity . . . 184
5.1.4 Numerical Implementation of Mass Diffusivity . . . 187
5.2 Chemical Kinetics Framework and Implementation . . . 189
5.2.1 Conceptual Overview: The “Wild Wilderness” of Chemical Kinetics . . . 189
5.2.2 Hierarchy of Combustion Mechanisms . . . 190
5.2.3 Philosophy and Context of the Reduced Mechanism . . . 190
5.2.4 Third-Body Considerations and Ambient Assumptions . . . 191
5.2.5 Algorithmic Implementation: The “Cantera Point” Concept . . . 191
5.2.6 Justification and Theoretical Framing . . . 192
5.2.7 Physical and Computational Relevance . . . 193
5.3 Interfacial Effects . . . 193
5.3.1 System Coupling and Feedback Loop Analogy . . . 194
5.3.2 Temperature Field and Flame Geometry . . . 194
5.3.3 Heat Conduction Contribution . . . 197
5.3.4 Radiative Transfer Contribution . . . 197
5.3.5 Total Energy Absorbed and Phase Change . . . 198
5.3.6 Stefan Flow and Surface Regression . . . 198
5.3.7 Comparison to Prior Models . . . 199

5.3.8 Domain and Boundary Conditions . . . 200
5.3.9 Ice Layer Effects . . . 203
5.3.10 Causal Pathways and Simulation Context . . . 204
5.4 CFD Postprocessing and Droplet Regression Overview . . . 209
5.5 Physical Framework and Quasi-Steady Approximation . . . 209
5.6 Computational Workflow Pipeline . . . 210
5.7 Data Handling and Wavelet Compression . . . 211
5.8 Droplet Regression Reconstruction and Temporal Backtracking . . . 212
5.8.1 Visual Summary and Interpretation . . . 213
5.9 Details within the CFD Postprocessing Stage: Handling Interfacial Effects . . . 213
5.9.1 Inspiration behind Parameterization and Motivation Behind Temporal Mapping . 213
5.9.2 Geometric Interpretation . . . 214
5.9.3 Generating Response Signal Function of Droplet Regression throughout Time . . . 214
5.9.4 Rate of Droplet Regression from Interfacial Effects in Postprocessing . . . 215
5.9.5 Postprocessing LOX Surface Area Ice Layer Coverage Fraction ψ . . . 216
5.9.6 Introducing the Ruffle-Factor Parameter $\phi(R)$ . . . 218
5.9.7 Leidenfrost-Type Correction to Decouple Effects . . . 219
5.9.8 Summary of Ad Hoc Interfacial Parameters . . . 221
5.9.9 Recapitulation and Outlook of Interfacial Phenomena during Postprocessing . . . 222

6 Results **223**

6.1 Comparison of Baseline Model with Theory and Experiment . . . 223
6.1.1 Classic D-Square Law Validation . . . 223
6.1.2 Flame Standoff and Droplet Diameter Evolution . . . 224
6.1.3 Flame Field Visualization: Stationary Temperature and Species Profiles of Various Droplet Radii . . . 225
6.1.4 Ruffle-Factor $\phi(R)$ Visualization . . . 227
6.2 Influence of Surface Ice Fraction ψ on Droplet-Regression . . . 228
6.2.1 Dataflow Schematic for $Q(t)$ and $D^2(t)$ Computation . . . 229
6.2.2 Interpretation: Why Different Diagnostic Plots $Q(t)$ and $D^2(t)$ Behave Similarly . 229
6.3 Effect of Ice Coverage ψ and Leidenfrost Adjustment upon Flame Standoff Radius throughout Droplet Lifetime . . . 230
6.4 Comparing Relative Effects of Radiation versus Conduction . . . 231
6.5 Droplet Lifetime Trends among all Parameters . . . 233

7 Discussion **234**

7.1 Non-Spherical Deformation of LOX Droplet 234

7.1.1 The Anisotropic Mechanisms Underlying Non-Spherical Deformation 234

7.1.2 Zooming into the Surface Ice 237

7.1.3 Ice Fraction and Its Modeling Implications 237

7.1.4 Modeling Logic Behind the Ruffle Factor $\phi(R)$ 239

7.1.5 Leidenfrost-Type Adjustment Factor 243

7.1.6 Strong Semblance of an Interpretable and Plausible Model 246

8 Conclusion **248**

8.1 Recapitulation, Novelty, and Significance 248

8.2 Future Work 251

8.3 Closing perspective. 251

References **252**

HYDRA Overarching Perspective

Our highly international, innovative, and interdisciplinary STEM research collaboration aims to use mathematics methods to engineer computational simulation technology for combustion science investigators.

1 Introduction

The demand for high-performance propulsion systems has grown in step with humanity's increasing ambition to expand into deep space. Among the many chemical propellants explored, liquid oxygen (LOX) combusting in gaseous hydrogen stands out as the state-of-the-art for cryogenic propulsion. The LOX–H_2 system achieves one of the highest known chemical specific impulses, surpassed only by hydrogen–fluorine, which is too toxic for practical use. This unique efficiency makes LOX–H_2 central to modern spaceflight, where minimizing propellant mass is a prerequisite for missions ranging from orbital transport to interplanetary travel. Beyond propulsion, LOX–H_2 fuel cells can supply electrical power and even potable water to spacecraft systems, extending their utility to life support. These combined attributes position the LOX–H_2 system as an indispensable enabler of long-duration missions and a foundation for humanity's eventual transition into a spacefaring civilization.

Despite its importance, the fundamental physics of LOX–H_2 combustion remain incompletely characterized, particularly in microgravity environments. In space, droplets of cryogenic propellant behave differently than in terrestrial settings: buoyancy, sedimentation, and gravitational instabilities are suppressed, while surface tension, diffusion, and thermal conduction dominate. Understanding the dynamics of single-droplet combustion under these conditions is critical, because droplet-scale processes form the basis for spray combustion, which governs practical rocket engines. By examining evaporation, flame structure, and transient kinetics at the single-droplet level, we can construct a foundation for predicting and optimizing the behavior of large-scale propulsion systems.

The HYDRA project addresses this challenge through an integrated program of experiment and computation. HYDRA is an international collaboration between the University of Washington (UW), the University of Bremen's ZARM facility, and Kyushu University. ZARM contributes world-class drop tower experiments, providing high-quality data on droplet ignition and flame propagation in reduced gravity. UW complements this with computational modeling, developing numerical frameworks to simulate the coupled heat, mass, and chemical processes at work. Together, these efforts advance both empirical and theoretical understanding, yielding insights neither approach could achieve alone.

2 Background

2.1 LOX–H2 Fuel System

The LOX–H_2 combination is favored in propulsion because it balances efficiency with practicality. Both propellants can be stored in cryogenic form, maximizing density while minimizing tank volume. Hydrogen's extremely low boiling point (∼20 K at 1 atm) makes it the natural vaporizing species, while oxygen (∼90 K) remains liquid at similar conditions. Introducing LOX droplets into gaseous hydrogen facilitates rapid evaporation and mixing, producing high flame speeds. Combustion yields water vapor, avoiding toxic byproducts associated with alternatives such as hydrogen–fluorine. These features improve engine performance while integrating with spacecraft resource systems, since exhaust water can be recycled for life support.

The combustion process operates as a positive feedback loop: heat from the flame evaporates oxygen at the droplet surface, generating vapor that reacts with hydrogen to sustain the flame. The droplet gradually shrinks until it vanishes. The timescale of this process depends on initial droplet radius, ambient pressure and temperature, and flame kinetics. In microgravity, buoyancy-driven convection is absent, allowing nearly perfect spherical symmetry in the flame envelope. This symmetry provides a simplified yet representative model for studying reactive transport phenomena.

2.2 Problem Setup: Fundamental Chemical Physics Context

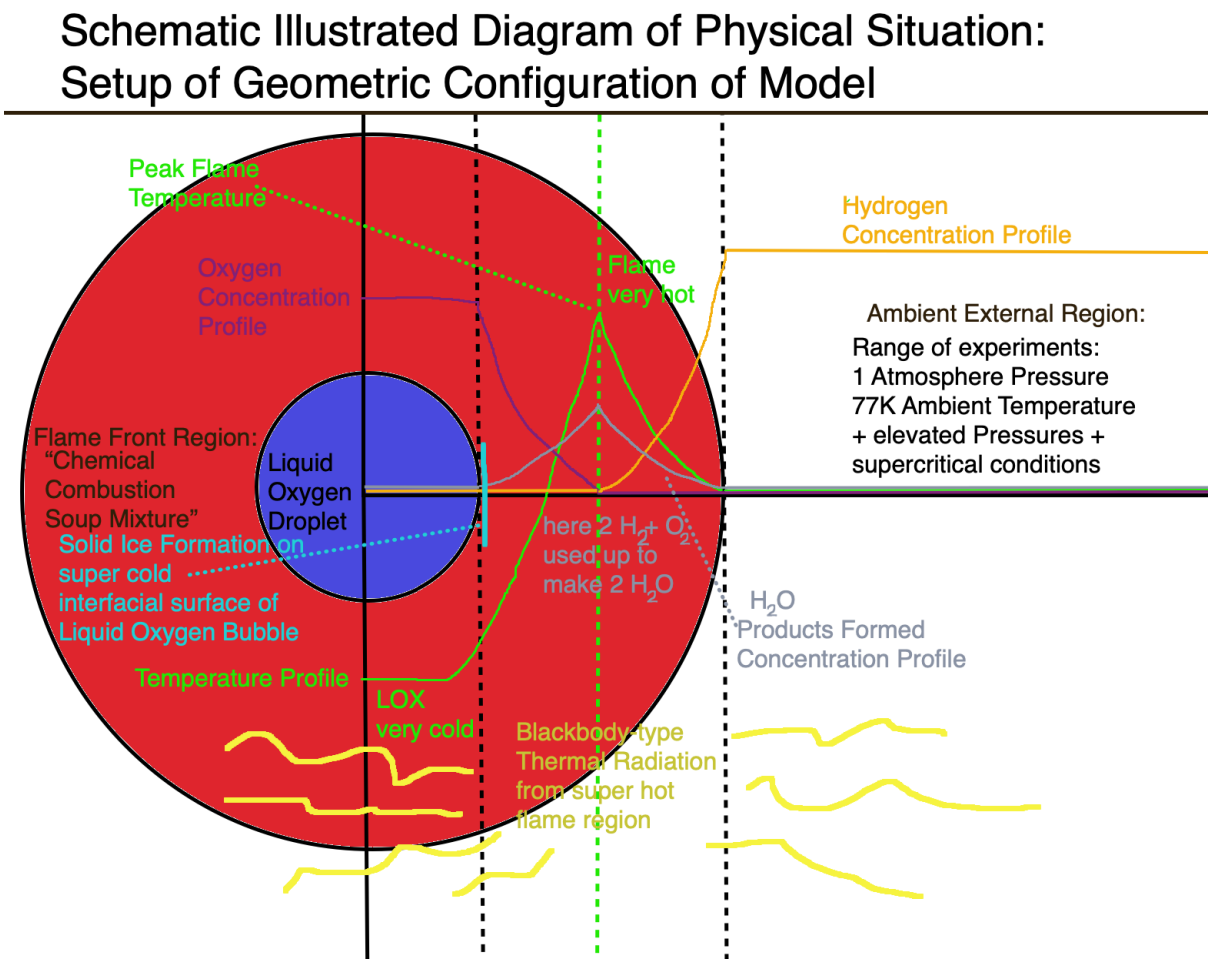

Figure 1: Schematic of the physical system: a cryogenic LOX droplet immersed in hydrogen gas. Following ignition, heat released from combustion evaporates oxygen from the droplet surface, which mixes with gaseous hydrogen to sustain the flame. This feedback loop produces a spherically symmetric flame structure, accompanied by radiation losses and possible ice formation that may perturb combustion. Symmetry assumptions reduce the problem to a one-dimensional radial framework.

At the center of the system lies a cryogenic LOX droplet, initially near $T \sim 80\,\mathrm{K}$, suspended in hydrogen. Ignition initiates the global exothermic reaction

$$\mathrm{O_2} + 2\,\mathrm{H_2} \quad \rightarrow \quad 2\,\mathrm{H_2O} + \mathrm{Heat}.$$

The flame then sustains itself through a feedback mechanism: thermal energy released at the flame front conducts inward, evaporating oxygen at the droplet surface; this vapor diffuses outward, mixes with hydrogen, and reacts, releasing more heat. Simultaneously, the system loses energy via endothermic boiling of the droplet and radiation to the environment. As long as sufficient LOX remains, the reaction is self-propagating. Ultimately, the droplet lifetime is determined by the interplay of transport, kinetics, and thermal balance.

The flame envelope contains not only major reactants and products but also transient intermediates such as hydroxyl (OH) radicals, which are optically active and widely used in chemiluminescence diagnostics, which has been a foundational flame diagnostic since Gaydon's spectroscopy work [1], and more recently laser-based techniques [2]. Experimental techniques such as OH* imaging and Schlieren visualization capture complementary aspects of the flame front: the former highlights chemically active regions through radical emission, while the latter resolves refractive index gradients associated with density and temperature. These methods are conceptually analogous to computational level-set or fast marching approaches in that all provide a means of tracking the evolving flame interface. Such intermediates and diagnostics underscore the chemical and structural complexity of the reaction zone.

2.3 Experimental and Computational Approaches

Experimental access to microgravity combustion is enabled by facilities such as ZARM's 150-meter drop tower, which provides several seconds of reduced-gravity conditions per run. In these experiments of Meyer et al (2022) [3], droplets are suspended, ignited, and recorded with high-speed optical diagnostics. While such data capture global flame structure and lifetimes, they are constrained by imaging resolution, sensor access, and experiment duration.

Computational modeling fills these gaps. Combustion simulations range from direct numerical simulation (DNS) to reduced-order CFD models. For LOX–H_2, challenges include cryogenic thermophysical properties, transient evaporation, and detailed chemical kinetics. Prior UW efforts (e.g., Gupta's OpenFOAM wedge simulations; Ponduri's EBI–DNS extensions) demonstrated that reduced mechanisms (4–6 steps) could reproduce flame temperatures near 3100 K, in line with experiments. However, these approaches were computationally demanding, often requiring cluster-scale resources and equilibrium assumptions. International efforts faced similar issues: Aachen's Matlab routines neglected real-gas dynamics (Ren et al 2021) [4], while Klinkov's spraylet model applied to droplets in different regimes (Eigenbrod et al 2012) [5].

Unlike prior UW implementations (e.g., Gupta, Ponduri) [6, 7] the present solver achieves significant computational and structural advantages. By exploiting one-dimensional spherical symmetry, each timestep scales linearly with the number of grid points ($\mathcal{O}(N)$). Typical runs with $N \sim 2000$ resolve transient flame evolution in minutes on a commodity laptop or free cloud platform, without GPU acceleration. This tractability enables rapid parametric studies and parallel execution across multiple sessions.

Beyond efficiency, the framework couples gas-phase reaction–diffusion dynamics with liquid-phase feedback at the droplet surface. Stefan flow arising from oxygen vaporization is incorporated directly via heat conduction (Fourier law) and radiative transfer between concentric spherical surfaces, ensuring that flame standoff distance, evaporation rate, and droplet regression are dynamically consistent. This

coupling was absent in prior UW codes, which either imposed equilibrium flame structures (Gupta [6]) or neglected surface feedback altogether (Ponduri [7]). Consequently, the present solver is the first UW framework capable of resolving fully coupled liquid–gas dynamics for LOX–H_2 droplets under microgravity conditions.

A detailed comparison with prior approaches, including strengths and limitations of each, will be provided in the Discussion.

2.4 Motivation for a New Approach

These limitations motivate a new solver, built from first principles in Python. By exploiting one-dimensional spherical symmetry, the framework reduces computational overhead while preserving essential physics. It integrates heat conduction, mass diffusion, chemical kinetics, and radiation into a coupled, time-dependent system of parabolic PDEs. This framework captures both equilibrium flame structures (e.g., Burke–Schumann profiles) and transient evolution, including ignition, extinction, and droplet lifetimes. Its modular design also permits extension to radiative losses and surface ice formation, both highly relevant to cryogenic combustion.

The UW solver thus advances HYDRA's mission by providing a rigorous yet accessible computational tool. The following chapters establish its theoretical foundation, detail its numerical implementation, and validate it against analytical and experimental benchmarks.

Existing combustion codes range from simplified Matlab-based solvers to large-scale DNS/LES frameworks (e.g., OpenFOAM, CHEMKIN, EBI codes). These tools are powerful in their intended domains, but present challenges when adapted to cryogenic droplet combustion. Simplified models often neglect critical physics (finite-rate chemistry, multi-phase coupling), while general-purpose CFD packages impose steep overhead in both computational cost and user-level customization. Moreover, the opacity of large frameworks can hinder physical insight: implementing targeted modifications requires familiarity not only with combustion physics but also with the internal numerics of multiphase solvers (e.g., operator splitting, stiff chemistry integration, Jacobian reduction). In practice, this barrier has limited progress in specialized microgravity droplet studies, where research groups often face trade-offs between fidelity, transparency, and usability.

The present work addresses this gap by constructing a one-dimensional solver from first principles. While mathematically general, the framework is transparent, computationally efficient, and directly tailored to the particular physics of cryogenic LOX–H_2 droplets. This approach enables precise control over the balance of chemistry, transport, and phase-change effects, while remaining extensible for future applications. In this sense, the solver is not only a tool for the HYDRA project but also a contribution to the broader combustion community: a case study in how clarity and accessibility in simulation design can empower domain-specific research. Furthermore, beyond reproducing canonical behaviors of combustion

systems, the framework is applied to specifically probe the interplay of radiative losses and surface ice formation, quantifying their influence on droplet regression rates, flame standoff distance, and deviations from idealized spherical symmetry.

3 Literature Review

The following review is organized to reflect the historical and conceptual development of droplet combustion theory, beginning with classical diffusion models, progressing through finite-rate and transient formulations, extending into modern stability and microgravity studies, and culminating in cryogenic droplet modeling. This structure highlights how successive refinements in kinetics, transport, and radiation coupling have progressively closed the gap between idealized theory and observed microgravity behavior.

A comprehensive mathematical consolidation of these classical ideas appears in the canonical spherical droplet combustion formulation (see, [8, 9])). Under the quasi-steady approximation and assuming spherical symmetry, the interfacial jump conditions at the droplet surface ($r = r_s$) yield the standard expressions for mass and energy conservation:

$$\begin{aligned} \lambda \frac{dT}{dr} &= \rho v Q_v, \\ \rho v Y_F - \rho D_F \frac{dY_F}{dr} &= \rho v, \\ \rho v Y_O - \rho D_O \frac{dY_O}{dr} &= 0. \end{aligned}$$

These relations, coupled with the Clausius–Clapeyron relation for vapor pressure and assuming the droplet surface remains at the boiling temperature T_B, lead to the classical expression for the burning rate:

$$\dot{m} = 4\pi r_s \left(\frac{\lambda}{c_p} \right) \ln\left(1 + B\right),$$

where B is the transfer number reflecting the ratio of thermal driving force to vaporization resistance. The droplet regression rate follows the well-known d^2-law:

$$d^2(t) = d_0^2 - Kt, \qquad K = \frac{8(\lambda/c_p)}{\rho_l} \ln(1 + B),$$

which remains a foundational benchmark for both experimental validation and numerical modeling. These equations represent the Burke–Schumann diffusion flame limit for a stationary, isolated droplet in a quiescent medium.

3.1 Classical Foundations (1920–1960)

The foundational period of droplet combustion theory laid the mathematical and physical groundwork for understanding diffusion-controlled flame behavior. Burke and Schumann's seminal 1928 work [10] defined the diffusion-flame limit, treating combustion as an infinitely fast chemical reaction localized along a stoichiometric surface that separates fuel and oxidizer regions. By modeling the laminar jet flame as a one-dimensional mixing problem under steady-state and constant-density assumptions, they introduced a framework that would later be adapted to spherical geometries such as droplet flames. Crucially, their work established that species diffusivity, rather than turbulence, governs flame structure in diffusion-dominated regimes. Building on these ideas, Spalding (1953) [11] introduced a quantitative model of droplet burning, deriving the mass-transfer number $B_M = \frac{Y_{F_s} - Y_{F_\infty}}{1 - Y_{F_s}}$ which relates vaporization flux to local fuel concentrations. His derivation of the d^2-law, $d^2(t) = d_0^2 - Kt$, linked the rate of droplet regression to a diffusion-controlled burn rate, encapsulated by the effective burning constant K. He also introduced the heat-transfer number B_T, unifying mass and energy conservation at the droplet surface, and showing that the steady burning rate is proportional to $\ln(1 + B_M)$. Experimental validation of this theoretical framework came shortly after in the landmark study by Godsave (1953) [12], who investigated the combustion of single suspended fuel droplets in quiescent air. Using high-speed cinematography to track droplet regression, Godsave confirmed the d^2-law and demonstrated that vaporization in high-temperature combustion is governed by heat transfer from a spherical diffusion flame that stands off from the droplet surface. Modeling the system as two concentric spheres—droplet and flame front—he accounted for conductive and radiative heat transfer, showing excellent agreement (within 1 %) between predicted and observed burn rates. Importantly, his work revealed that thermal properties such as heat of vaporization, rather than vapor pressure alone, dictate the droplet burning rate—an insight that refined earlier purely diffusive interpretations. Complementing these theoretical and experimental advances, Ranz and Marshall (1952) [13] provided widely-used empirical correlations for the Sherwood and Nusselt numbers under forced convection, notably $Sh = 2 + 0.6 Re^{\frac{1}{2}} Sc^{\frac{1}{3}}$, which have become foundational in modeling convective transport in droplet combustion. These correlations were later essential for interpreting droplet behavior in terrestrial experiments and contrasted with findings under microgravity. The collective insights of this period, including extensions by Frössling on moving droplets and early discussions of Stefan flow, established a canonical steady-state model. However, this classical model neglected transient heating, finite-rate chemistry, and real-fluid effects, paving the way for later theoretical expansions that moved from steady-state analytics to time-dependent, computational approaches. These classical formulations, though elegant in their analytic closure, inherently assumed steady-state burning and infinite chemical rates. Their limitations, particularly in capturing transient heating, ignition delays, and finite-rate kinetics, motivated the modern developments that followed.

3.2 Modern Droplet-Combustion Theory (1960 – 1980)

The period from 1960 to 1980 marked a significant advancement in droplet combustion theory, driven by the introduction of finite-rate chemistry, transient heating, and multi-component diffusion into the analysis. During this time, key theoretical frameworks emerged, building on the classical foundations established in the previous decades.

A major breakthrough came from Williams (1965) [14], who expanded on the earlier work by incorporating the full set of transport equations in spherical coordinates to describe the behavior of droplets during combustion. In this framework, the key dimensionless numbers—such as the Damköhler number (Da) and the Lewis number (Le)—were introduced, enabling a clearer distinction between different combustion regimes. The Damköhler number is defined as

$$Da = \frac{\dot{\omega} L^2}{D},$$

where $\dot{\omega}$ is the reaction rate, L is the characteristic length scale of the droplet, and D is the diffusivity of the fuel species. In the diffusion-controlled regime, Da is large, indicating a dominance of mass transfer, while a small Da suggests kinetic control. The Lewis number, defined as

$$Le = \frac{\alpha}{D},$$

where α is the thermal diffusivity, controls the flame standoff distance and is typically less than 1 for hydrogen (H_2), close to 1 for hydrocarbons, and greater than 1 for heavier fuels. The work of Williams distinguished the vaporization, ignition, and combustion phases of droplet combustion, providing a more nuanced understanding of the interaction between chemical kinetics and mass transfer.

A key feature of this period was the shift from steady-state assumptions to time-dependent models. Williams introduced non-steady diffusion solutions and applied matched asymptotics to analyze ignition dynamics. This allowed for the inclusion of transient heating effects, as opposed to the classical assumption of instantaneous steady-state burning. In particular, the analysis highlighted the significance of finite-rate kinetics, which involved considering activation energy asymptotics and their influence on the reaction zone thickness. This transitional phase was later synthesized comprehensively by Law (1982), who delineated the limitations of classical models—most notably the d^2-law and quasi-steady assumptions—highlighting the need to incorporate transient heating, vapor accumulation, and variable property effects into droplet combustion theory [15]. Law's synthesis marked a shift from empirical correlations to physics-based models, emphasizing that vapor accumulation and unsteady heating significantly affect ignition delay and flame standoff distance, especially in the early droplet lifetime.

Building on this, Matalon and Law (1983) conducted a focused theoretical analysis of gas-phase transient diffusion during droplet combustion, showing that while quasi-steady assumptions remain largely

valid under subcritical conditions, transient effects such as fuel vapor buildup can meaningfully alter the burning rate and flame structure [16]. Their analysis reaffirmed the utility of the quasi-steady framework while also defining its limits, especially in regimes where vapor accumulation and surface regression occur over comparable timescales.

Extending this work, Chao, Matalon, and Law (1985) incorporated a detailed treatment of gas-phase transient diffusion during droplet ignition, rather than just combustion. Their analysis revealed that ignition may occur within the transient diffusion zone rather than at the traditionally assumed reaction zone near the droplet surface—especially under conditions of low gas-to-liquid density ratios and high activation energies. This refinement led to a modified ignition Damköhler number that can substantially exceed classical predictions, highlighting the critical influence of unsteadiness on ignition delay and ignitability criteria [17]. Importantly, their work demonstrated that increased gas-phase unsteadiness, such as turbulence, can delay or suppress ignition altogether—contradicting quasi-steady ignition assumptions common in earlier models.

The development of these models led to the introduction of a new paradigm for droplet combustion that distinguished between the Burke-Schumann regime, characterized by a steady, diffusion-controlled flame, and the finite-rate regime, where chemical kinetics played a central role, assummarized by the classic textbooks on the subject of combustion. [14, 18, 19] In this context, the droplet combustion process was described in terms of two distinct phases: a vaporization phase governed by diffusion and a combustion phase governed by finite-rate chemical kinetics. The transition between these phases was influenced by the droplet response times, specifically the thermal response time (τ_T) and the diffusive response time (τ_D). These response times were shown to be crucial in determining the transient behavior of the droplet, such as the time required for the droplet to reach steady burning.

The finite-rate generalization of the Burke–Schumann model, as formalized by Matalon [8, 20, 9], extended this framework to include Arrhenius reaction kinetics and multicomponent diffusion.

Canonical Steady-State Profiles

To complete the analytical framework of steady droplet combustion, we briefly summarize the explicit solutions for temperature and species profiles in the vaporization-only and combustion cases. Although frequently omitted in experimental contexts, these profiles provide a rigorous mathematical structure that underlies classical results such as the d^2-law and are foundational in constructing numerical solvers or validating reduced-order models.

We note in particular the dependence of the dimensionless mass flux M (and thus burning rate) on the Damköhler number, which scales with droplet radius and ambient pressure as $Da \sim a^2 P_0$. Throughout this analysis, unity Lewis numbers are assumed ($Le = 1$).

Vaporization-only case ($Da = 0$):

$$
\begin{aligned}
Y_F(r) &= 1 - e^{-M/r}, \\
Y_O(r) &= Y_{O_\infty} e^{-M/r}, \\
T(r) &= T_s - L_v + L_v e^{M(1-1/r)},
\end{aligned}
$$

where $M = \ln\left(1 + \frac{1-T_s}{L_v}\right)$ ensures $T(1) = T_s$. In dimensional terms, the vaporization rate is:

$$
\boxed{\dot{m} = \frac{4\pi a \lambda}{c_p} \ln\left(1 + \frac{c_p(T_\infty - T_B)}{Q_v}\right)},
$$

with $B_v = \frac{c_p(T_\infty - T_B)}{Q_v}$ representing the classical Spalding transfer number.

Combustion case (Burke–Schumann limit, $Da \to \infty$):

The temperature and species fields are defined piecewise about the flame standoff radius r_f, determined by continuity and interfacial balance conditions. Define ν as the stoichiometric mass ratio and q the non-dimensional heat release:

$$
Y_F(r) = \begin{cases} 1 - (1 + \nu^{-1} Y_{O_\infty}) e^{-M/r}, & r < r_f, \\ 0, & r > r_f, \end{cases}
$$

$$
Y_O(r) = \begin{cases} 0, & r < r_f, \\ (\nu + Y_{O_\infty}) e^{-M/r} - \nu, & r > r_f, \end{cases}
$$

$$
T(r) = \begin{cases} (T_s - L_v)(1 - e^{-M/r}) + (1 + q\nu^{-1} Y_{O_\infty}) e^{-M/r}, & r < r_f, \\ 1 + (T_s - 1 + q - L_v)(1 - e^{-M/r}), & r > r_f. \end{cases}
$$

The matching condition at $r = 1$ enforces:

$$
M = \ln\left(1 + \frac{1 + q\nu^{-1} Y_{O_\infty} - T_s}{L_v}\right).
$$

The burning rate and flame location are then:

$$
\boxed{\dot{m} = \frac{4\pi a \lambda}{c_p} \ln\left(1 + \frac{c_p(T_\infty - T_B) + Q Y_{O_\infty}/\nu_O W_O}{Q_v}\right)},
$$

$$
\boxed{\tilde{r}_f = \frac{a \ln(1 + B_c)}{\ln\left(1 + \nu_F W_F Y_{O_\infty}/\nu_O W_O\right)}},
$$

where B_c is the combustion transfer number.

Finally, the flame temperature is:

$$\boxed{\tilde{T}_f = T_\infty + \frac{(Q/\nu_F W_F - Q_v)/c_p - (T_\infty - T_B)}{1 + \nu_O W_O/\nu_F W_F Y_{O_\infty}}}.$$

These explicit expressions represent the exact steady-state solutions in the infinite and zero Damköhler limits, and serve as useful benchmarks for validating asymptotic limits, estimating burning rates, or developing semi-analytical models in combustion simulations.

These steady-state solutions, derived in the canonical Burke–Schumann ($Da \to \infty$) and pure vaporization ($Da = 0$) limits, define the foundational structure of droplet combustion models. The burning rate, flame standoff radius, and flame temperature all emerge from a balance of diffusive transport, Stefan flow, and interfacial conditions, with the dimensionless mass flux M encoding the strength of the outward vaporization flow. This formulation predicts characteristic features such as the "S-curve" dependence of the burning rate on droplet size and ambient pressure ($Da \sim a^2 P_0$), as well as extinction thresholds and autoignition conditions. These transitions, later confirmed via activation energy asymptotics, underscore the sensitivity of droplet combustion to both chemical kinetics and transport parameters.

The interaction between the gas-phase and liquid-phase energy balances also became a focal point of this research. It was recognized that energy exchange between the gas and liquid phases had a significant effect on the droplet's combustion characteristics, particularly in the presence of transient heating. This was formalized by introducing the concept of a heat-transfer number (B_T), which represented the interplay between mass and energy conservation at the droplet surface.

In parallel, Sirignano (1999) [21] introduced a more detailed analysis that included the effects of internal circulation and liquid-phase conduction within the droplet. This extension took into account the transient heat conduction within the droplet, which was governed by the Biot number (Bi), providing a more complete understanding of the heat transfer process. Sirignano's work also explored the effects of convective and radiative heat losses at the droplet boundary, further enhancing the predictive capability of droplet combustion models.

Several key dimensionless numbers emerged during this period that provided insights into the different regimes of droplet combustion:

- The Damköhler number, Da, governs the balance between chemical kinetics and mass transfer, indicating whether combustion is diffusion-controlled or kinetically limited.
- The Lewis number, Le, controls the flame standoff and is particularly important for determining the structure of the flame front in various fuels.
- The Stefan number, Ste, defined as

$$Ste = \frac{c_p(T_b - T_\infty)}{L_v},$$

where c_p is the specific heat at constant pressure, T_b is the droplet surface temperature, T_∞ is the ambient temperature, and L_v is the latent heat of vaporization, governs the latent heat penalty and the efficiency of droplet vaporization. ($Q_v = L_v$ for a single-component droplet, where the vaporization enthalpy equals the latent heat of vaporization)

- The Péclet number, Pe, defined as

$$Pe = \frac{uL}{\alpha},$$

where u is the relative velocity between the droplet and the surrounding gas, governs the relative importance of convective and diffusive heat transport. This number is often suppressed under microgravity conditions, where convective transport is reduced.

Together, these dimensionless numbers provided a robust framework for characterizing droplet combustion across a variety of conditions. However, despite the analytical progress made during this period, many of the regimes identified remained challenging to describe fully through simple asymptotic solutions. This limitation underscored the need for experimental and numerical methods to probe regimes beyond the reach of classical theory. As the theoretical framework continued to evolve, it became clear that analytical models alone could not capture the complexity of droplet combustion across all conditions. This necessitated the development of advanced experimental techniques and computational models to explore transient and multi-phase phenomena that were beyond the scope of traditional asymptotic approaches.

While single-droplet models offered foundational clarity, their limitations became increasingly apparent in multi-droplet environments. Sangiovanni and Labowsky (1982) [22] provided one of the first systematic experimental and theoretical investigations of droplet–droplet interaction by analyzing linear arrays of monodispersed fuel droplets burning in a flat-flame environment. Their key finding—that burning time nearly doubles when droplet spacing is reduced to two diameters—highlighted how even moderate proximity can significantly disrupt the classical d^2-law behavior due to competition for oxidizer. Their work introduced the quasi-steady (QS) "halo model" to capture vapor field interactions and demonstrated that these effects are largely independent of fuel type, droplet size, or ambient conditions, indicating a universal behavior driven by spatial configuration. Using a Laplace-based method-of-images approach, they validated their model against high-speed photography experiments across various fuels and droplet sizes (100–300 μ m), achieving close agreement despite idealized assumptions. Crucially, they observed that interaction effects persisted even at large spacings (up to 25 diameters), establishing

that droplet isolation is rarely valid in practical spray conditions.

This work represents a critical bridge between classical isolated-droplet theory and the more complex reality of droplet clusters and sprays. It provided the first strong quantitative evidence that single-droplet data alone are insufficient for predictive modeling of real-world combustion systems, and it helped lay the groundwork for spray combustion frameworks that explicitly incorporate inter-droplet coupling via vapor field overlap, shielding, and collective heat and mass transfer.

3.3 Flame-Structure and Stability Analyses (1980–2000)

During the final decades of the 20th century, substantial progress was made in understanding the structure and stability of diffusion flames, particularly through the integration of theoretical, numerical, and asymptotic methods. This period marked a significant deepening in the theoretical framework connecting flame stability to radiation and hydrodynamic coupling, with notable contributions from Matalon, Ludford, Bechtold, and others. Matalon and Ludford (1980) [8], followed by Bechtold and Matalon (1987) [23], developed a linear stability analysis for diffusion flames, employing an eigenvalue formulation that enabled the identification of critical conditions for cellular instabilities. Of particular importance was their derivation of a critical Lewis number below which diffusion flames become unstable, which is especially relevant for hydrogen-oxygen mixtures where $Le < 1$. Their analysis also yielded an important scaling law for the flame standoff distance, $\delta_f \sim \sqrt{D/\dot{r}}$, providing insight into the balance between diffusion and surface consumption rates.

Building on this foundation, Jackson and Matalon (1992) [24] extended the analysis to stagnation-point flames, a configuration that serves as a local analog to spherical droplet flames. This work predicted the flame's response to imposed strain rates and laid the groundwork for later extinction and ignition diagrams by establishing critical strain conditions leading to flame extinction.

Meanwhile, a broader unifying framework emerged through the work of Buckmaster, Clavin, and Peters in the 1990s [25]. These researchers advanced the flamelet concept, wherein local flame structure is preserved despite global unsteadiness. Their stretched-flame theory helped clarify the parameter space, containing specifically the Karlovitz (Ka) and Damköhler (Da) numbers, that governs flame extinction and reignition behavior in turbulent flows. This theory provided essential tools for analyzing combustion in chaotic regimes characterized by large strain and curvature and extreme gradients.

Radiative heat transfer, long treated as a secondary effect, was also more rigorously integrated into flame stability analyses during this period. Kurdyumov (2002) [26] and Bechtold (2005) [27] incorporated gray-gas radiation into the energy equation, revealing how radiative heat loss alters the thermal structure of the flame. Their findings showed that radiation tends to flatten temperature gradients, thereby increasing susceptibility to extinction. Importantly, the energy equation now included a nonlinear radiative source term of the form $\dot{q}_{\text{rad}} \propto T_f^4 - T_s^4$, capturing the temperature-dependent nature of

thermal radiation more realistically.

In addition to these macroscopic insights, studies of micro-instabilities also began to emerge. These analyses predicted oscillatory "breathing modes" near the flammability limit—dynamic instabilities manifesting as periodic variations in flame position and structure. Such behaviors, once theoretical curiosities, such peered into through analytical modelling by Addabbo (2002) [28], were later corroborated in controlled droplet combustion experiments (e.g., Dietrich, 2000s) [29, 30], confirming the presence of flame-wrinkling and transient oscillations under near-limit conditions.

While these foundational studies provided crucial asymptotic and analytical insights into flame behavior, they typically treated key physical couplings, particularly diffusion, radiation, and finite-rate chemistry, in a decoupled or idealized fashion. In contrast, modern computational frameworks like with what we're doing at HYDRA now incorporate transient solvers that resolve these couplings explicitly. HYDRA's ability to simultaneously capture diffusion, radiation, and kinetic interactions in time-resolved simulations represents a direct numerical realization of the coupling mechanisms that were historically studied in isolation. This capability provides a powerful bridge from theoretical predictions to experimentally observable flame behaviors under realistic conditions.

3.4 Modern Stability Analyses in Hydrogen Flames (2000–Present)

While much of the early theoretical work on flame stability provided deep asymptotic insights, more recent studies have employed high-fidelity numerical and experimental methods to revisit these classical results under more realistic conditions—especially for hydrogen/air mixtures, which are of particular relevance for LOX–H_2 droplet combustion.

Frouzakis et al. (2015) [31] conducted a direct numerical simulation (DNS) study of hydrogen/air flame instabilities using the spectral element solver Nek5000. By resolving detailed transport and full chemical kinetics, they showed how both hydrodynamic (Darrieus–Landau) and thermo-diffusive instabilities govern flame propagation in two-dimensional domains of varying widths. Their findings confirmed that for rich and stoichiometric mixtures, hydrodynamic instabilities dominate, producing single-cusp flame fronts that propagate 24% faster than laminar speeds. In contrast, lean mixtures exhibited pronounced thermo-diffusive destabilization, producing highly wrinkled, cellular flames that propagate up to 60% faster. A key parameter was the effective Lewis number, which determined the relative dominance of the two instability types.

Crucially, the study validated linear instability growth predictions in the early regime and demonstrated how nonlinear perturbation growth transitions to complex cellular morphologies. These behaviors were found to depend strongly on domain size and Lewis number—highlighting a critical domain threshold above which instability grows. This work directly supports modern flame kernel modeling by quantifying how instability mechanisms alter flame surface area, which in turn affects burning rate and

droplet lifetime. It also validates the use of reduced-order models (e.g., Markstein number approaches) by comparing DNS results to classical theory, thereby justifying their use in larger-scale simulations.

Complementing these numerical insights, Beeckmann et al. (2017) [32] performed a comprehensive experimental and theoretical investigation of instability onset in spherically expanding hydrogen/air flames. Using high-speed Schlieren imaging in a pressurized combustion chamber, they captured the evolution of flame surface cellularity across a wide range of pressures (1–15 bar) and equivalence ratios (ϕ = 0.5–2.0). Their study introduced three critical radii—visual onset ($R_{c,1}$), full cellular development ($R_{c,2}$), and theoretical instability threshold ($R_{c,\text{theory}}$)—providing a more nuanced framework for quantifying the onset of instability.

They found that instability onset occurs at smaller radii with increasing pressure and that theoretical predictions often underestimate the actual observable threshold by a factor of 3–5. By extending linear stability theory with temperature-dependent transport, they achieved good agreement with experimental flame speeds. Importantly, their results highlighted the importance of defining the correct flame thickness and accounting for Lewis number variation, particularly under engine-relevant and near-limit conditions.

Together, these studies provide modern, high-resolution evidence for how flame instability modifies hydrogen/air combustion behavior. Their results support the development of instability-aware submodels for flame speed, burning rate, and ignition kernel growth—all of which are crucial when coupling vapor-phase flame dynamics to evaporating LOX–H_2 droplets. These contributions reinforce the broader narrative that instability-enhanced flame surface area can substantially alter combustion timescales and must be accounted for in accurate droplet lifetime predictions.

While these foundational studies laid the theoretical groundwork for understanding flame stability, they often relied on simplifying assumptions and decoupled physics. More recent work has sought to validate and extend these models using high-resolution simulations and experiments, particularly in hydrogen-rich systems.

3.5 Experimental and Microgravity Developments (1980 – Present)

While the high-fidelity simulations and laboratory studies discussed above have advanced our understanding of flame instability under controlled conditions, microgravity experiments have played a pivotal role in isolating these phenomena in canonical geometries, free from buoyancy-driven convection. Additionally, while theoretical and asymptotic analyses have provided deep insights into the behavior and stability of diffusion flames, the validation of these models, particularly under idealized conditions, has relied heavily on experimental investigations. Beginning in the 1980s and accelerating with the advent of space-based research platforms, a wide body of microgravity experiments has emerged, enabling precise observation of droplet combustion phenomena in the near-complete absence of buoyancy-driven convection.

NASA's drop towers and Space Shuttle missions for the FLEX series of experiments, notably the Flame-Drop and Droplet Combustion Experiment [DCE] [33, 34, 35], provided some of the earliest and most comprehensive datasets on single-droplet burning under reduced gravity. These experiments confirmed several foundational predictions of classical theory. For example, the d^2-law governing the quadratic decrease in droplet diameter over time, was validated under microgravity conditions, where the suppression of natural convection permits a nearly spherically symmetric flame structure.

Beyond confirming steady-state behavior, these studies revealed dynamic phenomena that previous models only hinted at. Flame oscillations, radiative extinction, and transient standoff dynamics were all directly observed. Accurate measurements of droplet surface regression, flame radius, and temporal evolution of flame temperature have provided critical benchmarks for validating and refining theoretical and computational models.

The ZARM drop tower in Bremen, Germany, offered another key platform, enabling approximately 4.7 seconds of drop mode freefall (9.3 seconds catapult mode) at $10^{-6}g$, during which combustion experiments involving LOX-H_2, n-heptane, and methanol droplets were conducted with high spatial and temporal resolution. This facility proved especially valuable in achieving symmetrical flame configurations, critical for isolating diffusion and radiation effects from convective artifacts.

Advanced diagnostics played a crucial role in characterizing flame behavior. Shadowgraph and Schlieren techniques were employed to resolve gas-phase density gradients, while chemiluminescence imaging (e.g., from OH*, CH*, and C_2* radicals) enabled precise identification of the flame front. Two-color pyrometry provided flame temperature measurements with an accuracy of $\pm 50K$, and high-speed imaging captured the evolution of flame standoff distances over time. Interferometric methods allowed for micron-level resolution of droplet radius changes, offering critical data for validating mass and heat transfer models.

Several representative studies underscore the insights gained through these experiments. The work of Dietrich and Dryer (1996-2002) [36, 37, 35, 38, 29, 30] on n-heptane and methanol droplets provided robust scaling laws for droplet lifetime and flame behavior across fuel types. More recently with HYDRA, Meyer et al. (2022) [3] investigated LOX-H_2 droplets, uncovering new behaviors such as ice formation on the droplet surface and radiative quenching—phenomena that challenge standard energy balance assumptions.

These microgravity experiments confirmed many features of the canonical diffusion-flame model, including near-spherical symmetry and a characteristic flame standoff distance of approximately two to three times the droplet radius. However, they also revealed significant deviations from idealized theory. Radiative heat losses, for instance, were found to accelerate extinction by approximately 15 percent compared to conduction-only predictions, highlighting the importance of non-negligible coupling between radiative and diffusive transport mechanisms. Similarly, near-limit behaviors such as surface

freezing and breathing-mode oscillations called into question the adequacy of models that assume either quasi-steady or decoupled physics.

Microgravity experiments distilled the droplet combustion problem into its canonical geometry, offering a uniquely clean platform to validate core theoretical principles. At the same time, they revealed emergent complexities, which range from radiative extinction to transient surface phenomena, that defy closure through simplified models. These findings underscore the need for fully coupled, transient simulations that capture the dynamic interplay among diffusion, radiation, and finite-rate chemistry.

3.6 Numerical Approaches: Supercritical and Cryogenic Droplet Modeling (2000–Present)

The turn of the 21st century ushered in a new generation of numerical models aimed at extending classical droplet combustion theory into cryogenic and high-pressure regimes, particularly relevant for liquid oxygen (LOX) and hydrogen systems. Among the seminal contributions in this space is the work of Lafon et al. (2008) [39], which introduced a fully conservative, spherically symmetric model for LOX droplet vaporization in both subcritical and supercritical ambient conditions. Their framework solved the full conservation equations for mass, momentum, energy, and species using an implicit finite-volume scheme with a moving mesh to capture the regressing droplet surface. Crucially, they integrated a unified treatment of thermodynamic and transport properties across the two-phase to supercritical transition. A key innovation was the introduction of two interface definitions: the critical temperature isotherm (useful for experimental comparisons) and the critical composition isopleth (more suitable for spray modeling). Their analysis revealed that, near the critical mixing state, the droplet loses a well-defined liquid–gas interface, transitioning smoothly to a single-phase supercritical fluid. This transition leads to acceleration in vaporization due to steep thermal gradients and diminished latent heat, the conditions under which the classical d^2-law begins to fail. The study also highlighted the importance of Lewis number effects: with $Le \gg 1$ inside the droplet, thermal diffusion outpaces mass diffusion, resulting in non-uniform vaporization behavior. Despite the complexity, Lafon et al. proposed a robust lifetime correlation valid across a range of hydrogen and water vapor mixtures, achieving prediction errors below 5 %. Water vapor was shown to have minimal impact on droplet lifetime, and cross-diffusion effects (Soret and Dufour) were found to be negligible. Their model has since become a reference framework for extending droplet simulations to convective flows, turbulent environments, and interacting droplet systems.

3.6.1 Ice Formation in LOX Droplet Systems

Lafon et al. (2008) [39] extended their droplet vaporization model to account for water condensation near the droplet surface under supercritical and high-pressure conditions. In their framework, water

vapor produced by LOX–hydrogen combustion could locally exceed saturation, leading to homogeneous nucleation of tiny water clusters, which then grow into liquid droplets. The model treated nucleation as effectively instantaneous once the saturation ratio exceeded unity, and incorporated thermophoretic and viscous forces on the condensed particles to predict their transport near the droplet interface. Condensation rates were computed using a pressure-difference formulation based on Onsager's irreversible thermodynamics, with the assumption that the phase change occurs rapidly relative to droplet vaporization timescales.

While Lafon et al.'s [39] condensation treatment provides a rigorous approach to liquid water formation under extreme conditions, it is important to note that the regime differs fundamentally from subcritical, 1 $\sim$ bar conditions such as those in the ZARM experiments. In the latter case, observed ice formation corresponds to direct vapor-to-solid deposition (frost), rather than transient liquid water droplets in a supercritical environment. Consequently, the quantitative predictions of water-particle nucleation, growth rates, or interface interactions from Lafon et al. are not directly applicable to our present study's modeling framework, in specifically the subcritical regime of interest. While Lafon et al. (2008) [39] is often cited for LOX droplet condensation, it addressed supercritical pressures where condensation is transient and negligible. In contrast, the ZARM [3] 1 bar experiments occur in a subcritical, humid regime with visible frost formation. No quantitative ice-layer data exist for such conditions; only qualitative observations from the ZARM experiment. Nonetheless, Lafon 2008 [39] serves as a conceptual reference, highlighting that condensation processes near cryogenic droplet surfaces can influence interfacial mass and energy transfer, albeit with very different mechanisms and timescales under subcritical conditions.

3.7 Hydrogen-Oxygen Combustion Kinetics in the Heat and Mass Transport Context

3.7.1 Historical Background and Canonical Frameworks

Chain-Branching Origins and Early Kinetics Theory

The theoretical foundations of combustion kinetics trace back to the early 20th century, when researchers first began to interpret flame propagation not simply as a thermal process, but as a chain-reactive phenomenon governed by radical intermediates. Seminal work by Semenov (1928) [40] provided one of the first mechanistic explanations of combustion as a radical-mediated chain process, proposing that flames could be self-sustaining through autocatalytic cycles. This was further developed in the 1930s by Hinshelwood and co-workers [41, 42], who analyzed hydrogen-oxygen reactions and identified key roles played by intermediate species such as H, O, and OH radicals. These early studies led to the concept of chain branching, whereby reactive radicals such as H or O collide with stable molecules to

produce more radicals, thereby accelerating the reaction. In hydrogen–oxygen systems, the reaction

$H + O_2 \rightarrow O + OH$

emerged as the prototypical chain-branching step. Counterbalancing this, chain termination reactions, such as third-body recombination:

$H + O_2 + M \rightarrow HO_2 + M$

serve to suppress radical growth by stabilizing intermediates, where M denotes a collision partner. This fundamental tension between branching and termination defines the reactivity and stability of the H_2/O_2 flame system and remains central in modern chemical kinetic mechanisms, including those proposed by Westbrook & Dryer (1984) [43] and more recent detailed models such as Li et al. (2004) [44] and O'Conaire et al. (2004) [45]. Understanding hydrogen combustion as a chain reaction set the stage for kinetic modeling frameworks that explicitly resolve elementary reactions and their coupling with thermochemical and transport processes. These early mechanistic insights form the backbone of modern high-fidelity reaction mechanisms employed in numerical simulation.

From Global to Diffusion-Limited Regimes

With the growing recognition that combustion involves both chemical kinetics and transport phenomena, a shift occurred in the 1930s–1940s toward integrated models. The work of Burke and Schumann (1928) [10] is especially notable in this context. Their formulation of the diffusion flame, which was originally intended to describe hydrocarbon-air combustion in laminar jets, provided one of the first quantitative couplings between chemical source terms and diffusive fluxes. They demonstrated that when fuel and oxidizer meet at an interface and chemistry proceeds rapidly compared to diffusion, a thin reaction sheet forms. The rate-limiting step is then no longer chemical reaction, but rather the supply of reactants via diffusion. This conceptual framework was extended by Damköhler (1940, 1947) [46, 47], who formalized the interaction of chemical kinetics and fluid transport through the now-fundamental Damköhler number (Da), capturing the key comparative ratio of the characteristic chemical time scale to the transport (diffusion or convective) time scale. When $Da >> 1$, chemical reactions are much faster than transport processes, leading to diffusion-controlled regimes, where the flame can be approximated as a sharp front at which reactants instantaneously convert to products. Conversely, when $Da << 1$, the regime becomes kinetics-limited, and the flame structure must be resolved over a finite reaction zone.

This dichotomy is particularly relevant in the modeling of microgravity flames, such as in the ZARM drop tower context, where convection is minimal and diffusion dominates transport. The flame-sheet approximation thus serves as a justified limiting case in the high-Da regime, engendering an assumption that simplifies the simulation of LOX-H_2 diffusion flames in spherically symmetric geometries.

Flame-Sheet and Equilibrium-Limit Conceptualization

The flame-sheet model, grounded in the high-Damköhler-number limit, represents the combustion zone as an infinitesimally thin interface where the reactants instantaneously reach chemical equilibrium

at constant enthalpy. This approximation, while neglecting detailed finite-rate kinetics, enables tractable modeling of flames in complex transport regimes, which is particularly relevant for your spherically symmetric diffusion-limited framework. The theoretical validity of this model has been discussed extensively in the literature. Lewis & von Elbe (1937) [48] offered early theoretical justifications for the concept of sharp flame fronts in premixed and diffusion flames. More modern treatments, such as Law (2006) [18] and the foundational Glassman (1977) [19] textbook, have further elucidated the conditions under which flame-sheet models can approximate the full solution to the reactive Navier–Stokes equations coupled with finite-rate chemistry. It is within this context that the current study adopts a quasi-steady, diffusion-limited model for LOX–H_2 combustion. The assumption of a locally equilibrated flame interface is justified by the high reactivity of the hydrogen–oxygen system, especially under cryogenic initial temperatures ($\sim$ 100 K ambient) and the near-ambient pressure (1 atm) used in the referenced drop tower experiments. The small droplet scale (1 mm diameter) further favors rapid chemical equilibration relative to the slower mass transport by diffusion. This section has established the conceptual and historical foundations of hydrogen–oxygen combustion kinetics, particularly as they pertain to the modeling of flame structures under diffusion-limited regimes. These principles form the basis for the simplified but physically grounded treatment of combustion adopted in the present numerical framework.

3.8 Textbook Frameworks and Analytical Formulations

The transition from historical combustion theory to modern modeling practice is bridged by several authoritative treatments of chemically reacting flows, which synthesize kinetic theory, thermodynamics, and transport phenomena into integrated frameworks for flame analysis. Chief among these are the canonical texts by Glassman (1977) [19] and Law (2006) [18], which provide rigorous yet practical approaches to modeling combustion phenomena under varying degrees of kinetic and transport coupling. These works extend the earlier analytical foundations laid by Burke, Schumann, and Damköhler, formalizing the theoretical conditions under which combustion can be considered either reaction-limited or transport-limited, with implications for ignition, flame stabilization, and extinction.

In particular, Law's framework emphasizes the role of non-dimensional analysis and asymptotic scaling, especially through the Damköhler number characterization, in establishing regimes of flame behavior. For instance, under high Damköhler number conditions (as found in the current microgravity scenario), flames tend toward the diffusion-limited regime, where the reaction zone collapses to a thin interface and the system dynamics are governed primarily by the transport of reactants. Conversely, in low-Da settings, finite-rate chemistry dominates, necessitating detailed kinetic resolution.

In the low-Mach-number limit, which is applicable to the present study's microgravity, quasi-isobaric environment, pressure variations are negligible across the flame front. This enables a simplification of the governing equations: pressure is treated as spatially uniform, acoustic waves are filtered out, and

energy transport is dominated by conduction and species diffusion. These simplifications are standard in low-speed reacting flows and are consistent with the operating assumptions of both the ZARM drop tower experiments and the associated numerical modeling.

Under this regime, ideal gas behavior is assumed, and the mixture-averaged transport approximation is typically employed to model species diffusion and thermal conduction. This approach is valid in dilute gas systems, especially at 1 atm ambient pressure and low initial temperatures ($\sim$ 100 K), where compressibility effects and bulk viscosity contributions can be neglected. In the present context of spherically symmetric, diffusion-limited combustion of a cryogenic liquid oxygen–hydrogen droplet, these simplifications provide a tractable yet physically grounded modeling base.

These classical combustion texts, particularly Bird, Stewart, and Lightfoot's Transport Phenomena (1960) [49], also rigorously address the coupling between mass and heat transport, which becomes particularly important in systems involving hydrogen. Due to hydrogen's low molecular weight and high diffusivity, Fickian diffusion alone is often insufficient to capture the true transport dynamics. Instead, multicomponent diffusion, Soret (thermal diffusion), and Dufour effects may become non-negligible, particularly near steep thermal or concentration gradients.

The multicomponent diffusion formulation accounts for species fluxes that arise not only from their own concentration gradients but also from the gradients of other species. Moreover, heat conduction is coupled to species diffusion through enthalpy transport, and the chemical source terms ($\dot{\omega}_i$) serve as internal sources in both species and energy conservation equations. This formulation inherently couples the flame's thermochemical structure to its diffusive characteristics, and is essential in correctly simulating hydrogen-oxygen flame dynamics under microgravity conditions.

In short, the low-Mach-number, constant-pressure, ideal-gas approximation creates a theoretical environment consistent with textbook formulations. However, due to hydrogen's extreme transport properties and the fine-scale coupling between species and thermal fields, accurate modeling must rely on detailed formulations that go beyond textbook simplifications. This sets the stage for more detailed treatment of the chemical kinetics underpinning hydrogen–oxygen combustion.

3.9 Hydrogen–Oxygen Chemical Kinetics

3.9.1 Foundational Kinetic Mechanisms

Classical Kinetic Structure

The hydrogen–oxygen system occupies a unique role in combustion science as both a standalone fundamental flame system and a modular subset embedded within more complex hydrocarbon oxidation mechanisms. Westbrook and Dryer (1984) [43] laid the foundation for the treatment of H_2/O_2 kinetics in this context, introducing a compact yet comprehensive framework for modeling high-temperature gas-phase combustion. Their work identified the H_2/O_2 subsystem as a "universal kernel" embedded within

broader hydrocarbon oxidation schemes. This kernel comprises the essential radical-mediated pathways governing energy release and species evolution, forming the baseline for virtually all subsequent chemical kinetic models.

Central to the hydrogen oxidation mechanism is the balance between chain-branching and chain-terminating reactions. Chain branching, particularly the elementary reaction

$$\mathrm{H} + \mathrm{O_2} \longrightarrow \mathrm{O} + \mathrm{OH} \tag{1}$$

is a dominant pathway for radical amplification and energy release. In contrast, the competing third-body termination step,

$$\mathrm{H} + \mathrm{O_2} + \mathrm{M} \longrightarrow \mathrm{HO_2} + \mathrm{M}, \tag{2}$$

acts to quench the radical pool by forming the relatively inert hydroperoxyl (HO_2) intermediate. The competition between these two reactions directly governs the flame speed, ignition delay, and reactivity of the H_2/O_2 mixture, especially in lean and low-temperature conditions.

Both reactions exhibit strong temperature and pressure sensitivity. The rate of reaction 1 increases exponentially with temperature due to its high activation energy, making it critical at flame front temperatures (∼2000–3000 K), whereas reaction 2 becomes more prominent under high-pressure or low-temperature conditions, where three-body collisions are frequent. This dynamic interplay controls not only flame propagation but also extinction thresholds and ignition limits across various regimes.

Mathematically, the disparity between fast chain-branching steps and slower termination or recombination pathways introduces numerical stiffness into the governing system of ordinary differential equations (ODEs). Solvers such as CVODE (used in Cantera) or CHEMKIN's proprietary stiff solvers are required to handle the multiscale temporal behavior inherent to hydrogen combustion. This stiffness becomes especially pronounced in transient simulations or when detailed kinetics are fully resolved, motivating the use of reduced or equilibrium-based schemes in many practical settings.

3.9.2 Validation Heritage

The development and calibration of hydrogen–oxygen kinetic models have historically relied on well-defined experimental benchmarks. Shock tube ignition delay data, flow reactor species profiles, and laminar premixed flame speed measurements have all contributed to the validation corpus for H_2/O_2 mechanisms. The early datasets compiled and modeled by Westbrook and Dryer (1984) [43] remain essential references, forming the empirical backbone against which later detailed mechanisms, such as those by Li et al. (2004) [44] and O'Conaire et al. (2004) [45], were assessed.

These foundational validations ensured that model predictions aligned with experimental observations

over wide ranges of equivalence ratio (ϕ), temperature (T), and pressure (p), particularly in the range relevant to atmospheric-pressure combustion under microgravity, namely $T \sim 3000$ K, $p \sim 1$ atm as in the ZARM drop tower environment. [3]

3.9.3 Modern Detailed Mechanisms

Li et al. (2004)

The mechanism by Li et al. (2004) [44] represents a comprehensive H_2/O_2 kinetic model, compiled from prior work by Mueller et al. (1999) [50] and others, and validated across a wide range of reactors and conditions. It includes over 20 elementary reactions and accounts for pressure-dependent falloff effects, radical recombination, and thermal decomposition processes.

Of note is the reaction:

$$\mathrm{H + OH + M \longrightarrow H_2O + M}, \tag{3}$$

which becomes increasingly significant at elevated pressures. While its influence at 1 atm is moderate, its inclusion ensures thermodynamic closure and robustness across the full parameter space, even if not strictly required for accurate modeling in the current study's operating regime.

Li's mechanism is widely implemented in contemporary combustion simulation platforms (e.g., Cantera, CHEMKIN) and serves as a benchmark for hydrogen combustion under high-fidelity numerical modeling.

O'Conaire et al. (2004)

The work by O'Conaire et al. (2004) [45] extends the applicability and validation of hydrogen combustion kinetics across pressures from 0.05 to 87 atm and temperatures from 298 to 2700 K. This makes it particularly robust for multi-regime modeling, including both ignition and flame propagation scenarios.

Through detailed sensitivity analysis, they identified rate-limiting steps such as reaction 1 and validated their pressure and temperature dependencies against experimental flame speeds and ignition delays. Although the present study operates in a well-defined high-temperature and near-atmospheric regime, this comprehensive mechanism serves as a reliable reference and supports the fidelity of any reduced mechanism derived from it.

3.9.4 Refinements and Low-Temperature Pathways

Gerasimov & Shatalov (2013)

While the present flame conditions are firmly in the high-temperature regime, the inclusion of studies such as Gerasimov and Shatalov (2013) [51] provides completeness to the kinetic framework. Their work

addresses the pressure-dependent behavior of low-temperature pathways, including HO_2 and H_2O_2 intermediates, and offers correction methods via the Lindemann–Hinshelwood formalism for falloff reactions. [41, 42]

Although such corrections are less critical at 1 atm and 2500 K, their conceptual relevance lies in ensuring the robustness of the mechanism across broader parametric bounds, particularly important for generalizing future extensions of the model to variable pressure environments or pre-ignition phenomena.

By incorporating their findings, the kinetic model remains theoretically sound even in transitional regimes, and better aligned with first-principles chemical physics.

This section has outlined both the fundamental and practical considerations that underpin the modeling of hydrogen–oxygen combustion kinetics. The combination of historical mechanisms, textbook simplifications, and modern detailed models allows for a flexible and physically consistent framework tailored to the specific demands of high-Damköhler-number, diffusion-limited spherical droplet combustion under microgravity.

The next section will examine how these kinetics integrate with mass and energy transport in the reacting flowfield.

3.9.5 Integration of Kinetics within the Transport Framework

Regime Definition: Diffusion-Limited, Low-Mach, Isobaric Conditions

The physical regime investigated in hydrogen–oxygen combustion within a microgravity environment around a cryogenic droplet, is characterized by several simplifying but important assumptions that directly affect the integration of chemical kinetics into the transport framework. First and foremost is the low-Mach-number approximation, under which the reacting flow can be considered quasi-isobaric. In such flows, pressure gradients are negligible across the combustion zone, enabling pressure to be treated as uniform in both space and time. This is consistent with the conditions in the ZARM drop tower, where gravitational acceleration is near-zero and convective flows are greatly suppressed. Under these assumptions, diffusive transport becomes the dominant mechanism for mass and heat transfer, while acoustic phenomena and compressibility effects are effectively filtered out. Consequently, the governing equations for mass, species, and energy conservation reduce to a reaction–diffusion system where chemical source terms are balanced primarily by diffusive fluxes, and energy is transported via conduction rather than advection. In this environment, the Damköhler number (Da) and Peclet number (Pe) emerge as the primary dimensionless quantities governing the flame structure. The Damköhler number quantifies the relative timescales of reaction and diffusion:

$$D_a = \frac{\tau_{\text{diff}}}{\tau_{\text{chem}}} \tag{4}$$

where τ_{diff} is the characteristic diffusion time and τ_{chem} the chemical timescale. For the LOX-H_2 system under cryogenic ambient conditions ($\sim$ 100 K) and 1 atm pressure, the flame temperature is sufficiently high ($\sim$ 3000 K) that $\tau_{\text{chem}} << \tau_{\text{diff}}$, placing the system firmly in the diffusion-limited regime. This justifies the flame-sheet approximation, wherein the combustion zone is treated as an infinitesimally thin interface at which reactants are consumed and products generated in local thermochemical equilibrium. The Peclet number, relating convective to diffusive transport, is also low due to the suppression of buoyancy in microgravity, reinforcing the quasi-steady, spherically symmetric diffusion model employed here. Together, these regime-defining approximations form the basis for both the numerical simplifications and physical fidelity of the present study.

Coupled Governing Equations: Role of Source Terms and Stiffness

In the governing equations of reacting flows, chemical source terms $\dot{\omega}_i$ couple tightly with mass and energy conservation. These terms represent the net production rate of species i due to chemical reactions, and are functions of local temperature, pressure, and species concentrations. In detailed kinetic models like those of Li (2004) [44] or O'Conaire (2004) [45], these source terms can span many orders of magnitude in timescale, particularly between fast chain-branching steps and slower termination pathways. This multiscale nature leads to stiffness in the numerical system of ODEs and PDEs, a hallmark of hydrogen combustion modeling noted as early as Westbrook & Dryer (1984) [43].

In computational practice, this stiffness imposes constraints on solver stability and timestep size, often necessitating implicit integration schemes or operator splitting methods. While the present study adopts a local equilibrium approximation at the flame sheet, thus sidestepping the need for fully resolved finite-rate kinetics within the reaction zone, the stiff character of the full system informs the numerical design. Outside the flame sheet, species evolution is governed by multicomponent diffusion and thermal gradients, with source terms either zero (in unreacted zones) or evaluated from equilibrium constraints (in the reaction zone), which considerably simplifies the numerical stiffness without sacrificing physical accuracy under the high-Da regime.

Local Equilibrium Closure: Flame Sheet Approximation and Enthalpy Conservation

The use of a local equilibrium closure at the flame interface rests on the physical reality that, in high-Da systems, chemical timescales are orders of magnitude shorter than diffusive timescales. As such, the reaction zone achieves thermodynamic equilibrium instantaneously relative to the surrounding transport processes. This allows for a constant-enthalpy assumption across the flame sheet, distinct from constant-temperature calorimetric models or closed-system bomb calorimetry. Instead, the flame is modeled as an open system where incoming fuel and oxidizer streams meet at a sharp interface and react adiabatically to form equilibrium products. This approach, grounded in the Burke–Schumann limit, reduces the complexity of the chemical kinetics to an algebraic or convex optimization equilibrium problem, solvable using tools such as Cantera's equilibrium() routines. Importantly, this closure method

is not merely a numerical convenience, as it is indeed a physically justified simplification that retains fidelity to the underlying kinetics under the given regime constraints.

The local equilibrium formulation also inherently captures the nonlinear dependence of flame temperature and product composition on local mixture fraction, as dictated by the stoichiometry and thermodynamic properties of the H_2/O_2 system. This enables the model to resolve flame position and structure in spherical geometry with appropriate coupling to species and energy transport, without requiring explicit integration of stiff kinetic ODEs at each timestep.

Globally Aggregated Continuua Coupled Models in Engineering Contexts

Representative coupled-field and transport-theory models in the literature further demonstrate the integration of kinetics with macroscopic heat and mass transfer. Two particularly relevant examples are those of Travis (1987) [52] and Metz et al. (1995) [53], which respectively exemplify continuum-scale coupling and kinetic-theory-based transport closure.

At the continuum scale, the interplay of chemistry, diffusion, and fluid motion was addressed in the coupled-field model of Travis (1987) [52], who solved the full Navier–Stokes, energy, and multispecies transport equations for hydrogen–oxygen flames in containment conditions. Although formulated for nuclear safety analysis, the work is conceptually significant as one of the earliest examples of fully coupled momentum–energy–species modeling with explicit combustion source terms. The use of a one-step global Arrhenius rate for $2H_2 + O_2 \rightarrow 2H_2O$ enabled coupling between heat release, buoyancy, and species diffusion, illustrating how macroscopic transport processes mediate the effective kinetics observed in large-scale hydrogen flames, while portraying their mutual interaction. While our model considers a quasi-steady, low-Mach limit at 1 atm without buoyancy or turbulence, the formal structure of the coupled equations remains analogous; only the transport simplifications and equilibrium closure differ.

Complementing the chemical-kinetic foundations, Metz et al. (1995) [53] derived transport coefficients for hydrogen/oxygen and hydrocarbon mixtures using first-order Chapman–Enskog solutions to the Boltzmann equation under chemical equilibrium composition. Their results provided high-temperature viscosity and diffusivity correlations (1000–7000 K, 10^3 – 10^6 Pa) that underlie modern mixture-averaged transport models used in codes such as CHEMKIN and Cantera. The work effectively established the kinetic-theory pedigree for the empirical mixture rules typically invoked in combustion simulations (and indeed hard-coded in ours), linking microscopic collision integrals to macroscopic diffusion fluxes. In the present work, these relations conceptually underpin the mixture-averaged transport formulation used in the quasi-steady droplet model, ensuring thermodynamic consistency between diffusion and reaction source terms.

Numerical Practice and Mechanism Lineage: Solver Traditions and Computational Ecosystem

While the main body of computational methodology belongs in the methods section, a brief overview

of the solver ecosystem provides context for the kinetic models referenced in this literature review. The standard tools for simulating combustion kinetics include CHEMKIN, Cantera, and NASA CEA, each of which supports detailed reaction mechanisms, equilibrium calculations, and transport property modeling: CHEMKIN pioneered the tabulated and modular use of chemical mechanisms in reacting flows, Cantera, an open-source alternative, allows flexible integration with Python and C++ and supports both equilibrium and finite-rate simulations, and NASA CEA is primarily used for chemical equilibrium calculations, useful for flame sheet modeling. These tools provide the computational infrastructure through which mechanisms like those of Westbrook–Dryer [43], Li [44], and O'Conaire [45] are implemented and tested. The modularity of mechanism input and the availability of validated thermodynamic and transport databases make them indispensable for accurate modeling of chemically reacting systems.

Mechanism Lineage: From Reduced Sets to Comprehensive Models

The mechanisms used in this study trace their lineage through several generations of increasing detail and scope. Early models such as the Bird–Lightfoot [49] 21-step mechanism focused on tractable simulations of hydrogen and simple hydrocarbons, suitable for engineering applications and analytical derivations. These were later refined into more canonical subsets, as seen in the works of Glassman [19], before evolving into the fully detailed kinetic models of Li (2004) [44] and O'Conaire (2004) [45]. This progression reflects a broader trend in combustion modeling: from simplified, globally parameterized reaction sets toward elementary-reaction-based models with full coverage of radical and intermediate species. The present study adopts a hybrid approach: employing a thermodynamically consistent equilibrium closure at the flame sheet, informed and validated by the underlying comprehensive mechanisms. This approach ensures that the simplified model remains rooted in physically accurate chemistry, while retaining computational tractability in a diffusion-limited, high-Da, low-speed flow.

3.9.6 Chemical Kinetics of H2-O2 Combustion in the Numerical Heat and Mass Transport Context

Experimental and Quantum Foundations of H_2-O_2 Chemistry (Grounding kinetic constants in fundamental physical data — a "physics-first" basis for reduced and global mechanism development)

Understanding hydrogen–oxygen combustion requires more than cataloguing reaction steps; it demands that the kinetic parameters underlying those steps be physically and experimentally grounded. The foundation of modern H_2-O_2 mechanism development rests on two complementary pillars: high-fidelity experimental kinetics and ab initio quantum-chemical studies. Together, these approaches anchor the rate coefficients, activation barriers, and reaction pathways used in both comprehensive and reduced models within measurable, verifiable physical chemistry.

Experimental Kinetic Constants

A cornerstone example of this experimental grounding is provided by Michael et al. (2000) [54], who

probed the fundamental initiation reaction

$H_2 + O_2 \rightarrow H + HO_2$

using shock tube techniques combined with atomic resonance absorption spectroscopy (ARAS). Their work represents one of the rare direct measurements of this key chain-initiating process under controlled high-temperature conditions. By isolating the reaction at low hydrogen concentrations and using krypton as a diluent, they were able to suppress secondary pathways and extract a clean rate constant for the initiation step, a critical quantity for ignition modeling through this mechanism's avenue.

Beyond the immediate numerical result, the conceptual advance of Michael et al.'s [54] work lies in its experimental transparency: it provides a direct, physics-based measurement of the reaction that triggers hydrogen chain branching. Their combination of precise diagnostics with theoretical support (via canonical transition state theory and tunneling corrections) bridges laboratory data with predictive modeling, ensuring that even reduced or global mechanisms inherit physically validated rate constants. These results are also entirely consistent with the experimental verification of the standard global one-step kinetic mechanism reduced from the full kinetic mechanism with Marinov's 1995 work [55]. In essence, these works "look under the hood" of the hydrogen flame to shed light with respect to its overall functionality, offering a benchmark that underpins all subsequent kinetic simplifications.

Ab Initio and Electronic Structure Studies

Parallel to the experimental investigations, ab initio computational chemistry has mapped the potential energy surfaces (PES) governing hydrogen oxidation, illuminating the quantum-level structure of transition states and intermediates. Karkach and Osherov (1999) [56] exemplify this approach with their detailed mapping of the triplet H_2O_2 surface. Their calculations reveal that certain reaction pathways previously assumed to be elementary bimolecular processes are, in fact, more complex, involving higher-order or electronically mediated transition states. This insight redefines how rate constants and reaction sequences are parameterized in kinetic models, cautioning against oversimplified reaction assumptions and supporting the physical fidelity of mechanism design. Although not itself a kinetic mechanism, such ab initio work supplies the theoretical electronic structure scaffolding that ensures reduced models remain consistent with the underlying quantum chemistry.

Building on that foundation, Konnov (2015) [57] introduced electronically excited species into a detailed hydrogen combustion framework. His analysis integrates quantum mechanical data on excited-state energetics and reaction reversibility to evaluate how these minor but energetic species influence ignition and flame propagation. The results demonstrate that while most excited states exert negligible influence under typical combustion conditions, singlet oxygen can significantly accelerate ignition even at trace concentrations. Importantly, Konnov's [57] work highlights the need for thermodynamic and electronic self-consistency in kinetic models, ensuring that even seemingly exotic pathways are treated with physically sound rate formulations.

Taken together, these experimental and theoretical efforts establish a physically rigorous substrate for mechanism construction. The combination of direct kinetic measurement, quantum-level mapping, and electronic-state analysis ensures that later reduced, global, and equilibrium-informed models are not merely curve fits to data, but physically rooted abstractions. This foundation frames the transition toward data-driven mechanism verification and uncertainty quantification, where such experimentally and theoretically validated parameters are tested, constrained, and refined within numerical combustion simulations.

Data-Driven Mechanism Verification and Uncertainty Analysis

(Establishing the empirical backbone for all reduced and global mechanism development)

The progression from fundamental kinetics to usable combustion models is, at its core, a process of informed reduction. Once the elementary rates and transition states of H_2 -O_2 chemistry were established through experiment and ab initio theory, researchers turned toward systematically testing, filtering, and condensing this knowledge into mechanisms that could be used in practical simulations. This stage represents the inflection point where the field transitioned from understanding chemistry to using chemistry predictively, a process grounded in empirical comparison, sensitivity analysis, and uncertainty quantification.

Conceptually, this data-driven phase functions much like a physicochemical analog of principal component analysis: high-dimensional kinetic networks are projected onto a lower-dimensional, yet still physically meaningful, subspace defined by the dominant reaction sensitivities. Rate coefficients and reaction pathways are weighted, adjusted, or occasionally pruned based on how much they actually influence measurable quantities, such as ignition delay, flame speed, species profiles, under specified thermodynamic conditions. The end goal is an Occam's razor equilibrium: the simplest model that still preserves fidelity to both experiment and first-principles chemistry.

Empirical Database Construction and Comparison

A defining example of this synthesis approach comes from Shatalov et al. (2009) [58], who compiled and harmonized a broad dataset of rate constants and thermodynamic parameters for the H_2-O_2 system. Their work represents one of the earliest large-scale efforts to benchmark multiple kinetic mechanisms against an integrated corpus of shock-tube ignition data. By identifying where different mechanisms diverged, particularly in the treatment of third-body efficiencies and key reactions such as an HO_2-forming channel, they showed how small parametric shifts could cascade into large differences in ignition prediction.

Building upon this foundation, Gerasimov and Shatalov (2013) [51] developed a database-informed kinetic mechanism explicitly tuned to low-temperature conditions ($T < 1000K$). Their emphasis on the H_2O_2 formation–decomposition loop addressed a persistent gap in prior models, which had struggled to capture ignition behavior in cryogenic or low-pressure environments relevant to LOX–H_2 systems.

Validated against a comprehensive set of shock-tube data, their work exemplified the principle that empirical curation, not just theoretical completeness, is central to achieving predictive accuracy in combustion modeling.

Systematic Uncertainty Quantification

Complementing these data compilations, Konnov (2008) [59] took a more formal approach by explicitly quantifying the uncertainty embedded in each kinetic parameter of the hydrogen oxidation mechanism. Through meticulous cross-referencing of rate constants from experimental and theoretical literature, Konnov introduced uncertainty factors and assessed how these propagated into global observables such as ignition delay and laminar flame speed. This work reframed mechanism validation as a probabilistic exercise: instead of seeking a single "true" set of rate constants, it emphasized bounding the plausible range of outcomes given known experimental uncertainties. In doing so, Konnov's study formalized what earlier works had practiced heuristically, serving as a recognition that the robustness of a combustion mechanism lies not in its nominal parameter values, but in its stability under epistemic uncertainty.

Pratical CFD Validation

Finally, the link between kinetic fidelity and numerical simulation was made explicit in Zhukov (2012) [60], who evaluated hydrogen combustion mechanisms within a coupled CFD framework using ANSYS CFX and CHEMKIN. By comparing simplified and detailed schemes under identical flow and thermal conditions, Zhukov demonstrated where reduced mechanisms preserve predictive power along with where they break down, within spatially resolved flow fields. The analysis revealed that at moderate to high temperatures, reduced models capture the essential flame dynamics with significant computational savings; however, at lower temperatures or in strongly nonuniform fields, missing intermediate chemistry (particularly HO_2 and H_2O_2 pathways) leads to measurable deviations.

This balance between computational tractability and chemical fidelity directly informs the design philosophy for simulations such as the present LOX–H_2 diffusion flame problem, where diffusion limitation and high Damköhler numbers permit reduced mechanisms to remain accurate, provided they are empirically validated against the kind of data-driven foundations described above.

Together, these studies illustrate how the modern hydrogen–oxygen mechanism landscape was shaped by an iterative feedback loop between data, theory, and modeling. The transition from detailed physics to validated reduction was not arbitrary; it followed a structured path of sensitivity-based refinement, uncertainty accounting, and empirical cross-verification. This lineage defines the epistemic backbone upon which all later algebraic, hierarchical, and equilibrium-informed mechanism frameworks, including the one adopted in this work, are constructed.

Algebraic, Reduced, and Hierarchical Mechanism Development

(Tracing the mathematical lineage of reduced kinetic modeling for H_2–O_2 combustion)

As kinetic datasets matured and empirical validation narrowed uncertainties, attention in the hydrogen-oxygen community turned toward building mathematically tractable yet physically faithful kinetic surrogates. These algebraic and hierarchical reductions represent the analytical counterpart to the data-driven filtering described earlier: instead of pruning by statistical sensitivity, they compress the chemistry through dynamical-systems reasoning, such as time-scale separation, eigenvalue analysis, and quasi-steady-state approximations (QSSA). The goal remains the same: to retain the dominant chemical modes governing heat release and radical propagation, while minimizing computational stiffness in numerical transport solvers.

The seminal analytical foundation of this lineage lies in Hersch (1967) [61], whose six-step hydrogen–oxygen mechanism remains the archetype for many reduced schemes used in engineering simulations. In particular, such six-step mechanism arises from pruning steps seven and eight, containing only HO_2 and H_2O_2 peroxide compounds, which can be mostly independently factored out of the proposed scheme. Hersch formulated coupled ordinary differential equations for species and radicals (H, O, OH, HO_2, H_2O_2) and analyzed their dynamics through matrix-based eigenvalue solutions. By distinguishing initiation, induction, and post-induction heat-release regimes, he provided one of the first explicit demonstrations that radical buildup follows distinct time-scales, illustrating a concept that later became the mathematical basis for quasi-steady-state elimination. In effect, Hersch's [61] six-step scheme marks the transition from phenomenological chemistry toward dynamical-systems reduction.

Within the local context of this work, Hersch's formulation is especially relevant, because our prior work with Mukund Gupta's and Phani Ponduri's MS theses at University of Washington implemented subsets of this very scheme in OpenFOAM, effectively reproducing Hersch's reduction without the peroxide extensions. It is possible this inadvertently was accomplished unknowingly, since neither of the MS theses made any allusion to Hersch's [61] more pendatic methodological approach even strictly including all intermediary M third-body terms, such nuanced intricacy beyond the scope of our project; while their focus was on computational practitioning for engineering implementation rather than analytical derivation, lacking a rigorous formal sensitivity analysis through Jacobian principal eigenvalue reduction diligence, these models trace their intellectual ancestry directly to Hersch's algebraic reduction, the same thread extended here toward thermodynamically informed, equilibrium-coupled modeling.

Recent efforts have revived algebraic reduction from a more thermodynamic perspective. Millán-Merino and Boivin (2024) [62] proposed a one-step, equilibrium-informed formulation that eliminates explicit radical transport altogether. Their approach derives reaction stoichiometry and heat-release rates directly from equilibrium constraints, solving for temperature and composition using Newton–Raphson iteration with a numerically evaluated Jacobian. By coupling this algebraic equilibrium closure with a passive-scalar evolution equation for radical buildup, they created a hybrid framework that blends equilibrium chemistry with weakly time-dependent dynamics. This direction exemplifies a modern trend

toward intelligent algebraic surrogates, formulating models that preserve thermodynamic realism while dramatically reducing numerical stiffness, aligning conceptually with the equilibrium-injection strategy adopted in the present study.

Parallel to these algebraic developments, the Williams research group established the canonical hierarchical reduction framework for hydrogen combustion. Beginning with the accepted baseline "ground-truth"-flavor detailed 21-step San Diego mechanism often referred to, Boivin et al. (2011) [63] systematically reduced it to 12-step, 4-step, and ultimately 3-step forms by applying steady-state assumptions to minor radicals such as O, OH, and H_2O_2. The resulting reduced sets preserved ignition and flame-speed accuracy across wide regimes, including autoignition and diffusion flames. Boivin et al. (2013) [64] expanded this hierarchy, tailoring 2, 3, and 4-step mechanisms to distinct temperature and ϕ equivalence-ratio regimes, while proposing a hybrid three-step scheme that remained valid across both high and low-temperature limits.

This systematic reduction philosophy was formally codified by Sánchez and Williams (2014) [65], who articulated a unified view of hydrogen oxidation through successive QSSA-based simplifications. Their exposition demonstrated that the essential combustion physics, including chain initiation, radical propagation, and heat-release feedback, can be captured within a few algebraically condensed reactions without losing predictive power. The intellectual roots of these efforts trace back to the classic text Gutheil, Balakrishnan, and Williams (1993) [66], whose algebraically-rigorous matrix reduction of the full hydrogen-oxygen system yielded a successive contraction from 21 down to 13, and particularly in Chapter 11 analytically manually from 4 down to 3, then to 2, and ultimately 1-step forms, capturing both which intermediates are passed through and also illustrating the characteristic rates. Their derivation, grounded in eigenvalue and Jacobian analysis, remains the popularly-referenced "textbook" template for algebraic reduction in combustion kinetics and continues to serve as the theoretical foundation for most modern reduced-mechanism work, including the simplified four-step scheme proposed by Gupta perhaps unknowingly without reference, hinting at the correctness and indicating the accuracy of intuitive chemically-informed blindfold heuristic methods.

For a consolidated overview of this reduction hierarchy, Hashemi et al. (2018) [67] provide perhaps the clearest comparative synthesis. Their study, particular the final appendix chart, tabulates Arrhenius parameters for mechanisms ranging from single-step global reactions to seven-step reduced schemes, evaluating each for predictive accuracy, temperature sensitivity, and computational cost. The progression summarized by Hashemi and colleagues effectively quantifies the trade-off surface between fidelity and tractability: one-step global models capture the broad energy-release profile, while three- to seven-step variants incorporate sufficient intermediate chemistry to reproduce ignition delays and flame structures with high accuracy. Their work validates the central premise of hierarchical reduction, a technique that simpler models, when properly parameterized, can utilize to representatively replicate the dominant

transport-coupled chemistry governing flame behavior. Of comparative note for aggregate synthesis, they directly allude to the following two-step Table 1 reaction scheme that passes directly through an OH intermediate, that is also specifically referenced and discussed in Huang et al.'s 2011 and 2012 works [68, 69] and Chinitz 1987 [70] claiming its effectiveness as a trigger species, serving as a signifant pareto-optimal-flavored example balancing the fidelity-complexity tradeoff; this is because the intermediate OH is the most prominent minor species radical at flame equilibrium, with mole fraction typically sitting around 10 % of the flame peak's mixture arising from solving the convex optimization problem for minimizing Gibbs Free energy of the species in the mixture, typically performed under the hood or pre-tabulated in common tools such as Cantera and CEA.

Table 1: Two-step reduced H_2–O_2 mechanism passing through the OH intermediate.

$$\begin{aligned}
&\mathrm{H_2 + O_2 \longrightarrow 2\,OH} && A = 2.3 \times 10^{16},\ T_a = 5134,\ n = 0 \\
&\mathrm{2\,OH + H_2 \longrightarrow 2\,H_2O} && A = 1.83 \times 10^{18},\ T_a = 11067,\ n = 0 \\
&k = A_0\, T^n \exp\!\left(-\frac{T_a}{T}\right), && (\mathrm{m, kg, mol, K, s})
\end{aligned}$$

Taken together, these algebraic and hierarchical reductions form the analytical backbone of reduced hydrogen combustion modeling. From Hersch's [61] eigenvalue-based six-step prototype to the Williams-group [63, 64, 65] hierarchies and modern equilibrium-algebraic surrogates, the trajectory is clear: a steady movement toward compact, thermodynamically consistent, and numerically efficient representations of H_2-O_2 chemistry. This lineage legitimizes the present study's approach, considering an equilibrium-point injection model that merges the algebraic reduction logic of earlier frameworks with a thermodynamic closure suited to diffusion-limited, high-Damköhler-number LOX–H_2 flames. In this sense, the method developed here is not a departure but the next rational step in the evolutionary continuum of reduced-mechanism combustion modeling.

Turbulence–Chemistry Interaction and Global Model Validity

The analytical and hierarchical reductions discussed previously provide a rigorous foundation for simplified kinetics, but their fidelity ultimately depends on how chemistry interacts with flow. In high-speed kinetics, diffusion-limited combustion such as liquid oxygen–hydrogen (LOX–H_2) systems, the coupling between molecular transport, turbulence, and local thermochemical state is not peripheral, as it defines the effective chemistry. Any global mechanism employed in such a context must therefore be interpreted not as a closed-form reaction law, but as a statistical closure of the underlying turbulent micro-kinetics.

An early and particularly influential step toward this statistical interpretation of kinetics is found in Chinitz (1987) [70], who formalized a comprehensive model for temperature–species fluctuation effects in reacting flows. Rather than treating the pre-exponential Arrhenius factor A as a fixed constant, Chinitz introduced $A(\phi, T)$, a turbulence-dependent coefficient obtained by integrating the instantaneous rate

expression over the joint probability density functions of equivalence ratio ϕ and temperature T. This formulation effectively embeds subgrid variability into the rate constant itself, expressing the "average" chemical activity of a statistically mixed, spatially intermittent flow.

The conceptual consequence of this approach is significant: the global reaction rate constant becomes a filtered quantity, reflecting the ensemble-averaged chemistry of a fluctuating environment. By introducing fluctuation amplification factors (Z_T and Z_S) and showing how they distort the apparent activation energy and pre-exponential term, Chinitz established a theoretical bridge between deterministic global kinetics and stochastic turbulence–chemistry interaction. This reasoning justifies the long-standing engineering practice of employing global, single-step mechanisms in turbulent flows, provided those mechanisms are appropriately renormalized to account for unresolved fluctuations. These notions strongly parallel Onsager's 1968 Chemistry Nobel-prize work on stochastic thermodynamics, including the well-known fluctuation-dissipation theorem along with the associated coined Onsager reciprical relations.

In high-Reynolds-number cryogenic systems, where Damköhler numbers are large and the thin-flame assumption holds, such fluctuation-adjusted global models are both necessary and sufficient, and constitute the basic premises of continuum mechanics. Within this framework, the flame sheet can be viewed as a statistical equilibrium interface separating nearly frozen reactants from near-equilibrium products. The internal radical pool (H, O, OH) evolves so rapidly compared to the mixing timescale that the chemistry collapses toward an effective equilibrium limit modulated only by transport, instituting a minor species radicals clean-up process outside the flame sheet. This physical picture directly motivates the present study's modeling strategy: a global Arrhenius formulation applied throughout the domain, augmented by a localized equilibrium-point injection at the Burke–Schumann flame surface. Here, the standard Arrhenius source terms are masked, and instantaneous equilibrium composition is imposed via in situ Cantera evaluation. The approach thus reconciles two limits within a single numerical framework:

I. Away from the flame sheet, the flow behaves as a statistically mixed, globally reacting field governmed by the Chinitz-type $A(\phi, T)$-weighted Arrhenius kinetics.

II. At the flame sheet, where turbulence and chemistry reach the asymptotic high-Damköhler regime, the system locally collapses to thermodynamic equilibrium.

Viewed in this context, the Cantera equilibrium "injection" is not an ad hoc numerical device but a logical continuation of the turbulence-filtered global rate idea. Where Chinitz embedded statistical averaging into $A(\phi, T)$, the present model extends that logic to its physical limit, which is the point at which fluctuations drive the chemistry fully to equilibrium. In both cases, the objective is the same: to capture the ensemble-averaged reactivity of a complex turbulent flow without resolving all molecular detail.

This synthesis between global kinetics, statistical correction, and equilibrium enforcement defines

the modern interpretation of global models in high-speed, diffusion-controlled hydrogen combustion. It validates the hybrid strategy employed here: combining traditional Arrhenius source terms with thermodynamically constrained equilibrium states, each active in the physical regime where it is most representative.

In summary, the turbulence-filtered perspective of Chinitz [70] and the equilibrium-limited framework adopted here converge on a common philosophical stance: that global kinetics can remain physically valid when their parameters and closures are informed by the dominant transport and thermodynamic constraints of the flow, modelled appropriately catered toward their respective regimes. This recognition sets the stage for the modeling tradition developed within the University of Washington hydrogen–oxygen research lineage, where each successive generation, beginning with the direct subset reductions of Mukund Gupta and Phani Ponduri, has progressively refined the balance between chemical fidelity and numerical tractability. The following section situates the present work within that progression, tracing how these earlier UW implementations of reduced H_2-O_2 chemistry evolve naturally into the equilibrium-informed, algebraically consistent approach advanced in this study.

Table 2: Hierarchy of Chemical Kinetic Schemes for H_2/O_2 Combustion

Scheme	**Reaction**	**Rate Expression / Parameters**	**Source**
One-step	$H_2 + \frac{1}{2}O_2 \rightarrow H_2O$	$k_{\text{global}} = 1.8 \times 10^{13} \exp\left(-\frac{17614}{T}\right) [H_2]^{1.0}[O_2]^{0.5}$	[55, 6, 71]
			([64, 62, 68, 52] different parametrizations)
Two-step	$H_2 + O_2 \rightarrow 2OH$	$A = 2.3 \times 10^{16}$, $n = 0$, $T_a = 5134$ K	[67, 68, 69]
	$2OH + H_2 \rightarrow 2H_2O$	$A = 1.83 \times 10^{18}$, $n = 0$, $T_a = 11067$ K	
		$k = A_0\, T^n \exp\left(-\frac{T_a}{T}\right)$ $(\text{m}, \text{kg}, \text{mol}, \text{K}, \text{s})$	([70] different parameters)
Four-step	$H + O_2 \rightarrow OH + O$	kinetic parameters and	[66] (chapter 11), [6]
	$O + H_2 \rightarrow OH + H$	third body collisional terms	
	$OH + H_2 \rightarrow H_2O + H$	can vary by source & physical conditions	
	$2H \rightarrow H_2$		
Six-step	$H_2 \rightarrow 2H$	kinetic parameters and	[61, 71, 6, 7]
	$H + O_2 \rightarrow O + OH$	third body collisional terms	
	$H_2 + O \rightarrow H + OH$	can vary by source & physical conditions	
	$H_2 + OH \rightarrow H + H_2O$		
	$2O \rightarrow O_2$		
	$H + OH \rightarrow H_2O$	–	
Eight-step	$H_2 \rightarrow 2H$	kinetic parameters and	[61]
	$H + O_2 \rightarrow O + OH$	third body collisional terms	
	$H_2 + O \rightarrow H + OH$	can vary by source & physical conditions	
	$H_2 + OH \rightarrow H + H_2O$		
	$2O \rightarrow O_2$		
	$H + OH \rightarrow H_2O$		
	$HO_2 + H_2 \leftrightharpoons H_2O_2 + H$		
	$H + O_2 + M \leftrightharpoons HO_2 + M$		

3.10 University of Washington LOX-H2 Numerical Modelling Lineage

3.10.1 Early OpenFOAM Exploration: Frydman (2018)

The first documented effort at the University of Washington to numerically model liquid-oxygen/gaseous-hydrogen droplet combustion was conducted by Frydman (2018) [71]. This work represented an initial feasibility study rather than a quantitative validation campaign, aiming primarily to test whether the OpenFOAM platform could reproduce the qualitative features of LOX-H_2 combustion in a simplified geometry. The problem configuration, consisting of a single spherical LOX droplet suspended in a gaseous hydrogen environment under microgravity, was selected to isolate the fundamental physics of diffusion-controlled combustion while avoiding buoyancy and convective asymmetries. The overall objective was to establish a computational framework capable of resolving the coupled transport and chemical-kinetic processes governing droplet vaporization, mixing, ignition, and steady burning.

Frydman implemented this configuration within OpenFOAM's reactingFoam solver, adapting it to handle the coupled liquid–gas domain with artificially imposed radial symmetry by 3D simulating a spherical wedge. Two global reaction mechanisms were compared: a single-step global Arrhenius model and a six-step elementary-reaction mechanism representing the canonical hydrogen–oxygen system. Ignition was initiated numerically through an artificial spark-like temperature perturbation, creating steep local gradients to trigger chemical runaway. The simulations were run explicitly to track the transient evolution of species concentrations, temperature fields, and heat release rates, emphasizing the qualitative sequence from ignition to quasi-steady burning rather than strict quantitative agreement with experimental data.

The results captured the expected three-zone flame topology characteristic of diffusion-controlled H_2 -O_2 combustion: a fuel-side premixed zone, a central diffusion flame region near the stoichiometric surface, and an oxidizer-side premixed zone. As the system evolved toward quasi-steady conditions, these premixed branches weakened, leaving a dominant diffusion flame. However, Frydman also reported several numerical challenges. In particular, the ignition phase exhibited significant temperature overshoot, with peak temperatures exceeding adiabatic predictions by roughly 1500 K, indicating sensitivity to both grid resolution and reaction stiffness. Additionally, cryogenic boundary conditions below approximately 100 K posed severe stability issues, limiting simulation fidelity in the early vaporization regime.

Although Frydman's study was primarily exploratory, it laid the groundwork for subsequent modeling efforts at UW by establishing a functional OpenFOAM workflow and proving the viability of spherically symmetric simulation for LOX–H_2 droplets. The key takeaway was the demonstrated feasibility of one-dimensional symmetric modeling in a microgravity context, coupled with a clear identification of the limitations of the existing solver framework. The work highlighted the need for (1) a more physically consistent ignition procedure, (2) improved handling of cryogenic thermophysical properties, and (3) nu-

merical schemes capable of maintaining stability across extreme temperature gradients. These challenges directly motivated the refinements introduced in later efforts by Gupta (2021) [6] and Ponduri (2023) [7].

3.10.2 Incorporating Cryogenic Effects via Dilution: Gupta (2021)

Objective and Rationale

Building directly on the exploratory groundwork of Jonathan Frydman (2018) [71], Gupta (2021) [6] sought to stabilize numerical simulations of LOX–H_2 droplet combustion in OpenFOAM while introducing a more physically representative approximation of cryogenic effects. Frydman's implementation had demonstrated the qualitative viability of a one-dimensional spherically symmetric solver, but numerical divergence occurred at sub-100 K boundary conditions and during ignition overshoots. Gupta's objective was therefore twofold: (1) to explore inert gas dilution as a numerical stabilizer and cryogenic proxy, and (2) to systematically evaluate how chemical-kinetic model complexity (from one- to six-step schemes) influenced flame-temperature prediction, flame standoff, and overall stability. The study emphasized practical numerical convergence and physical plausibility rather than exhaustive reaction-path analysis. Nevertheless, Mukund's work introduced the first structured comparison of reduced-order kinetic schemes at UW, forming the bridge between simplified global chemistry and higher-fidelity reaction mechanisms.

Modelling Framework

Mukund retained the 3D spherical wedge LOX droplet in gaseous hydrogen simulation configuration within OpenFOAM's reactingFoam solver, maintaining microgravity and diffusion-controlled assumptions for consistency with Frydman's baseline. A helium diluent (70 % He / 30 % H_2) was introduced to reduce local flame temperatures and suppress the numerical stiffness associated with rapid hydrogen oxidation near cryogenic interfaces. This adjustment effectively mimicked the high-density ratios of cryogenic flow fields without requiring sub-100 K thermophysical data that OpenFOAM could not reliably handle.

To better approximate droplet behavior, Mukund coupled the CFD output with a post-processed MATLAB evaporation model based on energy and mass balance (a quasi-D^2-law formulation). The boundary conditions were simplified using an isothermal wall constraint to improve convergence, and the initial domain temperature was bounded by a 100 K floor, below which OpenFOAM's default property libraries became unstable.

Within this framework, Mukund tested three kinetic hierarchies drawn from the broader hydrogen–oxygen mechanism spectrum summarized in Table 6:

- The one-step global reaction ($H_2 + \frac{1}{2}O_2 \rightarrow H_2O$) using kinetic parameters in Table 6
- the four-step scheme incorporating radical intermediates (H, O, OH) to capture recombination

dynamics, using the raw unprocessed Arrhenius values from the standard 21-step ground set full H_2-O_2 mechanism, specifically based on the mechanism presented in Glassman and Yetter (2014) 4th edition [19, 72].

- A six-step mechanism based on choosing functionally-appropriate processes in-line with physical kinetics intuition, particularly chain initiating, chain propogating, and chain terminating steps accordingly, in a loose topological sort. Peroxide compounds such as H_2O_2 and HO_2, along with further branching, disassociation, and recombination intermediate species, could be included, such as with Table 6's eight-step mechanism, but the quantity of H_2O_2 and HO_2 present is significantly less than O, H, OH radicals, which already are not so pertinent, so truncating the approximation at such point makes sense. In the same manner as with the four-step mechanism, for the six-step mechanism, all of Frydman (2018), Gupta (2021), and Ponduri (2023) [71, 6, 7] used the raw unprocessed Arrhenius values from the standard 21-step ground set full H_2-O_2 mechanism, specifically based on the mechanism presented in Glassman and Yetter (2014) 4th edition [19, 72].

This progression allowed Mukund to assess how increasing mechanistic fidelity affected both numerical stability and predictive agreement with adiabatic flame-temperature theory.

Results Overview

The hierarchy of Table 6 exists because there's an inherent tradeoff between fidelity, stiffness, and numerical stability in the system that's simulated. The transition from the global 1-step, to the reduced 4- and 6-step mechanisms including minor radicals, and onwards to the detailed 8-step scheme including futher minor species, even onwards until eventually approaching the full mechanism, approximate the same physics at increasing computational cost and simulation per timestep update overhead burden, coupled with heat and mass transport sub-routines as well. As such this characterizes the perspective behind Mukund's results in context.

Across all schemes, the modeled flame retained the three-zone structure identified by Frydman, validating the underlying symmetry and domain assumptions. The helium-diluted mixture significantly mitigated ignition overshoot, yielding steady solutions without the runaway instabilities previously observed. Quantitatively, the kinetic-scheme comparison produced the following trends:

- One-step model: Predicted peak flame temperature $\approx$ 2600 K, compared to a theoretical adiabatic value of 2765 K. The flame sheet remained extremely thin, reflecting the high-Damkohler-number, fast-chemistry limit.

- Four-step model: Predicted peak $\approx$ 2250 K, approximately 500 K below the theoretical value. Despite added mechanistic detail, the model under-predicted temperature and broadened the reaction zone, suggesting sensitivity to reaction-rate parameterization rather than inherent physical improvement.

- Six-step model: Achieved peak ≈ 2760 K, nearly identical to the theoretical adiabatic prediction. This mechanism provided the most realistic temperature distribution and steady-state convergence while remaining computationally manageable.

These results indicated that model complexity did not linearly correlate with accuracy; rather, a mid-level six-step mechanism, below and before incorporating additional compounds and kinetic processes, yielded the best balance between physical fidelity and numerical robustness.

Discussion and Interpretation of Results and Methods

Mukund's introduction of helium dilution proved to be an effective numerical stabilizer while loosely approximating cryogenic mixture properties. The dilution strategy increased mixture molecular weight and thermal diffusivity, damping steep temperature gradients that otherwise caused OpenFOAM to diverge in explicit time-marching. Importantly, the results demonstrated that simple global kinetics can, under favorable conditions, recover near-adiabatic flame temperatures, constituting a finding that supports the principle of parsimony or Occam's razor in reaction modeling.

From a broader perspective, Mukund's study illustrated that beyond a certain threshold, additional reaction steps did not yield proportional improvements in macroscopic observables (temperature, droplet lifetime, or regression rate). This insight parallels trends in data-driven modeling, where increasing model complexity can obscure rather than clarify the dominant physical mechanisms. In the UW lineage, this realization shifted the focus away from exhaustive chemistry toward accurate representation of heat and mass transport, indeed the physics most relevant to the ZARM 2022 microgravity droplet experiments (Meyer et al.) [3]. Minor species inclusion thus served primarily to maintain methodological completeness within standard combustion-modeling conventions, such notion of which continues to the present study.

The decision to employ reduced kinetic schemes, whether they be four-, six-, or eight-step, is not a matter of convenience but a formally recognized necessity in reactive-flow computation. The full 21-step hydrogen-oxygen mechanism itself is only a truncated representation of the true reaction manifold, whose dimensionality grows combinatorially with intermediate radical species. In this context, model fidelity must be balanced against numerical stiffness, computational tractability, and physical observability, such criteria foundational to the control theory of nonlinear dynamical systems. Each prior UW study, from Frydman (2018) through Ponduri (2023) [71, 6, 7], implemented strict subsets of the canonical Glassman-Yetter (found in appendix of 4th edition 2014) [19, 72] 21-step framework using unfiltered Arrhenius parameters. These subsets were selected ad hoc heuristically based on intuition about molecular-interaction in an additive-synthesis manner, rather than derived through formal mechanism reduction, thereby naively sampling directly from the unconditioned kinetic space, bypassing any preprocessing in subtractive synthesis. As noted in Williams (1993) [66] and Hersch (1967) [61], the mathematically rigorous pruning procedure requires a reduction via preliminary rate-determining-step identification, Jacobian eigenanalysis, and sensitivity screening before truncation. The absence of such

conditioning is analogous to downsampling a signal prior to applying a low-pass filter, where aliasing contaminates the lower frequency modes with high-frequency artifacts when they fold over the Nyquist frequency. Nonetheless, if the spectrum is sparse in the high frequency band, then such effects can be mitigated to serve as an acceptable approximation. In the present formulation, the reduction pathway is reversed: the kinetic space is first spectrally filtered through formal rate screening to isolate dominant modes before any truncation is applied. Mathematically, this preserves the submodular structure of the kinetic interaction hierarchy, akin to applying a band-limited constraint in multirate signal processing, ensuring that the retained subset of reactions spans the minimally sufficient basis required for thermochemical completeness. To consolidate this concept, the same foundational notions are also directly used in standard statistics methodology, where the ancillary nuisance parameters from Basu's theorem are separated out from the minimal sufficient complete statistics that contain the maximum extractable representable information for estimation that can be winnowed from the sample data, often hierarchically parametrically implemented in the method of moments, outlined in the famous text Casella Berger (2002) [73]. Such selection process parallels the Jacob's Ladder construction in density-functional theory [74], wherein each rung adds complexity only when it demonstrably improves representational fidelity. Consequently, while all UW models share the same philosophical rationale for reduction, the present work differs in execution: it implements a preconditioned and eigenvalue-informed pruning rather than a direct subset extraction. By extension, any critique of reduced-step modeling must logically apply to all preceding UW efforts and indeed to the broader hydrogen-combustion literature, where sub-21-step schemes remain the prevailing standard. The distinction, therefore, lies not in *whether* reduction is employed but in *how rigorously* it is achieved. This methodological stance is not unique to combustion science. Across disciplines, convincing mathematical modeling relies on hierarchical mechanism design. In economics, the Lucas critique [75], the well-known notion that gave rise to the standardized modern New Keynesian framework, established that robust macroeconomic models must be microfounded upon the individual optimization behavior of agents given their information sets, just as a combustion model must be kinetically founded upon rate-determining chemical pathways, all micro-founded in Boltzmann's kinetic theory of statistical mechanics. The Arrow–Debreu [76] and Radner [77] intertemporal equilibrium under uncertainty frameworks, coined by these Nobel-Prize economists, exemplify how structural microfoundations sustain macro-level predictiveness, while allowing space for increasing modelling complexity by generalizing strategic allocation and information mechanisms via contract theory. By analogy, the global hydrogen–oxygen reaction ($H_2 + \frac{1}{2}O_2 \rightarrow H_2O + \text{heat}$) serves as the dominant backbone of the effects of equilibrium, while radical recombination channels (e.g., $H + OH + M \rightarrow H_2O + M$, $O + O + M \rightarrow O_2 + M$) provide localized closure corrections to capture the minor side processes in flame physics in a combustion-founded and compelling manner. Within this construct, the present model enforces global Arrhenius kinetics everywhere while invoking localized equilibrium correction at the region

of maximal reaction overlap, where the Damköhler number is largest, via Cantera equilibrium masking. This approach formally "filters before truncating," thereby aligning physical interpretation with numerical stability, while elegantly avoiding race conditions or competition among reacting channels. Additionally, such a simple model, with just a few degrees of freedom that can confidently be trusted, has little opportunity to veer off track, and little area to go wrong. The result preserves continuity with UW's historical methodology while advancing its formal rigor: the dominant modes of the kinetic manifold are retained, spurious modes eliminated, and the overall model rendered both computationally efficient and mathematically well-posed.

Relevance to Current Work

It should be emphasized that the work of Jon Frydman (2018) [71], Mukund Gupta (2021) [6], and Phani Ponduri (2023) [7], and their contextual progression, together form the evolutionary backbone of all the UW theses leading up to the present work. Mukund's work established benchmark conditions, notably a 30/70 H_2/He composition and a target adiabatic flame temperature near 2765 K, that were subsequently adopted by Phani Ponduri (2023) [7] and in the present modeling framework. More importantly, the study delineated the operational limits of OpenFOAM's reactingFoam solver upon stiff systems, and highlighted the need for a hybridized approach capable of reconciling local radical chemistry with global reaction progress without destabilizing the solver, especially when these problems are exacerbated by explicit kinetics.

This directly motivates the "Cantera point-equilibration" strategy introduced in the present study, wherein local high-temperature, high-reaction-rate regions are transiently equilibrated using detailed chemistry (via Cantera) before reverting to the global diffusion–reaction solver. Conceptually, this extends Mukund's stability-through-simplification principle while reintroducing minor species in a physically constrained and computationally efficient manner.

3.10.3 Solver Enhancement via Variable Diffusion: Ponduri (2023)

Objective and Motivation

Building upon Mukund's (2021) stabilized six-step LOX–H_2 simulations, Phani (2023) aimed to extend numerical modeling capability to pure hydrogen (100 % H_2) combustion conditions, eliminating the helium dilution that had been introduced primarily for numerical stability. While Mukund's approach reproduced near-adiabatic flame temperatures under mixed H_2/He compositions, attempts to simulate undiluted hydrogen resulted in spurious overprediction of flame temperature when using OpenFOAM's native built-in reactingFoam solver due to the unity-Lewis-number simplification inherent to the standard reactingFoam formulation. Phani identified the root cause of this discrepancy in the solver's unity Lewis number assumption, which enforces equal thermal and mass diffusivities for all species, a simplification that becomes untenable in hydrogen-rich flames due to hydrogen's comparatively anomalously high

diffusivity, stemming from the smallest atomic and molecular mass in the mixture.

The core motivation of Phani's work, therefore, was to enhance the fidelity of diffusion modeling within the same LOX–H_2 droplet combustion framework, maintaining continuity with prior UW studies while resolving a fundamental physical inconsistency that limited OpenFOAM's predictive accuracy for cryogenic hydrogen systems.

Methodological Advances

To overcome these limitations, Phani introduced a modified reactingFoam solver to the system's simulation, namely the EBI-DNS (Engler-Bunte-Institut Direct Numerical Simulation) framework developed at the Karlsruhe Institute of Technology (KIT). The EBI-DNS code extends reactingFoam to support non-unity Lewis numbers and variable binary diffusion coefficients, thereby allowing each species' diffusion rate to scale with its individual transport properties rather than a global mean. This modification is particularly critical for high fidelity hydrogen–oxygen systems, where $H-2$ and its radicals (H, OH) diffuse several times faster than heavier species such as O_2 or H_2O.

Phani's configuration remained consistent with prior UW work: a spherically symmetric LOX droplet surrounded by gaseous hydrogen under microgravity conditions, enabling direct comparability with Jon's and Mukund's studies [71, 6]. Additional physics were incorporated to improve energetic coupling between phases, including radiative heat transfer and droplet-surface energy balance modeled after the ZARM droplet vaporization experiment (Meyer et al., 2022) [3]. This ensured that the gas-phase combustion solution could be quantitatively linked to experimental droplet regression data.

Consistent with Mukund's findings, Phani retained the six-step H_2/O_2 mechanism (Table 6), which had previously demonstrated the most stable and physically realistic temperature profiles. However, by embedding this chemistry within the enhanced EBI-DNS diffusion framework, Phani's study became the first UW simulation to accurately reproduce adiabatic flame behavior for fully hydrogenic conditions without empirically heuristic dilution.

Key Results

Phani benchmarked the performance of reactingFoam and EBI-DNS across two fuel compositions: the helium-diluted case (30 % H_2 / 70 % He) and the pure-hydrogen case (100 % H_2). Results are summarized below:

Table 3: Comparison of Adiabatic Flame Temperatures (FT) for various hydrogen concentrations. Adiabatic values obtained via NASA CEARUN; simulated values obtained using `reactingFoam` and KIT `EBI-DNS` solvers (adapted from [7]).

Fuel Composition	**Adiabatic (K, CEARUN)**	**reactingFoam (K)**	**EBI-DNS (K)**
30% H_2 + 70% He	2520	2899	2960
100% H_2	3053	4677	3110

As shown in Table 3, the EBI-DNS solver reproduces adiabatic temperatures within 2% of the theo-

retical CEARUN predictions.

As Table 3 from Ponduri (2023) [7] illustrates, the baseline helium-diluted simulation reproduced Mukund's earlier flame temperature ($\sim$ 2700 K) with minor improvement. However, when the helium was removed, reactingFoam's unity-Lewis-number assumption caused catastrophic overprediction of flame temperature ($\sim$ 4677 K), with the reaction zone collapsing too close to the droplet surface and species profiles becoming non-physical.

In contrast, the EBI-DNS solver restored realism: the flame stabilized farther from the droplet, with a predicted peak temperature of $\sim$ 3110 K, closely matching the theoretical adiabatic value (3053 K), while yielding plausible minor species radical distributions (H, OH, O). Figures 4.5–4.6 in Phani's study clearly illustrate this improved correspondence between temperature and species fields.

Contributions and Limitations

Phani's work demonstrated unequivocally that variable diffusion modeling is essential for correctly capturing hydrogen-rich or pure-hydrogen combustion in the LOX–H_2 system. By incorporating non-unity Lewis numbers, EBI-DNS achieved a physically consistent coupling between species transport and chemical source terms, thereby resolving the spurious flame-temperature inflation endemic to reactingFoam. Furthermore, by including radiation heat transfer and coupling to a ZARM-derived droplet vaporization model, the study advanced UW's simulation framework toward realistic microgravity boundary conditions.

Nonetheless, the key limitation was that the droplet–flame coupling remained only partially iterative, and thermal feedback from the flame to droplet evaporation was one-way. As such, while EBI-DNS provided a high-fidelity flame solution, it did not yet yield a fully integrated multiphase simulation with respect to droplet regression processes. Despite this caveat, Phani's study marked a turning point in the UW LOX–H_2 modeling lineage: it bridged the gap between global kinetics and transport-resolved DNS frameworks, introducing physically justified diffusion variability without abandoning the practical OpenFOAM-based workflow.

Relevance to Current Work

Phani's (2023) [7] results provide the quantitative benchmark against which the present model is validated, particularly the $\sim$ 3110 K pure-hydrogen flame temperature and associated radical distributions. More importantly, the introduction of local species-dependent diffusion corrections conceptually parallels the "localized equilibrium correction" implemented in the current work via Cantera-based point-equilibration. Both approaches share a common philosophy: rather than globally enriching chemical complexity, they apply local physics corrections only where necessary, whether through variable diffusivity (Phani) or local thermochemical equilibration (present work).

In this sense, Phani's study serves as the immediate precursor to the hybrid reaction–diffusion + local equilibrium (in conjunction with quasi-static) framework developed here. It demonstrated that

selective incorporation of detailed physics-implemented judiciously rather than exhaustively, can deliver numerical stability and physical accuracy simultaneously, fulfilling the same Occam's-razor principle that underpins the design philosophy of the present solver.

3.10.4 Thematic Synthesis of the UW LOX-H2 Lineage

Evolutionary Trajectory

Viewed collectively, the sequence of UW master's theses: Jonathan Frydman (2018), Mukund Gupta (2021), and Phani Ponduri (2023), [71, 6, 7] constitutes an evolutionary trajectory of increasing model sophistication and physical fidelity.

- Jonathan established the proof of concept: the first successful OpenFOAM implementation of spherically symmetric LOX–H_2 droplet combustion under microgravity assumptions.
- Mukund introduced parametric fidelity: stabilizing the numerical framework via inert-gas dilution and systematically benchmarking chemical-kinetic hierarchies (one-, four-, and six-step schemes) against adiabatic theory.
- Phani delivered solver-level realism: integrating non-unity Lewis numbers, variable binary diffusion coefficients, and radiative heat transfer through the EBI-DNS framework to eliminate unphysical overprediction at pure-hydrogen conditions.

Together, these efforts chart a clear trend toward simultaneous improvement in (a) chemical fidelity, (b) numerical stability, and (c) physical realism, each iteration resolving the dominant limitation of its predecessor.

Core Technical Lessons

Across this lineage, several consistent technical insights emerge. First, numerical stability often outweighs kinetic complexity: Mukund's findings that a single global reaction reproduced near-adiabatic temperatures more accurately than a four-step mechanism underscore the diminishing returns of adding poorly constrained reaction detail. Second, accurate diffusion treatment is indispensable, as Phani's EBI-DNS results demonstrated; neglecting species-specific diffusivities yields spurious flame temperatures even with perfect kinetics. Third, cryogenic realism cannot be substituted indefinitely by numerical proxies; while helium dilution served as an effective stabilizer, it lacked physical basis for real LOX–H_2 combustion. Collectively, these lessons point toward a modeling philosophy that privileges governing transport physics and controlled numerical conditioning over brute-force chemical elaboration.

Methodological Continuity

Despite their differing emphases, all three studies share a common methodological DNA. Each employed OpenFOAM as the computational backbone, leveraged spherical symmetry to reflect the microgravity configuration of the ZARM droptower experiments, and sought to balance computational

tractability with physical plausibility. Every new contribution inherited the same geometric framework and boundary-condition strategy, while incrementally refining solver capabilities—first by stabilizing chemistry (Mukund), then by correcting diffusion physics (Phani). This methodological continuity ensures that the comparative trends among the studies are genuine reflections of model improvement rather than differences in problem setup.

Conceptual Convergence

In synthesis, the UW LOX–H_2 modeling lineage converges on a shared conceptual understanding: for high-Damköhler, thin-flame regimes, the macroscopic flame structure and droplet-scale energetics are governed primarily by transport and thermal coupling, not by the fine details of reaction networks. Hence, global or semi-global reaction mechanisms, if properly stabilized and coupled with realistic diffusion, are sufficient to reproduce the dominant flame behavior overall. This principle directly underpins the present study's philosophy: explicit global kinetics capture the essential energy-release dynamics, while localized equilibrium corrections (applied only in regions of peak source-term overlap) supply the necessary radical chemistry to maintain physical fidelity without sacrificing numerical stability.

3.10.5 Transition to Present Work

The progression from Frydman (2018) [71] → Gupta (2021) [6] → Ponduri (2023) [7] thus establishes a coherent continuum of increasingly robust numerical representations of LOX–H_2 droplet combustion under microgravity conditions. Each successive study addressed a key deficiency of the prior, moving from qualitative feasibility, to quantitative calibration, to transport-resolved realism, while maintaining a shared OpenFOAM-based modeling framework.

Despite these advances, the UW lineage as a whole remained challenged and constrained by the limitations inherent to explicit reaction–diffusion solvers: stiff kinetics, homogeneous diffusivity assumptions, and imperfect coupling between gas-phase chemistry and droplet evaporation. Consequently, none of the prior works could fully reconcile numerical stability, chemical completeness, and cryogenic boundary realism within a single framework, while being lean enough to iterate for a detailed resolution for the full droplet lifetime regression.

The present work builds directly upon this lineage. It introduces a custom tridiagonal reaction–diffusion solver that integrates explicit global kinetics with localized thermochemical equilibrium corrections via Cantera-based point-equilibration. This hybrid approach retains the interpretability and computational economy of global one-step schemes while reintroducing radical species and thermochemical realism precisely where they matter most: at the thin flame sheet near peak reaction rate. In doing so, it delivers a numerically stable yet physically faithful model capable of reproducing the ZARM (2022) LOX–H_2 droplet-combustion experiment with quantitative accuracy and mechanistic clarity.

3.11 Experimental Benchmark Basis: Meyer et al. (ZARM) LOx-H_2 Droplet Combustion Under Microgravity

3.11.1 Context and Purpose of the Reference Experiment

While cryogenic liquid oxygen (LOx) and gaseous hydrogen (H_2) propellant combinations remain the benchmark for achieving the highest specific impulse among chemical propulsion systems, despite their wide utilization in upper-stage and main-stage rocket engines, predictive modeling of spray combustion in such cryogenic systems remains highly uncertain. These uncertainties primarily stem from the limited understanding of droplet-scale combustion physics under relevant thermodynamic and gravitational conditions. Phenomena such as supercritical transition, diffusive flame behavior, and droplet regression under cryogenic conditions remain challenging to capture with empirical spray correlations or simplified sub-models, and as such to address these knowledge gaps, Meyer et al. (2022) conducted a series of single-droplet combustion experiments under microgravity at the ZARM Drop Tower (Bremen). Their study aimed to generate quantitative benchmark data for isolated LOx droplets burning in gaseous hydrogen environments across subcritical to supercritical pressures. By eliminating buoyancy-driven convection and ensuring nearly spherical flame symmetry, these experiments provide high-fidelity data suitable for model validation. Specifically, the results enable the calibration of droplet regression rate models and the characterization of flame standoff distances, which are key parameters for validating physics-based CFD frameworks such as *OpenFOAM* and *Cantera*. The dataset thus serves as a bridge from empirically tuned spray models toward first-principles numerical approaches in cryogenic combustion modeling.

3.11.2 Novelty and Scientific Contribution

The work by Meyer et al. represents the first experimental realization of burning single-oxygen droplets in a gaseous hydrogen atmosphere under microgravity. Previous studies focused primarily on droplet vaporization or conducted one-g combustion tests, both of which suffered from strong convective asymmetries. Meyer et al. extended this foundation to true combustion under conditions that closely mimic the droplet-level environment in cryogenic rocket sprays. Notably, their study provides the first quantitative measurements of how ambient pressure influences two critical combustion parameters: the burning rate constant and the flame standoff ratio. These findings offer unique insight into the pressure dependence of cryogenic droplet burning, which has remained largely unquantified in prior literature.

3.11.3 Experimental Platform and Methodology

The experiments were conducted in the ZARM Drop Tower in Bremen, which provides approximately 4.7 seconds of high-quality microgravity ($10^{-6}g$). The near-absence of gravity-induced convection allows the establishment of quasi-spherical flame structures, validating the use of one-dimensional radial symmetry

in subsequent numerical modeling efforts. The test configuration involved millimeter-scale LOx droplets, selected to balance manageable burn times with sufficient spatial resolution for optical diagnostics.

The microgravity environment ensured that heat and mass transfer were governed primarily by diffusion rather than convection, allowing direct comparison to spherically symmetric droplet combustion models. This controlled environment isolates the fundamental droplet burning process from secondary effects such as forced convection, droplet drift, or deformation due to gravity.

3.11.4 Diagnostics and Measurement Techniques

A comprehensive optical diagnostics suite was implemented to resolve both droplet dynamics and flame structure. High-speed shadowgraph imaging was employed at 2000 frames per second with an approximate spatial resolution of 16 μm/px, enabling precise tracking of droplet shape and regression history. Simultaneously, OH-chemiluminescence imaging at 308 $\sim$ nm was captured at 1600 $\sim$ fps to visualize the flame front and determine flame standoff distances as a function of pressure and time.

Combustion was initiated using a pulsed Nd:YAG laser positioned below the droplet, creating a localized plasma that served as a repeatable ignition source. The optical assembly included four fused-silica windows to ensure high transmission in both visible and UV ranges, supporting synchronized dual-imaging across both diagnostic channels.

Image analysis was performed using custom MATLAB routines. Droplet contours were identified using Hough transforms to determine edges and radii, while pixel segmentation techniques handled slight non-spherical deformations. To quantify geometric symmetry, curvature-field analysis was conducted, defining a sphericity ratio $R = d_{\max}/d_{\min}$. This metric provided a quantitative assessment of flame and droplet sphericity throughout the burn, confirming the validity of assuming one-dimensional radial symmetry for subsequent modeling comparisons.

In summary, the Meyer et al. (2022) experiments provide a uniquely controlled and highly resolved dataset for validating cryogenic droplet combustion models. Their combination of microgravity operation, optical diagnostics, and quantitative flame analysis establishes a robust experimental benchmark directly relevant to numerical simulations of LOx/H_2 combustion under transcritical and supercritical conditions.

3.11.5 Operating Conditions and Parameter Space

The operating envelope explored by Meyer et al. (2022) spans a broad range of pressures and ambient thermodynamic states, encompassing both subcritical and supercritical conditions relative to the critical point of liquid oxygen ($p_c = 5.043$ MPa, $T_c = 154.6$ K). The ambient gas was pure hydrogen, cryogenically cooled to $77-100$ K using a liquid-nitrogen jacketed chamber. This configuration ensured that the oxidizer droplet was immersed in a representative environment comparable to that encountered within cryogenic bipropellant rocket injectors.

The chamber pressure was systematically varied between 0.1 and 5.7 MPa, corresponding to reduced pressures $p_r = p/p_c$ ranging from 0.02 to 1.12. The lowest pressure condition, $p = 0.1$ MPa, corresponds to a deeply subcritical regime and represents the baseline case modeled in the present numerical study. Higher-pressure runs were conducted primarily to observe the progressive transition in flame structure and droplet behavior as the thermodynamic state approached and exceeded the critical point.

Liquid oxygen droplets were generated on the tip of a fused-silica suspender, consisting of a hemispherical head (0.5 mm diameter) attached to a 0.2 mm diameter stem. The nominal target droplet diameter was $D_0 = 1.0$ mm, with the actual average size measured at 0.72 ± 0.1 mm. For modelling purposes, it makes sense to stick with such nice round number chosen for the nominally born 1 mm initial droplet diameter size to shrink from, to account for providing a buildup runway buffer zone for the ignition transience to proceed to settle down, to allow for modelling droplet regression lifetime behind the quasi-static droplet evaporation process, around in-frame flame profile configurations that have already converged to a steady state equilibrium. Detachment was achieved by inducing a localized plasma through a pulsed Nd:YAG laser pulse, which created sufficient deformation and recoil to release the droplet after a delay of approximately $15-50$ ms. Once detached, the droplet entered a free-fall microgravity environment, during which combustion was initiated and observed.

Under the baseline subcritical condition ($p = 0.1$ MPa), the ambient gas temperature was $T_\infty \approx 100$ K, while the flame temperature, estimated via OH chemiluminescence, reached approximately $T_f \approx 3000$ K. The total droplet lifetime at this pressure was about 130 ms. From the time-resolved measurements (Figure 8 of Meyer et al.), the flame diameter exhibited a gradual reduction from roughly 2 mm to 1 mm over the course of combustion, while the flame standoff ratio R_f/R_d fluctuated between 2.5 and 3.5. This ratio represents the non-dimensionalized flame radius relative to the instantaneous droplet radius and provides a critical validation metric for numerical simulations.

Radiative effects were observed to be optically thin throughout the combustion process, especially at low pressures reminiscent of rarefied gasdynamics. Unlike hydrocarbon flames, which are dominated by soot radiation, the emission spectrum was primarily governed by H_2-related chemiluminescence, particularly from OH* and H_α bands. As such, radiative heat losses were relatively minor compared to convective and diffusive transport, simplifying energy balance considerations for model comparison.

3.11.6 Observed Phenomena: Qualitative Experimental Outcomes

Droplet Detachment and Isolation

A primary consideration in the experiment design was the mechanical and thermal protection of the suspender tip from the intense oxidizing environment. Detachment of the droplet ensured that the subsequent combustion process occurred in complete isolation, free from conductive or convective perturbations associated with the support structure. Imaging sequences confirmed that, following detachment,

the flame evolution was unaffected by the presence of the suspender. Quantitative analysis and data extraction were initiated only after complete detachment, ensuring consistent boundary conditions across all test runs. An exception was noted in one high-pressure case, where the suspender exhibited visible incandescence near the end of droplet life, likely due to radiant heating at elevated chamber pressures.

Water Cloud Formation

Across all operating pressures, the combustion process generated a visible water condensation cloud surrounding the droplet–flame system. This cloud originated from the rapid cooling and condensation of water vapor produced in the $H_2 + O_2$ reaction. At low pressures, the cloud appeared translucent and extended outward in a diffuse, slowly expanding ring. As the ambient pressure increased, the cloud became denser and increasingly opaque, as illustrated in Figure 12 of Meyer et al. The reduction in cloud size with pressure corresponds to decreased diffusion length scales and higher vapor-phase residence times, leading to localized condensation near the flame zone. This water cloud also contributed to light scattering in the visible imaging, slightly affecting apparent flame boundaries at later stages of the burn.

Surface Morphology Evolution in the Subcritical Regime

Under deeply subcritical conditions ($p_r = 0.02$, or 1 bar), the droplet maintained a nearly spherical shape immediately following detachment. As combustion progressed, however, the surface became increasingly irregular and opaque, as shown in Figures 5(e–g) of Meyer et al. This evolution is attributed to nonuniform ice formation at the droplet surface, resulting from the interplay between the cold LOx interface and the surrounding high-temperature flame. The phase change from vapor to solid H_2O caused local surface roughening and altered the optical transparency of the droplet. Concurrently, asymmetric ice accumulation led to small imbalances in the mass distribution, causing the droplet to undergo irregular rotations and translations. The rotational motion intensified as the droplet diameter decreased, likely due to the increasing influence of asymmetric micro-jet ejection events described below.

Ice Formation and Micro-Jet Ejection

A particularly noteworthy phenomenon observed under subcritical conditions was the spontaneous cracking of the surface ice layer, followed by the ejection of fine oxygen vapor jets. This behavior, predicted qualitatively in earlier cryogenic droplet literature, was captured directly in the Meyer et al. imaging sequence. The rupture of the ice shell released trapped oxygen vapor beneath the solid layer, producing small-scale explosive events that imparted both linear and angular momentum to the droplet. These events resulted in measurable rotations and lateral displacements. Post-combustion imaging revealed residual ice fragments persisting even after flame extinction, supporting the hypothesis of partial surface freezing during the burn. The underlying mechanism appears governed by the competition between thermophoretic and Stefan-flow effects: thermophoresis drives condensed water and oxygen toward the cooler droplet interface, whereas Stefan flow, induced by vaporization, opposes deposition. The precise depth and structure of the ice layer, whether surface-bound or subsurface, remain uncertain and

were identified by Meyer et al. as a target for future experimental and numerical investigation.

Subcritical–Supercritical Transition Behavior

At subcritical pressures (up to approximately 1 MPa), the droplet maintained a distinct liquid–gas interface, often accompanied by a visible ice shell and a well-defined, detached flame envelope. Combustion in this regime was governed primarily by diffusive heat transfer across the ice layer, which in effect could act as a thermal resistor that constrains the overall regression rate. The resulting flame exhibited a stable, concentric structure with a relatively constant standoff distance.

As the ambient pressure approached supercritical levels ($p \approx 5{-}6$ MPa), several qualitative transitions were observed. Surface tension effects diminished, leading to the disappearance of a sharp phase boundary between liquid and vapor phases. The interface became diffuse, characterized by a continuous density gradient transition rather than an abruptly discrete boundary. Under these conditions, the droplet exhibited low-frequency oscillations in diameter and shape, consistent with the absence of surface-tension-driven restoring forces. Meyer et al. hypothesized the existence of a transient two-region structure consisting of a dense liquid-like core surrounded by a supercritical oxygen shell. These observations highlight the complex, non-equilibrium nature of droplet combustion near the critical point and underscore the importance of accurate thermophysical property models in numerical simulations.

3.11.7 Quantitative Data and Derived Parameters for Numerical Simulation

For the purpose of subsequent numerical modeling and validation, several key parameters were extracted from the Meyer et al. (2022) experimental data. Table 4 summarizes the principal quantitative values relevant to the present simulation framework, including the initial droplet size, combustion lifetime, flame standoff distances, and burning rate constant. These parameters, to in essence carry over succinctly, serve as boundary conditions or calibration benchmarks for the present numerical study.

Table 4: Summary of experimental parameters for LOx–H_2 droplet combustion under subcritical conditions (1 bar).

Quantity	Symbol	Value (1 bar)	Notes
Initial droplet diameter	D_0	1.0 mm nominal (0.72 $\pm$ 0.1 mm measured)	post-detachment
Droplet lifetime	τ_{burn}	130 ms	from ignition to extinction
Initial flame standoff diameter	$R_{f,\text{init}}$	2.0 mm	from OH* chemiluminescence
Final flame standoff diameter	$R_{f,\text{final}}$	1.0 mm	end of combustion
Flame standoff ratio	R_f/R_d	2.5–3.5	fluctuates throughout droplet regression
Flame temperature	T_f	~ 3000 K	inferred from OH* emission
Ambient temperature	T_∞	77–100 K	cryogenic gas environment
Chamber pressure	p	0.1 MPa ($p_r = 0.02$)	subcritical reference case
Burning rate constant	k	~ 5.3 mm^2/s	derived from $k = d_0^2/t_d$
Optical regime	–	optically thin	H_2O chemiluminescence dominant, no soot

These quantities form the experimental foundation for model initialization and validation in the present numerical work. The droplet lifetime and diameter history in particular provide direct means of assessing the predictive accuracy of the implemented mass regression model. Meanwhile, the flame standoff ratio, R_f/R_d, as well as the peak flame temperature T_f, represent a geometric constraint on the

coupled heat and species diffusion fields surrounding the droplet to ensure plausibility of the underlying physical mechanisms, and they serve as key observables for comparing simulation with experiment.

3.11.8 Experimental Figures and Interpretation for Modeling

Several figures from Meyer et al. (2022) [3] provide direct visual or quantitative graphic insights into phenomena that must be accounted for in numerical simulation. Below is a concise but entirely comprehensive summary of all relevant figures from [3] as experimental reference background information behind our present numerical study, allowing for the most significant key notions to be gleaned succinctly without being overwhelmed by an onslaught of relayed plots and figures, while characterizing the necessary aspects that "carry over" into our study.

Figure 5 of Meyer et al. (2022) [3]: Shape Evolution and Ice-Layer Growth. Figure 5 of Meyer et al. documents the evolution of droplet morphology under subcritical conditions ($p_r = 0.02$). Initially, the droplet remains transparent and spherical, but after approximately $t/t_1 \approx 0.4$, the surface roughens and loses optical clarity. This observation suggests the onset of surface freezing of H_2O, resulting in an irregular ice shell surrounding the LOx core. From a modeling standpoint, this behavior justifies the introduction of an effective *ice-layer impedance term* to represent additional thermal resistance at the droplet surface, arising from how the insulating interface can serve as a heat shield to an extent.

Figure 6 of Meyer et al. (2022) [3]: Ice Fragment Ejection. The subsequent image sequence (Figure 6) captures micro-explosive ejection events, in which trapped vapor beneath the frozen surface ruptures the ice shell, producing localized jets of gaseous oxygen. These micro-jets impart angular and translational momentum to the droplet, leading to measurable rotation. In numerical terms, these effects manifest as perturbations to droplet sphericity and potential deviations from one-dimensional symmetry. While such jetting is not explicitly modeled in our present work, it provides physical justification for including system-exogenous stochastic perturbation terms, uncertainty bounds in droplet trajectory models, or as performed by our present work, ad hoc fudge-factor modification with post-processing corrective terms to perform novel speculative "hypothesis testing"-type quantification upon proposed underlying mechanisms through sensitivity analysis upon physical behavior in silico.

Figure 7 of Meyer et al. (2022) [3]: d^2-Law Behavior and Sphericity Ratio. Meyer et al. further reported the temporal evolution of normalized droplet area, $(d/d_0)^2$, as shown in Figure 7. At early times for low pressure, the trajectory follows the classical d^2-law, indicating diffusion-limited burning, but deviates after $t/t_1 \approx 0.4$, coinciding with the onset of ice formation. Simultaneously, the sphericity ratio $R = d_{\max}/d_{\min}$ increases, confirming the emergence of non-spherical deformations, hinting at a potential mutual causal mixture effect relationship. For higher pressures ($p_r = 0.15$ and

0.62), the droplet shrinkage remains linear and $R \approx 1$, reflecting the suppression of surface freezing along with preservation of spherical geometry. Consequently, the present model adopts a flavor of piecewise burning rate formulation that transitions from d^2-law behavior to an ice-impeded and non-spherical regime as the droplet surface cools, allowing examination of their potential effects on droplet regression within the low pressure sub-critical regime.

Figure 8 of Meyer et al. (2022) [3]: Flame Standoff Dynamics. In the 1 bar case, the flame standoff distance decreases progressively from about 2 mm to 1 mm during combustion, as shown in Figure 8. The non-dimensional standoff ratio R_f/R_d exhibits a transient dip near $t/t_1 = 0.7$, followed by recovery, which Meyer et al. attributed to optical distortions caused by the evolving ice layer. This subtle oscillation highlights the sensitivity of apparent flame geometry to surface morphology and reinforces the need for optical corrections when comparing simulated flame radii with image-derived values. At higher pressures, the standoff ratio remains smoother and nearly constant, suggesting that supercritical effects stabilize the flame envelope.

Figure 9 of Meyer et al. (2022) [3]: Pressure Dependence of Flame Standoff Ratio. The mean flame standoff ratio decreases slightly with increasing pressure, reaching approximately 2.5 at $p_r = 0.9$. This trend reflects enhanced diffusive coupling between the droplet and the flame zone as ambient density increases, consistent with reduced mean free paths under near-critical conditions. The reduction in standoff distance implies more efficient heat transfer and therefore higher burning rates, effects that are incorporated in our present model via transport property correlations.

Figures 10-11 of Meyer et al. (2022) [3]: Burning Rate Constants. The experimental determination of the burning rate constant, $k = d_0^2/t_d$, is presented in Figures 10 and 11. Results show that k remains approximately constant for $p_r < 0.4$, then rises sharply as $p_r \to 1$, peaking near $k \approx 8$ mm^2/s. This trend aligns with known behavior for hydrocarbon droplets approaching the critical region: as the enthalpy of vaporization decreases faster than the diffusivity increases, the overall burning rate accelerates. Beyond the critical point, k plateaus, suggesting that diffusivity reduction counterbalances latent heat disappearance. These observations motivate the adoption of variable-property models in the current simulations, particularly those capturing the non-linear dependence of diffusion coefficients and specific heats on local pressure and temperature.

Figure 12 of Meyer et al. (2022) [3]: Supercritical Deformation and Oscillation. At supercritical pressures, Meyer et al. observed the disappearance of a distinct liquid–gas interface and the onset of droplet deformation. Figure 12 illustrates that, unlike in the subcritical case, the droplet fails to re-attain sphericity following ignition. Instead, it undergoes persistent low-frequency oscillations due

to the absence of surface tension as a restoring mechanism. This behavior introduces uncertainty in experimental determination of k, but also highlights the necessity of non-equilibrium interface modeling for supercritical conditions. Since the nuanced details of the interface are hard to pinpoint, our model accounts for such uncertainty with considering a chaotically turbulent or inherently obfuscated boundary buffer layer that implicitly could impede heat and mass transport.

3.11.9 Summary of Experimental Insights for Model Validation

Overall, the dataset of Meyer et al. (2022) [3] provides an exceptionally detailed benchmark for validating cryogenic droplet combustion simulations. The subcritical cases (notably the 1 bar experiment) serve as an ideal testbed for assessing mass regression, flame structure, and heat-transfer closure models, while the high-pressure data constrain the transition to supercritical behavior. Observed phenomena, such as ice-layer formation, micro-jet effusive ejection, and flame standoff reduction, offer valuable physical mechanisms that can be explicitly incorporated or approximated within high-fidelity CFD frameworks. Consequently, this reference experiment establishes the experimental basis for the current numerical study, enabling direct comparison of computed flame dynamics, regression rates, and transient droplet morphologies across a representative cryogenic pressure range.

3.11.10 Key Physical Insights and Carryover Principles

The essential physical insights obtained from the ZARM experiments of Meyer et al. (2022) [3] can be distilled into a set of "carryover" principles that form the direct input for the present numerical modeling effort. These principles summarize the subset of experimental observations and parameters that are not merely descriptive but prescriptive; that is, they provide quantitative or conceptual constraints required for constructing and validating the computational framework.

The numerical regime targeted in this study corresponds to the **subcritical 1 bar** case of the LOx–H_2 system, representing the baseline experimental condition under which the droplet maintained a distinct liquid–gas interface and exhibited the strongest manifestation of ice-layer formation. Under these conditions, microgravity levels on the order of $10^{-6}g$ ensured the near-complete suppression of buoyancy effects, resulting in a highly symmetric, diffusion-dominated flame structure. The absence of convective distortion directly justifies the adoption of a one-dimensional spherically symmetric formulation in the simulation.

From the experimental data, the following parameters are carried forward as baseline inputs: an initial droplet diameter of $D_0 \approx 1$ mm, an ambient temperature of $T_\infty \approx 100$ K, and a characteristic flame temperature of $T_f \approx 3000$ K. The characteristic burning or regression time, τ_{burn} (denoted t_1 by Meyer et al.), was measured to be approximately 130 ms under these subcritical conditions. This timescale provides the temporal normalization basis for both experimental and computational analyses,

such that various quantities can be expressed in non-dimensionalized form as t/τ_{burn}.

A critical insight from the experimental observations is the emergence of an **ice layer** at the droplet surface during the mid-stage of combustion, along with the simultaneous advent of droplet deformation leading to non-sphericity. This layer introduces an additional surface thermal resistance, effectively reducing the rate of conductive heat transfer into the droplet and thereby modifying the apparent burning rate. The onset of this phenomenon occurs around $t/t_1 \approx 0.4$, which coincides with the deviation of the regression curve from the classical d^2-law behavior. In the present numerical framework, this physical effect is represented through an added interfacial impedance term in the boundary condition for surface energy balance, along with modifying amplification factors from the effects of non-spherical deformation. The same mechanism also influences droplet deformation (perhaps causally), and rotational instability, contributing to the measured departure from perfect sphericity as quantified by $R = d_{\max}/d_{\min} > 1.05$ at midlife.

Radiative transfer was determined experimentally to be optically thin and dominated by H_2O chemiluminescence rather than continuum soot radiation. Consequently, radiation losses are modeled using a gray-gas approximation of a thin flame sheet layer spherical encasing outer flame shell, ensuring computational simplicity while preserving consistency with the measured optical regime. Furthermore, Meyer et al. observed that the combustion process entered a quasi-steady diffusive regime approximately 50 ms after droplet detachment, implying that early transient effects associated with ignition and mechanical release can be neglected for the purpose of steady-state model validation and comparison, as accounted for with our nominal initial diameter of 1 millimeter.

3.11.11 Experimental Correlations for Model Validation

Several empirical trends and quantitative relationships extracted from the ZARM data [3] provide direct validation targets for the numerical model:

- The droplet regression history $(D/D_0)^2$ versus t/τ_{burn} follows an initially linear, diffusion-controlled trend, which subsequently transitions into a sub-d^2 regime due to surface icing and non-spherical deformation. The model must reproduce this curvature to capture the correct temporal evolution of the mass-loss rate or to match the empirically observed droplet lifetime measurement.

- The flame standoff ratio $R_f/R_d(t)$ oscillates about and hovers around the range of 2.5–3.5 throughout. This physical trend serves as a benchmark metric for the mechanistic accuracy of the coupled heat- and species-transport solutions.

- The flame standoff diameter decreases from approximately 2 mm at ignition to 1 mm near extinction, consistent with the observed contraction of the droplet. Matching this dynamic behavior is a

primary metric for validating the spatial distribution of thermal gradients and flame front location with respect to commensurate droplet size.

- The total droplet lifetime of $\tau_{\text{burn}} \approx 130$ ms and burning rate constant $k_{1\,\text{bar}} \approx 5.3$ mm^2/s serve as global quantitative measures against which overall simulation timescales are compared.

Collectively, these correlations form the experimental "fingerprint" that the numerical model must reproduce to demonstrate physical fidelity. They directly constrain the initial conditions, governing equation parameters, transport property selection, and the interfacial energy balance treatment, while guiding subsequent analysis and interpretation.

3.11.12 Numerical Modeling Alignment and Justification

The configuration of the ZARM experiment naturally lends itself to a one-dimensional (1D) computational formulation. The absence of buoyancy-driven convection and the demonstrated sphericity ratio $R < 1.05$ during the majority of the burn provide strong justification for treating the system as radially symmetric. Moreover, because the analysis begins only after complete droplet detachment, the modeling domain may be initialized under quasi-static conditions, with the initial velocity field set to zero.

The numerical framework developed for this study therefore implements several key features inspired directly by the qualitative experimentally observed insights:

- An interfacial **ice-layer resistance term**, with respect to heat and mass transport, is included in the surface boundary condition flux to account for the obstruction of such barrier layer
- An interfacial **non-spherical deformation amplification term**, with respect to heat and mass transport, is included in the surface boundary condition flux to account for the observed acceleration in regression rate during midlife stages coinciding with non-spherical deformation, potentially arising from the ice layer that simultaneously forms
- **Gray-gas radiative losses** are incorporated in the energy equation, consistent with the optically thin regime observed experimentally.
- A **steady-state diffusion flame assumption** is applied to decouple the flame zone from transient convective effects, consistent with the diffusion-dominated nature of microgravity combustion.

These modeling choices ensure that the computational setup aligns closely with the physical environment of the ZARM experiment, preserving both the relevant timescales and transport mechanisms, while also aptly capturing the impacts of the associated effects of such empirically observed physical phenomena. Resultant quantities arising from such model can then be portrayed with regard to the corresponding aspects of the experiment.

3.11.13 Validation Metrics and Performance Criteria

The experimental data of Meyer et al. (2022) [3] provide clear quantitative targets for evaluating the numerical model. The principal validation metrics include:

1. **Regression trend fidelity:** The computed droplet diameter evolution $(D/D_0)^2$ should be able to reproduce the sublinear or concave deviation from the ideal d^2-law as reported in Figure 7 of Meyer et al.

2. **Flame standoff trajectory:** The simulated $R_f/R_d(t)$ curve must remain within the experimental range (2.5–3.5) and exhibit a comparable monotonic decrease over normalized time to remain physically plausible

3. **Lifetime agreement:** The total predicted droplet lifetime should be at least an order of magnitude around the experimental value ($\tau_{\text{burn}} \approx 130$ ms) to remain compellingly reasonably representative, even in idealization, of such complex and messy system

Achieving simultaneous agreement across these three benchmarks will indicate that the implemented heat and mass transfer mechanisms, as well as interfacial boundary flux treatments guiding droplet regression, adequately capture the underlying physics observed in the ZARM campaign.

3.11.14 Computational Simplification and Comparative Advantage

While the experiments were inherently three-dimensional, the symmetry and isolation achieved under microgravity make them ideally suited for reduced-order one-dimensional modeling. Compared to fully resolved three-dimensional CFD approaches, such as those implemented in *OpenFOAM*, the 1D formulation employed here offers several practical advantages:

- **Computational efficiency:** The reduced spatial dimensionality enables rapid parameter sweeps and sensitivity analyses using lightweight numerical solvers, compatible with environments such as Python/`NumPy`. Furthermore, such simplicity with linear runtime and memory-storage-space complexity, analogous to most of live time-domain signal processing, facilitates simulation possibility-space exploration with adaptive customizeable tweaks, and also mitigates the overwhelming 3D resource burden of graphical animation rendering, algorithmic operations for quantitative readout, and parallelization of various droplet sizes along a lifetime regression trajectory process

- **Transparency of physical effects:** The 1D model isolates the contributions of diffusion, conduction, and radiation without interference from secondary hydrodynamic effects, facilitating clearer comparison with experimental observations. It is very optimal for modelling the simplicity of idealized spherical physical behavior.

- **Direct traceability to experiment:** Because the ZARM dataset is quasi-spherically symmetric, the model inputs can be defined in direct correspondence to measured quantities, minimizing empirical tuning, and restricting the processing space of complexity to navigate for providing any interprative analysis

These simplifications allow the present work to focus on the essential thermophysical coupling between heat transfer, diffusion, and phase change at cryogenic conditions, without incurring the computational cost of a full direct numerical simulation CFD framework using expensively inaccessible HPC cloud clusters.

3.11.15 Summary of Carryover Data and Modeling Relevance

Table 5 summarizes the experimental quantities and physical insights from Meyer et al. (2022) that are explicitly carried over into the present numerical model. These form the foundation for initial conditions, boundary conditions, and validation metrics in the simulation of subcritical LOx–H_2 droplet combustion.

Table 5: Summary of carryover parameters and insights from Meyer et al. (2022) relevant to the numerical model.

Category	**Key Data / Insight**
Regime	Subcritical LOx–H_2 at 1 bar; microgravity environment ($\sim 10^{-6}g$).
Initial conditions	$D_0 \approx 1$ mm, $T_\infty \approx 100$ K, $p_r = 0.02$ (1 bar).
Lifetime	$\tau_{\text{burn}} \approx 130$ ms.
Dominant phenomena	Around $\frac{t}{t_1} \approx 0.5$ a surface ice layer forms impeding interfacial heat and mass transport; subsequent micro-explosions and droplet rotation arise; minor nonsphericity $R \lesssim 1.05$ in the beginning half of droplet regression $\frac{t}{t_1} \lesssim 0.5$, but afterwards abruptly increases significantly in later stage.
Geometry	Initially spherical, deviation from sphericity begins near $t/t_1 \approx 0.4$.
Flame structure	Flame standoff diameter contracts from 2 to 1 mm; R_f/R_d ranges 2.5–3.5.
Burning rate	$k_{1\,\text{bar}} \approx 5$ mm^2/s; sub-d^2 regression.
Relevant figures	Fig. 5 (surface evolution), Fig. 6 (micro-jets), Fig. 7 (d^2-law deviation), Fig. 8 (standoff dynamics), Figs. 9–11 (pressure dependence), Fig. 12 (supercritical transition).
Core insight	Ice-layer-induced resistance distorts d^2-law behavior and modifies regression kinetics and droplet geometry; flame contraction mildly pressure-dependent.
Modeling implication	Simulation focuses on post-detachment, quasi-steady combustion phase; target to aim for is to reproduce experimental regression curve, standoff contraction, and radial temperature/species profiles.

This carryover dataset serves as the direct experimental anchor and objective for the numerical modeling framework developed, ensuring that the simulation operates under physically consistent boundary conditions and can be quantitatively validated against measured behavior.

3.12 Computational Framework and Tools of the Trade

NASA CEA (1994) [78] → Cantera (2002) [79] → OpenFOAM (2007) [80] → EBI DNS (2015) [81]

Modern computational combustion research builds upon a lineage of open and extensible numerical tools that evolved from early thermochemical equilibrium solvers into general-purpose CFD and reacting-flow simulation environments. The historical foundation for most contemporary combustion codes traces back to the NASA *Chemical Equilibrium with Applications* (CEA) program [78]. Gordon and McBride (1994) formalized the minimization of Gibbs free energy, (often convex functional), as the standard computational method for determining equilibrium species composition and thermodynamic properties in chemically reacting systems. Their code integrated a comprehensive database of NASA polynomial species coefficients and provided capabilities for constant-pressure and constant-volume combustion, rocket performance analysis, and Chapman–Jouguet detonation calculations. These algorithms and data structures remain deeply embedded in nearly all subsequent combustion modeling frameworks.

Building on CEA's thermodynamic and algorithmic foundation, Goodwin (2002) introduced *Cantera*, an open-source software suite that generalized equilibrium, kinetics, and transport modeling within an object-oriented architecture [79]. Cantera preserved the NASA polynomial data model and CEA-style equilibrium routines while adding detailed chemical kinetics and transport calculations (though implemented manually explicitly in present study due to simplicity of our model, see methods section). It provided scripting interfaces in Python and MATLAB, thereby enabling flexible integration with numerical workflows and rapid prototyping of reacting-flow models. For most practical purposes, *Cantera* functions as a modern, programmatic analogue to *NASA CEA* or its batch interface *CEARun*. In this study employed within a Python/Google-Colab environment, *Cantera* is specifically only called up to compute the thermochemical equilibrium of stoichiometric $H_2 + O_2$ mixtures at varying conditions at 1 bar. Particularly, equilibrium calculations are performed within time-step to an isolated infinitesimal fluid parcel to determine peak adiabatic flame temperatures and equilibrium species fractions (H_2, O_2, H_2O, OH, O, H), upon encountering a localized region of especially high Damkohler number. The open-source nature of *Cantera* and its established thermodynamic fidelity make it a natural continuation of the NASA CEA heritage for equilibrium-based combustion studies.

While *Cantera* and *CEA* address the thermochemical foundation of combustion modeling, advances in computational fluid dynamics (CFD) enabled these models to be embedded within full-field, time-dependent solvers. The *Field Operation and Manipulation* (FOAM) framework introduced by Weller, Tabor, Jasak, and Fureby (1998) formalized an object-oriented, tensorial approach to finite-volume discretization, allowing partial differential equations to be expressed directly in C++ using algebraic syntax that mirrors their mathematical form [82]. This framework evolved into *OpenFOAM*, an open-source C++ library for continuum mechanics simulations formally presented by Jasak, Jemcov, and

Tuković (2007) [80]. OpenFOAM's modular structure and general PDE abstraction enabled efficient representation of multi-physics problems—including reacting flows, turbulence, and heat transfer—on arbitrary polyhedral meshes. Its architecture became a cornerstone of academic and industrial CFD, serving as the base for a wide range of combustion solvers, including *reactingFoam*, which provides built-in finite-rate chemistry and multi-species transport capabilities. Because *reactingFoam* is distributed as part of the OpenFOAM library, additional citation is not typically required beyond the standard OpenFOAM references.

Recognizing the need for fully resolved, high-fidelity modeling of turbulent combustion beyond the RANS and LES scales accessible with standard OpenFOAM solvers, Zhang et al. (2015) developed the *Engler-Bunte-Institut Direct Numerical Simulation (EBI DNS)* solver [81]. This code extends OpenFOAM's compressible flow infrastructure to perform direct numerical simulation of chemically reacting flows by tightly coupling it with *Cantera* for detailed chemical kinetics, thermodynamic properties, and transport coefficients. The EBI DNS implementation introduced a fully implicit, operator-split integration scheme, allowing it to efficiently handle the stiff ordinary differential equations associated with detailed reaction mechanisms. This operator splitting decouples the chemistry and flow solvers in time, providing numerical stability and enabling accurate resolution of extreme temperature and species gradients—conditions typical in cryogenic combustion or hydrogen–oxygen flames, where strong nonlinearity and rapid exothermicity challenge conventional solvers such as *reactingFoam*. Additionally, Zhang et al. demonstrated excellent parallel scalability of the EBI DNS solver on petascale architectures (up to 8192 cores on HLRS HERMIT), establishing it as a benchmark open-source platform for DNS-level combustion studies.

Together, these tools illustrate the progressive integration of thermochemical fidelity and numerical generality in combustion simulation software. From equilibrium solvers like NASA CEA and Cantera to fully coupled CFD frameworks such as OpenFOAM and its DNS derivatives, this ecosystem defines the computational infrastructure of contemporary combustion research. Although the present study employs Cantera exclusively for equilibrium thermochemistry, prior work within the same research lineage has utilized EBI DNS and OpenFOAM for fully resolved reacting-flow simulations, providing a valuable point of comparison for the present modeling approach.

It should also be noted that common open-source scientific Python libraries such as *NumPy*, *SciPy*, and *Matplotlib* were used for numerical linear algebra, sparse matrix operations, and visualization within the Google-Colab implementation. In present-day modern times, as these libraries are so ubiquitous in the global computational science ecosystem and provide general-purpose numerical utilities rather than domain-specific algorithms, they are not individually cited here.

3.13 Synthesis and Research Gap

Established Foundations

Hydrogen–oxygen combustion, due to its fundamental role in both propulsion and basic combustion science, is one of the most thoroughly characterized systems in the field. Detailed kinetic mechanisms have been extensively validated across a range of conditions using shock tube data, flow reactors, and laminar flame speed measurements. Theoretical frameworks such as the Burke–Schumann limit [10], Damköhler scaling [46, 47], and low-Mach-number asymptotics [8, 9, 18] are well established and provide a strong foundation for modeling hydrogen–oxygen flames under various regimes.

Gaps in Literature

Despite this rich heritage, several critical gaps remain unaddressed in the literature, particularly regarding the coupling of detailed H_2/O_2 kinetics with transport phenomena in microgravity spherical droplet flames: microgravity environments, such as those created in the ZARM drop tower, introduce fundamentally different transport regimes that challenge terrestrial assumptions about buoyancy and flame stabilization. There exists a scarcity of data validating kinetic models under cryogenic ambient conditions ($\sim$ 100 K), especially in spherical flame envelopes around evaporating droplets. The interaction between droplet evaporation, flame structure, and reaction–diffusion coupling has not been fully quantified, particularly in the high-Da, quasi-steady regime. Moreover, while flame-sheet models are theoretically justified, their quantitative validation against both detailed simulations and experimental data under these unique conditions remains limited. This lack of integration across scales and regimes constitutes a significant opportunity for new research and investigative modelling endeavors, which our study addresses.

Taken together, these theoretical, experimental, and numerical developments have progressively unified the understanding of droplet combustion under diffusion-controlled, finite-rate, and radiative regimes. Yet, under cryogenic conditions where phase-change kinetics, radiation, and quasi-isobaric constraints interact, direct validation remains limited. The present study builds upon this foundation to particularly examine the LOX-H2 combustion mechanism.

4 Interdisciplinary Contributions of the Original Simulator's Novel Methods to Combustion Science, Computational Physics, and Applied Mathematics

4.1 Establishing Model Assumptions:

Scientific Translation into Computer Language

Here we present general aspects of reacting flow CFD from previous work and related literature partic-

ularly through the lens of combustion science, illustrating the backdrop behind the contemplative journey of constructing a custom theoretical computational mathematical model that fits all our purposes.

In general, in the classic Burke-Schumann-flame problem framework, there do exist asymptotic analytical solutions for the quasi-static configuration approximation to such heat and mass transfer combustion problems in reaction diffusion systems, even in spherical coordinates (see Matalon 2013) [9]. Indeed, such analytical functions directly closely resemble the species concentration and temperature profiles that would intuitively arise from the physical description setup and visual sketch of the situation's layout. Intuitively, in the quasi-static state, the boundary conditions are set by the ambient properties of the fuel droplet and surroundings, and within the flame region's "chemical combustion soup", the reactants of fuel combined with gas are both used up to form the product of water and heat, explaining the dip in the fuel and gas concentration profiles in that critical region as well as the commensurately corresponding spike in the product and temperature profile in the same location, and this profile's shape is more or less held consistently on the bubble's journey through shrinkage to oblivion. While the Burke-Schumann flame limit can serve as a strong base-case reference, there are problematic limitations of such a simplified analytical solution: not only do we lose all the effects of transient behavior which could be significant, but also after we inherently invoked the constraining perhaps overly-restrictive quasi-static assumption upon the system, we do not know if such system ever naturally or spontaneously ever reaches such equilibrium on its own without any external influence or control, since we inherently forced it there in the first place; and as such we philosophically interpret our simulation to fundamentally demonstrate how this physical system intrinsically behaves autonomously on its own. It is also worth briefly mentioning that the classic Burke-Schumann flame problem doesn't investigate the radiative or freezing effects which will be of pertinent scientific interest to us down the road here at UW.

Since we are primarily interested in behavior of the liquid oxygen droplet at a more macroscopic scale as opposed to individual particle trajectories from Molecular Dynamics, this gives rise to our scheme of using Computational Fluid Dynamics (CFD) methods to analyze this system to make better sense of the aggregate properties of the bubble based on standardly-tabulated thermodynamic coefficients such as heat capacity and conduction of the substances involved.

We will briefly summarize in a nutshell the general consensus of literature upon reacting flow CFD numerical mechanisms. Typically, the current state of the system, described via a continuum distribution or concentration profile over space, is iteratively updated in simulation through an Euler-scheme time-stepping algorithm, as ultimately all reaction-diffusion systems have equations of motion that are parabolic partial differential equations, where the first order time derivative can be isolated to be expressed in terms of purely spatial terms of usually Laplacian operator form (assuming "stationary Markov process"), very analogously similar to the classic heat equation or Brownian Motion-type Fokker-Planck equation for drift-diffusion systems describing the time evolution behavior of the probability density

function. As such, we can always update the current state of the system by computing the amount of marginal perturbative change to add, completely based entirely on the "sufficient statistic" of the current spatial distribution configuration of the system alone, by computing the required discrete or graph Laplacian upon whatever finite element discretized mesh-grid scheme is attached to the system's coordinates. The complete entire state of the purely deterministic system should be indeed uniquely characterized by a temperature distribution, and a concentration distribution for each relevant species in question being tracked over time. Inclusion of minor species is typically needed to achieve reasonable peak flame temperatures that can precisely match experiment, and for the LOX-H2 system about four to six reaction steps should suffice. Naturally in the update step, balanced diffusion of heat and species is taken into account, while also considering the conservation laws of of heat, mass, and momentum transfer and tracking the "extent of reaction" and the amount of chemistry that happens via species stoichiometric balance throughout the type-transmogrification process. The instantaneous rate to progress the reaction forward can be instantaneous for simplicity, but often determined via an empirically fitted Arrhenius term, something commonly used in practice to determine detailed chemical kinetics of a reaction system. As such, the entirety of the "physics-cranking-engine" is compartmentalized and contained solely within the modular updating sub-routine algorithm of the simulation scheme, and indeed such "mechanics-cranking-engine" includes aspects from heat, mass, momentum, and chemical balance, and can be extended to include radiation and solid ice effects as well. From the perspective of advanced fluid mechanics, this is a "Lagrangian Description" of the fluid flow, perhaps more pertinently used for elasticity or plasticity problems in solid mechanics, as opposed to the standard classic flow-field type "Eulerian Description" more commonly used for fluid flow, as we are more interested in actually tracking the current configuration of the fluid control volume elements (especially with respect to our stationary droplet) to incorporate chemical reactions within the solution mixture, as opposed to tracking the vector or tensor field velocity profile.

In contrast to standard atmospheric combustion, the unique challenges associated with H2/O2 cryogenic combustion for simulation include contributions from the following: It is difficult to obtain properties for the associated species H_2, O_2, and H_2O at cryogenic temperatures, as experimentally measuring such using appropriate instrumentation is tricky. As such, implementing additional detailed kinetics is essential to combustion situations with oxygen to get a reasonable flame temperature. Additionally, preliminary calculations suggest that for this cryogenic situation along with radiation and ice effects that radiative heat flux and conductive heat flux are comparable in magnitude and should be considered in modeling efforts to incorporate in a representative simulation.

4.2 Original Simulator

The chief aspect of our efforts has gone into developing a completely new simulator from the ground up. Within the open-source environment of python and a few of its key built-in scientific computing subroutine packages including numpy and scipy, our simulator was truly constructed from absolute zero, initially beginning with zero lines of code in a completely empty blank ipynb Jupyter notebook that is easily accessible using Google Colab's browser cloud computing capabilities. This means every marginal update and each instruction was implanted intentionally with purpose, whose aggregate concisely visible computational mechanics under the hood can be accessed and comprehended. The connotation behind this choice of lexicon is to elucidate that the construction of such original simulator is an entirely novel endeavor, with an emphasis that it is not only a significant contribution to both the Hydra project, but also to an assortment of researchers who could benefit from a generalized open-source tool serving as a public good to the general scientific community, a common initiative of governmental grants. To the best of our current knowledge, there is no publicly available code, in an open-source computing environment accessibly published for dynamically simulating an arbitrarily chosen multi-component reaction diffusion system of one spatial dimension, let alone even just a general parabolic PDE numerical solver of just a single species. As such, we ended up assembling such a code completely from utter scratch, an entirely novel, completely original, and freshly genuine numerical simulator for such a purpose of foundational importance, with universal application to the analysis of any chemically reacting or catalyzing heat and mass transport system, arising in various contexts of chemical engineering, biochemistry, and thermal physics, and even some important niche aspects within the realm of quantitative finance. Along the way, the process of our software's development and excruciatingly rigorous accuracy testing and precise cross-validation with correspondingly derived mathematical theory, surprisingly also resulted in a plethora of corollary novel insightful results both with respect to mathematical physics theory and computational mathematics methods, even relevant in general to others externally outside of the HYDRA venture who practice scientific computing professionally or researching computational scientists alike. To reiterate, entirely originally novel aspects not only include the entire construction of the whole code for any general reaction-diffusion system, but also some of the associated mathematical results and computational methods developed, and additionally furthermore the synergistic consistently-matching mutual cross-validation of the mathematical result with its corresponding rote-mechanistic simulation overlaid in a side-by-side comparison. Therefore, in this section below, the entire process of deriving the fundamental underlying equations of motion and their closed-form mathematical expression solutions, the computational mathematical framework to implement simulation of these solutions into python, their mutual cross validation and matching side-by-side overlaid comparison, and the qualitative intuitive interpretation of all associated results, will be discussed in full detail.

4.3 Analytical Theory's Foundational Framework

In the context of building a completely-generalized precisely accurate reaction-diffusion system simulator that will always properly work for any arbitrary system of such class one could ever want to investigate, it's essential to preliminarily first lay out the inherent foundational mathematical equations that fundamentally define our system, delineate what each variable tracks and how it represents some relevant aspect of our system, and formulate some base-case and ground-truth analytical theory solutions that have closed-form mathematical expressions, that way there will be something concrete to compare the simulator output with to match for full solid verification of correctness down the road. As such, this section will focus on covering the primary "pencil-paper"-flavor mathematical theory behind the class of coupled parabolic partial differential equation systems of one dimension, referred to in physical sciences as "advection-diffusion systems", "convection-diffusion systems," "heat and mass transport phenomena," "drift-diffusion systems", "reaction-diffusion systems", or "stochastic differential equations" All these titles are pretty much mathematically synonymous, except for some additional nuances of the last two: reaction-diffusion systems might have the additional further connotation that there exist some undergoing chemical reactions in the system where one substance transforms into another (perhaps through undertaking various internal catalysis mechanisms), and stochastic-differential equations should be viewed through the lens of a mobile time-evolving probability mass distribution instead of a material property's moving mass distribution after implementing the corresponding Fokker-Planck parabolic PDE transformation to bridge the gap from the stochastic to deterministic setting.

In this section, we will review the entire process of invoking assumptions for our enterprise's engineering purposes, thereby establishing which are made and the reasons behind them, to construct a solid foundational mathematical bedrock which will serve as the structural integrity support to our scaffolding framework for our numerical modelling. A fair amount of these justifications will be elaborated in a more physically intuitive manner for such practical application, thereby ensuring pedantic arguments related to ZFC set theory and the axiom of choice are moot. After invoking our assumptions, we will fully derive the fundamental canonical equation of motion for a completely arbitrary generalized multi-component reaction-diffusion system or coupled system of parabolic PDEs, while going through particular scenarios of interest from various combinations of simplifying assumptions. This flavor and structure of analysis is entirely similar to the standard journey through the various classic toy-models commonly studied in quantum and statistical mechanics, (particle in a box, harmonic oscillator, rigid rotor, hydrogen atom, etc.) except our case will be an exhaustive treatise on pertinent scenarios arising in heat and mass phenomena, with situations corresponding to more quotidian macroscopic or common continuum settings. Going through these generalized but commonly occurring examples provide a relevant tie to physical scenarios and illustrate a strong consistent bond with physical intuition. Throughout the process, we will derive solution techniques for obtaining such closed-form mathematical expressions, and afterwards

verifying the correctness of such proposed solutions that they indeed satisfy all originally preimposed constraints and requirements. Additionally, to drive home the power of physical intuition consistency for these solutions, we'll analyze the asymptotic properties and convergence throughout both time and space for our various explicit-form mathematical solutions, allowing one get a strong mental sense sense of the system's behavior using such back of the envelope-type calculations without necessarily having to use a calculator or computer.

A significant amount of following mathematical results and analysis is entirely original as far as we can currently tell. In the general overarching field of reaction-diffusion theory, research efforts always center around one or more of the following three points of focus: scholars tend to be interested in either firstly, computational tools (sometimes proprietary) and methods for the practice of simulating such systems, secondly, explicit experimental simulation for a specific technology or for a particular nonlinear system that exhibits chaotic or complex Turing-patterns, or thirdly and lastly, pencil-paper analytical mathematical methods of approximation, such as singular perturbation theory stitching together matched asymptotics, usually specifically just for time-independent steady-state characterization only. While approximating tricky equations is an important strategic approach in many contexts including ours, scholars seem to seldom consider going back to the basics, returning to simpler more straight-forward scenarios where there actually exist exact time-dependent analytical solutions containing the transient dynamics, which is the specific purpose of this analytical section in the overarching simulation pipeline's context. Indeed we'll eventually allude back to these expressions when we return for comparison with simulation results. Therefore, this thorough report of our principal analytical investigation provides valuable documentation of the relevant intuitive theory behind the rest of our campaign.

The most generalized equation for any reaction-diffusion process so commonly used in heat and mass transport phenomena, grounded in the standard rudimentary principles of continuum mechanics, is represented by the following equation:

$$\frac{\partial Y_i}{\partial t} = \nabla_{\vec{x}} \cdot (D_i \nabla_{\vec{x}} Y_i - \vec{v}_i Y_i) + s_i \tag{5}$$

With spatial del/nabla operator $\nabla_{\vec{x}}$ with respect to $\vec{x}$, where the main variable Y_i displays the dynamic spatial concentration profile of the system's i'th species as a function of both spatial coordinate $\vec{x}$ and time t, which is customarily the primary quantity of interest to hone in on observing. Conventionally and in particular, it is worth focusing on tracking its certain trajectory over time to make sense of its overarching dynamic evolutionary behavior's trends. We can use $\vec{Y}$ to designate the ensemble aggregation of the collection of all species at once, a vector containing $\left[Y_1, Y_2, Y_3, ...\right]$ all together simultaneously.

Continuing, we now systematically proceed to cover the rest by clearly defining each system variable

in succession, which are listed out as follows:

$$\begin{bmatrix} D_i, \text{instantaneous local diffusivity of species } i \\ s_i \text{ instantaneous local source/sink of species } i \\ \vec{v_i}, \text{instantaneous local convection of species } i \end{bmatrix} \tag{6}$$

Observe that hypothetically in the utmost general sense, these could potentially depend on everything else in the system, including all other variables. Nevertheless, irrespective of any variable relationships, the definitions of all quantities shed light on how they impact the system and their direct denotation in physical context.

4.3.1 Intuition Conveyed by Pure Mathematical Physics: Explanation and Overview of the Underlying Mechanics

Intuitively as with all reacting drift-diffusion systems, hence its own self-explanatory name, D_i diffusivity at some spatial location at some point in time characterizes instantaneously how species concentration Y_i undergoes diffusive motion at such point. This means that this quantity characterizes that for whatever mass is currently at such location, how much it exhibits expansive spreading behavior for right now. D_i is always tacked onto the second order spatial derivative term, and is mathematically always defined to be non-negative, to not only be physical, but also to ensure that we have a well-formulated parabolic PDE. Continuing through the system's self-description of naming, $\vec{v_i}$ characterizes convective behavior, which provides information describing how species concentration Y_i undergoes advective movement at such point. This means that this quantity characterizes that for whatever mass is currently situated at such location, how much it exhibits drifting from purely translational motion right now. $\vec{v_i}$ takes on a vector quantity in any direction describing the actual trajectory of where particles at such location tend to be going presently, and will always be tacked onto the first-order derivative term. Intuitively, this characterizes how a small sand-pile lump of gel mass of pudding consistency will spontaneously spread out via diffusion, but could also end up being blown from an external wind which translates the whole mass together entirely, a notion that has implications for the study of optimal transport.

Intuitively, at any location at any point in time for the concentration profile Y_i, the drifting and diffusive motion will always transpire in a way to preserve the total amount of mass in the system. In other words, the system described by this equation, will ensure that even after non-uniformly deforming and shifting things around diffusely with convection, all with great variety throughout both space and time, at the end of the day, all alterations will ultimately only occur in a way that preserves the total amount of area or mass of our concentration profile, similar to how the time-dependent Schrodinger equation preserves normalization of total probability even throughout dynamic time-evolution, or Noether's

theorem on conserved quantities from the Euler-Lagrange equations which describe motion through an optimization problem with respect to total energy.

This is the standard calculus representation of modelling a control volume element for the continuous nature of molecular behavior at the macroscopic scale, as a clustered bulk of molecules which form aggregate matter in whatever phase state tend to behave as a continuum. The form of this equation can be derived from the continuum mechanics tensor-based conservation of mass and momentum laws and constitutive relations, which boil down to yielding Fick's laws of diffusion and Fourier's laws of heat transport with commensurate units to these above quantities and proportionality coefficients. Therefore following this foundation, whatever concentration profile we are dynamically tracking, the total area is going to remain conserved and constant from conservation of mass, irrespective of how D_i and v_i are computed, which ensures that mass never gets created nor destroyed within Y_i concentration profile from the effects of the terms of D_i and v_i themselves.

For new heat and mass to enter or exit its local micro-system to transform from one species to another via chemical reactions, we must include another additional term to account for such external flux, in addition the pair of both D_i and v_i who together on their own, simply mathematically alone cannot alter the total amount of mass presently in the i'th species concentration profile Y_i, without the advent of s_i. The s_i term is thus specifically and uniquely able to inject or delete mass into the i'th species concentration profile, and can be coupled with the corresponding source and sink terms of other species to preserve aggregate overall multi-species system conservation of heat and mass via direct "monetary" transfer analogous to our banking's fiduciary digital fiscal system, explaining the inclusion of such term in the equation designed for this specific purpose. It is worth briefly clarifying that these simply act as mathematical "creation and annihilation operators" used for electron arrangement structure in Fock states in quantum chemistry, as it takes intelligent selection of commensurate s_i for various species to ensure conservation, and the existence of this term simply mechanistically allows for the operation of adding heat or mass to some concentration profile Y_i.

As the language of mathematics is ubiquitous to many academic disciplines, it can be fascinatingly insightful to acknowledge that the same equation of motion above universally describes copious various phenomena with a diverse range of applications. Without loss of generality, we can track the temperature distribution profile, normally denoted by T_i, by absorbing it into the enumeration vector of all concentration profiles $\vec{Y}$, meaning mathematically structurally there does not need to be a distinction between chemical species concentration profiles and temperature distribution profile, which even extends to pressure and viscosity or other "system state space" profiles as well.

Our lengthy discussion on explicitly laying out the physical interpretation of the fundamental equation of motion will be significantly rewarding, as these are the first key steps in bridging our mathematical abstraction to reality while bringing about synthesized multi-faceted understanding. We'll continue on-

wards in the subsequent section to prune this equation to instigate more concrete tangibility. Not only do these equations describe heat, mass, and chemical transport, but they also can describe the dynamically-evolving probability distribution of Brownian-motion-based stochastic processes, with immense practical applications in quantitative finance, econometrics, and soft-matter thermal physics.

4.3.2 Progressively Invoking Simplifying Assumptions

Starting with such inherent premise backstage, we'll logically carry on by successively applying a sequence of simplifying assumptions to unravel the overwhelming mathematical complexities and to reduce abstraction by constraining to more realistic situations.

4.3.3 Causal System Assumption

No matter the amount of intertwined interdependence the system contains, this idiomatic canonical mathematical form of partial differential equation isolating change with time $\frac{\partial \vec{Y}}{\partial t}$ on the left hand side by convention, logically entails that $\vec{Y}$ dynamically evolves over time through an iterative forward structure analogous to the concept of an adapted filtration in stochastic process. Unlike a stochastic process though, this is a purely deterministic causal system, indicating that any future trajectory from now is uniquely predetermined given enough information of the instanced present and past states such that ambiguity is entirely eliminated after all remaining degrees of freedom are pinned down, a concept paralleling the notion behind Bellman's famous coined dynamic programming and backward induction. As such, we can eliminate any mathematical future dependence of anything present or past, ensuring that the right hand side of the partial differential equation which induces the change with time on the left hand side, cannot access any system information indexed by future time values. Naturally this is physically consistent with all our experiences in the observable universe.

4.3.4 Memoryless Property Assumption

Analogous to the high-dimensional state-space framework in control theory, without loss of generality we can always mathematically formulate our drift-diffusion equation as a first-order system, via a flavor of reduction of order from differential equation theory. This can be achieved by augmenting any metaphorical "minimally sufficient statistic" containing just enough relevant data to fully describe the system's current state, to also include any additional required "memory" of past trajectory history to be used down the road. Tacking on physical assumptions about drift-diffusion phenomena, we can be assured that heat and mass transport, chemical reactions, and and molecular motion occurs specifically only through the directly current spatial distribution of mass and energy, as opposed to any of its evolutionary history. As such, we can eliminate any mathematical past dependence of our equation of motion, ensuring that the right hand side of the partial differential equation which induces the change with time

on the left hand side, cannot access any system information indexed by past time values. This is in-line with experimental observations about heat and mass transport systems.

4.3.5 $\vec{Y}$'s Uniqueness in Generalized Dynamical System

The previous mathematical form, along with the memoryless and causality assumptions, convey that the only dynamically evolving element is going to be $\vec{Y}$ expressed commensurate to its isolated time derivative $\frac{\partial Y}{\partial t}$, or $\dot{\vec{Y}}$ in controls literature notation. As such, this idiomatically implies that there is no dynamical system-type evolutionary process for $D_i, \vec{v}_i, s_i$ as otherwise these variables should have in the first place originally been expressed with some relation to their respective time derivatives to be included in the definition for the ultimate global aggregate equation of motion. This logically entails that $D_i, \vec{v}_i, s_i$ can only be explicit functions of $t, \vec{x}, \vec{Y}(\vec{x}, t)$. While $D_i, \vec{v}_i, s_i$ could all be defined to be mutually dependent on each other, this does not change the ultimate topological sort property where $D_i\big(\vec{x}, t, \vec{Y}(\vec{x}, t)\big), \vec{v}_i\big(\vec{x}, t, \vec{Y}(\vec{x}, t)\big), s_i\big(\vec{x}, t, \vec{Y}(\vec{x}, t)\big)$ that cannot self-evolve, are arbitrary but known functions of present time t, spatial coordinate $\vec{x}$, and current configuration of species process $\vec{Y}(\vec{x}, t)$. Using statistical language to figuratively illustrate this important notion, the complete sufficient statistic of $\Big[\vec{x}, t, \vec{Y}(t)\Big]$ allows the arbitrary construction of a known transformation or direct "plug-in estimator" to compute the present $D_i, \vec{v}_i, \vec{Y}$ causally required to continue propagating the system's evolution. Additionally, usually we are only concerned with stationary processes with no explicit time coordinate dependence, so we can oftentimes eliminate reporting ancillary t data as well. In either case, we naturally know a priori the time coordinate and spatial coordinate, so ultimately updating our system mainly depends on our empirically observed particular instantiation of $\vec{Y}$.

4.3.6 One Dimensionality Assumption

what we end up with with some simplifications: constant diffusivity

If we model the spacetime of our universe with three spatial dimensions and one time dimension, and if we have isotropic drift-diffusion symmetric in all three dimensions, then via separation of variables, our drift-diffusion or heat equation solution ends up becoming the product of three independent profiles for each spatial dimension, and for simplicity we could simplify three degenerate repeated degrees of freedom into tracking just one dimension that represents three copies. Alternatively, we are mathematically allowed to warp our coordinate space to re-express each point in our new coordinate system defined from change of coordinates. The tricky part is determining how to perform a similar flavor of "dimensionality-reduction" in the new coordinate system, and if that is even mathematically feasible. This flavor of "dimensionality reduction" is less "aligned" with the notion of Principal Component Analysis from data science pre-processing of feature vectors for machine learning purposes, but rather more aligned with the black-hole holographic principle characterizing the inherent information dimensionality captured by

the system's behavior. If the diffusion coefficient is the same for each cartesian x, y, z dimension, and we assume that all of the drift, diffusion, and source /sink terms are all isotropic with respect to some epicenter coordinate, namely the centroid of the liquid oxygen droplet in our case, then we can represent everything happening in the system by one radial distance coordinate from the origin center, and everything that's happening inherently only depends on such parameter with degeneracy and symmetry across iso-distance spheres.

This isotropic description with zero dependence on azimuthal or polar angle is clearly implying a spherical-type coordinate system, and we can use the framework from differential geometry derive the relevant corresponding one-dimensional equations that arise from projection of the three spatial dimensions down to one radial coordinate. Using the Lamé metric coefficients from differential geometry, which characterize the various vector length elements involved with multi-dimensional and multivariable parameterized coordinate transformations, one can derive Jacobian transformation formulas for the gradient, curl, divergence, and Laplace operators in any coordinate system transformation, which is extremely pertinent in the context of continuum mechanics for converting between the equivalent Eulerian versus Lagrangian descriptions of deformable body motion, as well as probability theory for transformations of random variables. Usually these expressions associated with the standard curvilinear coordinate bases of spherical or cylindrical geometry are included in many references and have become common practice knowledge in many physical science fields.

This context provides the theoretical background that allows simplification of an isotropic three dimensional process into a representative one-dimensional process through spherical coordinate transformation while incorporating the associated Lamé coefficients. By limiting as many degrees of freedom as possible, this mathematical simplification is conducive for practical modelling of a spherical liquid droplet in our three dimensional world while only having to oversee one dimension.

This flavor of symmetrically degenerate analysis is common in many mathematical sciences to ensure the existence of a tractable solution to a complex system, often as representative-agent based modelling in economics, key for finding a game-theoretically valid Nash equilibrium associated with auction bidding functions or micro-founded macroeconomics, and is exactly the grounding for why we're proceeding for our modelling purposes with just one dimension, even though the world as we know is far more complex than that.

4.3.7 Canonical-Form Fundamental Equation of Motion in 1D

$$\frac{\partial Y_i}{\partial t} = a\big(\vec{Y}(x,t),x,t\big)\left[\frac{\partial^2}{\partial x^2}Y_i(x,t)\right] + b\big(\vec{Y}(x,t),x,t\big)\left[\frac{\partial}{\partial x}Y_i(x,t)\right] + c\big(\vec{Y}(x,t),x,t\big)Y_i(x,t) + d\big(\vec{Y}(x,t),x,t\big) \tag{7}$$

After all of our prior premises and formal arguments we arrive at this result, so presented here is the general form of our underlying one-dimensional equation laid out in all its glory. Even three-dimensional

geometries, such as spherical, can be mapped down to such canonical form in one dimension. Notice the structure of descending order of spatial derivatives, indicating this is a second order parabolic PDE. The actual mathematical forms of a, b, c, d will depend on both the coordinate geometry and the heat and mass transport properties of our system. In other words, drift and diffusivity may end up changing with both spatial location, e.g. farther away from the spherical center, and time, e.g. as chemical reaction rates accelerate. While the dependency structure of a, b, c, d can vary depending on context, without too much loss of generality we can implement a sort of mathematical shorthand to simplify expressions for our purposes.

Usually we can treat our system as quasi-linear, especially in the consideration of the limit of instantaneous update iteration from minute step size for our infinitesimal slice of time, such picture used throughout the analysis of numerical methods later. As such, we can merge $\vec{Y}$ dependence into t at such a small time scale, indicating that $\vec{Y}$ in some general way ends up throughout time dynamically contributing to the system's trajectory. Indeed within such an instantaneous snapshot picture, everything else further can be sort of be fully condensed down to or merged into x-dependence by construction for some arbitrary instantaneous profile varying purely based on spatial coordinate.

Mathematically this is illustrated as follows:

$$\frac{\partial Y_i}{\partial t}\Big|_{@t=\text{now}} = a\Big|_{@t=now} \frac{\partial^2 Y}{\partial x^2}\Big|_{@t=now} + b\Big|_{@t=\text{now}} \frac{\partial Y}{\partial x}\Big|_{@t=\text{now}} + c\Big|_{@t=\text{now}} Y_i\Big|_{@t=\text{now}} + d\Big|_{@t=\text{now}} \tag{8}$$

By restricting to looking at specifically just an infinitesimal instant slice of time at $@t = \text{now}$, for the present situation glued down or pinned to such instant in time, for any of the terms in the above expression viewed with such particularly fixed $@t = \text{now}$ plugged in, their dynamic time dependence ultimately sort of disappears due to irrelevance to the instantaneous update consideration currently at hand for $\frac{\partial Y_i}{\partial t}\Big|_{t=\text{now}}$. As such, with perhaps an abuse of notation, for shorthand to portray the system we can eliminate a, b, c, d's explicit dependence on $\vec{Y}$ and t. This should hopefully make sense, since we'll usually only consider situations where we've already determinedly fastened down the configuration of our system's present state, and so the main relevance to preserve indicating for our purposes is simply captured in x spatial dependence:

$$\frac{\partial Y_i}{\partial t} = a(x)\frac{\partial^2 Y_i}{\partial t^2} + b(x)\frac{\partial Y_i}{\partial t} + c(x)Y_i + d(x) \tag{9}$$

Additionally as rule of thumb, many pertinent systems are stationary processes which don't contain any explicit t dependence, and additionally, many common processes have quasi-linear mechanics with $\vec{Y}$ dependence eliminated too. In short, the main notion that needs to be captured for most practicality here is the fact that instantaneously speaking, these a, b, c, d coefficients can still vary with space, so they

may not necessarily be a flat constant function throughout space, which is key for representing spherical or any other geometry besides Cartesian.

All this lucubration guides how we will ultimately simulate the system numerically, by efficiently keeping track of the bare minimum of information required about our system's state of current configuration to be able to continue working ahead and push forward in time downstream iteratively, kicking the can down the road for dynamic simulation.

As such, we've now identified all variables and physical parameters, provided a full derivation and intuitive explanation of the system's mechanistic physics with established notation, and moving forwards we will glean a comprehensive overview of all the various flavors of combinations of boundary conditions that can be imposed upon our above equation, by immediately jumping straight into the following generalized boundary value problem examples, all of which nicely illustrate intuitive physical scenarios that our fundamental equation of motion can be applied to aptly describe.

4.3.8 Novel Extension and Original Universal Generalization

Here we provide an original and novel thoroughly unifying perspective integrating Continuum Mechanics, Solid Mechanics, Fluid Mechanics, Heat and Mass Transport PDEs, and Stochastic Probability Theory together, in a completely connected, compact, coherent, and consistent manner, encompassing applications that run the entire gamut, while hinting at further interdisciplinary extensions upon this framework.

There is a remarkably perceptive connection tying together the foundations underlying solid mechanics, fluid mechanics, continuum mechanics, and probability, onto one succinctly grounded scaffold supporting our compounded framework, that we will reveal and delineate in full detail in this section. Considering our extensive expounding upon the heat equation– a topic to be meticulously discussed directly in a barraging plethora of subsequent sections later– our fundamental abstract notion is conceptually easiest explained and characterized by providing a concrete illustrative example using such simple baseline entity. In our work, we predominantly focus on the constrained spatial one-dimensional case (dynamically varying with time). As such, observe the heat equation (infinite domain, no boundaries) from section 4.4.1:

Heat equation:

$\frac{\partial Y}{\partial t} = D\frac{\partial^2 Y}{\partial x^2}$

with corresponding solution:

$Y(x,t) = \frac{1}{\sqrt{4\pi Dt}} e^{\frac{-(x-\mu)^2}{4Dt}}$

The Brownian Bridge from Heat and Mass Transport to Stochastic Probability Theory

Without loss of generality, in loose line with the Buckingham pi theorem: we can pick arbitrary variable rescaling and set coordinates to absorb these parameters, and thus render the solution non-dimensional or normalized, allowing us to pick $\mu = 0, D = 1$ for simplicity:

$\frac{\partial Y}{\partial t} = \frac{\partial^2 Y}{\partial x^2}, \qquad Y(x,t) = \frac{1}{\sqrt{4\pi t}} e^{\frac{-x^2}{4t}}$

Mathematically speaking, without any loss of generality so far, we're going to re-interpret the same function $Y(x,t)$ as follows. We're going to re-interpret this function as a probability distribution PDF upon random variable X with shape or scale parameter t, (μ was already set to zero thereby eliminating the location parameter upon our information geometric 2-manifold), meaning at time t we have a zero-mean Gaussian distribution normal random variable here with variance $2t$:

$Y(x,t) = Y_{X,t}(x) = Y_t(x) = \frac{1}{\sqrt{4\pi t}} e^{\frac{-x^2}{4t}}$

Qualitatively descriptively, with respect to time, we ultimately have an ever expanding-with-time Gaussian-shaped species concentration profile, temperature profile, or a normal random variable PDF.

Intuitively, what does this function over space x parameterized by shape parameter time t represent?

In the language of heat and mass transport, $Y_t(x)$ represents the total quantity of mass at such spatial location x at such instant of time t. In the language of probability theory and stochastic Ito calculus from the Fokker-Planck equation, this characterizes relative (continuous measure Borel σ-algebra)-probability amplitude of finding the Brownian particle random walker at such location x at time t, evolving as t progresses with increasing time, characterized by random variable process X_t (idiomatic conventional notation for some general random process) or B_t, W_t (typical notation for standard Brownian motion, or Wiener process respectively, in context.)

Notice how they're all mathematically equivalently represented with the above expression for $Y_t(x)$. Now using the language of probability, we can define the cumulative distribution function or CDF of random variable X_t, describing where the particle is found at time t, at such moment invoking the Born Rule for wavefunction collapse (to generate snapshot statistics upon such t-instant). The CDF is defined as follows:

$\phi(x) = \phi_t(x) = \int_{-\infty}^{x} \frac{1}{\sqrt{4\pi t}} e^{\frac{-z^2}{4t}} dz$

and is highly related to the construction of the error function:

$\text{erf}(x) :\equiv \frac{2}{\sqrt{\pi}} \int_0^x e^{-z^2} dz$

From the continuous mapping theorem and associated measure theory, we know the CDF is strictly non-decreasing, or monotonically increasing alongside with increasing x. That means it's invertible, its inverse also differentiable by the implicit function theorem.

Transporting Stochastic Kinetics and Statistical Mechanics to Continuum Mechanics

Now we look at such inverse function $\phi^{-1}(x)$ and consider what it represents, given that we know $\phi(x)$ is the cumulative distribution, meaning at each point x, it accumulates all mass up to such point, aggregating the entire history of how much has been collected from $-\infty$ up to current present x-value, reflecting all mass picked up from $(-\infty, x]$.

Algorithmically speaking, consider someone following a trail of treats or candies and successively picking up the next one down along the way and continuing onward, and marking the increment arrivals of location where along the journey upon the trajectory the next marginal subsequent treat was discovered, bagged, then tagged. Eventually after walking the entire distance all the way to the end of the Earth $x = \infty$, each and every morsel necessarily must have been snatched up by that point of total integral to be stored into the trick-or-treating vessel. Considering each bonbon has been logged by which location point it was snatched up and captured at, it is hypothetically possible to backtrack the entire pursued route and remove each piece from the urn, and place them back to litter the entire hiking trail upon the full way back return-home trip, reverting to the configurational state it was originally before beginning to amass candies, with no noticeable discrepancy– lossless reconstruction with complete information. The implication of such, is that this loose-sense "algorithm" captures all the required information about where the candies ended up being placed at. As such, this directly implies that $\phi^{-1}(x)$ equivalently functionally serves as the (displacement) mapping function from the foundation of continuum mechanics!

Concretely Cementing Continuum Mechanics to Solid Mechanics

To characterize, the inverse CDF $\phi^{-1}(x)$, maps the entire set of mass parcels indexed by: $[0, 1]$ (due to PDF normalization) to coordinate space in x. So meaning $\phi^{-1}(m)$, with input domain $m \in [0, 1]$, tells you that infinitesimal mass element m indexed along $[0, 1]$ by such value in such region (Hotelling line of agents loosely), is going to be mapped or placed to such location x, characterizing the two-pass algorithmic process described earlier with collecting into the urn and then returning them all back to their original location upon the sweet trail of treats while logging each location in which each treat was originally found upon. This corresponds to the Lagrangian description of a continuous media material in continuum mechanics, usually affiliated with the discipline of solid mechanics, since in the Lagrangian picture, solid finite elements tend to be explicitly tracked as they move about through space to deform from the original configurational scaffolding structural mesh. In our specific particular example here, at each point in time t, this $\phi^{-1}(x)$ relays to us directly a secret recipe for how to reconstruct the expanding Gaussian profile, completely from scratch, only with the metaphorical 52 pick-up deck of cards in our hand to deal out to the corresponding spot's locations, but with a mass quanta continuum ordered index of $m \in [0, 1]$ upon our metaphorical shuffled playing deck of cards in hand.

Mixing Solutions with Fluid Mechanics and Fluid Dynamics

Now suppose we take the time partial derivative of such function: from continuum mechanics first principles, remarkably, that directly gives us the velocity field! Meaning $\frac{\partial}{\partial t}\phi^{-1}(x)$ directly tells us the velocity of each material element (meaning infinitesimal fluid or solid parcel) and characterizes an instantaneous snapshot of how it is moving. This directly corresponds to the Eulerian description of flow in continuum mechanics, usually affiliated with the discipline of Fluid mechanics, and particularly relevant when using the famous Navier-Stokes equations. In the Eulerian picture, net immigration and emigration upon each fixed finite control volume are assessed for determining aggregate flow fields throughout space.

Merging with Statistical Fundamentals and Computational Monte Carlo

Another convenient property from the motivating notion that is implied by working in inverse-CDF space $\phi^{-1}(x)$, is that the classic "Law of the Unconscious Statistician"– defining expectation values and the expectation operator– can be reformulated accordingly:

$E[X] = \int_{-\infty}^{\infty} xY_X(x)dx$

Notice how this is an inner product integral upon the functions $y_1(x) = x$ and $y_2(x) = Y_X(x)$, characterizing the area under the curve that is formed by their product $xY_X(x) = y_1 \times y_2$, which can be manipulated using integration by parts (when the distribution's tail-ends decay reasonably) into an expression involving the CDF. More abstractly and crucially really, is the notion that we can fundamentally reformulate calculations pertaining to the "Law of the Unconscious Statistician", serving as the foundational axiomatic premise mathematically defining the expectation operator with its WLLN-associated (Weak Law of Large Numbers) implications for interpretation. For applied purposes, we will not confuse ourselves or bog down our analysis with the pedantic intricacies and nuances associated with Lebesgue's decomposition theorem for mixed random variables that include singular measures, as discrete and continuous measures are sufficient for most actual practical implementations.

The continuous mapping theorem implies that any random variable, necessarily with an associated probability distribution function, has a corresponding CDF that monotonically maps from 0 to 1 total probability, and as such, has an inverse. Now rhetorically consider, if we have a high-performance high-resolution pseudorandom-number generator for the $U(0, 1)$ uniform random variable (perhaps using the Mersenne Twister or other modular arithmetic prime-number theoretic generators), we could equivalently simulate any random variable using the CDF inverse transform sampling procedure to map such uniform random variable to our desired random variable, akin to rejection/importance sampling, information projection, Boltzmann exponential tilting, or change of measure like with Girsanov's theorem. This also extends to multivariate PDFs, such as with the Box-Muller method as a classic example. In one dimension by inspection, the intuition of this procedure is self-evident from our previous 52-pickup analogy: we

can simulate any PDF by drawing a random card from our shuffled playing deck, and then returning the observed corresponding PDF location's x value associated with such selected card (from previous scavenger hunt collecting candies duly noted at each location).

With this established, suppose we want to find the "averaged" mapping (out in the wild forest) where any candy is to be located. This notion directly corresponds to taking the expectation upon the readout outputs from such inverse sampling procedure, or simply taking a sample mean empirically from a loose permutation test of resampling our pack of cards (akin to Jackknife and Bootstrap estimates). If we ignore reshuffling of our pack of cards and its associated reordering of mass quanta (since addition and integration loosely are both associative and commutative), ultimately this corresponds to:

$E[X] = \int_{-\infty}^{\infty} \phi^{-1}(x) I(0 \leq x \leq 1) dx = \int_{0}^{1} \phi^{-1}(x) dx$

This is loosely reinterpreted as an expectation of mapped values of a uniform random variable (mapping catered to our original desired PDF for X underlying $\phi(x)$).

Suppose we're interested in quantities related to the variance of X, then for the second moment:

$E[X^2] = \int_{-\infty}^{\infty} \left[\phi^{-1}(x)\right]^2 I(0 \leq x \leq 1) dx = \int_{0}^{1} \left[\phi^{-1}(x)\right]^2 dx$

This is because $\left[\phi^{-1}(x)\right]$ now directly corresponds to taking the x-coordinate location that such candy was found upon and then squaring it, and taking the sample average of the empirically observed squared values over the uniform distribution of draws from our random deck of cards or party favor mystery grab bag of goodies. In other words, to cognitively parse this integral expression, this is loosely the integral continuum limit of the sample sum of squares! (such quantity typically encountered in ANOVA tables). Directly following such intuition by induction, this naturally can be extended and extrapolated to ***any*** function of our random variable quantity accordingly:

$E[f(X)] = \int_{0}^{1} f\left[\phi^{-1}(x)\right] dx$

Addressing the Applicability and Significance of this Framework

While mathematically at its core fundamental essence, this may just be a very loosely informal constructive characterizing reformulation of the definition of the Radon-Nikodym derivative or Riemann-Stieltjes integral in Kolmogorov-axiomatic probabilistic context, but the novel aspect of our presentation is the absolute direct connection and associated bijective correspondence to continuum mechanics, binding two traditionally very disjoint orthodox fields, typically idiomatically viewed separately in isolation. Furthermore, even rooted within particularly continuum mechanics, both solid mechanics and fluid mechanics tend to be stratified hierarchically and classified as distinct (and mostly non-overlapping) sub-disciplines within the aggregate realm of classical mechanics. Intriguing philosophical principles aside, the practical result is this viewpoint explicitly provides an alternative method that could facilitate computation of relevant physical quantities through "interdisciplinary translation," employing the best tool for the task at hand from each field's language via cross-pollination, a philosophy famously embraced by Bruce Lee

for interdisciplinary situational adaptability in the blended mixed-martial-arts context, coined by his famously quoted lines and aphorisms including "be like water" and "the highest technique is to have no technique." Physics Nobel Laureate Richard Feynman also hinted at the same core principle in the chapter "A Different Box of Tools" in his autobiographical book, describing his unconventionally unique interdisciplinary situational approach to solving problems. [83]

A Conduit Consequence Connecting Statistical Data Science to Classical Mechanics

A practical corollary notion that naturally arises from integral integrated quantities for summary statistics presented earlier, is that these values have physical meaning in addition to their abstract data-driven informative inference interpretation from Tukey's book. [84]. In the realm of physics and economics, the connotative semantic sense of the term "distribution" is perceived differently from the strict denotative lexicon of statistical probability: while probability distributions are normalized to unity dictated by Kolmogorov's measure-theoretic axioms, distributions in physics and economics more loosely define an abstract configuration of mass/charge/density throughout space or distribution of money/resources among agents in an economic system, where the entire cumulative integral quantity, (that is not necessarily 1), explicitly represents the entire system's total value contained.

Naturally, the ground set of the system's information is contained in the original density function. If we ignore the scrupulously fussy aspects of singular distributions, for practical purposes, we can without loss of generality lump discrete probability mass functions into the mix of continuous probability distributions by allowing incorporation of Dirac measure delta atoms and generalized functions into our space of consideration, extending to linear mixture distributions, loosely akin to "Caratheodory's Extension Theorem." The point of such is to characterize that the fundamental information set of a distribution arises from some continuous function mapping, substantiating the implication that it would behoove of us to determine standardized methods for condensing and summarizing such uncountably infinite amount of information. While according to the data processing inequality this will inherently discard useful information intrinsically, simplification and compression is a practical necessity in many disparate contexts.

Condensation of aspects of the overall distribution into succinct summarizing parameters typically involve calculating an (expectation)-integral* (without loss of generality, point-wise-search quantities such as mode or argmin can be reformulated accordingly with passing appropriate characteristic indicator functions through the distribution's parsing). In probability, useful standardized statistically processed quantities include those arising from the classic "method of moments" and the "moment generating function", serving as widely accepted digested forms. For the corresponding analog in classical mechanics, these work out to be the values that make up the "moment of inertia" tensor. In addition to the shared terminology, structural similarities are also hinted at, considering the parallel axis theorem vaguely

parallels the linearity of expectation for summing variances of sums of independent random variables. More fundamentally speaking, even the center of mass and the centroid also have corresponding statistical cognates. As these principles apply to both rigid bodies and deformable bodies in classical mechanics, the power of this astute connection can be perceived.

Summary Diagram of Core Conceptual Relationships between Fundamental Entities

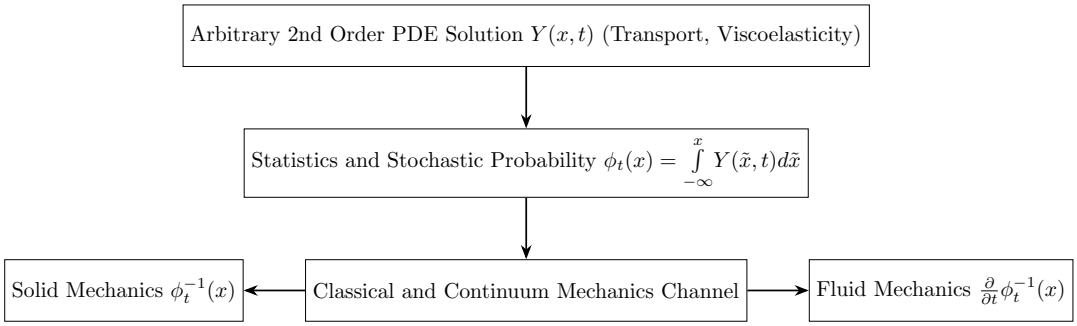

While identifying these perspicacious connections can be thoughtfully intriguing, it also serves a direct practical purpose, and has concrete applications beyond just serving as a mere thought-provoking curiosity. The convenience of such a formulation allows for efficient and effective implementation in numerical and computational simulation, especially in scientific computing which particularly involves dealing with aspects of storing and simulating continuous signal functions on a discrete binary-logic classical computer, with finitely limited processing power and memory storage, while further restricted by what is grammatically tractably humanly expressible in such Turing language system, indeed a binding constraint when representing and handling continuous systems. Additionally, unifying the disparate mathematical methods facilitates working with any relevant associated theory for analytical expression purposes, where a solved problem in one domain can cross-pollinate to solve a similar problem in a different domain, allowing for comprehensive completeness. Naturally these both have implications to endeavors relating to our physical world in real life.

Interdisciplinary Inspiration and Foundational Motivating Applications for Formulating the Universalized Unifying Framework

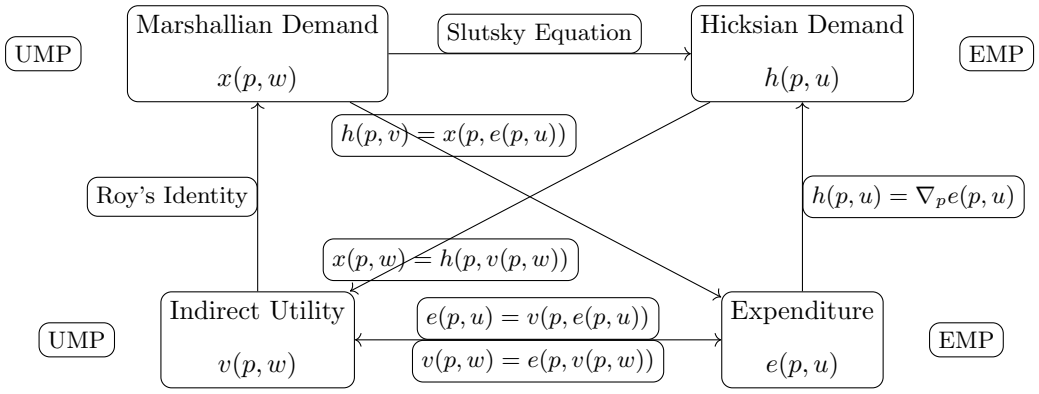

Structurally analogous to how all four functions depicted above (figure adapted from classic textbook

Mas-Colell-Whinston 1995 Pg. 75 [85])– Indirect Utility Function, Walrasian (Marshallian) Demand, Hicksian Compensated Demand, and the Expenditure Function– encode the exact same strategically rationally optimal consumer spending plan and purchasing decision behavior under budget constraint but expressed in various different forms, the core principle behind this framework is explicitly tracking the overall distribution dynamically through time, and then encoding it in the most appropriate format. The vector field of motion that captures movement at a particular location is most conducive for fluid dynamics endeavors. The displacement field mapping characterizes literally where particles are placed along with their relative neighboring geometric distances, facilitating strain and elasticity calculations for structural and solid mechanics. The distribution density characterizes how much "stuff" is actually accumulated at such location at any particular instant in time, whether that be probability mass or concentrated physical matter mass. While they each in their own setting behave "like water" quoting Bruce Lee, the key missing ingredient can be identified as the lack of an explicit tracking scheme for all fluid parcels of the system, particularly apparent in transport and fluids, the central focus of our current study, a unique aspect which specifically the subject of solid mechanics solidly addresses– directly with the displacement map formulation– which data structurally hard-codes the concrete locations of all material finite elements.

Direct Mathematical Economics Motivation behind Solidifying Mass Transport to Fluids

Outside of the field of econometrics (almost synonymous with statistics), which predominantly focuses on methods of empirical data acquisition and analysis in economic context, mathematical economics is subdivided into the two distinct categories of microeconomic theory and macroeconomic theory. Many nuances of microeconomic theory parallel aspects of operations research, where ultimately contingent transactions must happen under uncertainty, while taking place in a (potentially adversarial) game theoretic imperfect information setting, along with financial or incomplete contracts.

In Dynamic Stochastic General Equilibrium (DSGE) framework that profusely dominates modern macroeconomic literature, compelling models are supposed to micro-founded– grounded in the core principles of microeconomic foundations, hence the famous "Lucas Critique" that engendered such movement. (Lucas 1976, 1995 Economics Nobel Laureate) [75].

At the end of the day, the key "feature vector" from the microeconomics realm that is exported to the macroeconomics domain server is the instanced spot market's resultant economic equilibrium that ultimately clears upon market closure. In a sense, this is structurally very analogous to our in-timestep-frame chemical equilibrium modeling method using Cantera discussed later in section, where the chemical equilibrium vector that is algorithmically arrived at is passed along to the CFD chemical kinetics, as opposed to sending along the Rubinstein Bargaining and settled bartered market equilibrium state for transactional monetary resource exchanges to the macro DSGE process. 5.2.5.

Implicitly under the hood, DSGE macroeconomic modeling typically assumes that each recursive suc-

cessive spot market– the exchange interface for aggregate consumer-producer-user friendly interaction– opens shop in the morning, closes shop in the evening at the end of the day, and fully clears, eventually satiating all stores, firms and households under the tatonnement principle. There is certainly a diverse microcosm of nuance to determine the final General Equilibrium in microeconomics modeling: Game Theoretic Nash Equilibrium Solution Concepts [86] (1994 Economics Nobel Laureate), Fundamental Theorems of Walrasian Welfare Economics, Arrow-Debreu and Radner Intertemporal Equilibriums under Uncertainty [76, 77] (1972 and 1983 Economics Nobel Laureates), all following the "Folk-theorem"-flavored famous four P's of marketing principles: Product, Price, Place, and Promotion, all core concepts and central ideas for compelling microeconomics models from the viewpoint of rigorous operations research.

The current state of affairs in DSGE modelling is to consider a cohort of completely homogeneous agents and firms throughout the entire population of the fictional country's macroeconomic state for simplicity sake. The various aggregate summary economic variables of interest include, unemployment, GDP, inflation, and interest rate, as these are the main types of quantities that are actually observable by a centralized benevolent social planner governmental census entity, thus only controllable via monetary and fiscal policy to characterize the observability and the controllability of this control system. While this assumption– a herd economy constructed of copied clones of one specific bellwether representative agent– facilitates the mathematical well-posedness to tractably perform signal processing analyses, it seems like a gross oversimplification to characterize an entire population's demographic as an entirely uniform entity. This notion directly parallels how constant diffusivities fail to capture the detailed complexity of heat and mass transport in combustion flames, hence the shortcomings of the LOX Lever Rule that has an analytical solution and why we pursued numerical methods for simulating LOX-H2 combustion (see 4.5.1). To avoid such mistreatment, in more recent times, to adaptively update perhaps outdated DSGE methods, Heterogeneous Agent New Keynesian (HANK) Models have been introduced and formulated to address such discrepancy. Currently pursued HANK models typically pick a discrete handful of types of agents for heterogeneity, in-line with the flavor of low-medium-high typed players, producers, products, and prices typically used in principal-agent game theoretic modeling, such as Akerlof's lemons (2001 Economics Noble Laureate) [87]. Such trivial reduction in public population complexity tends to be for facilitating the dynamic analysis of the system over particularly long periods of time (on the order of human lifespans), as seen with the canonical classic optimal control models of: Solow-Swan (Solow 1957, Economics Nobel Laureate) [88], Ramsey-Cass-Koopmans (Koopmans 1965, Economics Nobel Laureate + Koopmans' Quantum Theorem) [89], and Overlapping Generations (Allais 1947, Samuelson 1958, Diamond 1965, all Economics Nobel Laureates)– all formulating the core foundations that are fundamentally central to all modern macroeconomic theory.

By nature, economic ecosystems are fundamentally very complex given the sheer volume and diver-

sity of involved agents, interactions, transactions, potential decision choices, and strategies that such environment comprises of. With modern information technology it is possible to wrangle such big data for empirical purposes related the endeavors of econometrics, but for constructing interpretable, explainable, and insightful models past a black-box convolutional neural network, aspects of the foundations of economic theory need to be reconsidered. The undertones of this scenario hint at how Boltzmann bridged statistical mechanics to macroscopic properties in thermodynamics, kinetic theory, and continuum mechanics, all before the confirmed existence of atoms, ensuring that classical theory was consistent with micro-foundations, the physics version of the correspondence principle or "Lucas Critique." This points to the key gap that can be addressed in the current macroeconomics framework.

In typical research economics curricula along with its associated math preparation review, PDEs are usually left out of the equation (compared to ODEs), because much of their primary relevance tends to be confined to only specifically– 1. mathematical finance with options pricing using Black-Scholes (discussed later in section 4.4.20), and 2. for the Fokker-Planck equation as applied to any generic stochastic variable adapted from Brownian Motion– both quite comparatively niche (but related) subjects which have somewhat branched off to evolve into a distinct discipline of specialization. While by strict mathematical definition the Hamilton-Jacobi-Bellman equation used for macroeconomics optimal control is considered a PDE, it effectively does not actually behave in the same conventional manner for this context. Therefore, PDEs are understandably overlooked as a potential tool in this setting.

Qualitatively, the key feature that PDEs can substantially address is by resolving the limitations of finite resolution among the heterogeneous agents and transactions in a complex economic ecosystem. Instead of being constrained to using just discrete sets of agents and transactions, macroeconomics models could enormously expand in expressive complexity– while maintaining tractability– by adopting an evolving continuum or distribution of agents and transactions. This tool is particularly apt for the situation since a continuum distribution conveniently captures a huge amount of information with a mathematically algebraic expression for a continuous function. Furthermore, from functional analysis, the curve can serve as an informative tool for the overall population trends.

Let us characterize this notion with a more a concrete example. By the Kakutani / Brouwer Fixed point theorem– which in economic modeling context is usually invoked under the hood to always guarantee the existence of a market-clearing equilibrium in the absence of externalities– we can basically "construct" a game, in the sense of a loose incomplete contract, to satisfy some fixed equilibrium allocation. This means we engineer a game and design it such that its Nash equilibrium is rigged to some desired outcome based on the inputs to its instancing. This is not so far off in flavor from encoding Newton's laws of motion embedded in an optimal Euler-Lagrange calculus of variations trajectory in Hamiltonian and Lagrangian Mechanics using the famous stationary or least action principle underlying all of theoretical physics. The point of this characterization is to convey that without loss of generality,

we can ultimately gloss over the micro-foundations of the model, as an appropriate one can always later be revisited and devised accordingly. Given the freedom to allocate resources at will in the spot market, we can determine the flow of resources as we wish at each instanced market encounter. Suppose we stratify our macroeconomic system by some loose notion of wealth, indexed in ascending order upon a Hotelling line from $x \in [0, 1]$ of sorts. We can characterize the quantity of wealth each continuum individual agent has by the function $f(x)$, where $f(x)$ is monotonically increasing. By construction, the integrated quantity $\int_0^x f(\tilde{x})d\tilde{x}$ turns out to be the Gini Curve for analysis of inequality, directly following the principles of our previous discussion. Now suppose we invoke the assumption that only neighboring elements or agents are able to mutually interactively communicate with each other. To make coherent economic sense, consider how high income earners– perhaps in more managerial roles up in the corporate hierarchy– likely primarily conduct economic exchanges with similarly placed individuals at other institutional firms, such topologically associative property stratified among all levels of the business ecosystem. As such, this characterizes a separating equilibrium of "fermions" as opposed to a gross coagulated pooling equilibrium of "bosons" among the continuum of agents. Perhaps there's also information asymmetry at play, where advantages from adverse selection and moral hazard lie with the more senior labor force participant and next door neighbor along the line $x, x^+ \in [0, 1]$. In the continuum limit, just like with neighboring fluid parcels and material finite elements of a continuous medium, this situation directly parallels a convection-diffusion system, where the Stefan velocity v_s blows wealth up the income ladder, thereby affecting the Gini Curve's shape in the classic scenario where "the rich get richer." Suppose the tides change, labor unions, monetary, and fiscal policies reform, and the wind starts blowing the other way, then we literally get "trickle-down-economics" where the flow of wealth reverses. In this scenario, we can explicitly follow the money flow with marked and tagged bills, while dying or tracing the streamlines, streaklines, and pathlines of transactions from the "real bills" doctrine, all the way back to the original source or any sinks, perhaps abruptly imposed or evanescent from, say, an exogenous rarefaction vacuum clearance or injection of wealth (maybe uninsured disaster, inheritance, newly levied tax, or updated policy for continuous subsidy). Furthermore, this construction allows us to calculate the "Velocity of Money" in circulation more than as just an abstract quantity, giving the technical term a more anchored meaning. Indeed, if there's actually no resistive energetic dissipation in the modes of transport (e.g. no sales or income tax per each transaction), then mechanically the monetary flow behaves like a superconductor– a superfluid carrying charges of "money" in a Bose-Einstein Condensate or BCS Cooper pairs. The loose current set up of this notion neglects accounting for how underlying bubbles, eddies, whirlpools, and vortexes within the macroeconomic system can affect the defined aggregated variable output and the original intent of such metric. From a macroeconomic modeling standpoint, the internal money motion structurally resembles any potential internal liquid phase circulation eddy currents within the LOX droplet that is not included in our simulation. Suppose, if two

major players hypothetically exchange the same expensive asset– such as real estate or ownership of a company– with a multitudinous number of logged cyclic transactions within the same day (as opposed to the informal cash economy), this significantly turbulently contributes to the overall motion of money momentum through localized whirlpools of vorticity transport, but without actually capturing the real contributions of liquidity changing hands. This thereby forgets the original fundamental intent: to track the detailed movement of the financial fluid parcels and characterize efficacy in serving as the Numeraire of exchange in the first place. As such, perhaps this touches upon the notion of Kolmogorov microscales in an economic context. This concept even extends to monetary policy when tracking inflation of the total supply of fiat currency due to the "money multiplier" based on the reserve ratio and leverage of banks, hence the discussion on physical/economic distributions versus probabilistic distributions which must be normalized to unity.

Typically in an economic setting, supply-demand curves or supply-demand schedules are viewed with the price on the vertical axis and quantity on the horizontal axis. If we reorient the plot and view it as the inverse function, with price on the horizontal axis and quantity on the vertical axis, and we assume the supply and demand schedules represent a continuum of agents and preferences among the entire population, then we have a separating equilibrium situation (as opposed to a pooling equilibrium) with perfect price discrimination. If we want to propagate forward as many transactions as possible as the societal benevolent social planner, the integral under the minimum(supply,demand) characterizes the instantaneous extent of reaction of fuel and oxidizer mixing, as seen with our LOX Lever Rule discussion later in section 4.5.1. The situation also equivalently applies to a high frequency trading or auction-theory type fin-tech Edgeworth-box platform, where people strategically tend to ever-slowly and progressively "quasi-statically" lower and relax their acceptable threshold offers for prices until a transactional match is made. This process highly depends on the heterogeneity of each agent's individual realized Arrow-Debreu State of the world situation and diverse pie-spoiling time discounting preferences, which ultimately parallels the maximum entropy principle from Boltzmann kinetics. This reaction-diffusion system situation again also boils down to our LOX Lever Rule 4.5.1.

The same reaction-diffusion system parabolic PDE framework can also be used to model adversarial geo-economics scenarios, perhaps with military campaigns among a continuum of scouting units of varying mobilities and reactive firepower. Ultimately, the same physics framework for viscoelastic materials, including wavefronts, shock fronts, fracture mechanics, stress-strain curves, and acoustic elastic vibrations, could even be extended to model economic elasticity, debt shocks, bank runs, and financial catastrophes, though typically macroeconomic modeling and DSGE primarily focus on the investigating static asymptotic equilibria (flavor of Nyquist/Routh-Hurwitz stability criterion) and the underlying economic environmental incubating conditions (that govern the dynamical system's evolution) for such phenomena to even eventually arise in the first place, analogous to how the method of characteristics

can provide a PDE solution for the inviscid Burgers equation right up to the point where the wave break happens, after which the shock forms and enters a different modeling paradigm.

It is absolutely crucial to make the clear distinction that this framework is not supposed to be for the purposes of "econophysics," a more postmodern heterodox hybrid field that perhaps academic physics and economics research communities regard as more of a novelty for constructing toy models for amusement, particularly when compared with each respective fundamentally pure discipline on its own in isolation. Borrowing from physics / economics, purely for the sake of borrowing in and of itself, is not particularly productive for either field's endeavors; this framework is to promote cross-pollination of relevant ideas between different disciplines, while more formally and coherently translating them into a mutually accessible format, facilitating the actual goals and real nontrivial pursuits of all disciplines involved. This conducive manner of synthesis is meant to serve as a rising tide to lift all boats. This mutually beneficial unified framework– inspired by mathematical statistics and economics– can be simultaneously used to both address relevant gaps actually pertinent to real mainstream economic research interest, and also to directly facilitate numerical simulations in computational physics for engineering technology.

Mathematical Nuances and Extensions

Topological Ordering Preservation A caveat in our framework is that labels of mass element particles become completely erased if they mutually cross through each other, meaning they pass through each other upon the permeable indexing line $m \in [0, 1]$. This could become problematic in chaotically noisy, stochastic, turbulent, or mixing ergodic systems, as this parallels aspects of ordered and labeled sets from Von Neumann-Morgenstern Utility upon simple lotteries and vector bundles of goods, De Finetti's theorem about data point probabilistic exchangeability, or Pauli exclusion principle with electron exchange upon Slater determinants, but this is not a problem for structured objects whose finite element mesh is topologically conserved throughout dynamics. Just like with the Gini Curve, if game theoretic strategy profiles or distributions are ordered by most likely to least likely, and two different strategy profiles have the same ordering, then if these two profiles are dealt to two separate players, one player's hand will receive something strictly more informative than the other player's. This is because the less flat distribution will have less "entropy to overcome" (as characterized in the cryptography and cybersecurity context), thereby minimizing uncertainty about the final outcome to be selected. In line with the previous notion working in inverse CDF space, viewing the strategy profile statistics of actual ex ante probabilities assigned to each strategy in the vector PMF allows one to get a sense of the distribution's information content. For heat and mass transport, if we no longer care about the actual individual names and labels of the particles and concern ourselves only with where any mass quanta is found, by just letting its index be arbitrarily based upon wherever it ends up being found upon and fetched in sequence, then this aspect no longer becomes a problem.

Extensions to Higher Dimensions

When expanding this concept to higher dimensions above 1 dimension here, such as 2D image processing for computer vision, this can have applications for Horn-Schunk-type optical flow or stable diffusion. Furthermore, this can be used for explicitly characterizing the optimal trajectories of mass-movement from optimal transport, or similarly with tracking phase space turbulent trajectories in chaos theory and dynamical systems. For optimal transport, this is especially true, because the notions of Wasserstein metric for Earth mover's distance is based on the total integral of the tracking error, difference, or disparity of two CDFs, which following the previous algorithmic intuition, loosely corresponds to aggregating how much total "work" had to be done along the whole hiking trail, characterizing in total the amount of rearranging is required to move all the treats encountered into another desired configuration. Additionally, this has implications to Kolmogorov-Smirnoff distance, which provides the maximum tracking error between the CDFs across all space, as opposed to the total integral of tracking error across all space like the Wasserstein Earth mover's distance, as well as the Glivenko-Cantelli theorem which aims to reconstruct the Empirical CDF from collected samples.

Another practical extension for real-time physics engines and video game world engines is to use $Z(x, y, t)$ to simulate a an arbitrary viscoelastic material on the ground floor of the environment– perhaps a beach's sandbox sandpile, a backyard's taut bouncy trampoline, a swamp's mud bath, or an ocean's gravity waves from water. While fast marching methods are primarily for smoke-tracing visualization of a precomputed vector field across the entire domain, and smoothed particle hydrodynamics can be computationally expensive for dynamics and lighting triangulation of large point clouds (perhaps with marching cubes), a continuum PDE formulation of a dynamically evolving interface could serve as a practical middle ground with various advantages. In particular– loosely akin to 1.5 or 2.5 dimensional graphics for games– instead of simulating the entire 3D globular blob of viscoelastic material with its interior, for the typically ubiquitous and omnipresent floor surface 2-manifold, it suffices to just simulate the 2D surface interface morphology with an arbitrary 2nd order PDE numerical solution. This avoids having to deal with storing information and simulating the interior region, while still preserving the same underlying physics from continuum mechanics, while only requiring bridging the interfacial interactions. What remains is then translating collisional impulses to maintain conservation of momentum, and accounting for imparted contact forces between the objects in simulation between object classes, likely all ubiquitously pulled down to the ground's surface by gravity. This works because this rests upon the assumption that the material elements, though perhaps with labels erased at this point, indeed stack in height in an incompressible laminar manner, just like bricks or plates that somewhat smoothly slide past each other to pile up structurally with vertical altitude.

This also works in general for any topologically orientable manifold with a defined interior and exterior region, such as a sphere, pyramid, or cube, but not a Klein bottle. For 2 manifolds parameterized by

two variables, the discrete mesh construction can be interpreted as samples upon a planar graph with its corresponding Euler characteristic. The carte-blanche free choice where to place nodes and connecting edges for such 2-manifold embedded graph allows for unique and efficient ways to capture the surface with intelligent resolution allocation, including (and not limited to) wallpaper groups, crystallographic glide planes, Hilbert space-filling curves, and Penrose tilings of space. This could even be further extended to 3D space manifolds using crystallographic space groups and point groups, although at this point we must consider aspects of the interior which was originally occluded. Ultimately, the differential geometry Jacobian or Lamé curvilinear coefficients, mechanics of materials, and topological deformation of any material composition of any dimension can be simulated with this framework that uses continuous functions for mathematical modeling of continuum mechanics, implying that this *Stuff Matters*, as characterized by Miadownik's aptly named book that portrays the important significance of materials science throughout human history and modern living. [90]

Devising techniques in computational differential geometry for characterizing curves and surfaces is a known branch of study, perhaps typically applied to the context of static 3D voxel medical image analysis from Radon-Transform Computed Tomography, Optical Coherence Tomography, and Magnetic Resonance Imaging, but the fundamental engineering context's motivation remains the same even for simulating PDEs numerically upon a manifold. For the purposes of LOX-H2 Combustion particularly, this could facilitate constructing numerical infrastructure for simulating a spherical surface meshgrid to accommodate radial variation to simulate the the interfacial surface process. Due to the planar nature of the parameterized 2D space ϕ and θ for spherical coordinates, the surface meshing and Delaunay triangulation is not drastically complex.

4.4 PDE Solutions: Single Species

Comprehensive Collection of Solutions for Various Boundary Conditions

Here we start by giving a comprehensive tour and provide a guided walk-through of our complete collection of one-species profile solutions, each expressed as a closed-form equation for a mathematical multivariable function of both space and time, which exhaustively satisfy just about all possible (physical) combinations of imposed boundary constraints. After constructing a bounteous stockpile of explicit expressions for analytically-expressible ground-truth theoretical solutions, we'll have an immense arsenal of examination tools for cross-checking the resultant output of any situationally-corresponding computational simulation for any discrepancy with what pure theory would prescribe. As we'll see among the nested simile-like fractal structure of subsequent analyses, we'll observe a sort of supermodular snowball network effect: throughout the adventurous journey of coming up with solutions for an exhaustive assortment of cases of boundary conditions for the underlying PDE, we'll continue to progressively reuse and structurally synthesize the foundational base cases to expansively build up an ever

stronger all-encompassing accumulation of applicable mathematical solution assets with compound interest; eventually, we'll even arrive at novel solutions developed from original math methods when we come across engaging with the most complex scenarios. After laying them all out, our mathematical solution expression assemblage can be reused as a ground-truth baseline that can ascertain the verified accuracy of any correspondingly associated numerical solution.

4.4.1 Diffusion without Source, Infinite Domain

The raw "vanilla" and canonical heat equation in the absence of any omnipresent sources or sinks is as follows:

$$\frac{\partial Y}{\partial t} = D\frac{\partial^2 Y}{\partial x^2} \tag{10}$$

Equation (10) Plain "vanilla" heat equation

Which has a well-known canonical Green's function heat kernel solution of a Gaussian or normal distribution spatial configuration with some arbitrary fixed central mean location parameter μ and variance scale parameter linearly expanding with time as $\sigma^2(t) = 2Dt$, which can be elementarily solved or derived via separation of variables, the result of which provided here:

$$Y(x,t) = \frac{1}{\sqrt{4\pi Dt}} e^{\frac{-(x-\mu)^2}{4Dt}} \tag{11}$$

Equation (11) Plain "vanilla" heat kernel (Green's function)

Since this differential equation is linear, the sum of solutions is closed and also a solution, which still holds even in the infinitesimally continuous limit, allowing for all subsequent time-dynamic behavior to be computed via spatial convolution of the time-varying Green's function kernel with the static initial configuration, via the impulse train sifting property from signals and systems. As such, one can interdisciplinarily interpret the convolution with the infinitely divisible Gaussian distribution to serve as a functional mollifier, or act as kernel from kernel density estimation, or perform like a smoothing low-pass filter from signal processing, all illustrating the need for its total integral to be normalized to unity to ensure its area, depending on context commensurate to total decibel gain, mass, energy, or probability, is conserved throughout. This fundamental mode of excitation of an expanding Gaussian profile will be reused and revisited throughout. This bedrock result qualitatively illustrates the key smearing-type characteristic behavior of parabolic PDE systems.

There are two contrasting but equivalent ways to interpret the physical meaning of this differential equation. One way is purely deterministically via a continuum mechanics framework through the heat equation or diffusion equation, grounded in Fick's law of diffusion or Fourier's law of thermal conduction, where any local concentration of heat or mass will ultimately increasingly flatten to expand through-

out space to fill out any unexplored emptiness. In the limiting case, if we begin with a Dirac Delta configuration at first, it will eventually fatten itself and spread out with a Gaussian profile whose scale width parameter continually enlarges indefinitely without bound. Naturally consistent with the sifting property in conjunction with the superposition principle, any starting configuration considered as a linear combination of deltas implies that any initial setup can be propagated forward with such dispersive behavior via collective ensemble superposition of population of expansively unfurling heat kernels.

Similar to the equivalence of the respective Heisenberg and Schrodinger pictures of quantum mechanics, a contrasting alternative yet equivalent formulation of the same fundamental equation of heat and mass transport is via the framework of stochastic calculus, where such equation arises after applying the Fokker-Planck equation to an appropriate Ito drift-diffusion process, namely the Wiener process or simply "vanilla Brownian motion" in this case, commonly used in quantitative finance and mathematical physics. As with any random walk process exhibiting the strong Markov property, the probability distribution of the Brownian particle or random walker continually spreads out over time from its more known initial coordinates, and the more we wait, the more unsure of the Brownian particle's current position we become, characterized by the increased variance parameterized by time elapsed since running loose.

Since both interpretations boil down to the same mathematically equivalent expression, it allows flexibility in how one can understand the system and translate to its physical meaning, which facilitates simulation methodology. The concrete advantage is it demonstrates that we can always potentially Monte-Carlo simulate the system's dynamics as opposed to purely deterministically, both of which come with unique benefits and drawbacks. All subsequent equations, as well as their ensuing derivatives and successive spin-offs, are all consistently in accordance with this dichotomy of equivalent representations: the purely deterministic setting versus the purely stochastic setting, both of which instrumentally facilitate grasping holistic abstraction and general intuitive understanding of this system.

4.4.2 Diffusion without Source, One-Sided Reflecting Boundary, Semi-Infinite Domain

Since the previous partial differential equation is spatially homogeneous, without loss of generality, we can place a reflective barrier at the origin to ensure nothing gets through past it, such that the continuum of all heat and mass is redirected to be contained within a half space, or all Brownian particles elastically bounce off the wall in the opposite direction with restitution coefficient of unity. It can also be called an adiabatic or insulating boundary condition in heat and mass transfer literature. The boundary condition implied by this enforces the spatial derivative or slope of our solution function to be zero or flat, essentially pinning $\frac{\partial Y}{\partial x}\big|_{x=0} = 0$. Due to linearity, we can use symmetry to construct an appropriate solution using the reflection principle as follows:

$$Y(x,t) = \frac{1}{\sqrt{4\pi Dt}} e^{\frac{-(x+x_0)^2}{4Dt}} + \frac{1}{\sqrt{4\pi Dt}} e^{\frac{-(x-x_0)^2}{4Dt}} \tag{12}$$

Equation (12) PDE solution from initial coordinate $\pm x_0$ with reflective boundary at origin

Observe that since this is an even function of x the spatial derivative at the origin must be zero and flat by mirror image symmetry. It follows that the initial position of the Brownian particle known with certainty corresponds to mean or location parameter $x = \pm x_0$ whichever positive or negative reals are chosen to be the domain of interest. Also, the total integral over the half space remains normalized to unity, as any Gaussian tail mass that mathematically bleeds through the barrier to the other side of the origin eventually folds over to come back, as this mass is recovered by an equal but oppositely reflecting tail returning from the contrary image Gaussian hill, ultimately preserving total area within our particular half-space domain of interest. This establishes an essential cardinal mathematical benchmark to validate the accuracy of any numerical simulator, here particularly how a reflective boundary is handled.

4.4.3 Diffusion without Source, One-Sided Absorbing Boundary, Semi-Infinite Domain

Since our partial differential equation is spatially homogeneous, without loss of generality, we can place an absorbing barrier at the origin to ensure that any heat and mass from the continuum that touches the origin is immediately absorbed and removed from the system entirely, to never return. All remaining heat and mass is confined to a half space, as all Brownian particles touching the sticky barrier undergo an inelastic collision with restitution coefficient of zero and become completely consumed by the wall upon contact, and subsequently eliminated after being eaten. This can also be called an isothermal boundary condition in heat and mass transfer literature, as this scenario resembles an ambient juggernaut external heat reservoir fixed to a specific constant temperature. A simple example to illustrate is a hot cup of coffee will eventually cool down to room temperature, and in turn will only negligibly heat the ambient room overall due to the comparatively enormous size difference, a thought experiment similar to considering dilute Henrian or Raoultian mixtures to derive their associated laws based on solubility perturbation from the surrounding majority. Mathematically, the boundary condition implied by this scenario enforces our solution's function to be pinned to a fixed relative value at some particular point in space throughout all time, namely a relative magnitude of zero (or the system's DC offset) placed at the origin for our purposes denoted by $Y(0, t) = 0$. Without loss of generality we can consider our domain of interest to be the positive real region of the number line, meaning any function over this domain $x \in \mathbb{R}^+, t \in \mathbb{R}^+$ with an appropriate solution that satisfies our desired boundary condition must pass through the origin. Due to linearity, we can use symmetry to construct an appropriate solution using the reflection principle as follows:

$$Y(x,t) = \frac{1}{\sqrt{4\pi D t}} e^{\frac{-(x-x_0)^2}{4Dt}} - \frac{1}{\sqrt{4\pi D t}} e^{\frac{-(x+x_0)^2}{4Dt}} \tag{13}$$

Equation (21) PDE solution for absorbing boundary at origin and x_0 initial position

Observe that since this is globally overall an odd function of x with zero total area since the positive and negative regions' contributions cancel, and via inspection by directly plugging $x = 0$ into $Y(x = 0, t)$, our mass distribution or concentration profile is indeed zero at the origin by reflective symmetry. It follows that the initial position of the Brownian particle known with certainty corresponds to mean or location parameter $x = x_0$.

The total integral over the positive half space does not remain normalized to unity, as there is now an outflux of mass constantly exiting the system upon adsorption by the sticky barrier, so intuitively the total amount of remaining mass still contained within our domain must decrease with time. This is mathematically consistent since the positive side's positive Gaussian tail effusively escapes through the origin, and the flipped negative side's image negative Gaussian tail protrudes over to the other side further eating away at the waning positive mass, both of which account for the aggregate outflow of mass. In conclusion, this solution also establishes an essential cardinal mathematical benchmark to validate the accuracy of any numerical simulator, here in this case particularly how an absorbing boundary is handled.

To facilitate synthesizing this knowledge into a deeply profound understanding, the direct connection to stochastic processes illustrates the rock-solid interdisciplinary consistency of the same powerfully versatile mathematical framework. Observe that if one integrates our solution's function $Y(x, t)$ over the positive spatial domain $x \in \mathbb{R}^+$, one will obtain the total amount of remaining mass within our system at time t, and if the original total amount of mass was initially unity, this yields the survival function or reliability function of time t for the lifetime of a representative agent Brownian particle before surface adsorption, which keeps track of the total number or proportion of survivors left with respect to time, commonly used in longitudinal statistical studies. Since the hit time or failure time cumulative probability distribution (CDF) is one minus the survival function, we can differentiate the CDF with respect to t to yield the probability distribution function (PDF) of the Brownian particle lifetime random variable. As such, we can derive the PDF for Brownian Motion's one-sided first passage time as:

$$f_T(t) = -\frac{\partial}{\partial t} \int_0^\infty \left[\frac{1}{\sqrt{4\pi D t}} e^{\frac{-(x-x_0)^2}{4Dt}} - \frac{1}{\sqrt{4\pi D t}} e^{\frac{-(x+x_0)^2}{4Dt}} \right] dt \tag{14}$$

Using the definition of the error function $\text{erf}(x) = \frac{2}{\sqrt{\pi}} \int_0^x e^{-z^2} dz$, we can rewrite as:

$$f_T(t) = -\frac{\partial}{\partial t} \left[\frac{1}{2} \left[\text{erf}\left(\frac{x_0}{2\sqrt{Dt}}\right) + 1 \right] - \frac{1}{2} \left[1 - \text{erf}\left(\frac{x_0}{2\sqrt{Dt}}\right) \right] \right] \tag{15}$$

With some cancellation we get:

$$f_T(t) = -\frac{\partial}{\partial t} \left[\text{erf}\left(\frac{x_0}{2\sqrt{Dt}}\right) \right] \tag{16}$$

Applying the chain rule to the definition of the error function we get:

$$f_T(t) = -\frac{2}{\sqrt{\pi}} e^{-\left[\frac{x_0}{2\sqrt{Dt}}\right]^2} \frac{\partial}{\partial t}\left[\frac{x_0}{2\sqrt{Dt}}\right] \tag{17}$$

Which further simplifies to:

$$f_T(t) = \frac{x_0}{\sqrt{4\pi D t^3}} e^{\frac{-x_0^2}{4Dt}} \tag{18}$$

Yielding the final PDF result for T , the absorbing time distributed as a Levy random variable with shape parameter $\frac{x_0^2}{2D}$, proving perfect consistency with the deterministic heat and mass transfer continuum setting.

To illustrate the overall consistency of this model, when $t \to 0^+$, the function in Equation (21) constructs a nascent Dirac delta in the limit, meaning it approaches a $\delta(x - x_0)$ Dirac delta spike, which matches the initial configuration. When $t \to \infty$, the positive mass and juxtaposed image negative mass piles end up ultimately completely canceling each other out due to their relative spatial proximity compared to the variance parameter proportional to time t, which makes sense as eventually all heat exits the system after long enough time, or the Brownian particle is absorbed almost surely with probability one, matching the recurrence property for symmetric random walks in one dimension entailing that the particle eventually visits every location if we wait long enough, including the absorbing barrier.

A particular feature to note is that the first passage time distribution only depends on one dimensionless parameter, namely the aforementioned PDF shape parameter $\frac{x_0^2}{2D}$. This concept is key for observing that the system in question and any physically relevant measurement of interest ultimately actually only depends on this quantity alone, which is in line with the principles of dimensional analysis and the mathematical grounding behind the famous Buckinham π Theorem invoked by Rayleigh's Method. As such, this is a key notion to keep in mind, as the subsequent scenarios can be boiled down to the simplest case with the least unknowns and fewest variable degrees of freedom, allowing the possibility to consider the non-dimensionalized version of our system without loss of generality. In a nutshell as a general rule of thumb, we can always absorb one parameter into the x variable via linear scaling redefinition of our spatial coordinate, and one parameter into the time t variable via linear scaling redefinition of our time coordinate, meaning we can always eliminate two empirically unknown measurement-based degrees of freedom with such modification of units.

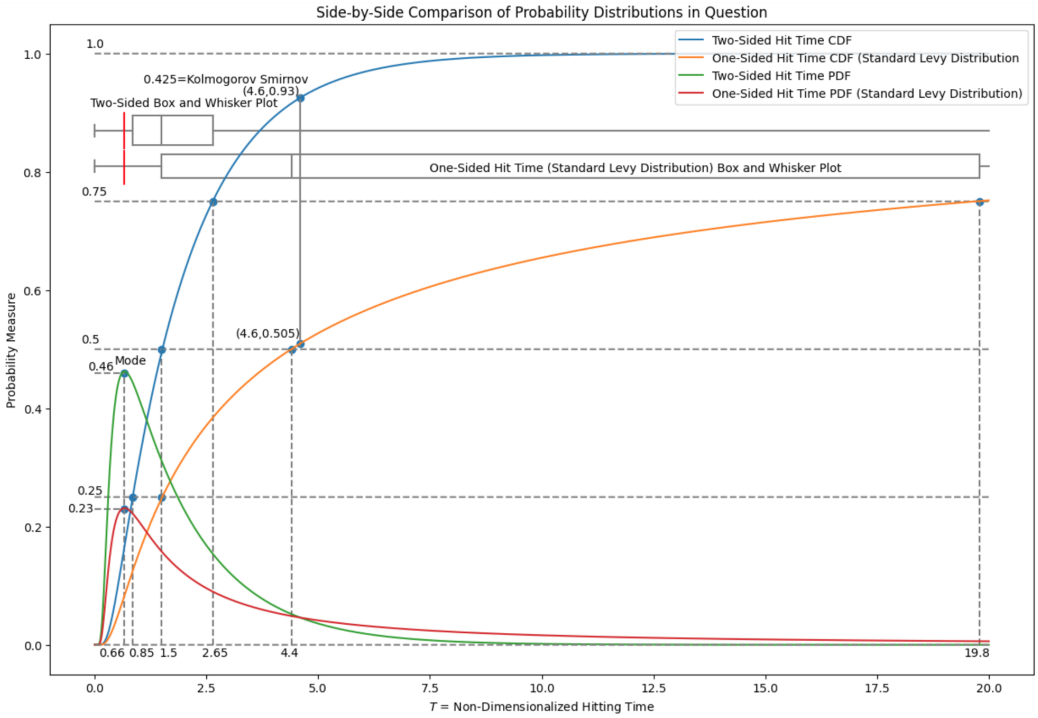

4.4.4 Source-less Diffusion upon Finite Domain between Two Insulating Walls: Neumann Boundary Conditions

Since our differential equation is spatially homogeneous, without loss of generality, we can symmetrically place reflecting barriers at $\pm a$ coordinate upon the x axis real number line, enforcing spatially flat endpoint Neumann boundary conditions such that $\frac{\partial Y(x,t)}{\partial x}\big|_{x=\pm a} = 0$ throughout all time. To continue preserving symmetry, we set the initial configuration to be $Y(x,0) = \delta(x)$ a centralized unit Dirac delta impulse at the origin.

Due to linearity of our system, similar to our previous one-sided reflecting boundary case, we can construct a valid solution that satisfies our two-sided boundary conditions by successively mirror image reflecting heat kernels across the boundary break-point coordinates at $x = \pm a$ to ensure each kernel is equivalently balanced at such fulcrum point, such process metaphorical to placing two reflecting mirrors facing each other. While the sequential reflections spread out ever farther away from the origin, such stable configuration is able to preserve the geometric property that each and every heat kernel always ends up having a correspondingly equally balanced opposite shadow image situated equidistant from both fulcrum boundary coordinates at $x = \pm a$. As such, our constructed solution is described by this expression:

$$Y(x,t) = \sum_{k=-\infty}^{\infty} \frac{1}{\sqrt{4\pi D t}} e^{\frac{-(x-2ak)^2}{4Dt}}, \text{ for } [-a \leq x \leq a, t > 0] \tag{19}$$

Equation (19) PDE solution confined between brick wall barriers at $x = \pm a$, expressed as an infinite sum over all integers $\mathbb{Z}$

A concise way to digest this is to view it as a convolution between our heat kernel with a periodic Dirac comb or sampling impulse train passing through the origin with interstitial spacing length $2a$, a common technique for proving the Nyquist-Shannon sampling theorem. Equivalently this can be perceived through the lens of materials physics through Bloch's theorem in relation to the crystalline Ewald summation formula for computing the crystallographic reciprocal space lattice or structure factor of alloys, where a translation-symmetric lattice of repeated but shifted atomic form factor scattering amplitude copies are equidistantly placed at every site.

Since our previous mathematical expression involves impractical infinities of sorts, we need to reformulate it in the limit of large N to facilitate inputting into a computer, the notion of which simultaneously demonstrates some indication of pointwise convergence from real functional analysis:

$$Y(x,t) = \frac{1}{\sqrt{4\pi Dt}} \left[e^{\frac{-x^2}{4Dt}} + \lim_{N\to\infty} \sum_{k=1}^{N} \left[e^{\frac{-(x-2ak)^2}{4Dt}} + e^{\frac{-(x+2ak)^2}{4Dt}} \right] \right], \text{ for } \left[x \in [-a,a], t \in \mathbb{R}^+ \right] \tag{20}$$

Equation (20) Same PDE solution as Equation (19), where infinite sum is re-expressed in a more digestible format as the limit of a successively ongoing sum that continues indefinitely, for as arbitrarily large N as resources permit.

Observe that for the expression above in the limiting case of $t \to 0^+$, we indeed recover an impulse train as previously described which is consistent with our delta initial condition over our x domain, and for the limiting case of $[t << 2Na] \to \infty$, assuming pointwise functional convergence and glossing over any detailed paradoxical mathematical intricacies of the flavor of dividing infinity by infinity, the resultant asymptotic steady state appropriately yields a flat distribution with height of the original average value, meaning $\frac{1}{2a}$ by applying the mean value theorem to $\delta(x)$ over $-a \leq x \leq a$. Though this bypasses rigorous theoretical proof, this can still be justified via intuitive numerical methods or formulating the above infinite sum as the exhaustive-limiting case of a Riemann sum approximation to a continuous integral in the limit of growing $t \to \infty$, a common technique in invoking the correspondence principle to bridging quantum statistical mechanics to classical statistical mechanics via enough coarse-graining compared to the Boltzmann temperature.

Roughly by using a classic $\epsilon - \delta$ type flavor of argument from real analysis, one can pick an enormously large N value to ensure sufficient convergence of numerical plotting of our distribution over any finite compact-support domain of interest, essentially allowing us to conditionally ignore bit-depth numerical precision error in our function over space $x \in [-a,a]$, and then pick a sufficiently large asymptotic long-time t , handily independent of the total number of elements in the sum contributing to aggregate computational cost, and then plot such result. No matter how large t is, we already conditionally engineered N to continue the sum so far past bit depth precision threshold for exponentially honing in on pinpointing numerical values analogous to information theoretic arithmetic coding, such that the

successive marginal terms in the sum also decay exponentially to contribute negligibly within the finite compact region of our function's domain $x \in [-a, a]$.

In short, this means we can trust the accuracy of plots over $x \in [-a, a]$ for $[t << 2Na] \to \infty$, and increasing the values of t, N while maintaining such structural relationship can only improve accuracy, and for large enough t the fixed value the function over $x \in [-a, a]$ approaches is $\frac{1}{2a}$. This yields consistency with reality, as following physical intuition, this result is expected because any concentration of heat in an insulated room is preserved to not escape, and eventually evens out and equilibrates to the ambient average room temperature.

In conclusion, this equation lays out an extremely useful benchmark closed-form solution to ensure the precise accuracy of any numerical simulation, especially with respect to insulating boundary conditions. Without loss of generality, we can non-dimensionalize our system with $D = 1$ and $a = 1$ by absorbing them into the time and space coordinates respectively, and construct a surface plot of the multivariate function, included below:

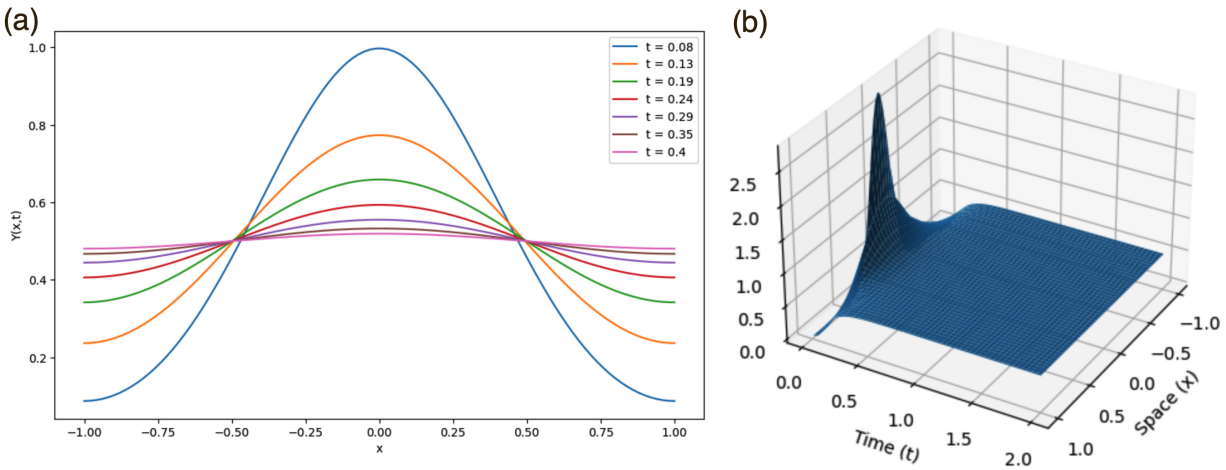

Figure 2: Plots of Equation (20) with (a) iso-time-contours over space, and with (b) a surface plot in 3D of both space x and time t, non-dimensionalized with $D = 1$ and $a = 1$

4.4.5 Source-less Diffusion upon Finite Domain between Two Insulating Walls: Neumann Boundary Conditions

$$Y(x,t) = \frac{1}{\sqrt{4\pi Dt}} e^{\frac{-(x-x_0)^2}{4Dt}} - \frac{1}{\sqrt{4\pi Dt}} e^{\frac{-(x+x_0)^2}{4Dt}} \tag{21}$$

Equation (21) PDE solution for absorbing boundary at origin and x_0 initial position

4.4.6 Source-less Diffusion upon Finite Region between Two Absorbing Walls: Dirichlet Boundary Conditions

Using pretty much the same line of reasoning as the previous in 4.4.5, we can construct a valid solution for double-absorbing Dirichlet boundary conditions using the same method of images, but this

time using anti-symmetric flipped sign reflections as can be seen with the successively alternating powers of -1 :

$$Y(x,t) = \frac{1}{\sqrt{4\pi Dt}} \left[e^{\frac{-x^2}{4Dt}} + \lim_{N\to\infty} \sum_{k=1}^{N} (-1)^k \left[e^{\frac{-(x-2ak)^2}{4Dt}} + e^{\frac{-(x+2ak)^2}{4Dt}} \right] \right], \text{ for } \left[x \in [-a,a], t \in \mathbb{R}^+ \right] \quad (22)$$

Equation (22) PDE solution confined between attenuating or killing barriers at $x = \pm a$, with infinite sum conveniently re-assembled to be represented as the limit of a successively ongoing sum that continues indefinitely, for as arbitrarily large N as resources permit. This is plotted graphically in the figure at the end of this section.

Observe closely that this periodically flip-flopping arrangement of heat kernels ensures that the absorbing boundary conditions with endpoints pinned to zero are constantly preserved throughout time. Across the boundary breakpoint coordinates at $x = \pm a$, there are always equidistant antiparallel pointing heat kernel reflections of each other on opposite sides of the fulcrum whose profile-perturbative contributions exactly cancel out to equal zero at both endpoints, as each and every heat kernel pointing upwards has an equal but opposite corresponding reflected buddy pointing downwards across the fulcrum point on the other side, and vice versa onwards. While contrary successive flipped reflections spread out ever farther away from the origin, such configuration's stable setup is able to obey the geometric antisymmetric organized balance across the entire spatial x axis everlasting throughout all time t.

Since we have the oscillatory term with increasing powers of $(-1)^k$ in the sum, this is an alternating series, and any real-analysis type argument about pointwise or functional convergence would be made easier as such, especially compared to the previous in 4.4.5 which doesn't interchange between ups and downs. For the above expression in Equation (22), in the limiting case of $t \to 0^+$, we indeed recover an alternating impulse train consistent with our delta initial condition over our $x \in [-a,a]$ domain, and for the limiting case of $[t << 2Na] \to \infty$, we essentially end up with a bounded zero profile from a loose convergence argument of an alternating series telescoping sum for any x position value, using the same flavor of reasoning as the previous in 4.4.5.

Glossing over theoretically rigorous proof, justification can be considered via intuitive numerical methods. In short, one can pick a very large N value to ensure sufficient functional analysis-type or bit-depth pointwise convergence of numerical plotting of our spatial distribution, and given such acutely precise resolution, conditionally pick a commensurate super comparatively large asymptotic-type t value (loosely a Gaussiam mixture "shape-parameter" of sorts), conveniently independent of the total number of elements in the sum contributing to aggregate computational cost, and then evaluate and plot such result. This is consistent with reality, since it as expected follows physical intuition, because eventually all heat ends up leaving the system as it dissipates outward and gets consumed and removed by the sandwiching absorbing barriers on both sides, leaving nothing remaining inbetween the bread slices if we

wait long enough.

As hinted by the oscillatory $(-1)^k$ term in this situation, which additionally applies to all PDE solutions generally speaking, the exact same boundary value problem solution can be arrived at using the Fourier series method of determining partial differential equation solution, which in fact was actually the original underlying intent of Joseph Fourier's invention and implementation of his famous equation apart from signal processing. Such solution will be written mathematically in the form of an infinite linear combination of sinusoids of various frequencies, the sum of which often times contain an oscillatory $(-1)^k$ phase term for successive overtone harmonics. Given the Dirichlet condition using a Dirichlet kenrel, the corresponding limits become mathematically equivalent. That means such Fourier series can essentially be directly redundantly re-expressed as Equation (22) using standard mathematical function definitions. Simplistically, the information content of such function's equations can be cross-translated by directly taking the Fourier series of the periodic function in Equation (22), already implied by the demonstrated well-known theoretical existence and uniqueness of both Fourier series and PDE solutions of this simple type (in stark contrast to the Millienium Prize 3D Navier-Stokes problem, for example.) The unique advantage of such sinusoidal eigenbasis representation is the clear decoupled structural separation of variables, decomposed into orthogonal spatial modes of excitation each time-evolving independently in parallel, fitting nicely with the framework of Sturm-Liouville theory, extremely conducive to quantum mechanics. While the eigenfunction of the Fourier transform is a Gaussian maximizing the Cauchy-Schwartz inequality (up to equality cap) justifying the time-frequency Heisenberg uncertainty theorem, the clear niche comparative advantage of the mathematical form of Equation (22) will be evident next, and its methodology apparent in later sections.

To again facilitate synthesizing this knowledge into a deeply profound understanding, the direct connection to stochastic processes illustrates the unshakable interdisciplinary agreement of the same unified powerfully versatile underlying mathematical framework in which all our speculations are grounded. Observe that if one integrates our solution's function $Y(x,t)$ over our available spatial domain $x \in [-a,a]$, one will obtain the total amount of remaining mass within our system at time t, and if the original total amount of mass was initially unity, this normalization yields the survival function or reliability function of time t. Naturally the particle itself or entire ensemble of independent random walkers are either binarily classified as alive in the system's domain $x \in [-a,a]$ or dead outside such region via the law of the excluded middle, so the total sum of all fractional probability mass, or population-proportional frequency occupancy, over the two possible ground set categories covering the x-real number line, must remain constant throughout all time without external presence of sources/sinks, a result also correspondingly true for convservation of total mass in any drift-diffusion system, easily proven using $x \in \mathbb{R}$ total-mass integration by parts upon the global parabolic-PDE equation of motion condition, integrand with appropriate zero-decaying boundaries at $x = \pm\infty$. In poetic lay-person's terms, it's not like any particular

member of the entire collection of random walkers is going to go quantum tunnel to a parallel universe or wormhole-warp to a different dimension, so they all must be contained to random walk upon the x axis, and will be binarily tagged as "dead" or "alive" based on each's own respective trajectory history whether it touched an endpoint within such timeframe considered, providing an accurate demographic longitudinal census accounting for the entire Brownian population. This result was likely obviously apparent in the previous 1-sided scenario in Equation (21) where our "wavefunction" did not require an infinite sum, so while verbose, it is worth a gentle reminder of such trivial fact for our more obfuscated scenario here.

As such, due to the mutually disjoint but all-encompassing sets for Schrodinger's cat-in-box style alive versus deceased states in our underlying σ-algebra, the hit time, mortality time, or failure time cumulative probability distribution (CDF) is the complementary probability of the survival function. We can differentiate the CDF with respect to t to yield the probability distribution function (PDF) of the random variable assigned to represent particle lifetime, path killing adsorption time, or trajectory exit time. As such, we can derive the random variable's PDF for Brownian Motion's two-sided first passage time, or two-sided first exit time as:

$$f_T(t) = -\frac{\partial}{\partial t}\int_{-a}^{a} \frac{1}{\sqrt{4\pi Dt}}\left[e^{\frac{-x^2}{4Dt}} + \sum_{k=1}^{\infty}\left[e^{\frac{-(x-4ak)^2}{4Dt}} - e^{\frac{-(x-4ak+2a)^2}{4Dt}} + e^{\frac{-(x+4ak)^2}{4Dt}} - e^{\frac{-(x+4ak-2a)^2}{4Dt}}\right]\right] dx \tag{23}$$

Equation (23) Computing the PDF for random variable T, the two-sided escape time from the strip $x \in [-a, a]$ as a function of t, by negative differentiating the total integrated quantity of remaining survivors throughout such safe-zone, commensurate to outward mass flux divergence at time t via mass conservation. Note that the sum from Equation (22) with oscillating powers of $(-1)^k$ was explicitly laid out here in expanded form with shifted index.

Plugging into Equation (23) the expression $\frac{1}{\sqrt{2\pi\sigma^2}}\int_{-a}^{a} e^{\frac{-(x-\mu)^2}{2\sigma^2}} dx = \frac{1}{2}\left[\text{erf}\big(\frac{a+\mu}{\sqrt{2\sigma^2}}\big) + \text{erf}\big(\frac{a-\mu}{\sqrt{2\sigma^2}}\big)\right]$ via definition of error function with $\sigma^2 = 2Dt$ and then merging like terms matched in pairs:

$$f_T(t) = -\frac{\partial}{\partial t}\left[\text{erf}\big(\frac{a}{\sqrt{4Dt}}\big) + \frac{1}{2}\sum_{k=1}^{\infty}\left[2\text{erf}\big(\frac{a-4ak}{\sqrt{4Dt}}\big) + 2\text{erf}\big(\frac{a+4ak}{\sqrt{4Dt}}\big) + 2\text{erf}\big(\frac{a-4ak+2a}{\sqrt{4Dt}}\big) + 2\text{erf}\big(\frac{a+4ak-2a}{\sqrt{4Dt}}\big)\right]\right] \tag{24}$$

Continuing algebraic simplification and using the property that the error function $\text{erf}(x) = \int_0^x \frac{2e^{-z^2}dz}{\sqrt{\pi}}$ passes through the origin and satisfies odd function symmetry such that $\text{erf}(-x) = -\text{erf}(x)$:

$$f_T(t) = -\frac{\partial}{\partial t}\left[\text{erf}\left(\frac{a}{\sqrt{4Dt}}\right) + \sum_{k=1}^{\infty}\left[-\text{erf}\left(\frac{(4k-1)a}{\sqrt{4Dt}}\right) + \text{erf}\left(\frac{(4k+1)a}{\sqrt{4Dt}}\right) - \text{erf}\left(\frac{a(4k-3)}{\sqrt{4Dt}}\right) + \text{erf}\left(\frac{a(4k-1)}{\sqrt{4Dt}}\right)\right]\right] \tag{25}$$

We can differentiate the error function using the fundamental theorem of calculus $\left[\text{erf}(x) = \int_0^x \frac{2e^{-z^2}}{\sqrt{\pi}} dz\right] \rightarrow \left[\text{erf}'(x) = \frac{2e^{-x^2}}{\sqrt{\pi}}\right]$ and use the chain rule out front as follows:

$$f_T(t) = \frac{a}{2\sqrt{4Dt^3}} \frac{2}{\sqrt{\pi}}\left[e^{\frac{-a^2}{4Dt}} + \sum_{k=1}^{\infty}\left[0 + (4k+1)e^{\frac{-\left((4k+1)a\right)^2}{4Dt}} - (4k-3)e^{\frac{-\left((4k-3)a\right)^2}{4Dt}} + 0\right]\right] \tag{26}$$

We can continue simplifying and rewrite as:

$$f_T(t) = \frac{a}{\sqrt{4\pi Dt^3}}\left[e^{\frac{-a^2}{4Dt}} + \sum_{k=1}^{\infty}\left[(4k+1)e^{\frac{-\left((4k+1)a\right)^2}{4Dt}} - (4k-3)e^{\frac{-\left((4k-3)a\right)^2}{4Dt}}\right]\right] \tag{27}$$

Equation (27) PDF for random variable T, the two-sided escape time from the strip $x \in [-a, a]$ as a function of t, arrived at this mathematical form by evaluating previous steps. This function is plotted graphically in the figure at the end of this section, with overlay comparison to the standard Levy distribution for one-sided hit time random variable.

Notice in Equation (27) our final expression above, $f_T(t)$ only depends on one non-dimensional parameter, namely $\frac{a^2}{2D}$ analogous to the Levy distribution shape parameter from previous 4.4.3, since this particular mathematical form still allows direct factorization out even among the infinite sum.

Since the function $f_T(t)$ is only nonzero in the positive region x^+, there exists a closed form expression for the Laplace transform of $f_T(t)$ with such gnarly infinite sum eliminated, thereby reducing such expression's "Kolmogorov complexity" in a loose sense, as a compressed but losslessly concise formula's storage routine facilitating human-cognitive commitment to memory. The derivation of such expression elegantly arises from invoking various reflection principle and symmetry arguments upon the stochastic process behind random variabe T_{ab} defined accordingly below. Such is as follows:

$$\phi(\lambda) = \mathbb{E}\left[e^{-\lambda T_{ab}}\right] = \frac{\sinh(\sqrt{2\lambda}|a|) + \sinh(\sqrt{2\lambda}|b|)}{\sinh\sqrt{2\lambda}(|a| + |b|)} \tag{28}$$

Equation (28), written as Theorem 6.7.1 in Resnick 1992 [91], where random variable T_{ab} is the standard Wiener process Brownian motion first exit time from the patch $x \in [b < 0 < a]$.

That being said, this moment generating function (MGF) must be complex valued in nature due to the fat tails property of our distribution $f_T(t)$ which is nowhere near the sub-exponential class, so this provides no physically meaningful results (e.g. if no real moments exist from such MGF then method of moments is out of the question), and inverting such Fourier transform to winnow into something more

comprehendible will not make progress due to Fourier inversion theorem unique mapping, not to mention would be extremely difficult anyways due to the branch cuts associated with evaluating such complex valued Fourier inversion integral, evident by the infinite sum in Equation (27) containing the upfront already-known resultant quantity. Reflective of engineering practice, Fourier Transform pair tables are usually constructed through trusting the Fourier inversion theorem, by considering only the easier one-way derivation and resting assured the inverse as an involutive operation must uniquely map back to the original, such structural intuition also applicable to convex conjugate pairs too.

The algebraic mathematical form of the Moment Generating Function in equation 28 can be difficult to work with, and for computing expectations it is sometimes easier to re-parameterize as follows: [91]

$$\left[\left. \frac{-\frac{d}{d\lambda}\phi\left(\frac{\lambda^2}{2}\right)}{\lambda} \right|_{\lambda=0} = \mathbb{E}\left[T_{ab}\right] \right] \rightarrow \left[\mathbb{E}\left[e^{\frac{-\lambda^2}{2}T_{ab}} \right] = \frac{e^{\lambda|b|} - e^{-\lambda|b|}}{e^{\lambda(|a|+|b|)} + e^{-\lambda(|a|+|b|)}} \right] \tag{29}$$

Equation (29)

Differentiating using L'Hopital's rule three times will yield: $\mathbb{E}\left[T_{ab}\right] = |a||b|$, [91], an interestingly intuitive quantity.

An important nuance is that due to the fat tails nature of the random variables associated PDFs plotted below, this resultant value $|a||b|$ is not defined in the usual sense, but rather, it should be interpreted as arising from a loose "Cauchy Principle value" flavor from an underlying divergent integral.

A worthwhile remark is that the original PDF from equation 22 can be extended to non-symmetric situations for the escape from a strip between $[b < 0 < a]$ using the same techniques of reflection and method of images using the same heat kernel, all principles portrayed in this chapter for constructing valid PDE solutions that correctly satisfy the underlying condition for the inherent equation of motion defining and constructing such PDE relationship.

Figure 2a

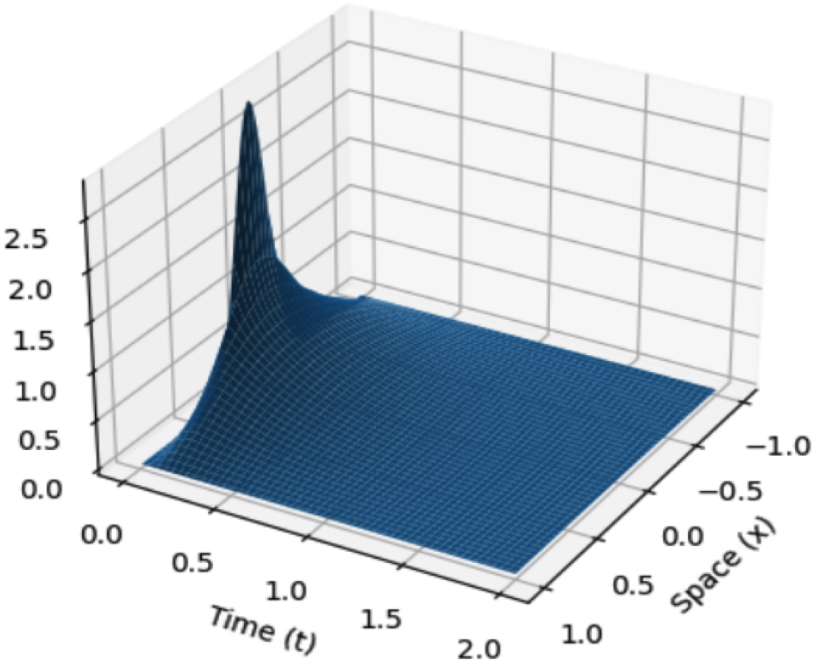

Figure 2b

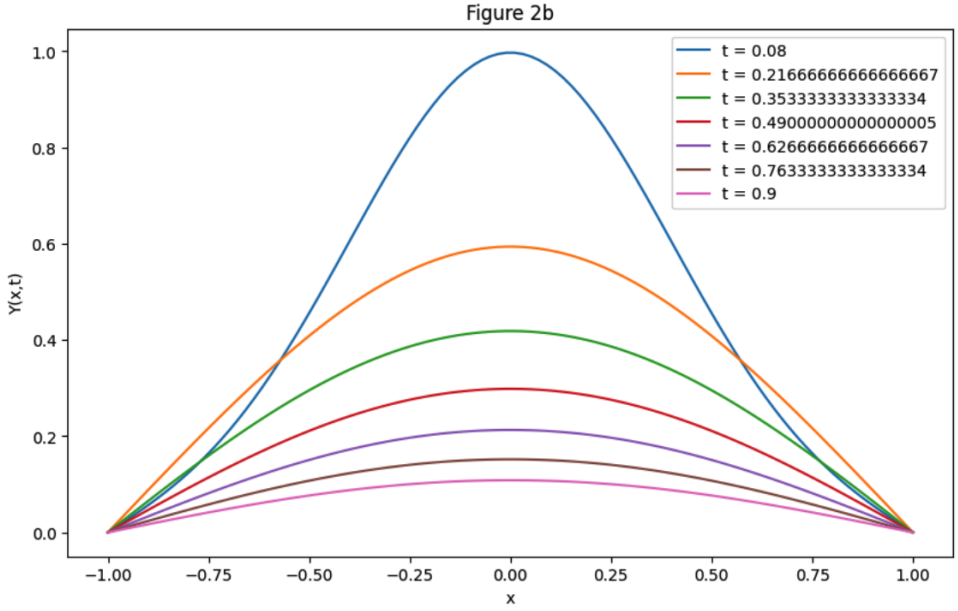

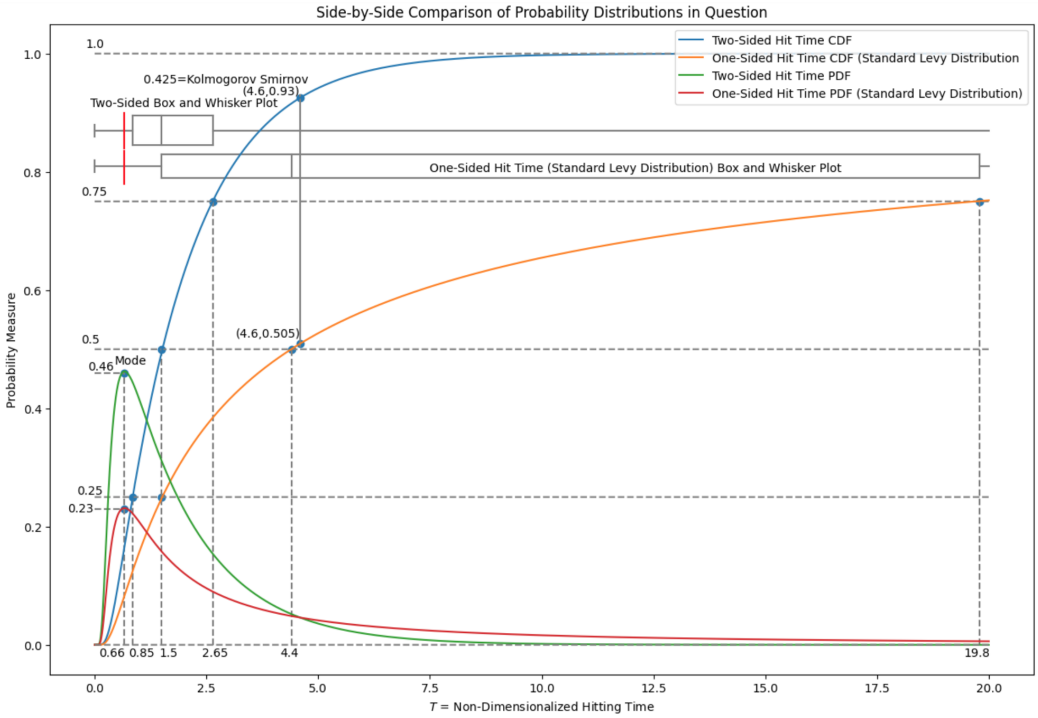

4.4.7 Diffusion without Source upon Finite Strip with Mixed Boundary Conditions

Due to spatial homogeneity of the underlying differential equation, we can place the initial position of the Brownian particle or heat concentration pile to be a Dirac delta at the origin, and we now subsequently place an absorbing barrier at $x = -a$ and a reflecting barrier at $x = a$ to preserve symmetry, creating a mixed boundary condition situation. This mathematical model scenario can be physically interpreted as having an initial concentration of gas in the center of an enclosed room but with a window left open to allow effusion, which equivalently describes a fruit-fly random walker roaming around an enclosed room until it escapes through the emergency exit door. Via the exact same repeated reflection method described earlier, we can construct the following solution:

$$Y(x,t) = \frac{1}{\sqrt{4\pi Dt}}\left[e^{\frac{-x^2}{4Dt}} + e^{\frac{-(x-2a)^2}{4Dt}} + \lim_{N\to\infty}\sum_{k=1}^{N}(-1)^k\left[e^{\frac{-(x+4ka-2a)^2}{4Dt}} + e^{\frac{-(x+4ka)^2}{4Dt}} + e^{\frac{-(x-4ka)^2}{4Dt}} + e^{\frac{-(x-4ka-2a)^2}{4Dt}}\right]\right] \quad (30)$$

Upon inspection, indeed this configuration places heat kernels in a crystalline manner that preserves the appropriate geometric symmetry to constantly maintain the delineated boundary conditions at the endpoints. Looking at equidistant points balancing upon the fulcrum at $x = -a$, every heat kernel on one side has contrasting to it an equal but opposite flipped shadow buddy on the other side of the lever, thereby ensuring balance since the aggregate function at $Y(x = -a, t)\big|_{x=-a}$ sums to zero through pairwise cancellation. Likewise, focusing upon equidistant lever points balancing about the fulcrum at $x = +a$, every heat kernel comes with a direct mirror image reflection buddy on the opposite side,

thereby ensuring balance since the aggregate function will be symmetrically flat with $\frac{\partial Y}{\partial x}\big|_{x=a} = 0$.

Through similar reasoning as previous, we can compute the flux to find the PDF of the Brownian particle's escape time from such confined strip:

$$f_T(t) = -\frac{\partial}{\partial t}\left[\frac{1}{\sqrt{4\pi Dt}}\int_{-a}^{a}\left[e^{\frac{-x^2}{4Dt}} + e^{\frac{(-x-2a)^2}{4Dt}} + \sum_{k=1}^{\infty}(-1)^k\left[e^{\frac{-(x+4ka-2a)^2}{4Dt}} + e^{\frac{-(x+4ka)^2}{4Dt}} + e^{\frac{-(x-4ka)^2}{4Dt}} + e^{\frac{-(x-4ka-2a)^2}{4Dt}}\right]\right]dx\right] \quad (31)$$

It is definitely possible to simplify this expression using the same previous methodology invoking the definition of the error function, which would yield the cumulative outflux of mass with time curve. This expression would be extremely useful for developing a simple model for particle effusion or escape time through an aperture, possibly extended to three dimensions for a cube or rectangular box with a hole on one face, as the other two dimensions undergo their own independent processes described by the Neumann boundary conditions scenario earlier, both parallel and non-interacting with the escape process dimension, justified by the heat equation being a separable partial differential in time and space variables. This has practical implications for molecular biology and biochemistry as it can characterize cellular membrane and nanopore transport processes.

In conclusion, this presents yet another model that provides a practical benchmark closed-form analytical expression for a solution to this unique situation involving mixed boundary conditions, and this ground truth can be compared with any simulation to verify its accuracy and mechanistic validity.

A non-dimensionalized plot of such multivariate function with $a = 1$ and $D = 1$ redefined to be absorbed into the re-scaled time and spatial coordinate is included below.

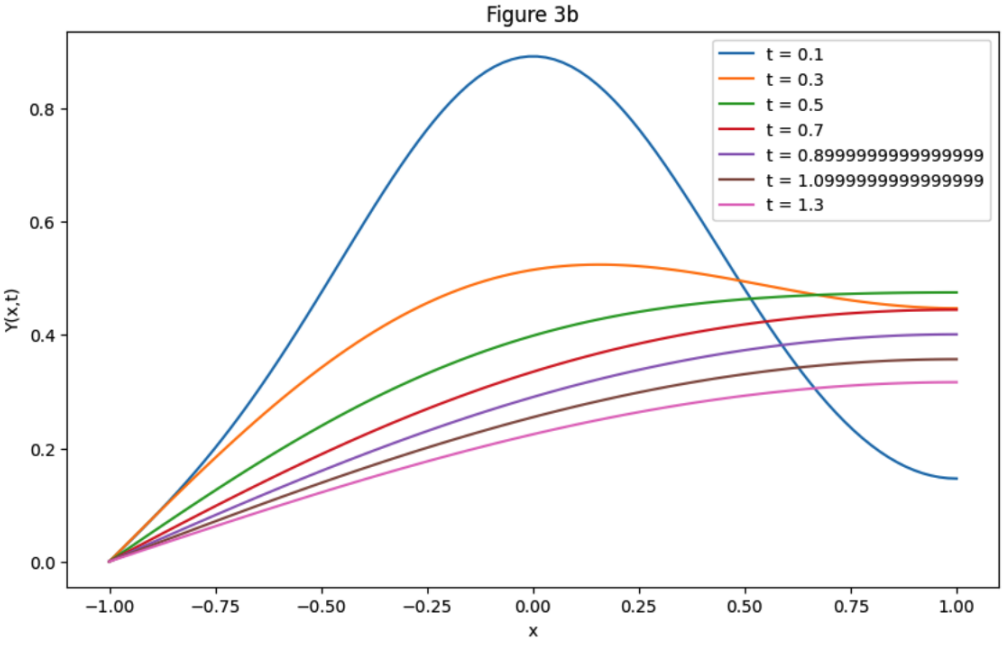

Figure 3a

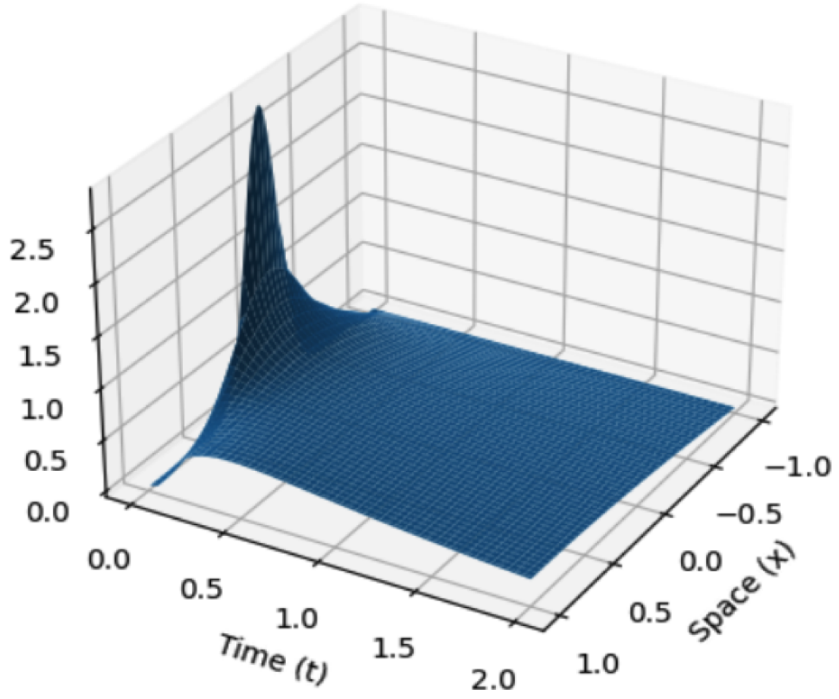

4.4.8 Heating the Expanse from One End, Semi-Infinite Domain

Suppose we start with a Heaviside step function $u(x) = \mathcal{I}(x > 0)$ initial condition, the subsequent "wavefunction" of time evolution from such starting configuration is dictated by convolution with the heat kernel, as follows:

$$Y(x,t) = u * h = \int_{-\infty}^{\infty} \frac{1}{\sqrt{4\pi Dt}} e^{\frac{-(z-x)^2}{4Dt}} u(z)dz = \int_{-\infty}^{\infty} \frac{1}{\sqrt{4\pi Dt}} e^{\frac{-(z-x)^2}{4Dt}} \mathcal{I}(z > 0)dz \tag{32}$$

We can rearrange and evaluate as follows:

$$Y(x,t) = \int_0^{\infty} \frac{e^{\frac{-(z-x)^2}{4Dt}}}{\sqrt{4\pi Dt}} dz = \int_{-x}^{\infty} \frac{e^{\frac{-z^2}{4Dt}}}{\sqrt{4\pi Dt}} dz = \int_{-\infty}^{x} \frac{e^{\frac{-z^2}{4Dt}}}{\sqrt{4\pi Dt}} dz = \frac{1}{2} + \int_0^{x} \frac{e^{\frac{-z^2}{4Dt}}}{\sqrt{4\pi Dt}} dz \tag{33}$$

Subsequently, we can make use of the definition of the error function $\text{erf}(x) = \frac{2}{\sqrt{\pi}} \int_0^x e^{-z^2} dz$

$$Y(x,t) = \frac{1}{2} + \int_0^{x} \frac{e^{\frac{-z^2}{4Dt}}}{\sqrt{4\pi Dt}} dz = \frac{1}{2} + \frac{1}{2}\text{erf}\big(\frac{x}{\sqrt{4Dt}}\big) = \frac{1}{2}\left[1 + \text{erf}\big(\frac{x}{\sqrt{4Dt}}\big)\right] \tag{34}$$

Observe that mathematically this expression is indeed a solution to the original heat equation because it is a linear superposition of the heat kernel computed as a convolution integral. Additionally, heat equation solutions are closed under vertical shifting + flipping + scaling, meaning these operations do not affect the validity of a heat equation solution. These properties allow us to use these permitted alteration rules to modify the previous expression into constructing the following heat equation solution:

$$Y(x,t) = 1 - \text{erf}\big(\frac{x}{\sqrt{4Dt}}\big) \tag{35}$$

In future sections we'll refer back to this equation as the "Heaviside Heat Kernel", alluding to the origination of such expression. There are four key mathematical characteristics of this expression to note, listed below:

$$\begin{bmatrix} 1.\ ,\ Y(x,t)\big|_{x=0} = 1 \\ 2.\ ,\ \lim\limits_{x\to\infty} Y(x,t) = 0 \\ 3.\ ,\ \lim\limits_{x\to-\infty} Y(x,t) = 2 \\ 4.\ ,\ \lim\limits_{t\to 0^+} Y(x,t) \overset{L^1}{\to} 2\left[1 - u(x)\right] \\ 5.\ ,\ \lim\limits_{t\to\infty} Y(x,t) \overset{L^1}{\to} 1 \end{bmatrix} \tag{36}$$

The first condition dictates that this function is always one at the origin throughout all time. The second condition dictates that this function approaches zero for large x far away to the right. The third condition indicates that the function approaches two for very large $-x$ far away to the left. The fourth condition says that initially at time $t = 0$ the function looks like a type of step function. The fifth condition says that eventually asymptotically after enough time the function looks like a flat constant with value one.

As such, this solution allows us to solve two boundary condition scenarios. The first one is directly through the original setup, where our initial profile over an infinite domain over all space starts as a type of Heaviside step function. This describes the process of a hot cup of coffee (at value 2 in the negative x region) cooling down to room temperature (at value 0 in the positive x region), but this time we account for air near the coffee cup heating up and coffee surface liquid cooling down throughout mutual thermal contact equilibration. Eventually, the total system settles at the fully mixed maximal entropy state of

$Y(x, \infty) = 1$.

The second boundary condition scenario that this profile satisfies is from a Dirichlet boundary condition at the origin constantly pinning the concentration profile to a value of one throughout all time. This situation is likely more ubiquitous, as it could describe the process of heat emanation outward after igniting a campfire flame, which maintains a constant hot combustion temperature as the logs burn to warm up the campsite. In this case, our campfire flame maintains a constant temperature of one at the origin while it heats up the rest of semi-infinite domain expanse over the positive x axis.

Not only does the same mathematical function satisfy the above two examples of boundary condition scenarios, but it also is the same mathematical solution to the Rayleigh problem from fluid dynamics, also known as Stokes first problem, which describes how flow velocity spreads from a surface plate that suddenly starts moving to drag the contact layer of the liquid through interfacial friction, momentum extending outward until the entire current is moving along with the plate velocity.

In conclusion, this mathematical expression that satisfies the heat equation for boundary conditions describing a variety of pertinent phenomena, serves as another useful ground truth benchmark case to compare the result of any numerical simulation to. A non-dimensionalized plot of such result, with $D = 1$ absorbed into the coordinate system, is included below:

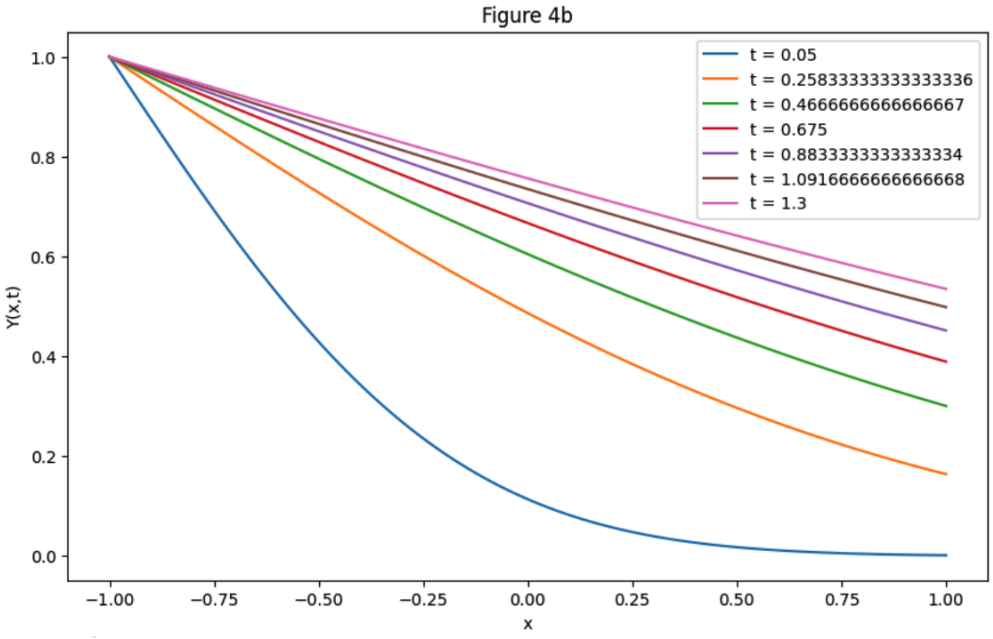

Figure 4a

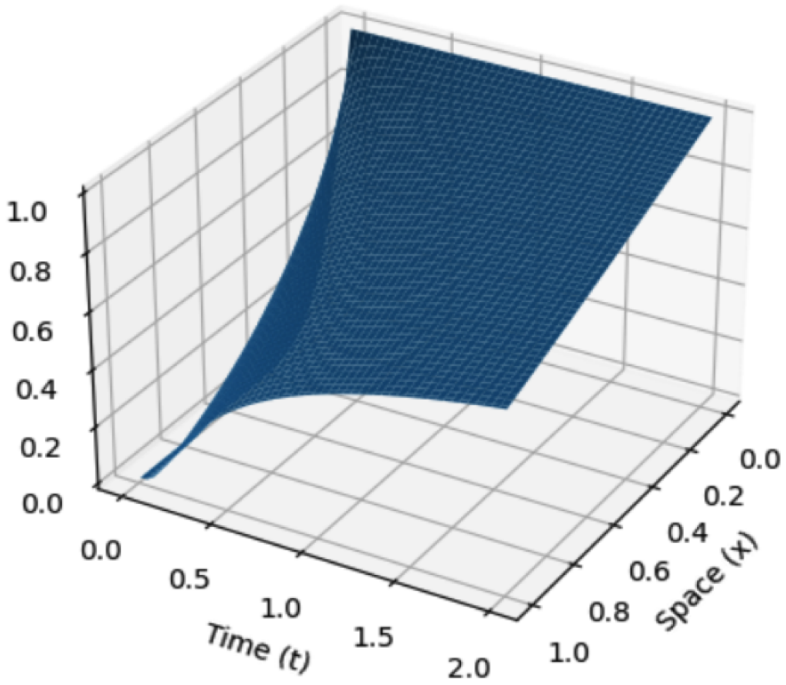

4.4.9 Heating Insulated Room from One Side

If we take our previous scenario with a campfire maintaining a dancing flickering flame of constant temperature emanating heat out into the cold starry night with nature outdoors, and we shove this into the fireplace of an insulating log cabin or brick hut, we'll now have a scenario where all the heat generated by burning firewood at a constant flame temperature gets trapped inside the building to get

toasty warm, meaning mathematically we place a reflecting or insulating barrier some distance away from the isothermal heat reservoir to contain the heat from spreading out into the infinite expanse of the x axis. Due to linearity and homogeneity, very analogous to Linear Time-Invariant (LTI) systems from signals and systems, without loss of generality, we can place the reflecting barrier at the origin and the isothermal heat reservoir to be pinned to the value of one at the coordinate $x = -a$, and the domain of interest or region where we track heat flow is from $x \in [-a, 0]$. This setup yields a mixed boundary condition for the differential equation solution, assigning $\frac{\partial Y}{\partial x}\big|_{x=0} = 0$ and $Y(x,t)\big|_{x=-a} = 1$. Using the same method of successive reflections as earlier, we can construct a solution as shown in the next equation; for brevity, a quick verification that this is indeed a valid solution will be provided instead of a detailed derivation, analogous to the notion of NP (Nondeterministic Polynomial Time) in complexity theory which characterizes how some difficult problems at least allow for comparatively instant checking of any proposed answer

$$Y(x,t) = \lim_{N\to\infty} \sum_{k=1}^{N} (-1)^{k+1} \left[\left[1 - \operatorname{erf}\big(\frac{x + (2k-1)a}{\sqrt{4Dt}} \big) \right] + \left[1 - \operatorname{erf}\big(\frac{-\big(x + a(1-2k)\big)}{\sqrt{4Dt}} \big) \right] \right] \tag{37}$$

At $x = -a$ our $Y(x,t)\big|_{x=-a} = 1$ because we have one original Heaviside Heat Kernel placed directly at such point with height of one, and the rest of the Heaviside Heat Kernels placed along the periodic lattice have an equal but opposite reflection partner or shadow buddy that is equidistant from the fulcrum point $x = -a$, ensuring complete cancellation such that no other extra contributions to $Y(x,t)\big|_{x=-a} = 1$ happen from the rest of the Heaviside Heat Kernels.

At $x = 0$, our $\frac{\partial Y(x,t)}{\partial x}\big|_{x=0} = 0$ by inspection due to reflective symmetry since each term or iteration in the infinite sum over k have a pair of matching heat kernel buddies for such k that flatten out at the origin $x = 0$, enforcing a balanced zero derivative there throughout all terms in the infinite sum.

While this is a loose argument analogous to the notion of Cauchy principle value, the spatial profile asymptotically becomes flat after long enough time indicated by $\Big[\lim_{t\to\infty} Y(x,t) = 1 \Big] \, \forall \, [x \in [-a, a]]$, since only the first Heaviside Heat Kernel placed on a fulcrum point itself at $x = -a$ does not have an equal but opposite buddy at the other end of the lever to cancel with on the other side of the teeter-totter, leaving remaining our previous scenario, which boils down to the previous analysis. An alternative view of this phenomenon is to perform some simple algebraic rearrangement to a more digestible form:

$$Y(x,t) = \lim_{N\to\infty} \sum_{k=1}^{N} (-1)^{k+1} \left[2 - \operatorname{erf}\big(\frac{x + (2k-1)a}{\sqrt{4Dt}} \big) - \operatorname{erf}\big(\frac{-\big(x + a(1-2k)\big)}{\sqrt{4Dt}} \big) \right] \tag{38}$$

Which shows some sort of alternating telescoping sum implying convergence of sorts, not to mention each successive term indeed approaches zero faster than the harmonic series due to small tails from the error function arising from the normal distribution being classified as a sub-exponential distribution. Additionally, at the other side of the spectrum, for the limit as $t \to 0^+$, we have our original Heaviside

step function throughout the domain of interest from $-a \leq x \leq a$, and all other Heaviside Heat Kernels as step functions are placed too far away for any contribution to happen from the zero part before the step.

As such, not only is this solution is mathematically consistent with our imposed boundary conditions, but it is also consistent with physical intuition. Intuitively, if we have our radiator fireplace or heater fixed to constant temperature one at $x = -a$ on the left side of our room from $-a \leq x \leq 0$, and we place an insulating wall at $x = 0$ on the right side of our room, the heat will eventually spread out over the empty room and be smooshed against the wall until the entire system fills up with heat to equilibrate to a flat profile of an ambient room temperature of $Y(x, t \to \infty) = 1$; so perhaps this scenario might be better described as a stone pizza cooking oven since the process only ends when the entire room is filled to the brim with heat to match the scalding flame source temperature.

Since math is a universal language, there is another equally valid physical interpretation of this mathematical solution. Suppose our baking oven has two heat sources at opposite ends of the chamber to ensure even cooking, meaning we have a heat bath fixed to temperature of one at both $x = a$ and $x = -a$, written more formally as $Y(x, t)\big|_{x=\pm a} = 1$. Notice directly by mirror image even symmetry with x of this function that the same solution previously proposed indeed satisfies these boundary conditions, constantly pinning both ends of the profile to the same fixed temperature of one throughout. The same mathematical asymptotic analysis holds which follows physical intuition, where the room or pizza oven eventually settles to the ambient heat source flame temperature but placed at both sides on opposite walls of the container. One could also view the opposite waves of heat clashing at the center to balance out to an insulating adiabatic barrier at the origin $x = 0$, metaphorically described by the tale of Moses releasing the parted seas, whose wave-fronts symmetrically collide at empty center path to refill it. This illustrates the consistency of all physical interpretations of the same abstract mathematical expression.

Included below is a visualization plot of the aforementioned mathematical function, non-dimensionalized to $a = 1, D = 1$ after absorbing them into the time and space coordinate system:

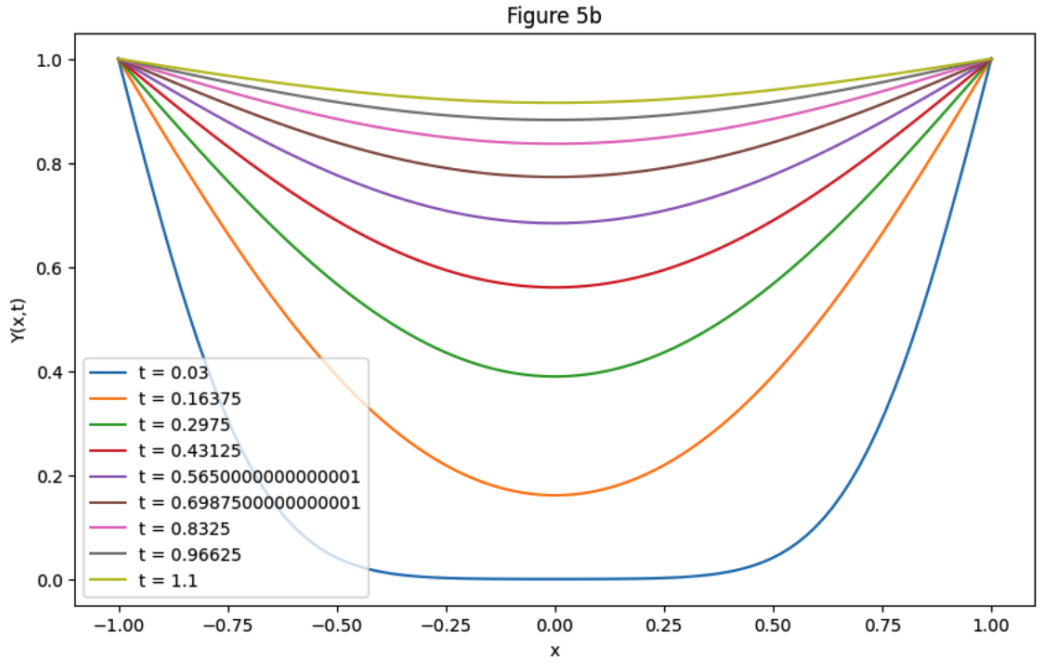

Figure 5a

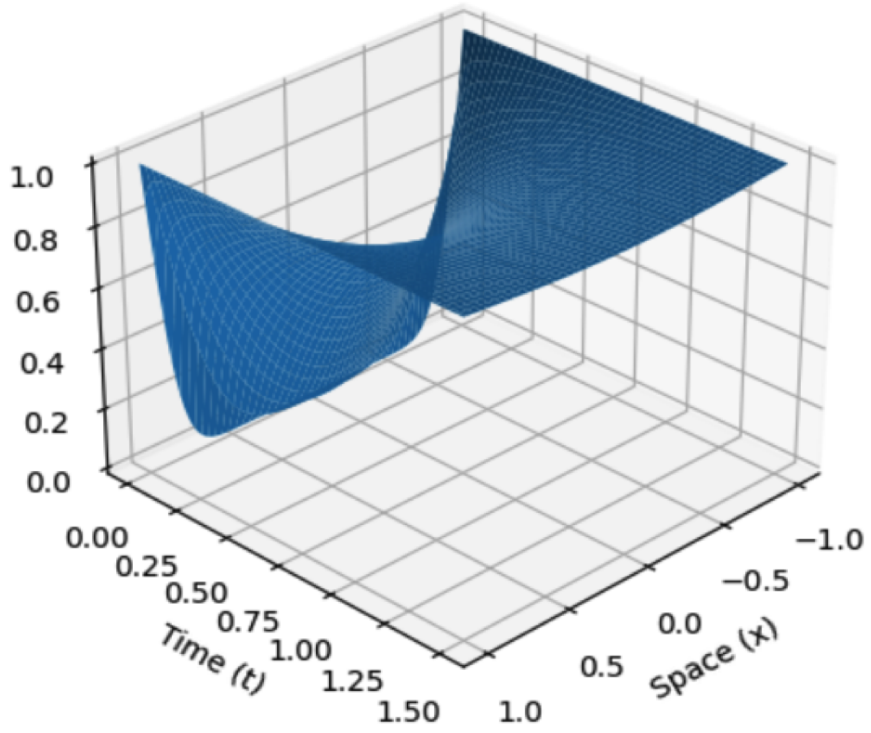

4.4.10 Heating Room with Absorbing Barrier

Suppose we're using fireplace heat source in a poorly insulated building with inadequate HVAC design, meaning all heat immediately escapes upon contact with the wall's window against the frigid winter snow outside. Or alternatively, the surface of a slice of steak is atop an isothermal sizzling

constantly hot metal frying pan's face, and the seasoned flip side of the slab is in isothermal contact with replenished ambient cool air of room temperature. This imposes boundary conditions of $Y(x,t)\big|_{x=a} = 1$ fixing the furnace temperature to one at the coordinate $x = a$ and $Y(x,t)\big|_{x=0} = 0$ fixing the window temperature to zero at the origin, which sucks away any heat that arrives, where we define our room to be in the strip of $0 \leq x \leq a$ region.

We can construct the following solution using the same method of reflections. The derivation details of such will be omitted, but the correctness of such solution can be easily checked:

$$Y(x,t) = \lim_{N\to\infty} \sum_{k=1}^{N} \left[\left[1 - \text{erf}\big(\frac{-\big(x + (1-2k)a\big)}{\sqrt{4Dt}}\big) \right] - \left[1 - \text{erf}\big(\frac{x + (2k-1)a}{\sqrt{4Dt}}\big) \right] \right] \tag{39}$$

Observe that this is an odd function with x, meaning at the fulcrum point at the origin $x = 0$, we have equal but contrasting Heaviside Heat Kernels cancelling each other out from equidistant lever-arm spacing, ensuring that $Y(x,t)\big|_{x=0} = 0$ always. Additionally, observe that with respect to the fulcrum break-point at $x = a$, we always have equal but opposite Heaviside Heat Kernels equally balancing each other out on this see-saw, ensuring that the only remaining unpaired Heaviside Heat Kernel left is the one at the fulcrum point placed at $x = a$ itself, which ensures that the boundary condition of constant furnace temperature of $Y(x,t)\big|_{x=a} = 1$ is preserved throughout.

As usual we'll perform a brief asymptotic analysis to match consistency with physical intuition. For $t \to 0^+$, the scenario boils down to localized Heaviside step functions, where the only one that matters is the one at $x = a$, matching intuitively that initially there is no heat anywhere in the system other than directly upon the heat reservoir at $x = a$ from the jump up from zero at the unit step break-point. This implies mathematically that $\lim\limits_{t\to 0^+} Y(x,t) = 0$.

To investigate what happens when $\lim\limits_{t\to\infty} Y(x,t)$, we can algebraically simplify the above expression into a more digestible format:

$$Y(x,t) = \lim_{N\to\infty} \sum_{k=1}^{N} \left[\text{erf}\big(\frac{x + (2k-1)a}{\sqrt{4Dt}}\big) - \text{erf}\big(\frac{-x + (2k-1)a}{\sqrt{4Dt}}\big) \right] \tag{40}$$

We know from numerical plotting $\lim\limits_{t\to\infty} Y(x,t) = \frac{x}{a}$ which creates a triangle profile sloping upwards from 0 up to 1 across the region of interest $0 \leq x \leq a$. It's tricky how to justify this analytically from such expression alone, but loosely it should be possible to rejigger the infinite sum as a continuous integral, and the difference in error functions to a Gaussian profile via definition of derivative in the limit of $t \to \infty$, and then invoke some sort of fundamental theorem of calculus argument to get such aggregate quantity to be proportional to relative error function spacing x in such interpretation. Regardless, this does naturally follow physical intuition that the asymptotic steady state profile of the heat equation is a solution to the Laplace or Poisson equation, namely a minimal-surface type linear profile connecting the endpoints from $Y(x,t)\big|_{x=0} = 0 \to Y(x,t)\big|_{x=a} = 1$, as we have a steady state equilibrium of heat flux

from the furnace on the right at $x = a$ being immediately absorbed by the cold window at $x = 0$.

This type of heat and mass transfer scenario is quite common in various contexts; the same equation can describe the transient behavior of an aircraft jet engine running at a constant hot temperature in the cold ambient surrounding atmosphere, or electron current through various media, such as semiconductors with material interfaces of differing electron diffusive mobility. Additionally this solution behaves as we'd expect, considering the cooked face of a slab of steak will end up heating up first, which explains why omelettes and pancakes should be flipped in the frying pan at some point to even out the temperature and cooking distribution. As such, this is an accurate and key closed-form analytical ground truth benchmark case for verifying the behavior of any simulation utilizing such boundary conditions. Additionally, this expression provides a useful tool in our solution arsenal to generalize to solving other exotic boundary conditions. A plotted visualization of our multivariable function, with non-dimensionalized $D = 1, a = 1$ absorbed into our coordinate system definition, is included below:

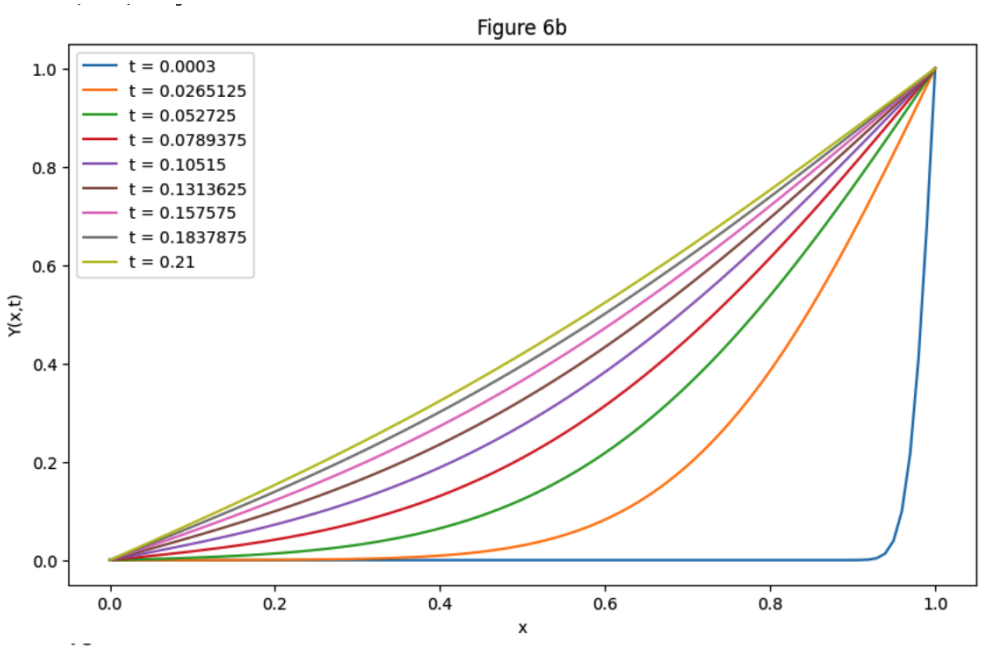

Figure 6a

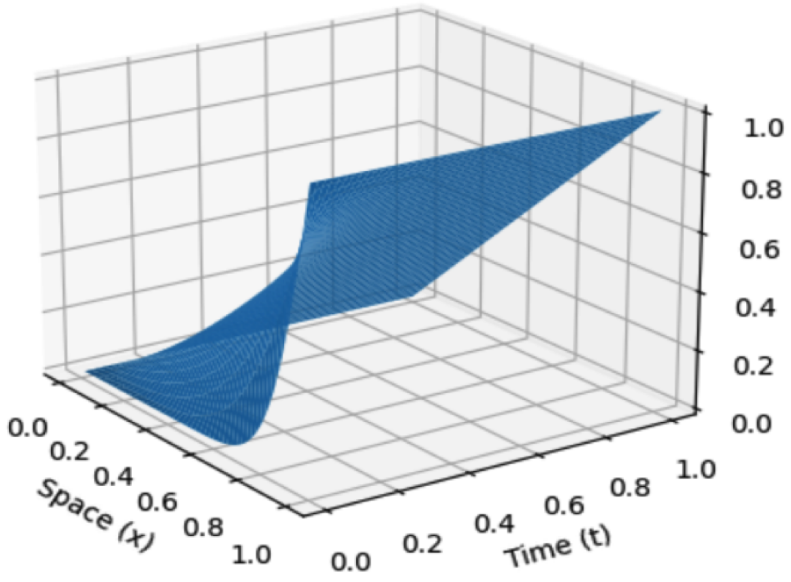

4.4.11 Extension: Heat Baths of Different Heights

In the event that we have two heat baths of different heights at opposite ends heating an initially empty or cold region, we can reuse two copies of the previous solution to construct an appropriate aggregate one here via their linear combination. This type of situation could arise if our waffle iron has a top folding cover that is less efficient at cooking than the bottom, with asymmetric mismatched isothermal heat reservoirs at the boundaries for heat to diffuse into the pancake to cook it. The previous

solution's steady state involved a triangle with linear slope ranging from the height of the reservoir to the zero-crossing absorbing sink across the region, and merging two of these for different heights allows an aggregate profile to sum to the desired Laplace equation steady state solution with a linear slope connecting the different reservoir heights. As such, this is a useful tool for determining more ground-truth cases for further verification of simulations in different scenarios.

4.4.12 Sourced Diffusion, Infinite Domain: "Flame Heat Kernel"

Notice how our heat equation's "impulse response" is the Green's function or Heat Kernel of an expanding Gaussian profile with time, meaning this is how an evanescent Dirac Delta excites the system, hence the self-explanatory name of this signal processing definition. We derived the previous Heaviside Heat Kernel to be the unit step response of our system, meaning the evolutionary behavior of our system with respect to a unit step initial input. We can continue with this line of thinking: what happens if we perturb the system with a continuous lasting spike source? This is entirely different from an evanescent short unit pulse initial condition source describing an atomic measure or discrete probability point, corresponding analogously to the Brownian particle's initial position with known certainty case. The reason why this scenario is different is because an initial pulse spreads out and eventually fades away as it smears over space, and the spike's height forever decays with time. This makes sense because any concentration of heat eventually spreads, and even if we know where the Brownian particle currently is, we eventually lose track of where it will end up going as such correlated information is eventually erased over time into the future. Hopefully this characterizes the key distinction of this new scenario.

In contrast to the previous Gaussian heat kernel and Heaviside heat kernel which eventually smooths out from the mathematical mollifier, in this physical scenario, we are continuously injecting a fixed amount of power, or heat at a constant rate, into such particular point in space, constantly throughout all time. Additionally, this is entirely different from an isothermal boundary, as that causally affects the system only in ways to maintain such boundary condition pinned to such particular value, unlike this case where some fixed point of reception always has an unrelenting energetic injection, irrespective of whatever happens with the system. In other words, an isothermal boundary condition is analogous to a closed-loop feedback control system, and an everlasting source is analogous to an open-loop uncontrolled system that is subject to perturbation from an external factor. As tricky as this may sound, we can work through this by using a single simple evanescent heat kernel to continuously "smear" throughout throughout time, thereby compounding its sourced effects as they continuously aggregate over time around the system in a linear superposition manner. In other words, an everlasting spike heat source is equivalent to repeatedly shoving an evanescent initial spike pulse injected into all times, which implies that mathematically, rather than computing the system response to $\delta(x,t)$, we here instead actually need to compute the system response to $\delta(x)$, or $\delta(x)u(t)$ to ensure that our initial is unperturbed at rest

at negative times. Observe metaphorically that eventually the convolution integral boils down into an aggregation of the wavefront or "wake" of the heat kernel "cruising" up to its current time, throughout its journey skimming throughout the domain along the time axis.

Since this is an entirely original and novel mathematical result as far as we know, it is worth laying out its full derivation details in totality:

We set up our derivation as follows, where we'd like to convolve the the following functions throughout the spatially homogeneous region without loss of generality:

$$\begin{bmatrix} \text{heat kernel filter: } h(x,t) = \frac{1}{\sqrt{4\pi D t}} e^{\frac{-x^2}{4Dt}} \mathcal{I}(t > 0) \\ \text{system perturbation input: } z(x,t) = \mathcal{I}(0 < t < \tau)\delta(x) \end{bmatrix} \tag{41}$$

Where $z(x,t)$ is how we're exciting or forcing the system, here by holding up a point candle constant flame heat injection source to the origin at $x = 0$ for a time duration of τ seconds from $0 < t < \tau$.

$$Y(x,t) = h * z = \int_{-\infty}^{\infty} \int_{-\infty}^{\infty} h(r,s) z(r - x, t - s) dr ds \tag{42}$$

Via definition of convolution, keep in mind this is now an image convolution or two dimensional convolution over both time and space simultaneously. The resultant distribution expresses how the now forced heat diffusion system responds to such a type of candle input perturbation. We plug this into our definition:

$$Y(x,t) = \int_{-\infty}^{\infty} \int_{-\infty}^{\infty} \frac{\mathcal{I}(s > 0)}{\sqrt{4\pi D s}} e^{\frac{-r^2}{4Ds}} \mathbb{I}(0 < t - s < \tau)\delta(r - x) dr ds \tag{43}$$

With some algebra and calculus, we can continue processing this expression:

$$Y(x,t) = \int_{-\infty}^{\infty} \frac{1}{\sqrt{4\pi D s}} \mathbb{I}(s > 0)\mathbb{I}(0 < t - s < \tau) \left[\int_{-\infty}^{\infty} e^{\frac{-r^2}{4Ds}} \delta(r - x) dr \right] ds \tag{44}$$

Via the sifting property or identity element of convolution operator we can evaluate the inner integral:

$$Y(x,t) = \int_{-\infty}^{\infty} \frac{1}{\sqrt{4\pi D s}} \mathbb{I}(s > 0)\mathbb{I}(0 < t - s < \tau) \left[e^{\frac{-x^2}{4Ds}} \right] ds \tag{45}$$

We can then rearrange the indicator functions' inside logical inequality expressions via chain of logical condition equivalences:

$$Y(x,t) = \int_{-\infty}^{\infty} \frac{e^{\frac{-x^2}{4Ds}}}{\sqrt{4\pi D s}} \mathbb{I}(s > 0)\mathbb{I}(s < t < \tau + s) ds \tag{46}$$

$$Y(x,t) = \int_{-\infty}^{\infty} \frac{e^{\frac{-x^2}{4Ds}}}{\sqrt{4\pi D s}} \mathbb{I}(0 < s < t < \tau + s) ds \tag{47}$$

We'd like to massage the logical innards of the indicator function into nice bounds to place into the definite integral. If we're integrating over s, clearly zero will be the integrand's lower bound. Considering $\tau > 0$ implied by definition of the system perturbation input, representing where we're turning on the heat source for a duration of $0 < t < \tau$, throughout this period, τ by constructed definition is going to be greater than both t and 0, and so that part of the indicator function is irrelevant with respect to the Riemann-Stieltjes integral's measure, and without externally altering anything about the relevant inner truth functionality we can continue rewriting the previous equation as:

$$Y(x,t) = \int_{-\infty}^{\infty} \frac{e^{\frac{-x^2}{4Ds}}}{\sqrt{4\pi Ds}} \mathbb{I}(0 < s < t) ds \tag{48}$$

$$Y(x,t) = \int_{0}^{t} \frac{e^{\frac{-x^2}{4Ds}}}{\sqrt{4\pi Ds}} ds \tag{49}$$

An integral of this form is quite a doozy to compute, so for brevity the solution will be stated without derivation along with a concise reverse verification via differentiation:

$Y(x,t) = \frac{1}{2D}\left[\sqrt{\frac{4Dt}{\pi}}e^{\frac{-x^2}{4Dt}} + |x|\left[\text{erf}(\frac{|x|}{\sqrt{4Dt}}) - 1\right]\right]$

$2D\frac{\partial}{\partial t}Y(x,t) = \frac{\partial}{\partial t}\left[\sqrt{\frac{4Dt}{\pi}}e^{\frac{-x^2}{4Dt}}\right] + |x|\frac{\partial}{\partial t}\left[\text{erf}(\frac{|x|}{\sqrt{4Dt}}) - 1\right]$ via linearity of differentiation

$2D\frac{\partial}{\partial t}Y(x,t) = \frac{1}{2}\sqrt{\frac{4D}{\pi t}}e^{\frac{-x^2}{4Dt}} + \sqrt{\frac{4Dt}{\pi}}e^{\frac{-x^2}{4Dt}}\frac{\partial}{\partial t}\left[\frac{-x^2}{4Dt}\right] + |x|\frac{\partial}{\partial t}\left[\text{erf}(\frac{|x|}{\sqrt{4Dt}}) - 1\right]$ via chain rule, power rule, and product rule

$2D\frac{\partial}{\partial t}Y(x,t) = \frac{1}{2}\sqrt{\frac{4D}{\pi t}}e^{\frac{-x^2}{4Dt}} + \sqrt{\frac{4Dt}{\pi}}e^{\frac{-x^2}{4Dt}}\left[\frac{x^2}{4Dt^2}\right] + |x|\frac{2}{\sqrt{\pi}}e^{\frac{-x^2}{4Dt}}\frac{\partial}{\partial t}\left[\frac{|x|}{\sqrt{4Dt}}\right]$ via definition of error function with chain rule

$2D\frac{\partial}{\partial t}Y(x,t) = \frac{1}{2}\sqrt{\frac{4D}{\pi t}}e^{\frac{-x^2}{4Dt}} + \sqrt{\frac{4Dt}{\pi}}e^{\frac{-x^2}{4Dt}}\left[\frac{x^2}{4Dt^2}\right] + |x|^2\frac{2}{\sqrt{\pi}}e^{\frac{-x^2}{4Dt}}\left[\frac{-1}{2\sqrt{4Dt^3}}\right]$ via power rule

$2D\frac{\partial}{\partial t}Y(x,t) = \frac{1}{2}\sqrt{\frac{4D}{\pi t}}e^{\frac{-x^2}{4Dt}} + 0 + 0$ as last two terms cancel

$\frac{\partial}{\partial t}Y(x,t) = \frac{1}{4D}\sqrt{\frac{4D}{\pi t}}e^{\frac{-x^2}{4Dt}} = \frac{1}{\sqrt{4\pi Dt}}e^{\frac{-x^2}{4Dt}}$ ✓

Which proves that our desired Flame heat kernel or Flame Kernel is of form:

$$Y(x,t) = \frac{1}{2D}\left[\sqrt{\frac{4Dt}{\pi}}e^{\frac{-x^2}{4Dt}} + |x|\left[\text{erf}(\frac{|x|}{\sqrt{4Dt}}) - 1\right]\right] \tag{50}$$

As such, we've derived an explicit closed-form solution to the one-dimensional heat equation with a continuous point source, expressed in terms of elementary and error functions. While the problem setup is classical, the resulting analytic form is not found in standard references and provides a compact, exact expression for the accumulated diffusion field from a stationary source. We refer to this as the "flame kernel", in analogy with the standard commonly known "heat kernel" representing an ephemeral instantaneous pulse source, laid out in the previous section with equation 11.

As we've done before, we'll perform a simple asymptotic analysis. Initially we have $\lim_{t\to 0^+} Y(x,t) = 0$ meaning the system begins at rest because the heat source has not had any duration of time to heat anything up yet, following physical intuition. For $\lim_{t\to\infty} Y(x,t) = \infty$, we have an unstable system where

relentless persistent heating blows temperature up to infinity, cooking all space into an infinite incendiary inferno eventually when the universe ends until eternity. This iso-enthalpy situation is interesting in contrast to the more trivial adiabatic situation where we have a confined enclosure of an sealed box presented in section 4.4.16, which directly following common sense intuition will obviously diverge. Akin to Boltzmann's original vision and prophecy of the entropic demise of the universe, this makes mathematical sense, as the universe's thermodynamic system cannot contain a constant unyielding delta injection of energy per unit space throughout the rest of time eternally, as it will all eventually start to pile up and accumulate indefinitely, implying there is some fundamental per volume specific spatial heat capacity of this model 1D universe, where there is not enough ambient wiggle room space to accommodate perpetually squeezing persistent concentrated power impulses into.

In an alternative but equivalent viewpoint, if one continuously populates a system's sample space with IID clone copies of random walkers with an endless supply of replenishment with nowhere for them to be consumed, naturally the system will eventually become overcrowded with random walkers wandering around roaming in the nearby region upon release. This interpretation can allow this PDE solution function to be viewed as the occupancy number profile or "distribution" (not literally, it is not mathematically normalized to one due to constant injection of heat) in a loose physics measurement sense just like the underpinnings of statistical mechanics utilizing dynamical system ergodic theory, characterizing relatively upon where in the system some of the indistinguishable random walkers are to be found, throughout constant injection continually releasing fresh new copies at the same start point, analogous to how every school's graduating class becomes simultaneously replaced by an incoming new class.

This is an even mathematical function with respect to x, and as such returns the same output value for the same magnitude of positive and negative x input, indicating horizontal mirror image reflective symmetry about the origin. In addition to spatial homogeneity, the heat equation is a linear system, and so negating this function ends up transforming this to the resultant cascading ambient effect of a lasting heat source point, to the resultant cascading ambient effect of a lasting heat sink point, where a constant amount of energy per space is consumed from the system per unit time, or a constant amount of power at such point location in space is removed throughout the system's evolution. At the end of the day these profiles function similar to electron holes or point defect dislocations in materials, where the aggregate superposition of the wave-functions characterizes the system as a whole. The existence of such Flame Heat Kernel then allows us to compute the mechanics of explicit energy creation and destruction in such system– paralleling the notion of creation and annihilation operators from second quantization in quantum mechanics– which is more detailed than the implicit energy alterations caused by isothermal pinned endpoint boundary conditions (perhaps upon the empty "vacuum state"), expanding the linguistic vocabulary and expressible configurational interaction situations using such heat and mass

transport language.

A couple fascinating further spinoffs with potential application is performing the same image convolution with different types of dynamically evolving point candle flame sources, such as an oscillatory flickering candle, or a candle that dynamically grows or shrinks in heating strength at such spatial coordinate. The exponential term in our convolution eventually approaches one in the limit for large integration variable s, and as such directly implies our flickering candle source must asymptotically decay faster than $O(\frac{1}{\sqrt{t}})$ for finite mathematical convergence of the windowed inner product integral in question in order for the universe to not eventually become overheated in the end, for the case of our toy-model one-dimensional universe.

Due to the separability of the underlying heat equation PDE for cartesian coordinates: as opposed to the standard "Heat Kernel" 11 with non-zero and evanescent forcing term to the original heat equation PDE of form $\frac{\partial Y}{\partial t} = \nabla^2 Y + \delta(t) \left[\prod_{i=1}^{N \text{ dimensions}} \delta(x_i) \right]$, our "Flame-Kernel" from eq. 50 arises from a persistent forcing source term of form: $\frac{\partial Y}{\partial t} = \nabla^2 Y + \left[\prod_{i=1}^{N \text{ dimensions}} \delta(x_i) \right]$ that is not evanescently modified by the product's prefactor $\delta(t)$. In this setting, the aggregate solution is now a product of one dimensional Green's functions of our previous "Flame Kernel" (50), compared to with an evanescent initialization with a product of Green's functions of the form of the "Heat Kernel" (11), leading to the standard isotropic multivariate Gaussian function with variance expanding with time, which is an elliptic distribution. Solving for the steady state configuration by setting the condition $\frac{\partial Y}{\partial t} = 0$ reduces the parabolic PDE into an elliptic PDE, namely the Poisson equation. At steady state, it is well known that in 2D $Y \sim \log(r)$ in terms of the isotropic radial coordinate $r = \sqrt{x_1^2 + x_2^2}$, and in 3D $Y \sim \frac{1}{r}$ in terms of the isotropic radial coordinate $r = \sqrt{x_1^2 + x_2^2 + x_3^2}$ for response solutions to the Poisson equation with forcing term configuration $\delta^{(N)}(\vec{\mathbf{r}})$. This implies that while a constant persistent source does eventually explode to obliterate a 1 dimensional universe, it does not overload a two dimensional or three dimensional universe accordingly, akin to the notions of transience and recurrence from isotropic Brownian motion of varying dimensionality and Polya's random walk constants. In other words, a persistent heat source in one dimension is volatile and the ambient temperature of such 1D galaxy explosively grows without bound, but in two dimensions and higher it stabilizes, with ties to the equipartition theorem about energy storage in each dimensional degree of freedom. Similarly, martingale random walks in one and two dimensions are recurrent, but are transient in three dimensions. This signifies that a bird aimlessly meandering and flying about in the three-dimensional space of the sky and atmosphere may actually never find its way home, to end up actually being lost forever in the abyss of outer space, whereas an aimlessly wandering human, Langton's ant, or turtle-graphics turtle walking about on an infinite plane will surely definitely make it back to return home at some point, eventually down the road if we patiently wait long enough.

In conclusion, the flame kernel (50) is the most important analytical solution verification tool to match any simulation to, as it is able to provide the ground truth comparative result to capture what

should be expected to happen for heat sources and sinks (or chemical and mass sources and sinks) in any context, which is the in silico scaffold behind the transmogrification "bus-channel" for routing of any heat and mass between the independent species concentration and temperature profile "audio track" channels.

A non-dimensional plot of such result, with $D = 1$ absorbed into the time or space variable, is included below to visualize how a point source affects the 1D system throughout time.

Figure 7a

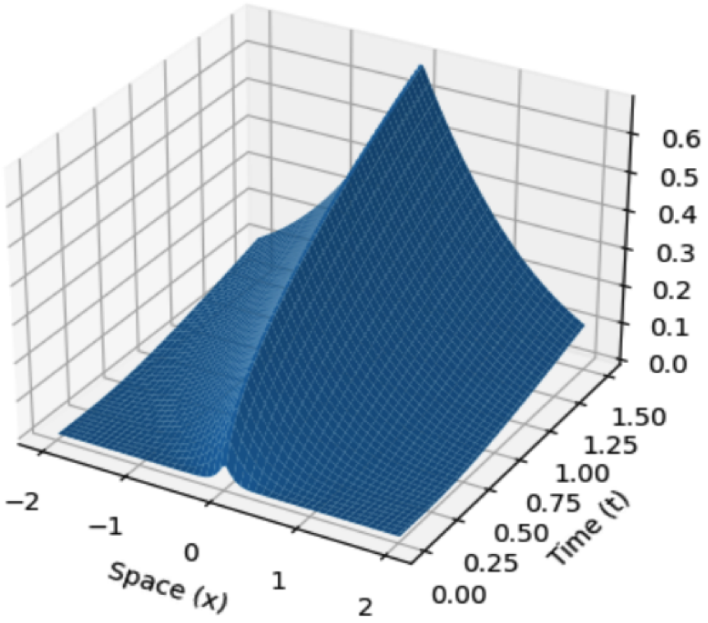

Figure 7b

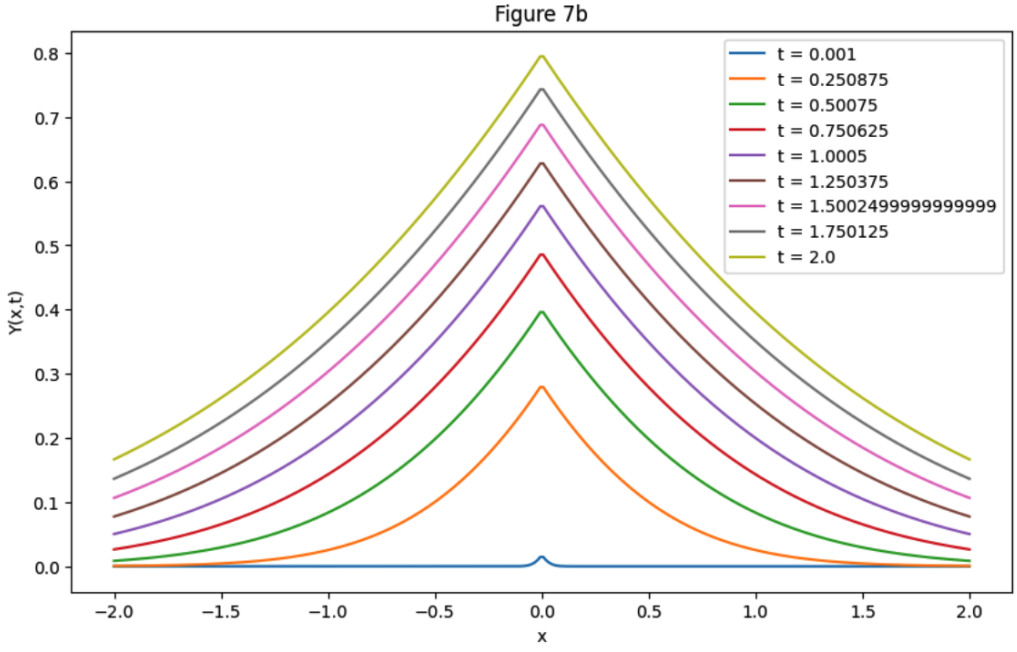

4.4.13 Flame Family solutions

The subsequent sections will provide an analysis of heat equation PDE solutions of various boundary conditions, but now with the advent of an energy heat injection point candle flame source constantly contributing energy to increase temperature within the domain. Previously, we constructed families of solutions to the linear heat equation using a superposition of Green's functions, including the "raw vanilla"-flavor standardly known expanding Gaussian profile heat kernel, succeeded by its convolution with a unit step to formulate the "Heaviside Heat Kernel" 35. group of solutions. Now we can use the exact same symmetry arguments while incorporating our newly derived Flame Kernel as the basis function for periodically repeating translated versions and flipped copies upon our lattice. As such, we can present the Flame Family of solutions for for the heat equation, piggybacking on the notion behind the common folk terminology of "Exponential Family" from statistics which characterizes an extremely important class of random variable distributions all of similar mathematical form (namely Gibbs measure which facilitates computation and analysis of its properties.) So of course, each of the "Flame Family Solutions" as a simile to the Exponential Family, are all constructed from the same Candle Flame kernel derived and presented in 4.4.12.

4.4.14 Diffusion with Source, One-Sided Reflecting Boundary

The derivation and justification of this mathematical solution for the boundary condition of $\frac{\partial Y(x,t)}{\partial x}\big|_{x=0} = 0$ utilizes the exact same line of reasoning as previous sections:

$$Y(x,t) = \frac{1}{2D}\left[\sqrt{\frac{4Dt}{\pi}}e^{\frac{-(x+x_0)^2}{4Dt}} + |x+x_0|\left[\text{erf}(\frac{|x+x_0|}{\sqrt{4Dt}}) - 1\right]\right] + \frac{1}{2D}\left[\sqrt{\frac{4Dt}{\pi}}e^{\frac{-(x-x_0)^2}{4Dt}} + |x-x_0|\left[\text{erf}(\frac{|x-x_0|}{\sqrt{4Dt}}) - 1\right]\right] \tag{51}$$

Due to even symmetry about the variable x from the "twin-flame" configuration, we can say our candle flame source is situated at $x = \pm x_0$ and pick whichever corresponding semi-infinite domain. This situation describes the emanation of heat from a concentrated point candle source while insulating, blocking, and reflecting any heat that touches the origin from crossing through over to the other side, or alternatively, the brick wall barrier or electric fence at the origin prevents any pet random walkers from passing through to proceed onwards into the other domain, containing them to graze within the pasture of the number line's positive half.

Indeed, matching our previous asymptotic analysis of the flame kernel alone, $\lim_{t\to 0^+} Y(x,t) = 0$ and $\lim_{t\to\infty} Y(x,t) = \infty$ as all heat gets reflected back to the same side, which was already originally going to grow to infinity regardless.

This can be seen in the following non-dimensional plot, where without loss of generality we can set $D = 1$ and $x_0 = 1$ by absorbing them into the space and time variable. Visually, the asymptotic analysis

can be more apparently seen:

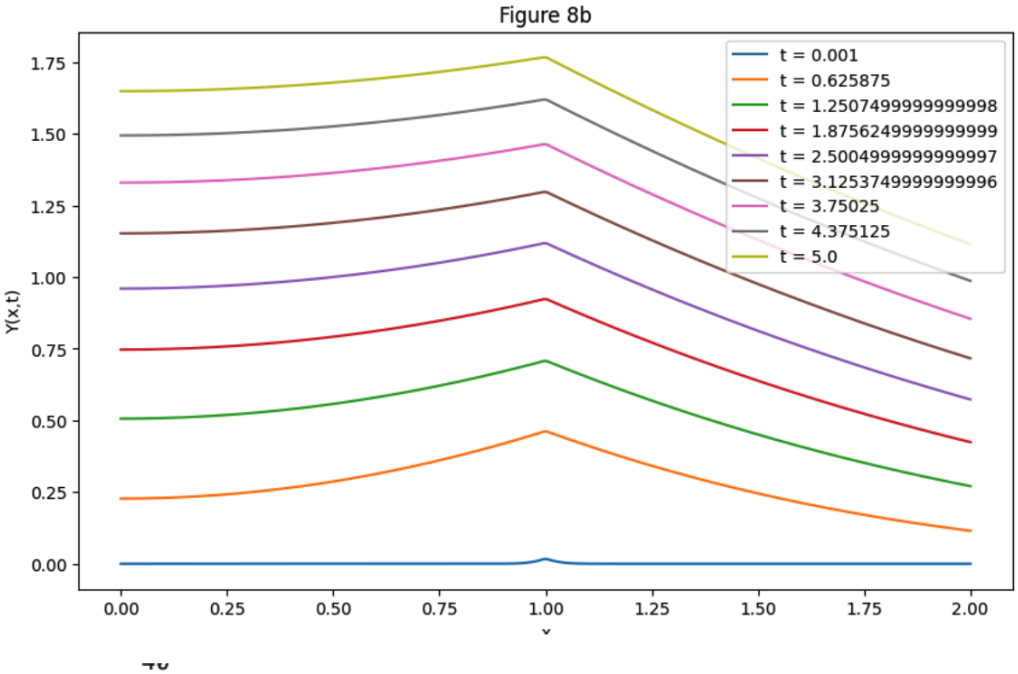

Figure 8a

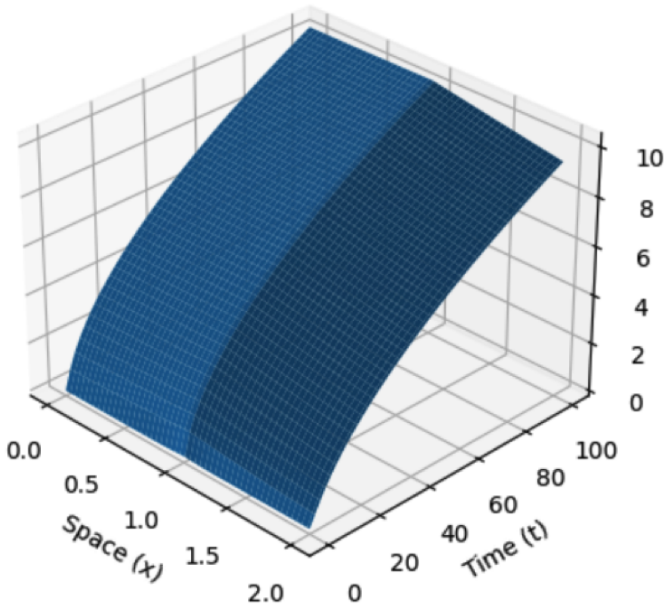

4.4.15 Diffusion with Source, Absorbing Boundary

The derivation and justification of this mathematical solution, for the boundary condition of $Y(x,t)\big|_{x=0} = 0$ with candle flame point situated at $x = a$, utilizes the exact same line of reasoning as previous sections:

$$Y(x,t) = \frac{1}{2D}\left[\sqrt{\frac{4Dt}{\pi}}e^{\frac{-(x-x_0)^2}{4Dt}} + |x-x_0|\left[\text{erf}(\frac{|x-x_0|}{\sqrt{4Dt}}) - 1\right]\right] - \frac{1}{2D}\left[\sqrt{\frac{4Dt}{\pi}}e^{\frac{-(x+x_0)^2}{4Dt}} + |x+x_0|\left[\text{erf}(\frac{|x+x_0|}{\sqrt{4Dt}}) - 1\right]\right] \quad (52)$$

This equation with odd symmetry about variable x represents the solution to the PDE system where a candle point flame source is held at the coordinate $x = x_0$, emanating heat outwards about the positive region of the semi-infinite domain, with an absorbing barrier situated at the origin. Any heat that touches the origin instantly becomes annihilated and removed from the system, also entailing no passage to the other side as a corollary. Alternatively, the contrasting view of tracking the herd of a population of constantly released random walkers is equivalent, where any random walker that arrives at the origin ends up becoming stuck to the absorbing wall to be eliminated from the system.

Indeed, matching our previous asymptotic analysis of the flame kernel alone, $\lim_{t\to 0^+} Y(x,t) = 0$.

This time though:

$\lim_{t\to\infty} Y(x,t) \sim \frac{1}{2D}\left[\sqrt{\frac{4Dt}{\pi}}e^0 + |x-x_0|\left[\text{erf}(0)-1\right]\right] - \frac{1}{2D}\left[\sqrt{\frac{4Dt}{\pi}}e^0 + |x+x_0|\left[\text{erf}(0)-1\right]\right]$

$\lim_{t\to\infty} Y(x,t) \sim \frac{1}{2D}\left[\sqrt{\frac{4Dt}{\pi}}\times 1 + |x-x_0|\left[0-1\right]\right] - \frac{1}{2D}\left[\sqrt{\frac{4Dt}{\pi}}\times 1 + |x+x_0|\left[0-1\right]\right]$

$\lim_{t\to\infty} Y(x,t) \sim \frac{1}{2D}\left[\sqrt{\frac{4Dt}{\pi}} - |x-x_0|\right] - \frac{1}{2D}\left[\sqrt{\frac{4Dt}{\pi}} - |x+x_0|\right]$

$\lim_{t\to\infty} Y(x,t) \sim \frac{1}{2D}\left[\sqrt{\frac{4Dt}{\pi}} - |x-x_0| - \sqrt{\frac{4Dt}{\pi}} + |x+x_0|\right]$

$\lim_{t\to\infty} Y(x,t) = \frac{1}{2D}\left[0 - |x-x_0| - 0 + |x+x_0|\right]$ cancellation, no longer any t dependence

$\lim_{t\to\infty} Y(x,t) = \frac{1}{2D}\left[|x+x_0| - |x-x_0|\right]$

This is the steady state profile's shape, which consistently matches our dynamic PDE heat equation's corresponding steady state ODE Laplace or Poisson equation's solution to:

$-D\frac{d^2}{dx^2}Y(x) = \delta(x-x_0) - \delta(x+x_0)$

when setting the time derivative to zero for steady state computation, making use of the framework of Singularity Functions used in Euler-Bernoulli beam theory.

This makes sense as intuitively the system responds to an infinite army onset of random walkers through commensurate adsorption upon the barrier where they stick to be removed from the system, thereby allowing the onset of an overall bounded solution from counteracting effects.

This can be seen in the following non-dimensional plot, where without loss of generality we can set $D = 1$ and $x_0 = 1$ by merging them into the space and time variable. Visually, the asymptotic analysis can be more apparently seen:

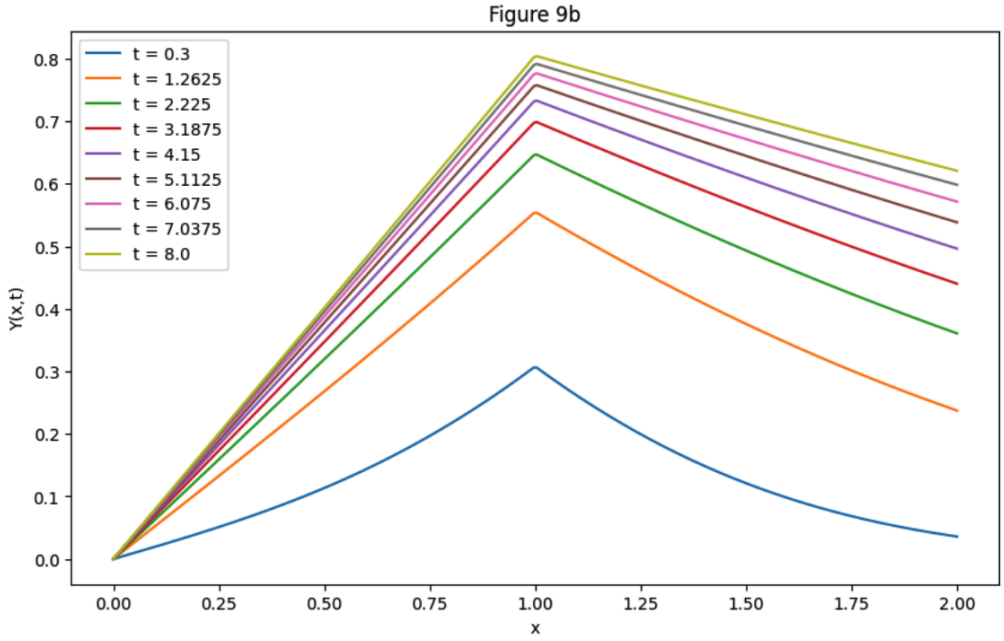

Figure 9a

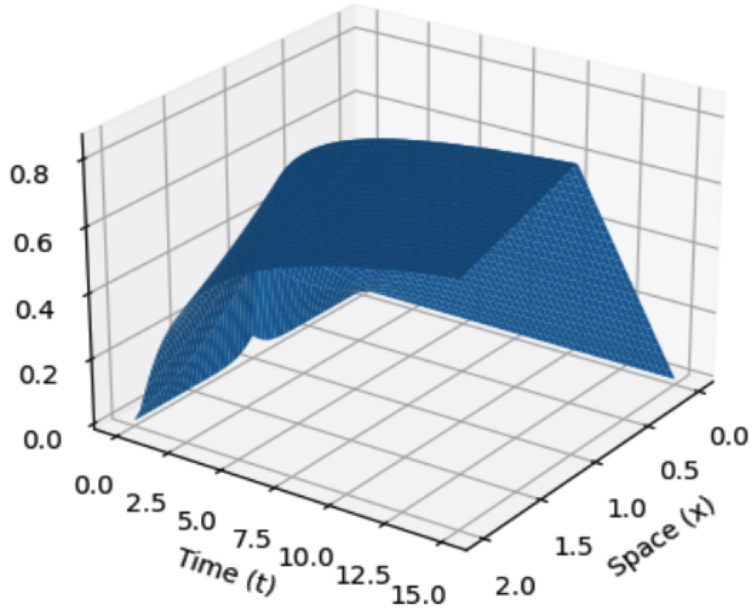

4.4.16 Diffusion with Source, Neumann Boundary Conditions

The derivation and justification of this mathematical solution, with boundary conditions of $\frac{\partial Y(x,t)}{\partial x}\big|_{x=\pm a} = 0$ with candle flame point situated at the origin $x = 0$, utilizes the exact same line of reasoning as previous sections:

$$Y(x,t) = \frac{1}{2D}\sum_{k=-\infty}^{\infty}\left[\sqrt{\frac{4Dt}{\pi}}e^{\frac{-(x-2ak)^2}{4Dt}} + |x-2ak|\left[\text{erf}(\frac{|x-2ak|}{\sqrt{4Dt}}) - 1\right]\right] \tag{53}$$

To reformulate into a more computationally digestible form, we can write it as:

$$
\begin{aligned}
2DY(x,t) = &\sqrt{\frac{4Dt}{\pi}} e^{\frac{-x^2}{4Dt}} + |x| \left[\operatorname{erf}\left(\frac{|x|}{\sqrt{4Dt}} \right) - 1 \right] \\
&+ \lim_{N\to\infty} \sum_{k=1}^{N} \left[\sqrt{\frac{4Dt}{\pi}} e^{\frac{-(x-2ka)^2}{4Dt}} + |x-2ka| \left[\operatorname{erf}\left(\frac{|x-2ka|}{\sqrt{4Dt}} \right) - 1 \right] \right. \\
&\left. + \sqrt{\frac{4Dt}{\pi}} e^{\frac{-(x+2ka)^2}{4Dt}} + |x+2ka| \left[\operatorname{erf}\left(\frac{|x+2ka|}{\sqrt{4Dt}} \right) - 1 \right] \right]
\end{aligned}
\tag{54}
$$

This mathematical form facilitates asymptotic analysis and computation to make sure successive terms in the sum are decreasing.

Indeed, matching our previous asymptotic analysis of the flame kernel alone, $\lim_{t\to 0^+} Y(x,t) = 0$ as the raw original flame kernel initially begins as a flat function, such zero profile repeated periodically over the lattice. We can also immediately see that $\lim_{t\to\infty} Y(x,t) = \infty$ because we have an infinite sum of non-negative flame kernels, each of which already blows up to infinity. Due to symmetry, just looking at our internal domain of $-a \leq x \leq a$, the total amount of energy that originally spread out over all ambient surrounding space from a single flame kernel source alone is folded over onto itself to all be contained within such strip of $-a \leq x \leq a$, implying all such heat ends up being compressed to be confined within such region of compact support, in accordance with the principles of how reflecting or insulating walls should qualitatively behave. Given this qualitative description, we could distinguishably name this "lit-flame-in-a-box" scenario as an ever increasing "hot-box" or "bomb-calorimeter" colloquially due to how the "oven" is completely sealed trapping all heat with no escape, eventually generating an infinite inferno. An equivalent alternative interpretation is to view the expanding profile as a relative probability amplitude of finding some particle somewhere, which potentially could be re-normalized, similar to exponential tilting and partition functions.

This behavior can be seen in the following non-dimensional plot, where without loss of generality we can set $D = 1$ and $a = 1$ by absorbing them into the space and time variable. Visually, the asymptotic analysis can be more apparently seen:

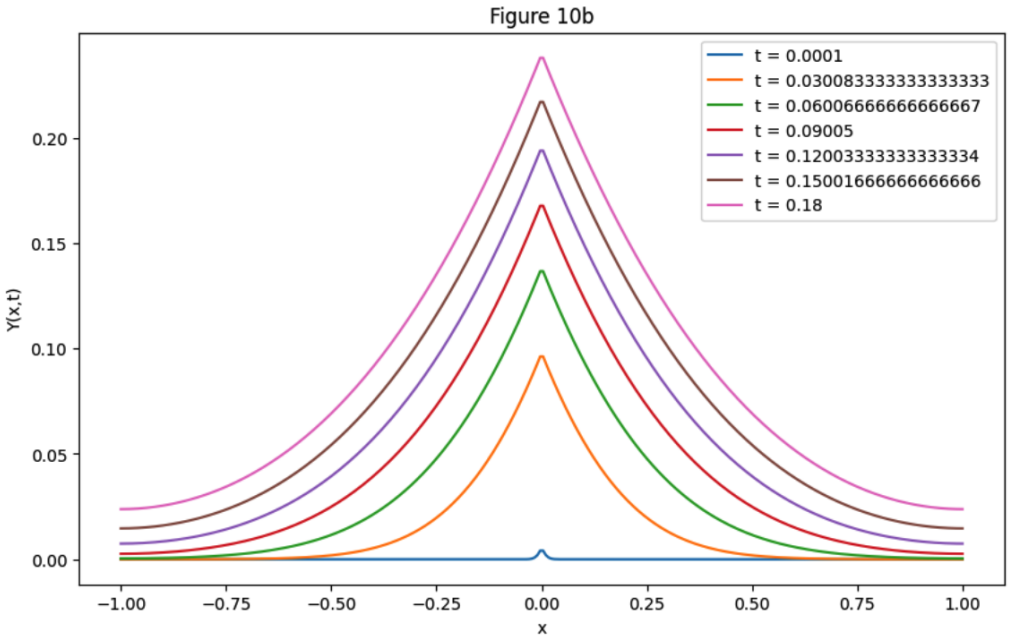

Figure 10a

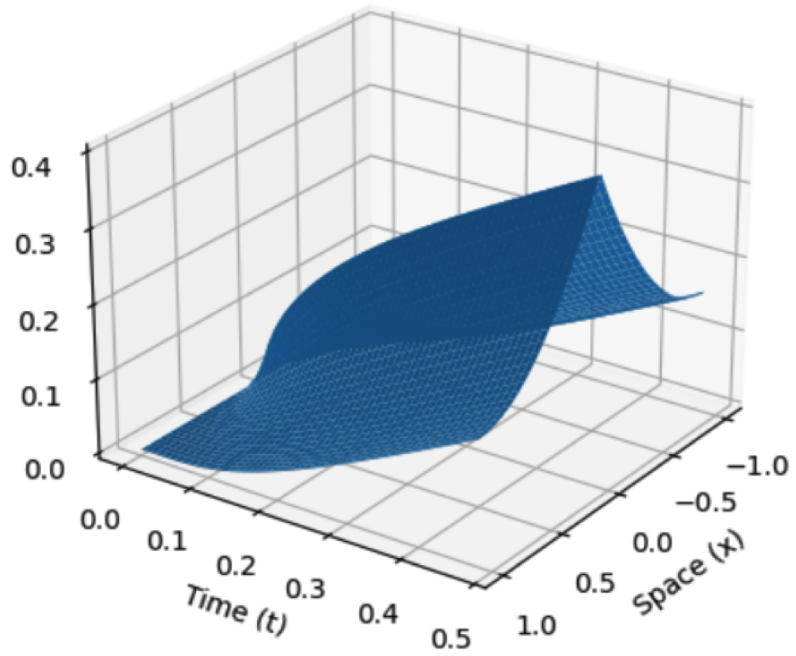

4.4.17 Diffusion with Source, Dirichlet Boundary Conditions

The derivation and justification of this mathematical solution, with boundary conditions of $Y(x,t)\big|_{x=\pm a} = 0$ with candle flame source situated at the origin $x = 0$, utilizes the exact same line of reasoning as previous sections:

$$2DY(x,t) = \sqrt{\frac{4Dt}{\pi}}e^{\frac{-x^2}{4Dt}} + |x|\left[\text{erf}\left(\frac{|x|}{\sqrt{4Dt}}\right) - 1\right] \tag{55}$$
$$+ \lim_{N\to\infty}\sum_{k=1}^{N}(-1)^k\left[\sqrt{\frac{4Dt}{\pi}}e^{\frac{-(x-2ka)^2}{4Dt}} + |x-2ka|\left[\text{erf}\left(\frac{|x-2ka|}{\sqrt{4Dt}}\right) - 1\right]\right.$$
$$\left. + \sqrt{\frac{4Dt}{\pi}}e^{\frac{-(x+2ka)^2}{4Dt}} + |x+2ka|\left[\text{erf}\left(\frac{|x+2ka|}{\sqrt{4Dt}}\right) - 1\right]\right]$$

This mathematical form facilitates asymptotic analysis and computation to make sure successive terms in the sum are decreasing in magnitude.

Indeed, matching our previous asymptotic analysis of the flame kernel alone, $\lim_{t\to 0^+} Y(x,t) = 0$ as the raw original flame kernel initially begins as a flat function, such zero profile repeated periodically over the lattice.

It's actually very tricky to analyze the case of $\lim_{t\to\infty} Y(x,t)$, but it does indeed converge to a bounded solution given that we have an alternating series telescoping sum with successive terms decreasing in magnitude as the flame kernels wiht increased k get farther and farther away from a particular fixed x neighborhood of interest, and it can likely be algebraically transformed into the infinite Fourier series of a triangle wave. Regardless, for brevity, via numerical analysis, the behavior can be seen in the following non-dimensional plot, where without loss of generality we can set $D = 1$ and $a = 1$ by absorbing them into the space and time variable. The asymptotic long-time solution within our domain $-a \leq x \leq a$ approaches the function $Y(x) = \frac{a}{2D}\left[1 - \frac{|x|}{a}\right]$, which consistently matches what we'd expect from the solution to the corresponding Laplace or Poisson analytical steady state condition to such heat equation by setting the time derivative to zero: $-D\frac{d^2}{dx^2}Y = \delta(x)$, making use of the framework of Singularity Functions used in Euler-Bernoulli beam theory. This situation could be interpreted as how a concentrated candle or fireplace that injects a fixed amount of power to a point in space, namely unit power at the origin here, radiates heat throughout an enclosure (from $-a \leq x \leq a$) that is in direct contact with the blizzard outside $x = \pm a$, instantly sucking out and removing any and all arriving heat energy to zero upon contact, $Y(x,t)\big|_{x=\pm a} = 0$. This makes intuitive sense because because constant candle heat injection with proportional heat removal at the endpoints is eventually able to balance out to yield a bounded solution profile upon equilibration. The solution to this Poisson equation parallels that of Gambler's ruin absorbing random walk exit location probabilities if one wants a more stochastic interpretation of this scenario. Visually, the asymptotic analysis can be more apparently seen below:

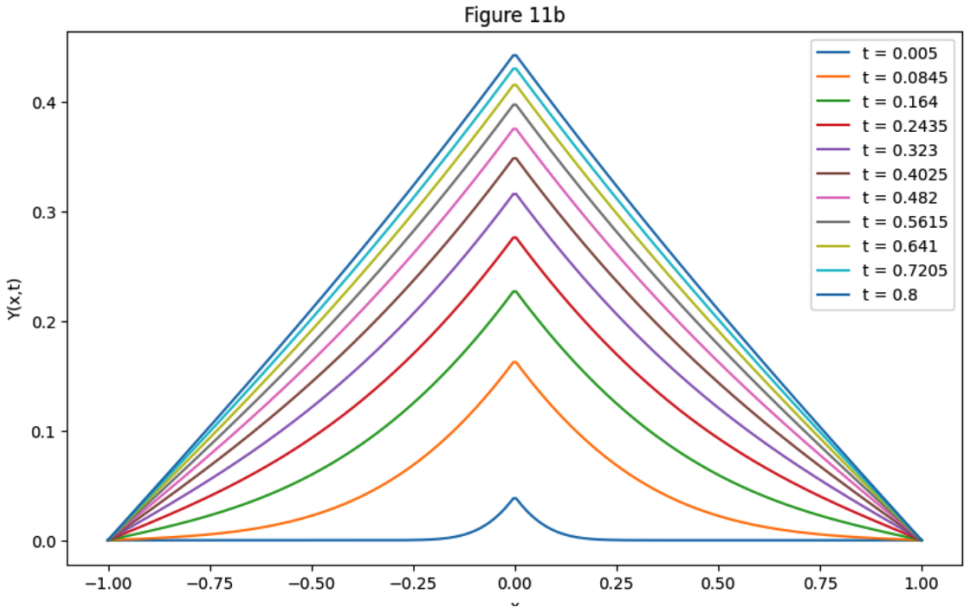

Figure 11a

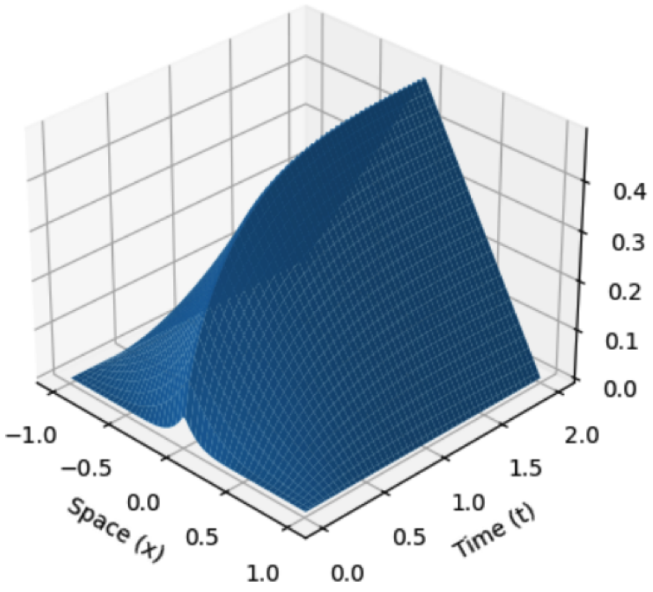

4.4.18 Diffusion with Source, Mixed Boundary Conditions

The derivation and justification of this mathematical solution, with boundary conditions of $\frac{\partial Y(x,t)}{\partial x}\Big|_{x=-a} = 0$ and $Y(x,t)\Big|_{x=a} = 0$ with candle flame source situated at the origin $x = 0$, utilizes the exact same line of reasoning as previous section by using the same pattern as before, derivation and justification omitted, but a plot included for brevity:

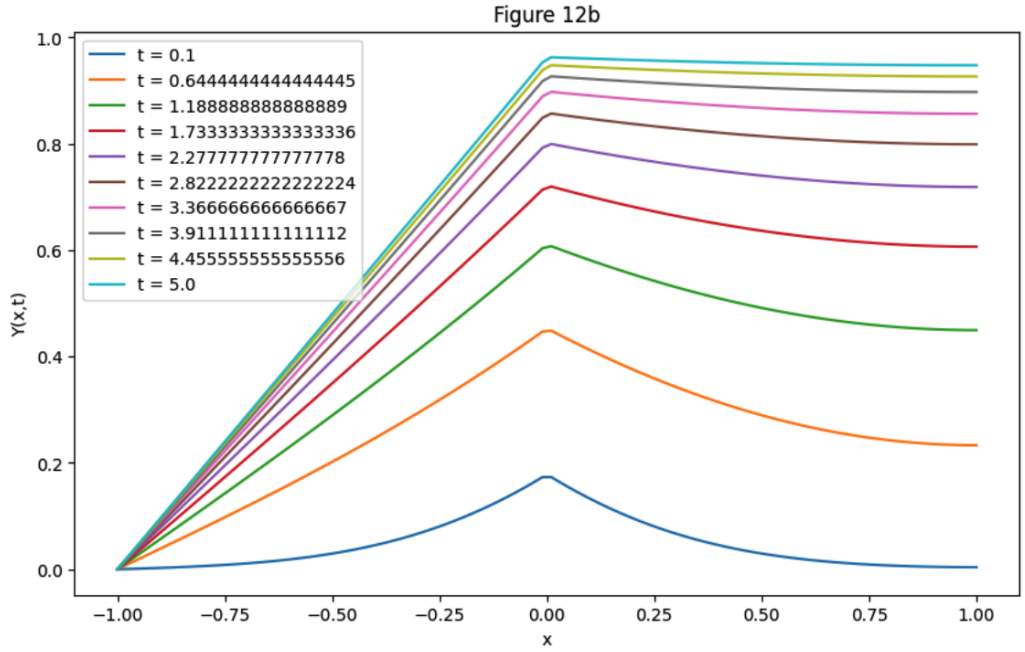

Figure 12a

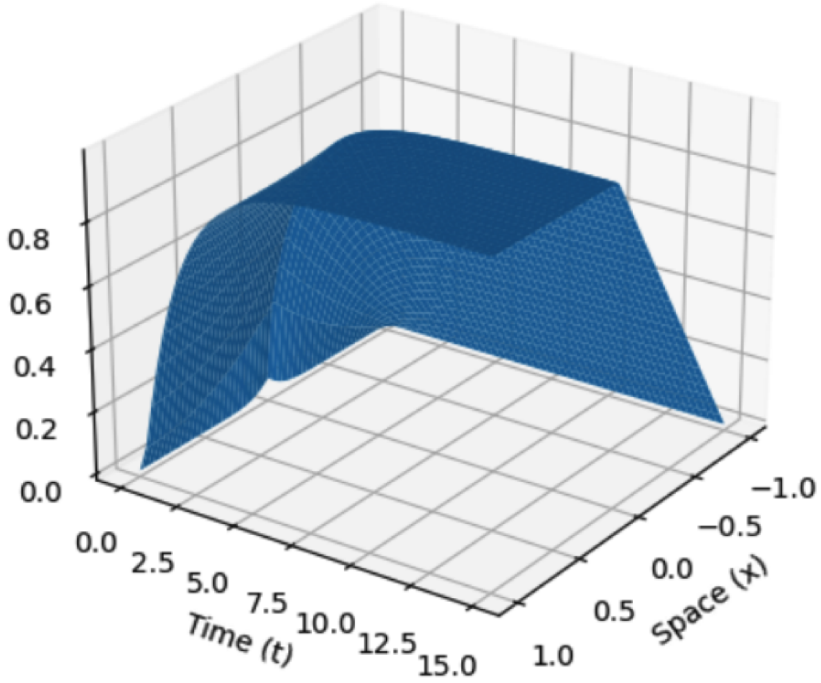

4.4.19 Drift Diffusion and Moving Source Cases

There are also ways to solve via change of variables for the PDE solution of a Brownian particle undergoing both drift and diffusion simultaneously, and is mathematically equivalent to the relevant reaction diffusion equations in question here. An analytical solution can be derived via nondimensionalization of both the spatial and time variable absorption into those dimensions via linear scaling, always allowed

hence the Buckingham Pi theorem. A direct derivation of such by using a Galilean shift, which arises from an ambient constant homogeneous velocity field in both space and time, is presented in section 4.4.20. Since the original overall underlying equation of motion PDE is shown to hold with these properties, this extends to moving "Flame-kernel" (4.4.12) sources as well by applying such Galilean shift to the solutions presented. This physical situation is intuitively characterized by tracking the temperature profile of an emanating candle flame point heat source that is translating constantly throughout space at a fixed velocity.

This is also mathematically and intuitively equivalent to constant coefficient Fokker-Planck equations that commensurately correspond to some equivalent reaction diffusion process, and as such implies that every reaction diffusion equation could be solved via Markov Chain Monte Carlo methods, which has an advantage of being massively parallelizable by simulating a giant herd of Brownian walkers and capturing a histogram of their statistical trajectories using Tukey's data analytics methods presented in his book [84]. In the large data sample size limit, hence Donsker's theorem and the Glivenko-Cantelli theorem, this functionally converges to the equivalent species concentration and temperature profiles from the corresponding deterministic setting.

4.4.20 Direct Spherical Transformation Invertible Mapping

All the solutions in cartesian coordinates can also be directly bijectively mapped to spherical coordinates, and as such, any spherical configuration of boundary conditions for such parabolic PDE in one dimension can be conformally mapped to a cartesian-land grid, which is much easier solved, and then transformed back to the originally desired spherical radial coordinate system. In spirit of the famous aphorism that says, "a problem well-stated is a problem half-solved" attributed to Charles Kettering (General Motors researcher), the forward-reverse involution mapping transformation is a useful technique that parallels many other mathematical methods, as sometimes algorithmically transforming the problem's fundamental information, into another easier domain to work with, and then solving before reverting it back, greatly facilitates tractable simplicity. This parallels the following analogous techniques: solving the Laplace PDE or elliptic type PDEs using harmonic functions in the complex plane, using the method of Laplace or Fourier frequency domain as the "passband-channel" to solve ODE's back in time domain, or invoking unitary transformations upon the Hamiltonian to resolve time-dependence and orbital transformations in quantum chemistry, and solving the dual optimization problem using the convex conjugate involution from the Fenchel-Legendre transform, and mapping an adapted stochastic process derived from the Wiener Process Ito Calculus Lemma back into the canonical form "vanilla" Brownian motion to apply its associated standard techniques before reverting back again (e.g. to GBM, Ornstein-Uhlenbeck, Langevin, Johnson-Nyquist Noise integrated to BM etc). This is particularly pertinent in our case since our droplet exhibits spherical geometry, and as such using cartesian solutions to

help us find pertinently applicable spherical solutions is very useful in our context. The way to do it is via a fractional substitution of the spatial variable, and then the spherical radial coordinate can transform into a cartesian coordinate once total derivative the chain rule cancels out from the time derivative change side of the master equation of motion for parabolic PDE and reaction diffusion systems. The interpretation is analogous to the continuous mapping theorem from topology and probability, which allows someone to use conformal mapping or the perspective function to conveniently find solutions in curvilinear or exotic geometries, and as such all ambient space from continuum mechanics can be topologically transformed into a more convenient configuration. This allows someone to solve for heat diffusing inward inside an enclosure, modeling cooking a turkey, or nutrient porous osmosis into a cell through the lipid bilayer cell wall, or the liquid phase heat transport from the flame onto the interfacial surface of the spherical LOX droplet, or even the heat transport process of hard boiling cooking an egg, everything mathematically equivalent and naturally modeled as the classic "spherical cow" in this spherical geometry setting. Additionally, this allows one to determine the hit time for Isotropic brownian motion in 3D to escape from a spherical enclosure, which indeed happens to be equivalent to the aforementioned Levy distribution discussed earlier. Not every solution exists though, we do have a pole or blow up in our mapping, and additionally we may not have a Hilbert space with compact support, and as such we really only have Bessel functions to work with in our function space– complete and orthonormal but only under a particular weighting– which constrains the support of functions in our space, analogous to the Time-Frequency Heisenberg Uncertainty inequality principle. This aids in generalizing the results and formulas that combustion researchers use with particular prior assumptions in place.

Ultimately, the culmination of the following derivation, explicitly showing the direct invertible transformation from spherical coordinates to cartesian coordinates (and back potentially due to the invertible property of such), is to allow for the *entirety* of PDE solutions reflected in 4.4 all presented in cartesian coordinates, to generalize to spherical coordinates as well, which is highly relevant to simulating a spherically-shaped liquid oxygen droplet within an isotropic coordinate system of radial symmetry.

Heat Equation's Direct and Invertible Transformation-Mapping Reduction from Spherical to Cartesian Coordinates

Notation: We use the shorthand $Y_t = \partial Y/\partial t$, $Y_r = \partial Y/\partial r$, $Y_{rr} = \partial^2 Y/\partial r^2$, etc.

Start from the radial PDE

$$y_t = D\, y_{rr} + \frac{2D}{r}\, y_r + c(r,t), \qquad r > 0.$$

Factor out diffusivity term D:

$$y_t = D\left[y_{rr} + \frac{2}{r}\,y_r\right] + c(r,t), \qquad r > 0.$$

Set

$$y(r,t) = \frac{Y(r,t)}{r}.$$

Compute derivatives using product rule (or quotient rule) and power rule:

$$\begin{aligned} y_t &= \frac{Y_t}{r}, \\ y_r &= \frac{d}{dr}\Big(\frac{Y}{r}\Big) = \frac{Y_r}{r} - \frac{Y}{r^2}, \\ y_{rr} &= \frac{d}{dr}\Big(\frac{Y_r}{r} - \frac{Y}{r^2}\Big) = \frac{Y_{rr}}{r} - \frac{2Y_r}{r^2} + \frac{2Y}{r^3}. \end{aligned}$$

Now form the spherical operator:

$$\begin{aligned} y_{rr} + \frac{2}{r}y_r &= \Big(\frac{Y_{rr}}{r} - \frac{2Y_r}{r^2} + \frac{2Y}{r^3}\Big) + \frac{2}{r}\Big(\frac{Y_r}{r} - \frac{Y}{r^2}\Big) \\ &= \frac{Y_{rr}}{r} \quad \text{(the lower-order terms cancel).} \end{aligned}$$

Substitute into the PDE: $y_t = D\left[y_{rr} + \frac{2}{r}\,y_r\right] + c(r,t)$ by using $y_t = \dfrac{Y_t}{r}$ and $\left[y_{rr} + \frac{2}{r}y_r\right] = \frac{Y_{rr}}{r}$ to plug in accordingly:

$$\frac{Y_t}{r} = D\frac{Y_{rr}}{r} + c(r,t).$$

Multiply by r (for $r > 0$) to obtain the transformed PDE:

$$\boxed{Y_t = D\,Y_{rr} + r\,c(r,t)\,.}$$

This can be further nondimensionalized:

$$\boxed{\frac{1}{D}Y_t = Y_{rr} + \frac{r}{D}\,c(r,t)\,.}$$

With $[t = \tau/D] \to [\tau = tD] \to \left[\frac{d\tau}{dt} = D\right]$ then the chain rule gives:

$$\frac{dY}{dt} = \frac{dY}{d\tau}\frac{d\tau}{dt} = \frac{dY}{d\tau}D \to$$

$$Y_t = DY_\tau$$

Substitute $Y_t = DY_\tau$ into the left hand side of the PDE:

$$D\,Y_\tau = D\,Y_{rr} + r\,c\big(r, t(\tau)\big).$$

With $t(\tau) = \frac{\tau}{D}$:

$$D\,Y_\tau = D\,Y_{rr} + r\,c\big(r, \frac{\tau}{D}\big).$$

Divide both sides by D (valid for $D \neq 0$):

$$Y_\tau = Y_{rr} + \frac{r}{D}\,c\big(r, \frac{\tau}{D}\big).$$

This now algebraically looks like a cartesian PDE, so we can define:

$\widetilde{c}(r,\tau) \;:=\; \frac{r}{D}\,c\big(r, \frac{\tau}{D}\big)$. (which contains/keeps track of original $c(r,t)$'s warping transformations)

Then the final canonical rescaled equation is

$$\boxed{Y_\tau = Y_{rr} + \widetilde{c}(r,\tau)}, \qquad \text{where } \widetilde{c}(r,\tau) \;:=\; \frac{r}{D}\,c\big(r, \tfrac{\tau}{D}\big).$$

Considering the linearity property of the original PDE $\big[y_t = D\,y_{rr} + \frac{2D}{r}\,y_r + c(r,t)\big]$, analyzing the Green's function-type impulse response (for persistent source throughout time) is insightful, so we'll define:

$$c(r,t) = C\delta(r - r_0)$$

Plugging that specific form of $c(r,t)$ into the PDE $\big[Y_\tau = Y_{rr} + \frac{r}{D}\,c\big(r, \frac{\tau}{D}\big)\big]$:

$$Y_\tau = Y_{rr} + \frac{r}{D}C\delta(r - r_0)$$

Functional analysis and measure theoretic pedantics aside, for all practical intents and purposes, the sifting property of the Dirac delta function basically implies that $\big[\frac{r}{D}C\delta(r - r_0) = 0\big] \,\forall\, [r \neq r_0]$, and when $r = r_0$ we sift out its value accordingly, yielding essentially $r \in \mathbb{R}$ domain response-functional equivalence of $\frac{r}{D}C\delta(r - r_0) = \frac{r_0}{D}C\delta(r - r_0)$, implying:

$$Y_\tau = Y_{rr} + \frac{r}{D}C\delta(r - r_0) = Y_{rr} + \frac{r_0}{D}C\delta(r - r_0)$$

$$\boxed{Y_\tau = Y_{rr} + \frac{r_0}{D}C\delta(r - r_0)}$$

Notice that this arrives at the underlying PDE for the impulse response from the "Flame-Kernel" (4.4.12) family set of solutions from the presented tour of PDEs section, which portrays the underlying inherent equivalence of the LOX lever rule 4.5.1 in both radial spherical and cartesian coordinates after our appropriate transformation-mapping. If we want the resultant solution back in spherical coordinates, we revert back using the original definition of our mapping (basically divide whatever ultimate solution you end up getting for $Y(r,t)$ by r) and then you can arrive at getting:

$$\left[\frac{Y(r,t)}{r} = y(r,t)\right]$$

As expressed in the original spherical system in $y(r,t)$ land space.

Drift-Diffusion Equation Reduction using Galilean shift

Notation: Again using $Y_T = \partial Y/\partial T$, $Y_X = \partial Y/\partial X$, $Y_{XX} = \partial^2 Y/\partial X^2$, etc.

Start from the Cartesian convection-diffusion or advection–diffusion PDE

$$y_t = a\, y_{xx} + b\, y_x + c(x,t), \qquad x \in \mathbb{R},\ t > 0,$$

with constants $a \neq 0$ and b.

Step 1: Remove diffusion prefactor by time rescaling. Define a new time variable

$$T = a\, t \quad \Longrightarrow \quad t = \frac{T}{a}, \qquad \text{and} \qquad \frac{dT}{dt} = a,$$

Step 2: Remove advection by moving frame (Galilean shift). Choose a moving spatial coordinate

$$X = x - \beta t,$$

and set, without loss of generality, by pinning to equivalence:

$$y(x,t) = Y\big(X,t\big) = Y\big(X,\, T/a\big).$$

Compute derivatives (with chain rule; $X_t = -\beta,\ X_x = 1$), differentiate both sides of our above equivalence condition by same operations:

$$y_t = Y_T\, \frac{\partial T}{\partial t} + Y_X\, X_t = a\, Y_T - \beta\, Y_X, \ \text{(total derivative with } t)$$

$$y_x = Y_X,$$

$$y_{xx} = Y_{XX}.$$

Then plug into the original PDE characterizing a globally-holding algebraic equivalence condition:

$$y_t = a\,y_{xx} + b\,y_x + c(x,t), \qquad x \in \mathbb{R},\ t > 0,$$

$$a\,Y_T - \beta\,Y_X \;=\; a\,Y_{XX} + b\,Y_X + c\big(x,t\big).$$

Collect the X first-derivative terms on the right:

$$a\,Y_T = a\,Y_{XX} + (b+\beta)\,Y_X + c\big(x,t\big).$$

To eliminate the Y_X term choose to set $\beta = -b$ and define accordingly. With that choice the Y_X terms cancel, leaving

$$a\,Y_T = a\,Y_{XX} + c\big(x,t\big).$$

Recall the relation between x and X:

$$X = x - \beta t = x + bt \quad \Longrightarrow \quad x = X - bt.$$

Replace t by T/a (since $t = T/a$) to express the source in the new variables:

$$c\big(x,t\big) = c\Big(X - b\frac{T}{a},\ \frac{T}{a}\Big).$$

Divide the PDE relationship condition through by a to get the canonical form:

$$Y_T = Y_{XX} + \frac{1}{a}\,c\Big(X - \frac{b}{a}T,\ \frac{T}{a}\Big).$$

Finally, define the transformed source

$$\widetilde{c}(X,T) \;:=\; \frac{1}{a}\,c\Big(X - \frac{b}{a}T,\ \frac{T}{a}\Big),$$

so the PDE becomes the target form

$$\boxed{Y_T = Y_{XX} + \widetilde{c}(X,T)}\,.$$

Summary of the full transform:

$$\begin{aligned}
&\text{spatial shift:} && X = x + bt \quad (\text{equivalently } x = X - bt),\\
&\text{time rescale:} && T = at \quad (\text{equivalently } t = T/a),\\
&\text{function map:} && Y(X,T) = y\big(x,t\big) = y\Big(X - \frac{b}{a}T,\ \frac{T}{a}\Big).
\end{aligned}$$

Under these maps the source transforms as

$$\widetilde{c}(X,T) = \frac{1}{a}\, c\Big(X - \frac{b}{a}T,\ \frac{T}{a}\Big).$$

Remark (intuition): the spatial shift $X = x + bt$ is a Galilean move to a frame that travels with the advection and kills the first derivative. The time rescale $T = at$ normalizes the diffusion coefficient to 1. The source is reparametrized (shifted in x) and scaled by $1/a$.

Remark (with respect to Spherical Coordinates): Since the Galilean transform creates a moving reference frame, we can no longer directly use the convenient sifting property used in the earlier derivation with the spherical coordinate conversion mapping to translate the motion.

Remark (Equivalent Black-Scholes Equation Transformation): Using the exact same flavor of techniques from this section, the Economics Nobel-Prize winning Black Scholes equation:

$$\frac{\partial V}{\partial t} + \frac{1}{2}\sigma^2 S^2 \frac{\partial^2 V}{\partial S^2} = rV - rS\frac{\partial V}{\partial S}$$

can be converted into the standard canonical heat equation.

This can be done as follows:

Start from the Black–Scholes PDE (backwards form)

$$\frac{\partial V}{\partial t} + \tfrac{1}{2}\sigma^2 S^2 \frac{\partial^2 V}{\partial S^2} = rV - rS\frac{\partial V}{\partial S},$$

where $0 \le t \le T$, $S > 0$, and r, σ are constants.

Introduce the usual change of variables

$$\tau = T - t, \qquad x = \ln\Big(\frac{S}{K}\Big) + \big(r - \tfrac{1}{2}\sigma^2\big)\tau, \qquad u(x,\tau) = e^{r\tau}\, V(S,t).$$

(Here K is a constant with dimensions of S; it only shifts x and does not affect the PDE form.)

We will express the derivatives of V in terms of derivatives of u. Because $u(x,\tau) = e^{r\tau}V(S,t)$ and x depends on τ, take care with chain rules.

1. Time derivative. Since $\tau = T - t$ we have $\partial_t = -\partial_\tau$. Also, at fixed S,

$$\frac{\partial u}{\partial \tau}\Big|_S = u_\tau + x_\tau\, u_x = u_\tau + \big(r - \tfrac{1}{2}\sigma^2\big)u_x.$$

Because $V = e^{-r\tau}u$,

$$V_\tau = e^{-r\tau}\big(u_\tau + (r - \tfrac{1}{2}\sigma^2)u_x - ru\big),$$

and therefore (using $V_t = -V_\tau$)

$$\boxed{V_t = e^{-r\tau}\big(ru - u_\tau - (r - \tfrac{1}{2}\sigma^2)u_x\big).}$$

2. Spatial derivatives. From $x = \ln(S/K) + \cdots$ we have $\partial x/\partial S = 1/S$. Hence

$$V_S = e^{-r\tau}\frac{1}{S}u_x, \qquad V_{SS} = e^{-r\tau}\frac{1}{S^2}\big(u_{xx} - u_x\big).$$

3. Substitute into Black–Scholes. Compute LHS and RHS (factor out $e^{-r\tau}$):

LHS:

$$V_t + \tfrac{1}{2}\sigma^2 S^2 V_{SS} = e^{-r\tau}\Big(ru - u_\tau - (r - \tfrac{1}{2}\sigma^2)u_x + \tfrac{1}{2}\sigma^2(u_{xx} - u_x)\Big).$$

RHS:

$$rV - rSV_S = e^{-r\tau}\big(ru - ru_x\big).$$

Equate LHS and RHS and cancel the common factor $e^{-r\tau}$ and the ru terms. The remaining terms give

$$-u_\tau - (r - \tfrac{1}{2}\sigma^2)u_x + \tfrac{1}{2}\sigma^2 u_{xx} - \tfrac{1}{2}\sigma^2 u_x = -ru_x.$$

Collect the u_x coefficients:

$$-u_\tau + \tfrac{1}{2}\sigma^2 u_{xx} + \big[-(r - \tfrac{1}{2}\sigma^2) - \tfrac{1}{2}\sigma^2 + r\big]u_x = 0.$$

The bracket vanishes, so the first-derivative terms cancel exactly. Thus we obtain the canonical heat equation

$$\boxed{u_\tau = \tfrac{1}{2}\sigma^2\, u_{xx}}.$$

This completes the (short) derivation: under the substitutions above the Black–Scholes PDE is equivalent to a heat equation in (x, τ)-coordinates.

4.4.21 ODE when PDE too Complicated

Since nonlinearities arise from physics, deriving closed-form expressions can be impossible, and convergence to settling to a steady state equilibrium cannot be taken for granted. As such, as test functions, sometimes we are left with using the spherical Bessel eigenfunctions for verification of time dynamics in this domain. This is nice for bounded or constrained functions or "bounded" orbital states as referenced in quantum mechanics, and in fact is the solution for quantum dots or the hard wall potential of a synthetic atom, but it's hard to fit some generalized framework for any arbitrary boundary condition or function behavior. If we know that the diffusive term in the parabolic PDE is strictly non-negative, then this implies a positive semidefinite Hessian with dominant eigenvalues, and implies via some energy or convex dual entropy argument from functional convex analysis, that the solution will be some sort of Laplace equation minimal surface solution at which will eventually be arrived via a gradient descent flow. In the flavor of the philosophy of E.T. Jaynes, a simple example is how an expanding Gaussian profile maximizes entropy and satisfies the aforementioned traits.

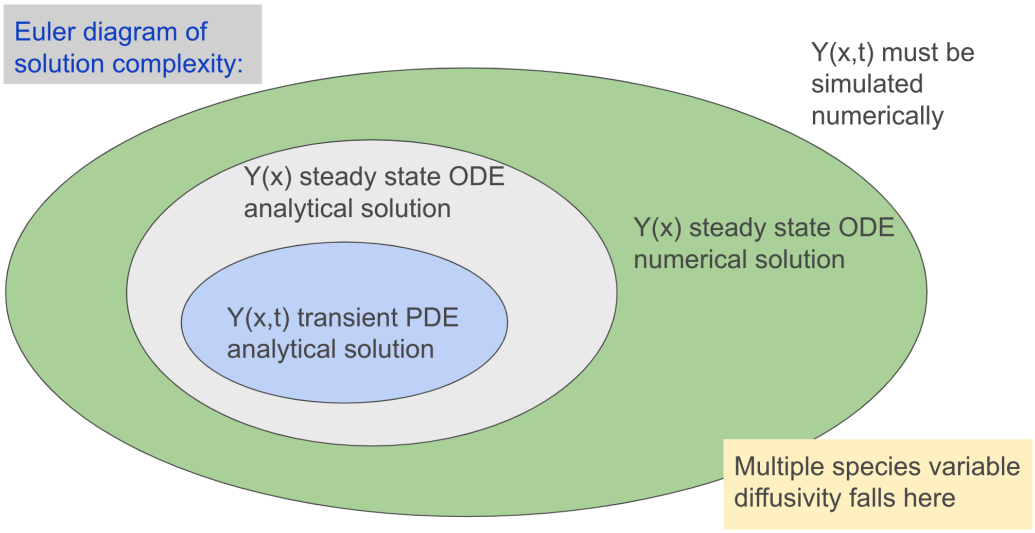

Radial Reduction of the Advection–Diffusion–Reaction Equation with Variable Diffusivity

Notation: We write partial derivatives in shorthand:

$$c_t = \frac{\partial c}{\partial t}, \qquad c_r = \frac{\partial c}{\partial r}, \qquad c_{rr} = \frac{\partial^2 c}{\partial r^2}, \qquad D_r = \frac{\partial D}{\partial r}.$$

1. Starting vector PDE

We begin with the general advection-diffusion-reaction equation, which is the Eulerian form obtained by expanding the material derivative $\frac{\mathcal{D}c}{\mathcal{D}t} = \nabla \cdot (D\nabla c) + R$:

$$c_t = \nabla \cdot \big(D\nabla c\big) \; - \; \vec{v} \cdot \nabla c \; + \; R(\mathbf{x}, t),$$

where $D = D(\mathbf{x}, t)$ may vary in space and time, and $\vec{v}(\mathbf{x}, t)$ is a prescribed velocity field (could be varying with space and time as well.)

2. Spherical symmetry assumptions

Assume:

$$c(\mathbf{x}, t) = c(r, t), \qquad D(\mathbf{x}, t) = D(r, t), \qquad \vec{v}(t) = v(t)\,\hat{r},$$

so advection is purely radial and magnitude-wise homogeneously uniform throughout space, but perhaps dynamically varying with time, akin to a deterministically fluctuating and varying Federal Reserve interest rate after applying Girsanov's theorem to change the probability measure from stochastic stock prices undergoing geometric Brownian motion back into standard canonical "vanilla" Brownian motion, eliminating such dynamic drift bias.

Under spherical symmetry, the Laplacian term becomes

$$\nabla \cdot \big(D\nabla c\big) = \frac{1}{r^2}\frac{\partial}{\partial r}\big(r^2 D c_r\big)\,.$$

Thus the PDE becomes

$$c_t = \frac{1}{r^2}\frac{\partial}{\partial r}\big(r^2 D\, c_r\big) \; - \; v(t)\, c_r + R(r, t).$$

3. Expanding the diffusion term

We now expand the divergence explicitly using the product rule. First:

$$\frac{\partial}{\partial r}\big(r^2 D\, c_r\big) = 2r\, D\, c_r + r^2\, \frac{\partial}{\partial r}(D\, c_r).$$

Expand the inner derivative using the chain rule:

$$\frac{\partial}{\partial r}(D\, c_r) = D_r\, c_r + D\, c_{rr}.$$

Hence

$$\frac{\partial}{\partial r}\big(r^2 D\, c_r\big) = 2r D c_r + r^2\,(D_r c_r + D c_{rr})\,.$$

Divide by r^2:

$$\frac{1}{r^2}\frac{\partial}{\partial r}\left(r^2 D\, c_r\right) = \frac{2}{r} D c_r + D_r c_r + D c_{rr}.$$

Rearrange:

$$\frac{1}{r^2}\frac{\partial}{\partial r}\left(r^2 D\, c_r\right) = D\, c_{rr} + \left(\frac{2D}{r} + D_r\right) c_r.$$

4. Final radial PDE

Insert this back into the spherical PDE with advection:

$$c_t = D\, c_{rr} + \left(\frac{2D}{r} + D_r\right) c_r - v(t)\, c_r + R(r,t).$$

Combine first-derivative coefficients:

$$\boxed{c_t = D\, c_{rr} + \left(\frac{2D}{r} + D_r - v(t)\right) c_r + R(r,t).}$$

5. Optional renaming of the dependent variable

If one prefers to work with a new dependent variable $Y(r,t) = c(r,t)$, then the PDE takes the form

$$\boxed{Y_t = D(r,t)\, Y_{rr} + \left(\frac{2D(r,t)}{r} + D_r(r,t) - v(t)\right) Y_r + s(r,t),}$$

where $s(r,t)$ is simply $R(r,t)$ written in new notation.

6. Remarks

Observe that for numerical simulation in the finite difference framework, an estimate for D_r must be performed, also implying the evolution of the PDE depends on both D and D_r throughout space and time. The key takeaway of this derivation of the fundamental parabolic PDE equation of motion underlying our Finite Difference Method numerical solver– where v_s in particular is the Stefan-Flow or Stefan Velocity from LOX evaporative blow-off to the flame region domain– is to observe the sophisticated nature of this equation, with intricate variable dependencies and intertwining complexity, often making it intractable to analytically solve, even for the ODE steady-state configuration case when invoking the stationary condition $Y_t = 0$.

An interesting aside is that the mathematical formulation derived in this chapter's section can be directly and conveniently applied to atmospheric meteorology and weather climate geophysics, where integration with the concentric spherical geometric setup of a radially symmetric solid Earth encased by its ambient surrounding gaseous atmosphere, is quite similar to our situation, a configuration with a LOX

droplet within a surrounding flame region where we simulate the gasdynamics of H_2 combustion, which as clean energy does not have a carbon footprint, conducive to the objectives and goals of environmental sustainability engineering endeavors. In fact, in the mid 20th century, 2021 Physics Nobel Prize Laureate Syukuro Manabe numerically simulated the atmospheric gasdynamics in both vertical-radial altitude and latitude coordinates, to help facilitate accurately predicting the eventual future empirical observational trends attributed to the scientific study of global warming and climate change (Manabe 1961, 1964, 1965). [92, 93, 94]

4.5 Multiple Species Scenario

During the pioneering age of the interdisciplinary foundations of cybernetics in the mid 20th century, renowned Alan Turing published his distinguished seminal paper *The Chemical Basis of Morphogenesis* (1952) [95], proposing the first mathematical theory of pattern formation in biology, connecting disparate intellectual fields in a coherent manner. Arising from Turing instabilities (or diffusive-thermal instability in combustion literature) in reaction diffusion systems, surprisingly complex *Turing Patterns* can emerge to form biological structures resembling fingerprints, zebra stripes, and cow spots, just as Zeldovich (1944) [96] observed with cellular structures forming in lean hydrogen flames. With many parallels to chaos, information, and pattern theory, these examples portray the nuanced sophistication of possible behaviors deriving from multiple species reaction diffusion systems, and finding any sensible trend is a significant matter.

4.5.1 LOX Lever Rule: Novel Mathematical Result

Theoretical Underpinnings behind Derivation, Justification of Mathematical Mechanics, and Relevant Applications

The LOX lever rule is an analytical expression for both the flame standoff distance and the peak flame temperature for any configuration of fuel reservoir (stationarily fixed and not moving, diagram left), oxidizer reservoir (stationarily fixed and not moving, diagram right), stoichiometry (fixed "pecuniary exchange rate" quantities translating between reactants and products), and species diffusivities (constant throughout space and time for such species), all indicated in the illustrated visual depiction diagram below. Mathematically equivalently, we can generalize the flame standoff distance and peak flame temperature to the correspondingly analogous quantity from any reactant to product chemical reaction transformation under instantaneous chemical kinetics. Our assumptions imply full forward propagation upon mutual coexistence contact, demonstrating that in this infinitely high Damkohler number regime setting, both fuel and oxidizer instantly form product (at the stoichiometric exchange rate) upon touching. The time-dependent transient convergence settling to such steady state stationary configuration can be constructed using the "Flame-Kernel" PDE solutions derived earlier in section 4.4.

Furthermore, it can be formulated in a completely non-dimensional manner, determined by purely proportional value ratios alone based on relevant physical quantities, and even directly extended to the spherical radial coordinate regime via conversion using the methods from 4.4.20, which provides a solid rule of thumb (for both cartesian and spherical ambient geometries) when performing comparative statics analysis for how perturbative changes to the associated variables affect the ultimate final settling configuration of the flame standoff distance and height peak flame temperature, handy especially when the equations become more nonlinear and increase in nuanced complexity in terms of transport properties.

The LOX-Lever rule can be derived via the continuity / constitutive relations from continuum mechanics and algebraically solving directly for the first order condition for stability and stationarity by "teeter-totter" leverage-balancing Fick's law or Fourier's law for diffusive flux / transport and using a sort of "Envelope Theorem" flavor of solution Ansatz where the profiles osculate right at the intersection at the Tatonnement region of their mutual Edgeworth Box, using an analogy from economics. On that note via an interesting comparative statics analysis, notice and observe that the final outputs of the various calculations below only depend on non-dimensional ratios of the relevant physical parameters. Additionally, the balancing act standoff fulcrum point here upon the seesaw between the Fuel and Oxidizer reservoirs is very akin to finding the centroid of an empirical probability distribution from Quantile Regression, that structurally (by using slack variables) can be converted to a Linear Programming optimization problem that can be tackled using Dantzig's algorithm and the like. A modeling nuance worth clarifying is that we do not account for dynamic diffusivities varying through space or with mixture composition; we always assume the fuel inherently moves like just pure fuel itself and has a fixed intrinsically associated diffusivity attributed to such substance, and likewise with the oxidizer and product/temperature transport as well. This assumption remains mostly reasonable, since upon steady state, the key regions tend to be mostly pure anyways as seen in the LOX Lever rule diagram below.

To clarify the allusion's etymology, the naming of the LOX Lever Rule is inspired by the actual classical thermodynamic lever rule for binary phase equilibria, in which the position of a composition point along a tie line determines relative phase fractions, employed inbetween the solidus and liquidus lines upon a binary or eutectic phase diagram, with horizontal axis denoting mass fraction of substance A versus substance B in the mixture, and the vertical axis representing the system's temperature. Analogously here with our LOX Lever rule, we can determine shape characteristics of a resultant steady temperature or species profile derived from fast chemical combustion of a diffusion flame, where the flame standoff distance and peak flame temperature is determined by a flux-balance "lever" between fuel and oxidizer sides. This is not to be confused with the Gibbs phase rule, with eerily uncanny mathematical resemblance to Euler's formula for polyhedra, none of which are actually directly related to each other.

LOX Lever Rule Pseudocode Summary and Visual Depiction

$$\boxed{\textbf{Balanced Equilibrium Settling Point's Proportional Arm-Length}}$$

$$\left[\left[\begin{array}{c}\text{Cartesian:}\\ \lambda = \frac{1}{1+\left(\frac{a}{b}\right)\left(\frac{B}{A}\right)\left(\frac{D_O}{D_F}\right)} L\end{array}\right] \quad \left[\begin{array}{c}\text{Spherical:}\\ \lambda = \frac{1}{1+\left(\frac{a}{b}\right)\left(\frac{r_{\max} B}{r_{\min} A}\right)\left(\frac{D_O}{D_F}\right)} L\end{array}\right]\right] \tag{56}$$

$$\begin{array}{ll} & \textbf{Pseudocode Routine for Computing Flame Point Location and Height} \\ 1. & \text{input } [A, B, a, b, c, D_F, D_O, D_P, x_{\min}, x_{\max}] \rightarrow \\ 2. & \text{if spherical, then update: } A \rightarrow x_{\min} A, B \rightarrow x_{\max} B \\ 3. & d = \frac{\left[x_{\max} + \left[\frac{a}{b}\frac{B}{A}\frac{D_O}{D_F}\right] x_{\min}\right]}{1+\left[\frac{a}{b}\frac{B}{A}\frac{D_O}{D_F}\right]} \\ 4. & \text{if spherical, then update: } D_P \rightarrow dD_p \\ 5. & h = \frac{\left[\frac{D_F A}{a}\right]+\left[\frac{D_O B}{b}\right]}{\left[\frac{D_P}{c}\right]} \frac{\left[\frac{a}{b}\frac{B}{A}\frac{D_O}{D_F}\right]}{\left[1+\left[\frac{a}{b}\frac{B}{A}\frac{D_O}{D_F}\right]\right]^2} \\ 6. & \text{output } [d, h] \end{array} \tag{57}$$

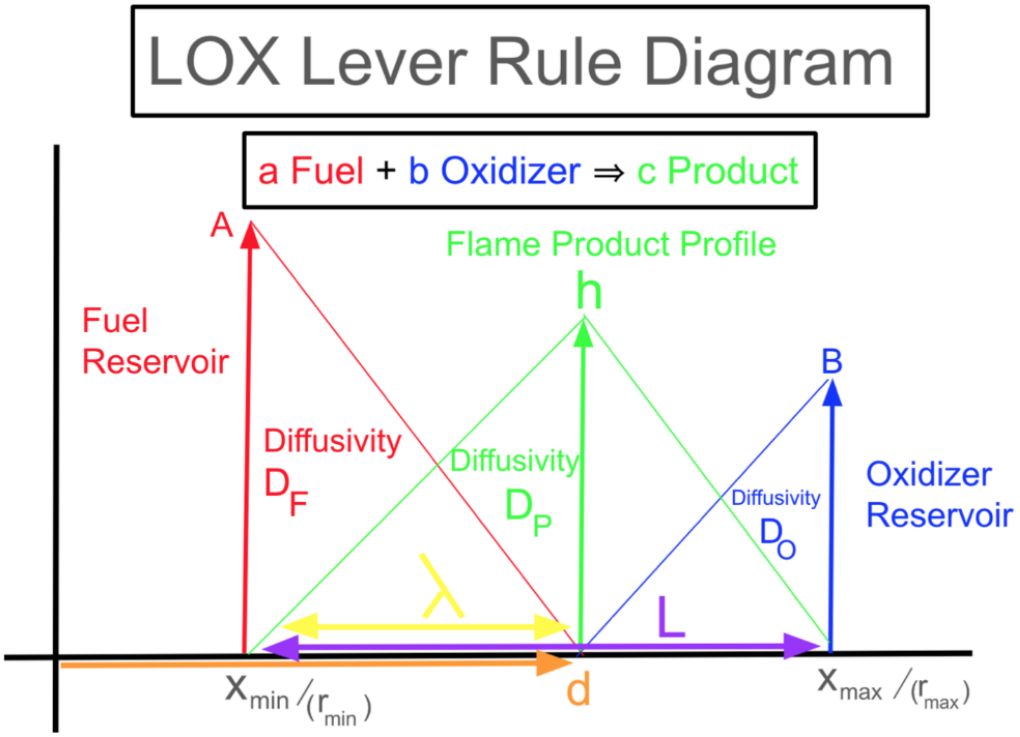

4.6 Numerical Analysis Theory

Why Use a Numerical Scheme?

Sometimes our mathematical models for describing scientific technology, physical systems, and social phenomena become too complicated for an analytical closed-form mathematical solution to exist,

meaning it cannot be expressed in standardly known math functions used in "Folk" common practice. Sometimes they exist but are just extraordinarily tedious to compute by hand, such as the manipulating the astronomical tensors in Einstein's field equations which tend to have higher spacetime geometric complexity compared to the tensors from continuum mechanics. Sometimes the solutions that can be found by hand are in a difficult to digest form, such as those proposed earlier involving intractable infinite sums, which is why providing bounds and approximations for back-of-the-envelope type calculations tend to be useful in practice. This Euler diagram of what mathematical science we can do parallels that of the ergodic hierarchy, or the increasing structural complexity of Boolean to propositional Logic, onwards to First Order Logic then Set Theory. As such, just because such function that satisfies our differential equations cannot be expressed in our standard mathematical notation language, doesn't mean we are limited to having zero accessible information about the shape of such. Hence the Nyquist-Shannon sampling theorem from digital signal processing, we are often able to discretely sample our function at ever higher resolution and frequency to get a strong sense of how our function behaves. Horizontal resolution among the spatial grid for functional signal sampling is the dominant limiting factor compared to pinpoint precise vertical "bit-depth" resolution, so concern is focused on sampling frequency restraints as opposed to anything related to quantization additive noise arising from the Lloyd-Max conditions. Just like how a continuous band-limited audio signal sampled above the Nyquist Frequency threshold can theoretically be perfectly reconstructed via the Whittaker-Shannon interpolation formula, we can attempt to achieve similar results with numerical solutions to differential equations, provided sufficient coarse-graining of our grid mesh or finite element approximation scheme. As such, this allows a mathematical workaround for tricky problems by solving for the sample points of our function at discrete points in time and space, or alternatively a discrete set of weights of basis functions such as Fourier or Wavelet bases. This is the motivation behind the field of scientific computing and numerical analysis, where hopefully sufficient course graining of discrete computer schemes will approach continuous behavior in the infinitesimal calculus limit. Examples of occasions when such methodology is implemented is in the context of the Hartree-Fock method for approximating the many-electron molecular Schrodinger Equation, or solving the Black-Scholes Equation numerically for exotic options pricing.

4.6.1 Process of Converting to Numerical Scheme

A preliminary discrete numerical conversion of our continuous partial differential equation is necessary to be able to compute numerical solutions, as unlike symbolic computing since we've resorted to numerical methods, the computer can only store a finite list or array of numbers. Similar to the correspondence principle bridging classical physics to quantum physics, we must ensure that in the limit, our discrete representation of our solution and finite approximation to our continuous system consistently matches. As such, we utilize the discrete calculus of differences to approximate the system's dynamics to derive

the underlying corresponding finite-difference scheme.

4.6.2 Derivation of Finite Difference Scheme

We start with the current instantaneous fundamental equation of motion or, where the current change with time as the present update iteration to our system, is isolated on the left hand side of the equation:

$$\frac{\partial Y}{\partial t}\Big|_{t=\text{right now}} = a(x)\frac{\partial Y^2}{\partial x^2} + b(x)\frac{\partial Y}{\partial x} + c(x) \tag{58}$$

Notice that because we are looking at only an infinitesimally thin slice of time of $t =$ "right now" and the update only depends on the present configuration alone, for our practical purposes, the right hand of the side of the system does not actually depend explicitly on time, and only depends on transformations of the information describing the current state of our system, which hopefully explains our notation, detailed below:

$a(x,t) \rightarrow a(x) \geq 0$: Instantaneous Local Diffusion

$b(x,t) \rightarrow b(x)$: Instantaneous Local Drift

$c(x,t) \rightarrow c(x)$: Instantaneous Local Source/Sinks

Intuitively, $a(x) \geq 0$ represents how much the concentration of mass at such point currently momentarily spreads out. $b(x)$ characterizes how mass at that point momentarily undergoes translation motion to shift along the x axis. Finally, $c(x)$ characterizes instantaneously how much mass at such point gets injected or removed from the system. As such, all three factors will play a role in updating our system at its current present state.

Following the Method of Finite Differences, we can now discretize the system with a time and space coordinate mesh grid as follows:

$Y(i\Delta x, n\Delta t) \rightarrow Y_i^n$

$a(i\Delta x), b(i\Delta x), c(i\Delta x) \rightarrow a_i, b_i, c_i$

And using such we now rewrite our equation of motion in Finite Difference Form:

$$\frac{Y_i^{n+1} - Y_i^n}{\Delta t} = \frac{a_i}{(\Delta x)^2}[w\left[Y_{i+1}^{n+1} - 2Y_i^{n+1} + Y_{i-1}^{n+1}\right] + (1-w)\left[Y_{i+1}^{n} - 2Y_i^{n} + Y_{i-1}^{n}\right]] + \frac{b_i}{2\Delta x}[v\left[gY_{i-1}^{n+1} + qY_i^{n+1} + sY_{i+1}^{n+1}\right] + (1-v)\left[gY_{i-1}^{n} + qY_i^{n} + sY_{i+1}^{n}\right]] + c_i \tag{59}$$

Collecting similar terms, we can rewrite this expression using vector inner product or dot product notation as follows:

$$\begin{bmatrix} \frac{-a_i w}{(\Delta x)^2} - \frac{b_i v g}{2\Delta x} & \frac{1}{\Delta t} + \frac{2wa_i}{(\Delta x)^2} - \frac{b_i vq}{2\Delta x} & \frac{-a_i w}{(\Delta x)^2} + \frac{-b_i vs}{2\Delta x} \end{bmatrix} \begin{bmatrix} Y_{i-1}^{n+1} \\ Y_i^{n+1} \\ Y_{i+1}^{n+1} \end{bmatrix} = \begin{bmatrix} \frac{a_i(1-w)}{(\Delta x)^2} + \frac{b_i(1-v)g}{2\Delta x} & \frac{1}{\Delta t} - \frac{2a_i(1-w)}{(\Delta x)^2} + \frac{b_i(1-v)q}{2\Delta x} & \frac{a_i(1-w)}{(\Delta x)^2} + \frac{b_i(1-v)s}{2\Delta x} \end{bmatrix} \begin{bmatrix} Y_{i-1}^{n} \\ Y_i^{n} \\ Y_{i+1}^{n} \end{bmatrix} + c_i \tag{60}$$

Since this is a linear equation, we can multiply both sides by $2(\Delta x)^2$:

$$\begin{bmatrix} -2a_i w - b_i v g \Delta x & \frac{2(\Delta x)^2}{\Delta t} + 4wa_i - b_i vq\Delta x & -2a_i w - b_i vs\Delta x \end{bmatrix} \begin{bmatrix} Y_{i-1}^{n+1} \\ Y_i^{n+1} \\ Y_{i+1}^{n+1} \end{bmatrix} = \begin{bmatrix} 2a_i(1-w) + b_i(1-v)g\Delta x & \frac{2(\Delta x)^2}{\Delta t} - 4a_i(1-w) + b_i(1-v)q\Delta x & 2a_i(1-w) + b_i(1-v)s\Delta x \end{bmatrix} \begin{bmatrix} Y_{i-1}^{n} \\ Y_i^{n} \\ Y_{i+1}^{n} \end{bmatrix} + 2(\Delta x)^2 c_i \tag{61}$$

We pause at our intermediate result here: observe that we have isolated the future time configuration corresponding to the vertical vector with $n+1$'th superscript on the left hand side, in terms of our present time configuration corresponding to the vertical vector with n'th superscript on the right hand side. This implies that we can indeed solve this linear system for the unknown future state purely in terms of its present state using Gauss-Jordan Elimination to compute the Row-Reduced Echelon Form (RREF), and indeed we've eliminated enough degrees of freedom such that this mathematical structure preserves how the current configuration Y_*^n is a "Sufficient Statistic" completely containing the necessarily required information to figure out Y_*^{n+1} to update.

4.6.3 Defining Numerical Parameters

The previous expression left a lot of fine-tuning parameters free to allow "on-site" adjustment of numerical scheme to fit the task at hand in practice, and as such one can experiment playing around with tweaking these parameters to see which combination provides the best overall results, or performs the best for whichever niche purposes purposes, as all of these parameters have a trade-off of various benefits. Regardless, they all equivalently converge to the true function in the continuum limit for $\Delta t, \Delta x \to 0$ infinitesimally small time step size and coordinate grid spacing.

Table of Adjustable Parameters

Altering t temporal-dimension/aspect of numerical scheme:

$$\begin{bmatrix} & \text{fully implicit} & \text{fully explicit} & \text{Crank-Nicolson} & \text{Additive Runge-Kutta} \\ \text{tune drift } \vec{b} \to v: & 1 & 0 & \frac{1}{2} & v \in [0,1] \\ \text{tune diffusion } \vec{a} \to w & 1 & 0 & \frac{1}{2} & w \in [0,1] \end{bmatrix} \tag{62}$$

Altering x spatial-dimension/aspect of numerical scheme:

$$\begin{bmatrix} \left[\text{centered difference scheme approximation of } \frac{\partial Y}{\partial x}\right] \to \begin{bmatrix} g \\ q \\ s \end{bmatrix} = \begin{bmatrix} -1 \\ 0 \\ 1 \end{bmatrix} \\ \left[\text{right upwind scheme of } \frac{\partial Y}{\partial x}, \text{ usually for } \vec{b} \geq 0\right] \to \begin{bmatrix} g \\ q \\ s \end{bmatrix} = \begin{bmatrix} 0 \\ -2 \\ 2 \end{bmatrix} \\ \left[\text{left upwind scheme of } \frac{\partial Y}{\partial x}, \text{ usually for } \vec{b} \leq 0\right] \to \begin{bmatrix} g \\ q \\ s \end{bmatrix} = \begin{bmatrix} -2 \\ 2 \\ 0 \end{bmatrix} \\ \left(\text{ second order upwind scheme of } \frac{\partial Y}{\partial x} \to \cdots \text{ various coefficient choices }\right) \end{bmatrix} \tag{63}$$

Before we get into the actual meaning of each coefficient in the next section, observe that indeed each

unknown numerical scheme parameter, independent of any actual system physical state measurements, is defined by one of the choices above, meaning the the rest of the variables are known quantities, thereby eliminating the possibility of an undetermined system. Additionally, considering we know the present configuration $[Y_i^n]\,\forall i$, the present state motion dynamics $[a_i, b_i, c_i]\,\forall i$, and the unknown future state Y_*^{n+1} is the same size from the same number of grid points for dimensions, we ultimately have a bijective mapping of sorts, eliminating the possibility of an over-determined system as well. This implies that after careful choice of numerical scheme fine-tuning tweaking coefficients, mathematically we have enough information to update and are good to go.

4.6.4 Meaning of Numerical Parameters and Interpretation of Coefficients

The big picture of any finite difference scheme is that it is ultimately a direct translation of the original underlying equation's relationship into the components' respective discrete local approximations, hopefully representative of the corresponding continuous function's approximate behavior. As such, there are some grammatical nuances to such "word-by-word" flavor of translation, as a simile to a professional native speaker idiomatically picking up on such custom cues in context, analogous to the subtle expressive differences between various synonyms and prepositional phrases in spoken language. Hopefully this characterizes the importance of including a brief description of how these numerical scheme parameters work in this section, as this is an important aspect of the pipeline of translating physics to mathematical equations and then into computational numbers.

4.6.5 Time-Weighting v/w Hyper-parameters

v and w are coefficients between 0 and 1 that characterize the relative time-weighting scheme for determining which approximation to the present first and second spatial derivative to include in our equation for determining the next future update step. To illustrate how and why this is done, imagine if we were tasked to provide a number for the quantitative estimate of "the average representative shoe size of a household". Just like the epistemology of mathematical decision theory, there are many equally reasonably justifiable methodologies and philosophies of how to determine the most appropriate estimate. In effect, in such grand strategy space, there's usually never a clear winner that globally dominates for any game played, and everything comes with its own set of unique situational trade-offs. In the Bayesian framework this becomes an admissible decision rule that is Pareto efficient with respect to a chosen loss function, emphasis on the "chosen" indicating there is always some amount of human-opinionated subjectivity upon which mathematical premises and information processing assumptions are used for modelling. Given this thought process, there's not an immediate clear winner if federal census personnel by policy report the equal weighted sum of all shoes found in a household's shoe cabinet including the baby's, provide stratification based on gender, or decide to put higher weight emphasis from the first-

born to capture a measure of what to expect from adult foot size, as there is some subjectivity and wiggle room for interpretation in executing the loosely-worded arbitrary command of "estimating the average representative household shoe size." As such, this is exactly what particular values of v and w do, they provide the convex mixture or weighting scheme slider for "fading in and out" in how we relatively account for the present concentration profile or future concentration profile for computing the first and spatial derivatives.

When we determine a strategy for how to computationally move from the present to the future state, $v = 1$ means the the first spatial derivative is algebraically representatively captured by only information from the future configuration in a "fully implicit" scheme, $v = 0$ means the the first spatial derivative is algebraically representatively captured by only information from the present configuration in a "fully explicit" scheme, and $v = 0.5$ means an equally weighted average mixture between the two.

When we determine a strategy for how to computationally move from the present to the future state, $w = 1$ means the the second spatial derivative is algebraically representatively captured by only information from the future configuration in a "fully implicit" scheme, $w = 0$ means the the second spatial derivative is algebraically representatively captured by only information from the present configuration in a "fully explicit" scheme, and $w = 0.5$ means an equally weighted average mixture between the two.

At the end of the day, it is up to the computer numerical software user to decide when or how in time to account for capturing spatial derivative information when running the simulation propagating forward, which is done through choice of v, w. For our purposes we investigated all v, w combinations, but excluded Additive Runge-Kutta cases as they are not common in practice and don't have any particular benefit compared to only considering the others.

Noticeably conveniently, whichever choice is implemented at the end of the day, there's surprisingly very little that can go wrong in the continuum limit, as only for a very few particularly niche edge cases of $v \neq 0$ did numerical solution simulations start slightly deviating from what analytical theory would predict.

4.6.6 Spatial-Weighting $g/q/s$ Hyper-parameters

Just like with the Time-Weighting parameters previously, there's some amount of flexibility for pinpointing spatially where in question one should "take measurements" so to speak, to best compute the first order spatial derivative of our concentration profile function, to use such information to plug into our update computational routine. To characterize this notion, similar to the the thought experiment from Hotelling's model firm location game theory model, an urban planner would likely want to place a gas station on the side of the highway that has the most traffic, but it is up to interpretation which side is more actually more important in practice considering traffic flow might depend on time of day or season, and in either case it's not a huge problem for motorists to make a simple U-turn for a quick pit stop.

As such, the decision policy for picking $g/q/s$ values is very similar and can be somewhat situationally dependent, but in any case it's difficult to go wrong in the continuum limit. $[g, q, s] = [-1, 0, 1]$ is the centered difference approach where our local spatial derivative slope at such location is computed by from the left-neighboring point and the right-neighboring point. $[g, q, s] = [0, -2, 2]$ is the right upwind scheme, usually attributed to positive convective drift values of $\vec{b} \geq 0$, where our local spatial derivative slope at such location is computed where we are situated along with the right-neighbor juxtaposed point. $[g, q, s] = [-2, 2, 0]$ is the left upwind scheme, usually attributed to negative convective drift values of $\vec{b} \leq 0$, where our local spatial derivative slope at such location is computed where we are situated along with the left-neighbor juxtaposed point. Noticeably conveniently, each choice of measurement policy does a solid job of capturing the local first-derivative behavior of our concentration profile. While there exist second order upwind schemes for different choices of coefficients, the plain "vanilla" flavored centered difference scheme always seems to sufficiently work fine for any purpose.

4.6.7 Arranging to Appropriate Mathematical Form

After fully deriving our discretized equation of motion for our finite difference scheme, we are now ready to rearrange the expressions involved to reformulate this as a computational linear algebra matrix equation, as this enormously facilitates computation and implementation on a computer through programming.

Observe, from a topological sort of the elements defined by the discrete profile values Y_i^n, each mesh grid point only depends on its direct neighbors in space and time, thereby eliminating the majority of graph connectivity from its associated adjacency matrix, meaning the adjacency matrix will be quite sparse unlike that of a mostly saturated edge matrix representing a more fully-connected graph with each vertex of high degree. Additionally, not only is the matrix sparse, but connectivity restricted to neighboring elements in space and time allows for further convenient structural simplification past the sparse structure. Given that each Y_i^n can only depend juxtaposed elements that are in direct contact in time and space (or differing by one in terms of index value i, j), this imposes a special tridiagonal structure of all matrices involved with representing this aggregate linear system, which can be rewritten as the following:

$$[\text{ Left Tridiagonal Matrix}]\, \vec{Y^{n+1}} = [\text{ Right Tridiagonal Matrix }]\, \vec{Y^n} + 2(\Delta x)^2 \vec{c} \tag{64}$$

$$\overset{N\times N}{\begin{bmatrix} B_0^L & C_0^L & 0 & 0 & 0 & 0 & \cdots & 0 \\ A_1^L & B_1^L & C_1^L & 0 & 0 & 0 & \cdots & 0 \\ 0 & A_2^L & B_2^L & C_2^L & 0 & 0 & \cdots & 0 \\ 0 & 0 & A_3^L & B_3^L & C_3^L & 0 & \cdots & 0 \\ \vdots & \vdots & \vdots & \vdots & \ddots & \ddots & \ddots & 0 \\ 0 & 0 & 0 & 0 & 0 & A_{N-2}^L & B_{N-2}^L & C_{N-2}^L \\ 0 & 0 & 0 & 0 & 0 & \cdots & A_{N-1}^L & B_{N-1}^L \end{bmatrix}} \overset{N\times 1}{\begin{bmatrix} Y_0^{n+1} \\ Y_1^{n+1} \\ Y_2^{n+1} \\ Y_3^{n+1} \\ \vdots \\ Y_{N-2}^{n+1} \\ Y_{N-1}^{n+1} \end{bmatrix}} = \overset{N\times N}{\begin{bmatrix} B_0^R & C_0^R & 0 & 0 & 0 & 0 & \cdots & 0 \\ A_1^R & B_1^R & C_1^R & 0 & 0 & 0 & \cdots & 0 \\ 0 & A_2^R & B_2^R & C_2^R & 0 & 0 & \cdots & 0 \\ 0 & 0 & A_3^R & B_3^R & C_3^R & 0 & \cdots & 0 \\ \vdots & \vdots & \vdots & \vdots & \ddots & \ddots & \ddots & 0 \\ 0 & 0 & 0 & 0 & 0 & A_{N-2}^R & B_{N-2}^R & C_{N-2}^R \\ 0 & 0 & 0 & 0 & 0 & \cdots & A_{N-1}^R & B_{N-1}^R \end{bmatrix}} \overset{N\times 1}{\begin{bmatrix} Y_0^n \\ Y_1^n \\ Y_2^n \\ Y_3^n \\ \vdots \\ Y_{N-2}^n \\ Y_{N-1}^n \end{bmatrix}} + 2(\Delta x)^2 \overset{N\times 1}{\begin{bmatrix} c_0 \\ c_1 \\ c_2 \\ c_3 \\ \ddots \\ c_{N-2} \\ c_{N-1} \end{bmatrix}} \tag{65}$$

Where we can define $\vec{B^L} \in \mathbb{R}^N$ to be the diagonal elements of the Left Tridiagonal Matrix, $\vec{C^L} \in \mathbb{R}^N$ to be the directly-above off-diagonal elements of the Left Tridiagonal Matrix, and $\vec{A^L} \in \mathbb{R}^N$ to be the directly-below off-diagonal elements of the Left Tridiagonal Matrix. Likewise, we can define $\vec{B^R} \in \mathbb{R}^N$ to be the diagonal elements of the Right Tridiagonal Matrix, $\vec{C^R} \in \mathbb{R}^N$ to be the directly-above off-diagonal elements of the Right Tridiagonal Matrix, and $\vec{A^R} \in \mathbb{R}^N$ to be the directly-below off-diagonal elements of the Right Tridiagonal Matrix.

Considering we can similarly define $[(a_i, b_i, c_i)\forall i] \to (\vec{a}, \vec{b}, \vec{c}) \in \mathbb{R}^N$ we can obtain the following quick vector-based "plugin" relationship for the Tridiagonal Matrix elements as follows:

$$\begin{bmatrix} \vec{A_L} = -2w\vec{a} - vg\Delta x\vec{b} \\ \vec{B_L} = \frac{2(\Delta x)^2}{\Delta t} + 4w\vec{a} - vq\Delta x\vec{b} \\ \vec{C_L} = -2w\vec{a} - vs\Delta x\vec{b} \\ \vec{A_R} = 2(1-w)\vec{a} + \Delta x(1-v)g\vec{b} \\ \vec{B_R} = \frac{2(\Delta x)^2}{\Delta t} - 4(1-w)\vec{a} + q(1-v)\Delta x\vec{b} \\ \vec{C_R} = 2(1-w)\vec{a} + s(1-v)\Delta x\vec{b} \end{bmatrix} \tag{66}$$

This works out nicely because our expressions do not contain mixed references to multiple locations for different values of i of a_i, b_i, c_i, meaning each expression depends on only one value of i for a_i, b_i, c_i at a time, allowing efficient notation expressed as $\vec{a}, \vec{b}, \vec{c}$ directly aligned matching with $\vec{A_L}, \vec{B_L}, \vec{C_L}, \vec{A_R}, \vec{B_R}, \vec{C_R}$ without any reshuffling or reordering.

With this mathematical processing, we have finally acquired all our ingredients for our computational recipe which we can now cook from scratch in the next section.

4.7 Numerical Methods Computational Implementation

In the previous section we processed all the math into a much more digestible standardized form of which to conveniently feed into the computer. Now we will discuss some of the details of the algorithmic mechanics of numerically solving this system, as well as its associated computational complexity theory.

4.7.1 Computational Complexity Theory

All computers have limitations in terms of time and space complexity, and if not, we'd be an omniscient species by now. Classical computers have a finite amount of resources for data memory storage, and

calculations take time to complete as electrical operations flowing over bivalent digital logic gates are not performed instantaneously. Quantum computers also have a similar flavor of limitations in this regard, since only a finite number of Qubits, repeated experimental measurements, and Qubit gate operations in particular, can be physically managed in practice. Therefore, when designing and analyzing algorithms, an essential consideration is keeping track of the computational time cost and space burden required to run such routine to completion. Though it is always possible to brute-force check the entire astronomical space of combinatorics of a problem, this procedure, requiring exponential time, is entirely intractable in practice, even if it guarantees accuracy in a surefire manner. The unit of measurement for numerical algorithms tend to be FLOPs, which stands for "Floating Point Operations," although sometimes they can be referred to as "MADs" denoting "Multiply-Adds" or "Multiply-Accumulate Operations" in the field of digital signal processing, the details of which tend to be unimportant for most contexts because the only quantity of note is the asymptotic scaling behavior with little or big-O notation, as nobody sweats the small stuff which are pennies on the dollar in the grand scheme of things.

To help portray the scale of comparison, it's worth briefly reviewing the complexity analysis results of some commonly used numerical algorithms. A Fast Fourier Transform mapping a vector of n elements to another vector with n dimensions requires $O\big(n\log(n)\big)$ operations using butterfly diagrams arising from the Cooley-Tukey algorithm. Meanwhile, the same procedure of a Quantum Fourier Transform happens almost instantaneously due to parallelization, as it instead is implemented via Qubit operations which are able to affect all superimposed states of Schrodinger's cat being both dead and alive simultaneously. This example characterizes two aspects: some algorithms scale by take more operations to complete than the number of inputs itself, and the topological sort of the ordering of procedural steps influences the total runtime, depending which are rate-determining bottlenecks that depend on previous processing. For this reason, some applications of signal processing run faster using the Fast Wavelet Transform which is linear $O(n)$ complexity, but comes with a different set of trade-offs from using a Wavelet basis instead of the Fourier basis. Meanwhile for comparison, the travelling salesman problem does not have an exact method for solving, and the best we can do is $O(n!)$ for n cities. Sometimes we want to characterize the complexity of an algorithm based on some other metric other than the size of its input size. For RSA and ElGamal encryption schemes in cryptography, this boils down to $O\big(\log(p)\big)$ operations for Alice and Bob to encrypt their secret message (using Diffie Hellman Key Exchange) vs $O\big(\sqrt{p}\big)$ for Eve the eavesdropper to decipher it (using collision attack), meaning Alice and Bob can rest assured that their secret remains safe if they choose a large enough prime number p where Eve's computational burden becomes comparatively massive, which ultimately the security of our entire banking system and credit cards loosely depends on.

This brief overview of the associated computational costs of various algorithms portrays the insight why this aspect is important in any engineering scenario, which highlights the advantages of our numerical

scheme.

4.7.2 Solving Linear Systems expressed as Matrix Equations

While it is always possible to Markov Chain Monte Carlo simulate multitudinous IID identical clone copies of the inherent Brownian-Motion drift-diffusion process in parallel, invoke the Glivenko-Cantelli theorem or Law of Large numbers, and estimate the desired underlying Fokker-Planck PDE solution via histogram counting or Kernel Density Estimate methods, for particularly reaction-diffusion systems containing mutually interacting particles, and via the Folk well-known curse of dimensionality, there's no easy way to perform importance sampling to ensure some empirical observation of collision, and so for specifically reaction-diffusion systems the continuum mechanics purely deterministic concentration profile partial differential equation framework is the most apt, and at long lost it boils down into solving our linear system expressed as a matrix equation.

The accuracy of our numerical solution entirely depends on the scale of coarse-graining we approximate our system with, and the mathematical quantification of the trade-off between reconstruction accuracy versus the expensive data resolution sampling rate is captured in the Nyquist-Shannon Sampling theorem, the Heisenberg Time-Frequency Uncertainty principle, or the Von Neumann or CFL stability criterion. There's no free lunch, as reconstruction via simple linear interpolation between the samples can only get you so far in terms of recovering resolution, and similarly the fundamental limits of accuracy of a Monte Carlo sampling routine would be limited by the sampling rate through variance reduction when the Law of Large numbers to kick in. As such, it is important to consider the most efficient and tractable manner to solve matrix equations on a computer to make the best use of the computational resources we have.

In general, performing plain "vanilla" standard RREF Gauss-Jordan elimination on a dense square $n \times n$ matrix using the standard pivot to Lower/Upper triangular form would take $O(n^3)$ operations, and performing standard matrix multiplication upon a vector would require $O(n^2)$ operations to run through the entire matrix. Luckily in our case, we can make some simplifications due to the unique sparsity patterns of our matrices.

4.7.3 Sparse Matrix Solutions

Much of the study of numerical linear algebra involves analyzing the accuracy convergence and computational complexity of relevant algorithms related to matrices, and the correctness convergence feasibility of some of these problems depend on the condition number and eigenvalues of the matrix in question. Luckily, the analysis gets enormously simplified when the matrix is sparse, and the computer just stores a list of the coordinates of where the comparatively few non-zero values of the matrix lie. When working with sparse matrices in general, usually a sort of Cuthill-McKee algorithm pre-processing

step is upfront performed on a matrix to ensure it has a band-limited structure, with hopefully the smallest bandwidth possible.

For our purposes, in observing the previous matrix equation with nonzero entries directly right above and below the diagonal, our matrix is band-limited of bandwidth 1, satisfying the tridiagonal structure, and as such, we really only need to specify $3N - 2 = O(N)$ values to completely fill all non-zero degrees of freedom of this $N \times N$ square matrix of tridiagonal sparsity pattern. Due to the limited information contained in this tridiagonal matrix, hopefully any devised processing scheme will only need to sift through these unique values a few times over at most, passing through forwards and backwards for just an iteration or two, until convergence to correctness is reached, to preserve linear time complexity of $O(N)$ for our aggregate procedure. This is indeed possible with the famous Tridiagonal Matrix Algorithm or Thomas Algorithm (Thomas 1949) [97], which optimally takes advantage of this sparsity structure, leveraging how the data storage space complexity is linear while also ensuring limited mutual interlocking data cross-term interaction to ensure linear time processing complexity as well.

4.7.4 Thomas Tridiagonal Matrix Algorithm

Here we peak under the hood to lay out the mechanics of the Thomas Tridiagonal Matrix Algorithm [97] as follows:

Input Data to the Thomas Tridiagonal Matrix Algorithm:

$$\overset{n \times n}{\begin{bmatrix} b_1 & c_1 & 0 & 0 & 0 & 0 & \cdots & 0 \\ a_2 & b_2 & c_2 & 0 & 0 & 0 & \cdots & 0 \\ 0 & a_3 & b_3 & c_3 & 0 & 0 & \cdots & 0 \\ 0 & 0 & a_4 & b_4 & c_4 & 0 & \cdots & 0 \\ \vdots & \vdots & \vdots & \vdots & \ddots & \ddots & \ddots & 0 \\ 0 & 0 & 0 & 0 & 0 & a_{n-1} & b_{n-1} & c_{n-1} \\ 0 & 0 & 0 & 0 & 0 & \cdots & a_n & b_n \end{bmatrix}} \overset{n \times 1}{\begin{bmatrix} x_1 \\ x_2 \\ x_3 \\ x_4 \\ \vdots \\ x_{n-1} \\ x_n \end{bmatrix}} = \overset{n \times 1}{\begin{bmatrix} d_0 \\ d_1 \\ d_2 \\ d_3 \\ \ddots \\ d_{n-1} \\ d_n \end{bmatrix}} \tag{67}$$

Thomas Tridiagonal Algorithm Matrix Processing Pseudocode

$$\left[\begin{array}{cccc}
1. & \text{for } k \text{ in:} & k = 2, 3, 4, ..., n : & (n-1) \text{ repeats:} \\
2. & | & m = \frac{a_k}{b_{k-1}} & 1 \text{ FLOP} \\
3. & | & b_k = b_k - mc_{k-1} & 2 \text{ FLOPs} \\
4. & | & d_k = d_k - md_{k-1} & 2 \text{ FLOPs} \\
5. & \text{end for loop} & (2+2+1) \times (n-1) & = 5n - 5 \text{ FLOPs} \\
6. & \text{set:} & x_n = \frac{d_n}{b_n} & 1 \text{ FLOP} \\
7. & \text{for } k \text{ in:} & n-1, n-2, n-3, ..., 3, 2, 1 : & (n-1) \text{ repeats:} \\
8. & | & x_k = \frac{d_k - c_k x_{k+1}}{b_k} & 3 \text{ FLOPs} \\
9. & \text{end for loop} & 3 \times (n-1) & = 3n - 3 \text{ FLOPs} \\
10. & \text{return resultant output:} & \vec{x} \in \mathbb{R}^n = [x_1, x_2, x_3, ...x_{n-1}, x_n] & \\
\text{total runtime :} & [5n-5] + [3n-3] = & = 8n - 8 \rightarrow & \propto O(n) \checkmark
\end{array}\right] \tag{68}$$

Observe that the two-pass algorithm sweeps through all values once forwards and then again backwards, resulting in just a few or handful of iterations, preserving linear time complexity. Additionally, since the algorithm directly alters the input data, accessibly modifying such inputs a_k, b_k, c_k, d_k throughout its journey to compute the correspondingly correct x_k, there's pretty much no additional memory storage space required other than whatever was required for the raw original input data itself, implying linear space complexity as well. As such, this characterizes that for any sequential algorithm it's optimally efficient in terms of time and space complexity, as it preserves linear space and time complexity from its input size of $O(n)$ to output size of $O(n)$ without significant higher order mutual cross-interaction connectivity processing between the various input data values, as that would contribute to higher than linear complexity. However though, rather than the above sequential algorithm, while there is theoretically a potential way to asymptotically sacrifice space complexity $O(n) \rightarrow O\big(n \log(n)\big)$ to instead improve upon time complexity $O(n) \rightarrow O\big(\log(n)\big)$ using GPU parallel computation methods (Heath 2013) [98], for the purposes of running a simulation on a simple personal consumer laptop machine of generic computer architecture, there's not much room for improvement upon the good old tested, tried, and true Thomas Tridiagonal Algorithm, [97] implying that this is pretty much going to be, for our purposes, the state-of-the-art tool. Naturally such parallelization only extends to solving the entire spatial profile together at a fixed time slice as opposed to parallelization through time to compute the entire evolution of the system's dynamics.

It is also worth mentioning that in addition to parabolic PDEs (reaction-diffusion-type systems) in one dimension, the Thomas Tridiagonal Algorithm easily extends to Hyperbolic PDE's that are second order in time, often used to describe materials exhibiting viscoelasticity and their boundary interface (usually an orientable manifold with an interior, unlike a Klein bottle.), where the Finite Difference

numerical stencil includes two profiles, meaning the current and the previous, using both yesterday and today's information, to determine tomorrow and calculate the updated profiles for the next next step. Additionally, the Thomas algorithm can extend to separable PDE's in higher dimensions, analagous to how a multi-dimensional Fast Fourier or Wavelet transform can be done by each dimension, e.g. rows versus columns separately in images. Non-separable PDE's in 2 Dimensions still maintain some sparse matrix patterns, its structure facilitating computation, but the Thomas Tridiagonal Algorithm would then no longer hold.

4.7.5 Python Implementation

Arguably the most important component of an automobile might be considered the engine, and while the heart and brain are likely the most vital anatomical parts of the human body, all members that system comprises must collaborate synergistically as a whole collective to function together, and so the Thomas Tridiagonal Matrix [97] algorithm needs to be robustly ensconced within a proper Python scaffolding. Considering the sequential core routine's Thomas algorithm works in linear time and space complexity, it would behoove of us to preserve such Pareto optimal order of magnitude without exceeding linearity, and a brief outline of its structural implementation is as follows.

4.7.6 Python Code Structure

Ultimately, the main course key central subroutine is calling up SciPy's in-house Tridiagonal algorithm built into the solve_banded function and setting the matrix bandwidth parameter to 1, thereby upfront indicating that we have a tridiagonal matrix as it internally preliminarily determines how to best tackle this problem. The rest of the code structurally provides the buns of the burger or the bread of the sandwich containing the meat, which of course are still important in the overall context.

The code ultimately initializes i different species concentration profiles with N spatial grid points of specified equal interstitial length, and upfront establishes the timestep, characterizing the equally spaced amount of time to nudge forward within each iteration of the simulation, as well as boundary conditions and numerical scheme parameter choices.

The code then iteratively runs the simulation using whatever the user wants to input for each species' instantaneous diffusive profile term $\vec{a_i}(x)\big|_{t=\text{now}}$, their convective drift profile term $\vec{b_i}(x)\big|_{t=\text{now}}$, and their source/sink term $\vec{c_i}(x)\big|_{t=\text{now}}$, which can naturally be mathematically chosen to fit whatever physics the user would like to represent, including the effects of mutual coupling between species. The simulation then takes all the necessary "Sufficient Statistics" information from our instantaneous snapshot, which contains $\vec{a}, \vec{b}, \vec{c}$ describing the current mechanics, as well as the present concentration profiles of each species $\vec{Y_i}$, and implements them into the Thomas Tridiagonal Algorithm [97], which computes the update to our system to arrive at the next future profile configuration throughout time. This rote

process mechanically cranks the handle that pushes forward the evolutionary dynamics of our system so we can observe its trajectory. At successive intervals, we store a particular image visual snapshot plot (using python's matplotlib package) of our system's concentration profiles into permanent storage into an ordered list of frames, as well as the corresponding iteration index number which yields the corresponding time value when multiplied by the dt time spacing value. Eventually, we can replay all these successive frames into a visual moving animation which can be analyzed qualitatively, while also being aesthetically appealing and visually informative.

As to why not each and every simulation iteration is permanently stored and expressed as visual animation frames: The human eye can only detect about 30-60 flickering frames per second which is already comparable to High Definition (HD) video, and anything past such frame rate is past the band-limited Nyquist rate of marginally useful video time resolution without slow-motion capture, and so it's worth ensuring that video time resolution, purely for visual purposes, is much less than the actual simulation time resolution for mathematical computation purposes, or alternatively, the dt time step for purely animation purposes is much larger than the dt time step for purely mathematical computation purposes. Intuitively, we don't want to display literally every intermediate state of our simulation, and we just want to display maybe one state every few thousand or so, meaning the simulation was able to propagate through a few thousand of compounded subdivided time steps before the next visual display.

As such, the total runtime is $O\big((\#dx) \times (\#dt)\big)$ as it it cranks the Thomas Tridiagonal Algorithm $O(\#dx)$ [97] in linear time with respect to the total number of spatial grid points, and it repeats such process for a total number of iterations linearly proportional to the total number of time steps of $O\big(\#dt\big)$, and so their product yields the total sequential time cost, assuming we only have a handful of different species concentration profiles to keep track of. It's also worth noting it is not possible to simulate the system in parallel over time because the next subsequent iteration directly depends on the previous iteration's concentration profiles, even if we were able to Monte Carlo simulate the system which still has such causal structure. Although it is hypothetically possible to run numerous non-interacting random walkers simultaneously together in parallel, but we already eliminated that option.

The total amount of memory cost will only be comparatively $O\big((\#dx) \times (\#\text{frames})\big)$ since we can dispose of intermediate time steps in-between frames after we're done with passing through them, considering we're only permanently storing about one every few thousand or so for animation purposes. It is worth mentioning that this scales astronomically in a multiplicative manner to high power with number of dimensions, as not only do the total number of spatial grid points increase as a power of such dimension, but the neighborhood spectral graph connectivity of each grid-point also exponentially grows hence the curse of dimensionality, which highlights the key beneficial aspect of restricting to one-dimensional spherical geometry for our simulation.

4.7.7 Handling Boundary Conditions

There are some nuances with how to represent imposed boundary conditions upon the simulation. Ultimately, all boundary conditions need to be captured in the first and last rows of the tridiagonal matrices involved, and sometimes that will bleed over one more layer into the second and the second to last rows.

The simulation software can handle three types of boundary conditions: Dirichlet Boundary Conditions where both ends of the concentration profile are pinned to some arbitrary value throughout time, Neumann Boundary Conditions where both ends of the concentration profile are enforced to be adiabatic with flat zero derivative, or mixed boundary conditions with one on each side.

As a general rule of thumb, computational science practitioners often pair fully implicit numerical schemes with Neumann boundary conditions and fully explicit schemes with Dirichlet boundary conditions.

This is primarily due to the stability and ease of implementation of each method with its respective boundary type: implicit schemes handle Neumann's flux-based constraints more robustly, while explicit schemes are easier to implement with Dirichlet's fixed-value boundaries. These pairings tend to work well together, but deviations from this guideline introduce complexities, making it computationally challenging to manage mismatched scenarios. In particular, mixed boundary conditions or the Crank-Nicholson scheme, with its equal weighting of implicit and explicit methods, create an inherent ambiguity. To address this, we developed a novel, generalized ad hoc method that effectively handles all possible combinations, as outlined below.

$$\underset{N\times N}{\begin{bmatrix} B_0^L & C_0^L & 0 & 0 & 0 & 0 & \cdots & 0 \\ A_1^L & B_1^L & C_1^L & 0 & 0 & 0 & \cdots & 0 \\ 0 & A_2^L & B_2^L & C_2^L & 0 & 0 & \cdots & 0 \\ 0 & 0 & A_3^L & B_3^L & C_3^L & 0 & \cdots & 0 \\ \vdots & \vdots & \vdots & \vdots & \ddots & \ddots & \ddots & 0 \\ 0 & 0 & 0 & 0 & 0 & A_{N-2}^L & B_{N-2}^L & C_{N-2}^L \\ 0 & 0 & 0 & 0 & 0 & \cdots & A_{N-1}^L & B_{N-1}^L \end{bmatrix}} \underset{N\times 1}{\begin{bmatrix} Y_0^{n+1} \\ Y_1^{n+1} \\ Y_2^{n+1} \\ Y_3^{n+1} \\ \vdots \\ Y_{N-2}^{n+1} \\ Y_{N-1}^{n+1} \end{bmatrix}} = \underset{N\times N}{\begin{bmatrix} B_0^R & C_0^R & 0 & 0 & 0 & 0 & \cdots & 0 \\ A_1^R & B_1^R & C_1^R & 0 & 0 & 0 & \cdots & 0 \\ 0 & A_2^R & B_2^R & C_2^R & 0 & 0 & \cdots & 0 \\ 0 & 0 & A_3^R & B_3^R & C_3^R & 0 & \cdots & 0 \\ \vdots & \vdots & \vdots & \vdots & \ddots & \ddots & \ddots & 0 \\ 0 & 0 & 0 & 0 & 0 & A_{N-2}^R & B_{N-2}^R & C_{N-2}^R \\ 0 & 0 & 0 & 0 & 0 & \cdots & A_{N-1}^R & B_{N-1}^R \end{bmatrix}} \underset{N\times 1}{\begin{bmatrix} Y_0^n \\ Y_1^n \\ Y_2^n \\ Y_3^n \\ \vdots \\ Y_{N-2}^n \\ Y_{N-1}^n \end{bmatrix}} + 2(\Delta x)^2 \underset{N\times 1}{\begin{bmatrix} c_0 \\ c_1 \\ c_2 \\ c_3 \\ \ddots \\ c_{N-2} \\ c_{N-1} \end{bmatrix}} = \underset{N\times 1}{\begin{bmatrix} F_0 \\ F_2 \\ F_3 \\ F_4 \\ \ddots \\ F_{N-2} \\ F_{N-1} \end{bmatrix}} \tag{69}$$

$x_{\min}$ Left-Hand Side Boundary Condition Modifications

$$\begin{bmatrix} \text{boundary type} \downarrow \text{ numerical scheme } \rightarrow & \text{Explicit } w=0 & \text{Crank-Nicolson } w=0.5 & \text{Implicit } w=1 \\ \text{Dirichlet } Y\big|_{@x_{\min}} = p & \begin{bmatrix} \text{pre-processing:} \\ B_0^L = 1 \\ C_0^L = 0 \\ F_0 = p \end{bmatrix} & \begin{bmatrix} \text{pre-processing:} \\ B_0^L = 1 \\ C_0^L = 0 \\ A_1^R = 2A_1^R \\ F_0 = p \end{bmatrix} & \begin{bmatrix} \text{post-processing:} \\ Y_0^{n+1} = Y_1^{n+1} = p \end{bmatrix} \\ \text{Neumann } \frac{\partial Y}{\partial x}\big|_{@x_{\min}} = 0 & \begin{bmatrix} \text{pre-processing: } B_0^L = -C_0^L, F_0 = 0 \\ \text{post-processing: } Y_0^{n+1} = Y_1^{n+1} \end{bmatrix} & \begin{bmatrix} \text{pre-processing:} \\ \begin{bmatrix} B_0^L = -C_0^L \\ F_0 = 0 \end{bmatrix} \\ \text{post-processing:} \\ Y_0^{n+1} = Y_1^{n+1} \end{bmatrix} & \begin{bmatrix} \text{pre-processing:} \\ \begin{bmatrix} B_0^L = -C_0^L \\ F_0 = 0 \end{bmatrix} \\ \text{post-processing:} \\ \begin{bmatrix} Y_1^{n+1} = Y_2^{n+1} \\ Y_0^{n+1} = Y_2^{n+1} \end{bmatrix} \end{bmatrix} \end{bmatrix} \tag{70}$$

$x_{\max}$ Right-Hand Side Boundary Condition Modifications

$$\begin{bmatrix} \text{boundary type} \downarrow \text{ numerical scheme } \rightarrow & \text{Explicit } w=0 & \text{Crank-Nicolson } w=0.5 & \text{Implicit } w=1 \\ \text{Dirichlet } Y\big|_{@x_{\max}} = h & \begin{bmatrix} \text{pre-processing:} \\ B_{N-1}^L = 1 \\ A_{N-1}^L = 0 \\ F_{N-1} = h \end{bmatrix} & \begin{bmatrix} \text{pre-processing:} \\ B_{N-1}^L = 1 \\ A_{N-1}^L = 0 \\ C_{N-2}^R = 2C_{N-2}^R \\ F_{N-1} = h \end{bmatrix} & \begin{bmatrix} \text{post-processing:} \\ Y_{N-1}^{n+1} = Y_{N-2}^{n+1} = h \end{bmatrix} \\ \text{Neumann } \frac{\partial Y}{\partial x}\big|_{@x_{\max}} = 0 & \begin{bmatrix} \text{pre-processing: } B_{N-1}^L = -A_{N-1}^L, F_{N-1} = 0 \\ \text{post-processing: } Y_{N-1}^{n+1} = Y_{N-2}^{n+1} \end{bmatrix} & \begin{bmatrix} \text{pre-processing:} \\ \begin{bmatrix} B_{N-1}^L = -A_{N-1}^L \\ F_{N-1} = 0 \end{bmatrix} \\ \text{post-processing:} \\ Y_{N-1}^{n+1} = Y_{N-2}^{n+1} \end{bmatrix} & \begin{bmatrix} \text{pre-processing:} \\ \begin{bmatrix} B_{N-1}^L = -A_{N-1}^L \\ F_{N-1} = 0 \end{bmatrix} \\ \text{post-processing:} \\ \begin{bmatrix} Y_{N-2}^{n+1} = Y_{N-3}^{n+1} \\ Y_{N-1}^{n+1} = Y_{N-3}^{n+1} \end{bmatrix} \end{bmatrix} \end{bmatrix} \tag{71}$$

A couple clarifications about the notation and implied order of operations: $\vec{F} \in \mathbb{R}^{N\times 1}$ denotes the resultant vector that would arise from computing the right hand side of the equation, as we do currently know our present configuration $\vec{Y}^n$ on the right hand side which we're using to compute the unknown next configuration $\vec{Y}^{n+1}$ on the left hand side. For the Thomas Algorithm [97], we will ultimately end up feeding in both $\vec{F}$ the result from computing the linear algebra operations on the right hand side of the equation, and the tridiagonal matrix from the equation's left hand side. As such, the lexicon of "Pre-Processing" has the denotation of serving as the necessary preliminary antecedent steps before being fed into the Thomas Algorithm [97], and "Post-Processing" involves slightly editing our final result after the execution of the Thomas Algorithm. While these modification methods may seem a bit crude, the accurate results illustrate that such rough heuristic technique actually is in check with what to expect from intuition.

As can be seen from each of our simulation comparison test results, this novel ad-hoc method is able to generate simulations with animations that exactly match to pixel and to machine precision of

any corresponding solution arising from theoretical pure math parabolic partial differential equation theory, given reasonably sufficient resolution for coarse-graining naturally. Why this heuristic works reasonably well boils down to comprehension of the fundamental intuition of heat and mass transport at the infinitesimal time and length scale; ultimately, an isothermal boundary will constantly periodically replenish or flush out the boundary to maintain its fixed constant value, and an adiabatic barrier will constantly periodically smooth out neighboring fluid elements near the boundary to remain flat and glued to each other, which can be gleaned from careful inspection of the boundary condition modification routine. With this novel ad-hoc method, it is possible to overcome the fundamental challenging hurdle of inherently mismatched numerical schemes and boundary conditions, allowing complete and total user flexibility for catering the simulation routine to any need at all.

4.7.8 Steady State ODE: Tridiagonal Algorithm Numerically Unstable

In the event someone wants to skip over all transient dynamics and jump right to arriving at the steady state profile, one would want to solve the Finite Difference Scheme for the corresponding Ordinary Differential Equation with time dependence removed and set to zero. While it is possible to interpret the time-dependent dynamical PDE simulator as an iterative method for converging to the true time-dependent steady state solution, which indeed literally is mathematically consistent with the theory of Parabolic partial differential equations, it would still be faster overall to use one ODE routine as opposed to iteratively running the PDE routine many times. From the previous outline of the Thomas Tridiagonal algorithm's pseudo-code, the unintelligent machine goes through processing the list of elements in order of appearance, which leads to numerical instability when solving an ODE. Usually for numerical PDEs, the present configuration $\vec{Y}^n$ tends to not differ drastically from the next update future configuration $\vec{Y}^{n+1}$ due to the comparatively small time step separation, so successive computations tend to be numerically stable. However, algebraically directly solving for jumping right to the steady state vector instead of solving for a slight perturbative nudge forward for successive relaxation is tends to be ill-conditioned, as the vector $\vec{F}$ tends to be quite sparse stuck with lots of immobile zeros. Therefore, using numpy's generalized sparse matrix linear algebra package is highly recommended for solving the corresponding steady state ODE as opposed to specifically a band matrix algorithm or tridiagonal algorithm; this way, the solver knows that it needs to find an intelligent workaround instead of performing the rote Tridiagonal Algorithm which problematically defaults to processing elements in order of appearance.

4.8 Testing Code against Theory: Results

Earlier we fully derived the equations of motion and came up with a complete smorgasbord set of valid analytical expression solutions for all the differential equations of various geometries, along with a whole plethora of boundary condition arrangements corresponding to a diversity of physical scenarios that run

the entire gamut, establishing the pure mathematical physics theory behind all relevant equations investigated. With that in place, we installed a tight-knit and entirely generalized computational mathematical framework to be able to efficiently numerically simulate the systems in question. Now we merge these two distinct schools of thought through mutual comparison. Since both the pencil-paper mathematical theory and the computational representation harmoniously match consistently, it allows a deep unified understanding of the fundamental concepts at play; after all, words in a dictionary are self-defined via other different words in the same dictionary, so ideas only contain meaning through their embedded representative relationships, illustrating the onset of a positive mixture effect from a strongly bonded alliance between theory and practice.

As such, a huge aspect of our research effort was to excruciatingly rigorously and thoroughly test the code against theory and vice versa, which ensures a solid mutual cross-validation, where everything checks out and is in alignment.

For actual moving visual animations to accompany the brief blurbs about the results' implications, see the animations appendix. Each of these animations contain an overlaid or side-by-side simultaneous comparison of the theoretical dynamically evolving concentration profile versus the corresponding approximate numerical solution representation of the same system's trajectory. Notice that every time the curves continuously exactly track each other, and the behavior of their motion follow each other and what would be expected from the physical analogue. Additionally, the numerical correspondence principle, analogous to the classical to quantum physics limiting correspondence principle, holds accurately, where increased precision arises along with ever smaller time step size dt and dx fine-resolution spatial grid gap for the continuum limit.

4.8.1 One Species Case

4.8.2 Single Species PDE Solution Comparison Testing

Below is a table characterizing the entire menu of possible flavors of test cases to verify, many math expressions of these external physics combinations of selections contained in the analytical equation solutions section. The entire set of available combinatorics is mostly in the overall Cartesian product of all these associated dimensions that characterize degrees of freedom arising from user a la Carte custom-choice aspects. These free-choice aspects include internal numerical hyper-parameter intricacies under the hood of the simulator, as well as physical representations that matter without opening the hood, divided into separate sections within the table.

Pretty much the entire ground set of combinations were excruciatingly double checked and verified.

The different "geometries" in question here are characterized by the mathematical form of the equation of motion, which will be outlined in the following table:

$$
\left[\begin{array}{c}
\textbf{Internal Numerical Mechanical Aspects of Simulation} \\
\left[\begin{array}{cccc}
w \text{ choices:} & \left[\begin{array}{c} w=0 \\ \text{Explicit } \frac{\partial^2 Y}{\partial x^2} \end{array}\right] & \left[\begin{array}{c} w=0.5 \\ \text{Crank-Nicolson } \frac{\partial^2 Y}{\partial x^2} \end{array}\right] & \left[\begin{array}{c} w=1 \\ \text{Implicit } \frac{\partial^2 Y}{\partial x^2} \end{array}\right] \\
v \text{ choices:} & \left[\begin{array}{c} v=0 \\ \text{Explicit } \frac{\partial Y}{\partial x} \end{array}\right] & \left[\begin{array}{c} v=0.5 \\ \text{Crank-Nicolson } \frac{\partial Y}{\partial x} \end{array}\right] & \left[\begin{array}{c} v=1 \\ \text{Implicit } \frac{\partial Y}{\partial x} \end{array}\right] \\
[g,q,s] \text{ choices:} & \text{Centered Difference Scheme} & \text{Left Upwind Scheme} & \text{Right Upwind Scheme}
\end{array}\right] \\
\textbf{External Physics Connotation of Simulation} \\
\left[\begin{array}{cccc}
\text{Geometry choices:} & \text{Cartesian Geometry} & \text{Spherical Geometry} & \text{“Exotic” Geometry} \\
\text{Boundary Choices:} & \text{Dirichlet } Y\big|_{@\text{endpoints}} = \text{ constant} & \text{Neumann } \frac{\partial Y}{\partial x}\big|_{@\text{endpoints}} = 0 & \left[\begin{array}{c} \text{Mixed Boundary} \\ \text{one of each of both:} \\ Y\big|_{@\text{endpoint}} = \text{const.} \\ \frac{\partial Y}{\partial x}\big|_{@\text{endpoint}} = 0 \end{array}\right] \\
\text{Source Choices:} & \text{Stationary Source} & \text{No Sources} & \text{Moving Source} \\
\text{Initial Condition Chocies:} & \text{Start @ 0} & \text{Delta Configuration} & \text{Random Noise} \\
\text{Global Convection Choices:} & \text{No external overall bulk flow} & \text{Uniform left-bias drift} & \text{Uniform right-bias drift}
\end{array}\right]
\end{array}\right] \tag{72}
$$

$$
\left[\begin{array}{c}
\left[\begin{array}{c} \textbf{General Canonical Form:} \\ \frac{\partial Y}{\partial t} = a(x)\frac{\partial^2 Y}{\partial x^2} + b(x)\frac{\partial Y}{\partial x} + h(x)Y + c(x) \end{array}\right] \\
\textbf{Specific Form Geometric Interpretation} \\
\left[\begin{array}{ccc}
\text{Cartesian} & \text{Spherical} & \text{“Exotic” } \downarrow \\
\frac{\partial Y}{\partial t} = D\frac{\partial^2 Y}{\partial x^2} + v\frac{\partial Y}{\partial x} + c\delta(x-x_0) & \frac{\partial Y}{\partial t} = D\frac{\partial^2 Y}{\partial x^2} + D\left[\frac{2}{x} - \frac{M}{x^2}\right]\frac{\partial Y}{\partial x} + c\delta(x-x_0) & \text{General Canonical Form} \\
\left[\begin{array}{c} a(x) = D \\ b(x) = v \\ c(x) = c\delta(x-x_0) \\ h(x) = 0 \end{array}\right] & \left[\begin{array}{c} a(x) = D \\ b(x) = D\left[\frac{2}{x} - \frac{M}{x^2}\right] \\ c(x) = c\delta(x-x_0) \\ h(x) = 0 \end{array}\right] & \left[\begin{array}{c} a(x) = ? \\ b(x) = ? \\ c(x) = ? \\ h(x) = ? \end{array}\right]
\end{array}\right]
\end{array}\right] \tag{73}
$$

While the structural architecture of the simulation routine cannot directly handle $h(x) \neq 0$ and can only handle equations of form:

$$
\frac{\partial Y}{\partial t}\Big|_{@\text{present snapshot}} = a(x)\Big|_{@t=\text{now}}\frac{\partial^2 Y}{\partial x^2} + b(x)\Big|_{@t=\text{now}}\frac{\partial Y}{\partial x} + 0 \times \left(h(x)Y_{\text{current}}\right) + c(x)\Big|_{@t=\text{now}} \tag{74}
$$

as the direct inclusion of $h(x) \neq 0$ provided erroneous results, we can still sufficiently include such term's effects into the simulation by shoving it into the $c(x)\big|_{@t=\text{now}}$ term, a novel ad hoc workaround in this context, as ensuring $h(x) = 0$ simplifies analysis greatly within the realm of drift-diffusion systems. The reason why this computationally mathematically works is in the limit of small time enough time scale dt where we are honing in upon an infinitesimal slice of time for our instantaneous snapshot, ultimately to first order, the $h(x)Y_{\text{current}}$ term ends up just contributing a source or sink term at each x point in space that is directly proportional to such instantaneous $h(x)Y_{\text{current}}$ value at such location, implying that without loss of generality we can actually merge $c(x)\big|_{@t=\text{now}}$ together with $h(x)Y_{\text{current}}$ to capture both of

their effects simultaneously, a much more digestible format for the simulator to handle, and the resultant animations show that this works in practice when applied to various commonly-known time-dependent problems from partial differential equations of this form, such as the various flavors of Hermite, Bessel, Legendre, Laguerre, and Chebshev equations' fundamental solutions and orthonormal excitation modes moving along with their corresponding eigenvalue in the operator's spectrum. This sheds an interesting light on differential equation theory, that one could interpret many "Folk" differential equations as generalized drift-diffusion systems.

4.8.3 Handling PDE Time Dynamics without Analytical Solution

There are times when the underlying Single Species PDE equation of motion is too complicated to have an appropriate time-dependent analytical solution capturing the system's transient dynamics, usually due to some combination of arbitrary spatially varying coefficient profiles for diffusion, drift, and source terms, which could even introduce non-linearity if these happen to directly depend on our current snapshot of our single species concentration profile: $a(x), b(x), c(x), h(x) \rightarrow a(x, Y), b(x, Y), c(x, Y), h(x, Y)$. While there may not exist time-dependent closed-form mathematical equations expressing such system's transient dynamics, it is still often possible to solve for a closed-form expression characterizing the steady-state concentration profile where the system eventually comes to rest after settling down. The existence of an analytical equation for the stationary measure profile allows cross-validation to be performed for an expanded class of problems by simply verifying that asymptotically the simulation seems to approach what would be predicted by steady state. This is a novel workaround method analogous to how we handled verifying situations with "exotic geometry" discussed previously, as sometimes determining the time-dynamics arising from a standard mode's eigenvalue can be difficult for a general instantiation of a solution with arbitrarily chosen boundary conditions.

At the end of the day, the settling animations overlaid upon the predicted steady state profile consistently match as a verification of accuracy. This also is in line with theoretical thermodynamic arguments using the principles of energy and entropy. Hence the second law of thermodynamics, systems tend to become disordered to maximize their entropy, which is mathematically equivalent to minimizing free energy via strong convex duality from a Fenchel-Legendre Transform of their corresponding Lagrangian objective functions with constraints, a common mathematical result from convex analysis, optimal control, calculus of variations, or information geometry. This maximum entropy school of thought can be applied to all sorts of systems following the philosophy of its pioneer E.T. Jaynes. The stationary measure of a stochastic process's Fokker-Planck equation is the corresponding steady state solution for the asymptotic occupancy statistics of Markov state exploration, and likewise for heat and mass transport processes through diffusive spread, which both mathematically yield maximum entropy solutions. This provides a promising argument why the simulations consistently converge to predicted steady state

irrespective of start point. The Dirichlet energy landscape functional is convex from second variation analysis due to $a(x)$ being defined as strictly positive for any second order parabolic reaction diffusion system, ensuring that its Hessian is positive semi-definite, which implies that the stationary configuration is also a stably attractive state that the system wants to settle in as well, these notions attributed to the standard necessary and sufficient conditions for optimality. Intuitively, the diffusion is an irreversible process as the concentration profile continually spreads out horizontally, until it is as flat as possible via the Poisson or Laplace equation, which maximizes Shannon entropy from a distribution that is as flat as possible. This analysis allows increased confidence in our code and reassures the validity of our simulations.

4.8.4 Multiple Species Case

The numerical code is also promising for multiple species simulations, which also verifies the associated novel theory arising from such scenario. Using the working rote routine that mechanistically cranks the simulation procedure forward, the LOX-Lever Rule's 4.5.1 theoretical experiment consistently matches the corresponding simulation for a huge variety of choices of physical parameters. The simulator of various geometries is able to properly handle various reaction stoichiometric balances and species diffusivities, indicating that both the theory and code is sound for simulations of instant one-way chemistry and spatially constant diffusion. For spatially-dependent diffusion, while there are no analytical solutions for such, our simulation results for Chapman-Enskog diffusivity where all species diffusion constants are proportional to $D \propto \sqrt{T}$, the square root of the current Temperature profile, look promising as they are numerically stable and match what intuition would expect from diffusivity increasing with exothermic heat generated. A really useful noteworthy point about the instantaneous chemistry Chapman-Enskog Model's structure is that the upstream simulation of fuel and oxidizer reacting can be non-dimensionalized with respect to the downstream simulation's nominal Temperature, conditioned on proper choice of exothermic stoichiometric ratio. The nominal temperature matters due to the nonlinear square root term, but considering the only aspect that feeds into the temperature profile is the stoichiometric proportionality from instantaneous maximal extent reaction, it can always be chosen appropriately to be invariant to scaling of upstream simulation fuel and oxidizer concentration profiles. Additionally, since the temperature profile downstream is constrained to being nominal, and the Finite-Difference scheme is linear in terms of the temperature profile's snapshot, such scaling does not actually affect the shape of the dynamics of the species profiles other than just height scaling, so these are all equivalent representations from scaling symmetry. However, this does change for Arrhenius kinetics which explicitly depends on the actual real quantity of matter as opposed to its relative mixture composition, as will be discussed further on in a later section (see 5.2.3).

5 Methods

In this section, we will detail all the standard, conventional, and idiomatic computational combustion physics methods that are common to the discipline's principles, and highlight which are relevant to our study. While engaging with derivation assumptions behind the physical premise foundations along the way, we will lay out the important calculation procedures used in the field of gas dynamics, and present them in an organized manner to facilitate interpretation for our scientific context. We will also indicate the significance of how they were implemented into our simulation and analysis.

5.1 Transport Properties and Diffusivities

5.1.1 Underlying Physics and Theoretical Framework

A complete and comprehensive summary of all the relevant phenomena, derivations, and equations are outlined in specifically Chapter 1, Chapter 9, and Chapter 17 of "Transport Phenomena" by Bird, Stewart, and Lightfoot (2002) [99], a well-known standard textbook used for the subject. The key equations that form the core of our original simulator are presented and explained in full detail throughout the following sections, along with an intricate but structurally organized dissection to identify the mechanical functions of the various components.

Dynamic Viscosity of a Gas Mixture

Although dynamic viscosity is not directly used in our quasi-static combustion model in the reaction-diffusion PDE framework, it is still presented here for completeness, as it forms the basis for analogous mixture-averaging applied to thermal conductivity. According to Bird et al., the mixture viscosity is given by equation 1.4-15:

$$\mu_{\text{mix}} = \sum_{i=1}^{N} \frac{x_i \mu_i}{\sum_{j=1}^{N} x_j \phi_{ij}} \tag{75}$$

where x_i is the mole fraction of species i, μ_i is its pure-species viscosity, N is the total number of species in the mixture, and ϕ_{ij} is a nondimensional interaction coefficient between species i and j. The coefficient ϕ_{ij} accounts for asymmetry in molecular interactions, following equation 1.4-16 in Bird et al:

$$\phi_{ij} = \frac{1}{\sqrt{8}} \left[1 + \left(\frac{m_i}{m_j}\right)\right]^{-1/2} \left[1 + \sqrt{\frac{\mu_i}{\mu_j}} \left(\frac{m_j}{m_i}\right)^{1/4}\right]^2 \tag{76}$$

where m_i and m_j are molecular masses. This is Wilke's well-known mixing rule and forms the prototype for thermal conductivity mixing.

Thermal Conductivity and Heat Diffusivity Path

By analogy, the mixture-averaged thermal conductivity is given as equation 9.3-17 from Bird et al:

$$k_{\text{mix}} = \sum_{i=1}^{N} \frac{x_i k_i}{\sum_{j=1}^{N} x_j \phi_{ij}} \tag{77}$$

where the same structural form is used as Eq. (75), but μ_i is replaced by the species thermal conductivity k_i, and the interaction coefficient is defined analogously:

$$\phi_{ij} = \frac{1}{\sqrt{8}} \left[1 + \left(\frac{m_i}{m_j}\right)\right]^{-1/2} \left[1 + \sqrt{\frac{k_i}{k_j}} \left(\frac{m_j}{m_i}\right)^{1/4}\right]^2 \tag{78}$$

This rule preserves desirable properties of the convex linear combination structure, and empirically reproduces measured values for dilute gas mixtures used in combustion modeling.

Pure-Species Thermal Conductivity

Each species' thermal conductivity k_i is derived from Chapman–Enskog kinetic theory, presented as equation 9.3-13 in Bird et al:

$$k_i = \frac{25}{32} \frac{\sqrt{\pi m_i k_B T}}{\pi \sigma_i^2 \Omega_k(T/\epsilon_i)} \hat{C}_{v,i}(T) \tag{79}$$

where k_B is the Boltzmann constant, T is temperature, σ_i and ϵ_i are Lennard–Jones potential parameters, Ω_k is the dimensionless collision integral, and $\hat{C}_{v,i}$ is the per-molecule heat capacity at constant volume. The dependence $k_i \propto \sqrt{T}$ reflects the temperature scaling of molecular velocity from Maxwell–Boltzmann statistics.

Thermal Conductivity k_i We now verify the dimensional consistency of the molecular thermal conductivity expression from Bird, Stewart, and Lightfoot (Eq. 9.3-13):

$$k_i = \frac{25}{32} \frac{\sqrt{\pi m_i k_B T}}{\pi \sigma_i^2 \Omega_k(T/\epsilon_i)} \hat{C}_{v,i}(T) \tag{80}$$

Let's identify the meaning and SI units of each term:

- m_i: molecular mass $\rightarrow$ [kg]
- k_B: Boltzmann constant $\rightarrow [\mathrm{J{\cdot}K^{-1}}] = [\mathrm{kg{\cdot}m^2 s^{-2} K^{-1}}]$
- T: temperature $\rightarrow$ [K]
- σ_i: effective molecular diameter $\rightarrow$ [m]
- Ω_k: collision integral $\rightarrow$ dimensionless
- $\hat{C}_{v,i}$: constant volume specific heat capacity per unit mass $\rightarrow [\mathrm{J{\cdot}kg^{-1} K^{-1}}] = [\mathrm{m^2 s^{-2} K^{-1}}]$

We now carry out the dimensional analysis step by step, showing each simplification clearly:

$$[k_i] = \frac{\sqrt{[m_i][k_B][T]}}{[\sigma_i]^2} [\hat{C}_{v,i}]$$

$$= \frac{\sqrt{(\mathrm{kg})(\mathrm{kg{\cdot}m^2 s^{-2} K^{-1}})(\mathrm{K})}}{\mathrm{m^2}} (\mathrm{m^2 s^{-2} K^{-1}})$$

$$= \frac{\sqrt{\mathrm{kg}^2\mathrm{m}^2\mathrm{s}^{-2}}}{\mathrm{m}^2}(\mathrm{m}^2\mathrm{s}^{-2}\mathrm{K}^{-1})$$

$$= \frac{\mathrm{kg{\cdot}m{\cdot}s}^{-1}}{\mathrm{m}^2}(\mathrm{m}^2\mathrm{s}^{-2}\mathrm{K}^{-1})$$

$$= (\mathrm{kg{\cdot}m{\cdot}s}^{-3}\mathrm{K}^{-1})$$

$$= (\mathrm{kg{\cdot}m{\cdot}s}^{-3}\mathrm{K}^{-1}) = (\mathrm{kg{\cdot}m}^2\mathrm{s}^{-3}\mathrm{m}^{-1}\mathrm{K}^{-1})$$

$$= [\mathrm{W{\cdot}m}^{-1}{\cdot}\mathrm{K}^{-1}] \quad \checkmark$$

Thus, the expression for k_i is dimensionally consistent with the SI definition of thermal conductivity, an important step in clarifying how ultimately heat diffusivity α only depends on ratios of heat capacities, especially in the context of our model, further elaborated upon in the subsequent sections.

Since we are considering standard, non-exotic conditions, in typical combustion modeling, the pressure P is assumed to remain constant, usually taken as some fixed value (1 bar in our case). Under this assumption, the gas density varies inversely with temperature, and as such, in practical calculations, ρ is often not tracked explicitly; instead, its temperature dependence is incorporated implicitly through temperature-dependent diffusion coefficients, while its actual quantitative value is ultimately embedded or merged into an extra power of temperature via localized ideal gas law-type assumptions, a common principle in conventional combustion analysis. However, there are niche cases under extreme conditions where this assumption could be violated with significant virial effects, such as with high Mach number flows or with turbulent flows, but we are not considering these effects in our current work.

Ideal Gas Law and Mixture Density.

Using the ideal gas relation $PV = Nk_BT$, we express number density $n = N/V = P/(k_BT)$. The mass density of the mixture is then

$$\rho = nm_{\mathrm{mix}} = m_{\mathrm{mix}}\frac{P}{k_BT} \tag{81}$$

Thermal Diffusivity.

Thermal diffusivity is defined by

$$\alpha = \frac{k_{\mathrm{mix}}}{\rho\hat{C}_{p,\mathrm{mix}}} = \frac{(k_BT)k_{\mathrm{mix}}}{Pm_{\mathrm{mix}}\hat{C}_{p,\mathrm{mix}}(T)} \tag{82}$$

indicating that $\alpha \propto T^{3/2}/P$ when we implement the ideal gas law relation. The Mayer relation,

$$\hat{C}_{p,i} = \hat{C}_{v,i} + k_B,$$

connects constant-pressure and constant-volume capacities, allowing direct use of the standardized NASA polynomial $C_p(T)$ data, particularly for constant pressure heat capacity, in both Eq. (90) and in equation Eq. (87).

Alternative Heat Capacity Treatment (Current Work).

In the present work, a slightly modified evaluation of the thermal diffusivity α is employed. While the conventional formulation

$$\alpha = \frac{k_{\text{mix}}}{\rho \hat{C}_{p,\text{mix}}}$$

is both standard and convenient, it implicitly assumes that C_v can be directly obtained or consistently inferred from the same data source as C_p. While the NASA polynomial fits are the standard tool used for thermodynamic quantities, and commonly used by popular combustion solvers such as CHEMKIN and OpenFOAM, in practice, this is not always the case, because the NASA polynomials provide only the constant-pressure heat capacity $C_p(T)$ and omit $C_v(T)$.

Rather than relying on empirically tabulated C_v values or secondary fitting procedures, the present approach is motivated by an ab initio "from first principles" kinetic-theory perspective. The intent is to minimize dependence on empirical corrections and to retain physical transparency, to thereby construct the model from the most fundamental quantities possible. Specifically, the treatment begins from the kinetic definition of thermal diffusivity,

$$\alpha = \frac{\lambda \bar{c}}{3\gamma},$$

where λ is the mean free path, $\bar{c}$ is the mean molecular speed, and $\gamma = C_p/C_v = (f+2)/f$ is the heat capacity ratio determined by the number of molecular degrees of freedom f.

This formulation emphasizes the molecular-level basis of transport arising from the statistical mechanics framework, rather than the macroscopic empirical coefficients. With a structural parallel, the use of γ links directly to the discrete degrees of freedom of each species, which are quantities that are physically well-defined and not subject to empirical adjustment. For mixtures, γ is then treated as a weighted average (with appropriate mixing rules), representing the effective ratio of heat capacities in the continuum limit, analogous to the classic correspondence principle from physics. In practice, this introduces a modest "fudge factor" consistent with how molecular-level structure manifests statistically in bulk thermodynamic properties.

Because NASA polynomials provide only $C_p(T)$, the implementation approximates the denominator via the reciprocal heat capacity ratio, $\gamma^{-1} \approx f/(f+2)$, while evaluating the numerator using the C_p-

weighted mixture. This maintains the correct scaling behavior while avoiding situational inconsistencies that arise from combining mixed C_v- and C_p-weighted quantities when restricted to NASA polynomials for only $C_p(T)$ and not $C_v(T)$. In particular, while the denominator of the expression for α in Eq. (90) will contain a heat capacity mixture weighted by mole-fraction, the k_mix numerator contains a different estimate weighted by the mixing coefficients ϕ_{ij} from Eq. (88), and as such is subject to the lessons about biased estimates arising from the classic "Stein Paradox" from statistics tradition.

An additional practical benefit of this formulation is enhanced numerical stability. The explicit dependence on γ ensures that the denominator of the diffusivity expression remains nonzero and well-behaved across all conditions. Although this stability feature was not the original motivation, it emerges naturally from the physically grounded formulation. The primary rationale remains the logical consistency of constructing α directly from kinetic-theory premises, ensuring that each modeled quantity originates from a well-defined physical assumption. As such, our present implementation prioritizes formal simplicity and numerical stability, using only dimensionless heat capacities derived from NASA polynomials and a single effective γ closure. Further verification of such method's soundness continues with an analysis of its physical units.

Dimensional Consistency of Thermal Diffusivity (and particularly for our treatment of computing heat capacity ratio)

Thermal diffusivity is defined conventionally as

$$\alpha = \frac{k_{\mathrm{mix}}}{\rho\, C_{p,\mathrm{mix}}},$$

which carries SI units of $[\mathrm{m^2 s^{-1}}]$.

In combustion-oriented kinetic-theory form, this expression may be recast as

$$\alpha = \frac{(k_B T)\, k_{\mathrm{mix}}}{P\, m_{\mathrm{mix}}\, \hat{C}_{p,\mathrm{mix}}(T)},$$

where

- $k_B T$ is the characteristic molecular energy scale [J per molecule],
- k_{mix} is the mixture thermal conductivity $[\mathrm{W\,m^{-1}\,K^{-1}}]$,
- P is pressure $[\mathrm{Pa} = \mathrm{J\,m^{-3}}]$,
- m_{mix} is the mixture molecular mass [kg],
- $\hat{C}_{p,\mathrm{mix}}$ is the mass–specific heat capacity at constant pressure, $[\mathrm{J\,kg^{-1}\,K^{-1}}] = [\mathrm{m^2\,s^{-2}\,K^{-1}}]$.

For completeness, we also revisit the mean-free-path formulation on which our simplified transport

model is based:

$$\alpha = \frac{\lambda\,\bar{c}}{3\gamma},$$

where $\bar{c}$ is the mean molecular speed, λ is the mean free path, and $\gamma = C_p/C_v = (f+2)/f$ is the specific-heat ratio determined by the molecular degrees of freedom f. This formulation conveniently avoids inconsistencies between tabulated C_p and C_v values, while maintaining compatibility with the conductivity-based form above.

Because NASA polynomial data provide only $C_p(T)$, we adopt the mixture-averaged dimensionless specific heat,

$$\hat{C}_{p,\mathrm{mix}} = \frac{C_{p,\mathrm{mix}}}{R},$$

as a practical proxy for f, which yields the approximation

$$\gamma^{-1} \approx \frac{\hat{C}_{p,k_{\mathrm{mix}}}}{1+\hat{C}_{p,x_{\mathrm{mix}}}}.$$

Because NASA polynomial data provide only $C_p(T)$, we adopt the mixture-averaged dimensionless specific heat

$$\hat{C}_{p,\mathrm{mix}} = \frac{C_{p,\mathrm{mix}}}{R},$$

as a practical proxy for f, which yields the working approximation

$$\gamma^{-1} \approx \frac{\hat{C}_{p,k\text{-mix}}}{1+\hat{C}_{p,x\text{-mix}}}.$$

Here the numerator employs the k-weighted mixture (consistent with the thermal-conductivity mixing rules), while the denominator uses the usual mole-fraction mixture, reflecting the distinct averaging procedures that appear in the transport coefficient and the heat capacity, respectively. This preserves the expected kinetic-theory scaling $\alpha \propto T^{3/2}/P$ while ensuring dimensional consistency and numerical stability, and the resulting model still appropriately and accordingly aligns with the foundational relation $\alpha \sim \lambda\bar{c}/3$ while retaining temperature-dependent flexibility through $\hat{C}_{p,\mathrm{mix}}(T)$.

Dimensional Verification

We verify that the kinetic-theory–based expression recovers the correct units:

$$\alpha = \frac{(k_B T)\,k_{\mathrm{mix}}}{P\,m_{\mathrm{mix}}\,\hat{C}_{p,\mathrm{mix}}} = \frac{\frac{J}{K}K\,\frac{W}{mK}}{\frac{J}{m^3}\,kg\,\frac{J}{kgK}} = \frac{\frac{JW}{mK}}{\frac{J^2}{m^3K}}$$

$$= \frac{\frac{JW}{m}}{\frac{J^2}{m^3}} = \frac{JW}{J^2/m^2} = \frac{W\,m^2}{J} = \frac{J/s\cdot m^2}{J} = \frac{m^2}{s},$$

as required.

5.1.2 Binary Mass Diffusivity

The binary diffusion coefficient between species A and B follows the kinetic–theory expression given in Bird, Stewart & Lightfoot (Eq. 17.3–11):

$$cD_{AB} = \frac{3}{16}\sqrt{\frac{2RT}{\pi}\left(\frac{1}{m_A}+\frac{1}{m_B}\right)}\,\frac{1}{N_A\sigma_{AB}^2\,\Omega_{D_{AB}}\left(T/\sqrt{\epsilon_A\epsilon_B}\right)}, \tag{83}$$

where $R = N_A k_B$, c is the molar concentration, and the terms inside the square root represent the mixture-averaged reciprocal molecular masses in the usual kinetic-theory form. The combination $\frac{1}{m_A} + \frac{1}{m_B}$ is closely related to the inverse reduced mass and reflects the fact that diffusion is driven by the relative motion of colliding pairs rather than by individual species alone, flavor akin to a harmonic mean for reciprocal quantities.

Lennard–Jones mixing rules. The molecular interaction parameters entering the collision integral use the standard combining rules:

$$\sigma_{AB} = \frac{\sigma_A + \sigma_B}{2}, \qquad \epsilon_{AB} = \sqrt{\epsilon_A\epsilon_B},$$

i.e. an arithmetic mean for the collision diameter and a geometric mean for the well depth. The dimensionless collision integral $\Omega_{D_{AB}}$ is then evaluated at T/ϵ_{AB}, which nondimensionalizes the molecular kinetic energy by the characteristic strength of the 12–6 Lennard–Jones potential. These mixing rules are not unique but are widely adopted and physically interpretable: σ_{AB} approximates the kinetic collision diameter for an A–B pair, while ϵ_{AB} captures an averaged attractive well depth that controls scattering behavior.

Ideal-gas conversion and Bird Eq. (17.3–12). Using the ideal-gas relation

$$\frac{\text{moles}}{\text{volume}} = c = \frac{P}{RT}, \qquad P = cRT,$$

Eq. (83) can be rewritten in terms of pressure. Substituting $c = P/(RT)$ gives Bird's Eq. 17.3–12:

$$D_{AB} = \frac{3}{16}\sqrt{\frac{2(RT)^3}{\pi}\left(\frac{1}{m_A}+\frac{1}{m_B}\right)}\,\frac{1}{N_A P\,\sigma_{AB}^2\,\Omega_{D_{AB}}\left(T/\sqrt{\epsilon_A\epsilon_B}\right)}. \tag{84}$$

This form makes explicit the classical scaling

$$D_{AB} \propto \frac{T^{3/2}}{P},$$

i.e. diffusivity increases as molecular thermal velocity increases and decreases as intermolecular spacing shrinks under higher pressure.

Dimensional Verification of Bird's Binary Diffusion Expression

For completeness, we explicitly verify the dimensional structure of the Bird–Stewart–Lightfoot (2002) binary diffusion coefficient (their Eq. 17.3–12). The purpose of this subsection is strictly algebraic: every conversion and cancellation is written out so that no hidden assumptions remain regarding the role of "per mole" versus "per particle" quantities. This is useful because different kinetic-theory derivations use different mass conventions (amu vs. kg, k_B vs. R, etc.), and the internal bookkeeping must be completely explicit.

We begin by restating the formula exactly as printed in Bird et al.:

$$D_{AB} = \frac{3}{16}\sqrt{\frac{2(RT)^3}{\pi}\left(\frac{1}{m_A}+\frac{1}{m_B}\right)}\frac{1}{N_A P \sigma_{AB}^2 \Omega_{D_{AB}}(T/\sqrt{\epsilon_A \epsilon_B})}. \tag{85}$$

All quantities appearing above are interpreted under the following conventions:

- R is the universal gas constant written as

$$R := \frac{N_A k_B}{\text{mol}}, \qquad [R] = \text{J K}^{-1}\text{mol}^{-1}.$$

- T has units K.

- Molecular masses are reported in

$$1 \text{ amu} = \frac{\text{kg}}{\text{mol}}, \qquad [m_A] = [m_B] = \frac{\text{kg}}{\text{mol}}.$$

- N_A is treated as a dimensionless pure number.

- P has units N/m^2.

- σ_{AB} is a Lennard–Jones collision diameter, so that σ_{AB}^2 has units m^2.

- The collision integral $\Omega_{D_{AB}}$ is dimensionless.

Step 1: Dimensional structure of $(RT)^3$. Using

$$RT = \left(\frac{N_A k_B}{\text{mol}}\right) T, \qquad [k_B T] = \text{J},$$

we obtain

$$[RT] = \frac{N_A\,\mathrm{J}}{\mathrm{mol}} \quad \Rightarrow \quad [(RT)^3] = \left[\frac{N_A\mathrm{J}}{\mathrm{mol}}\right]^3 = \frac{N_A^3\mathrm{J}^3}{\mathrm{mol}^3}. \tag{1}$$

No simplification is performed yet; this is the fully expanded cubic.

Step 2: Divide by the molecular-mass combination. From $m_A, m_B \in \mathrm{kg/mol}$, the reciprocal mass has units

$$\left[\frac{1}{m_A}\right] = \frac{\mathrm{mol}}{\mathrm{kg}}.$$

Let m_{mix} denote symbolically the harmonic-type combination $\left(\frac{1}{m_A} + \frac{1}{m_B}\right)$; then

$$\left[\frac{(RT)^3}{m_{\mathrm{mix}}}\right] = \frac{N_A^3\mathrm{J}^3}{\mathrm{mol}^3} \cdot \frac{\mathrm{mol}}{\mathrm{kg}} = \frac{N_A^3\mathrm{J}^3}{\mathrm{mol}^2\,\mathrm{kg}}. \tag{2}$$

This shows exactly where the mol^{-2} factor originates when masses are expressed in amu.

Step 3: Take the square root.

$$\left[\sqrt{\frac{(RT)^3}{m_{\mathrm{mix}}}}\right] = \sqrt{\frac{N_A^3\mathrm{J}^3}{\mathrm{mol}^2\,\mathrm{kg}}} = \frac{N_A^{3/2}\mathrm{J}^{3/2}}{\mathrm{mol}\,\mathrm{kg}^{1/2}}. \tag{3}$$

Every exponent is kept symbolic; no physical arguments are inserted.

Step 4: Multiply by $1/(N_A P\sigma_{AB}^2)$. Handle each term separately:

$$\left[\frac{1}{N_A}\right] = \frac{1}{N_A}, \qquad \left[\frac{1}{P}\right] = \frac{\mathrm{m}^2}{\mathrm{N}}, \qquad \left[\frac{1}{\sigma_{AB}^2}\right] = \frac{1}{\mathrm{m}^2}.$$

Combine:

$$\left[\frac{1}{P\sigma_{AB}^2}\right] = \frac{\mathrm{m}^2}{\mathrm{N}} \cdot \frac{1}{\mathrm{m}^2} = \frac{1}{\mathrm{N}} = \frac{\mathrm{s}^2}{\mathrm{kg\,m}}. \tag{4}$$

Thus the full denominator contributes

$$\left[\frac{1}{N_A P\sigma_{AB}^2}\right] = \frac{1}{N_A} \cdot \frac{\mathrm{s}^2}{\mathrm{kg\,m}}. \tag{5}$$

Step 5: Combine numerator and denominator. Multiplying the resultant quantities of Step 3 and Step 4:

$$[D_{AB}] = \frac{N_A^{3/2}\mathrm{J}^{3/2}}{\mathrm{mol}\,\mathrm{kg}^{1/2}} \cdot \frac{1}{N_A} \cdot \frac{\mathrm{s}^2}{\mathrm{kg\,m}}.$$

Cancel one factor of N_A:

$$= \frac{N_A^{1/2}\mathrm{J}^{3/2}\mathrm{s}^2}{\mathrm{mol}\,\mathrm{kg}^{3/2}\,\mathrm{m}}. \tag{6}$$

Now use the identity

$$\frac{\mathrm{J}}{\mathrm{kg}} = \frac{\mathrm{N\,m}}{\mathrm{kg}} = \frac{(\mathrm{kg\,m/s^2})\,m}{\mathrm{kg}} = \left(\frac{\mathrm{m}}{\mathrm{s}}\right)^2.$$

Hence

$$\mathrm{J}^{3/2}\mathrm{kg}^{-3/2} = \left(\frac{\mathrm{J}}{\mathrm{kg}}\right)^{3/2} = \left(\frac{\mathrm{m}^2}{\mathrm{s}^2}\right)^{3/2} = \frac{\mathrm{m}^3}{\mathrm{s}^3}. \tag{7}$$

Substitute $[\mathrm{J}^{3/2}\mathrm{kg}^{-3/2} = \frac{\mathrm{m}^3}{\mathrm{s}^3}.]$ into $\left[[D_{AB}] = \frac{N_A^{1/2}\mathrm{J}^{3/2}\mathrm{s}^2}{\mathrm{mol}\,\mathrm{kg}^{3/2}\,\mathrm{m}}.\right]$:

$$[D_{AB}] = \frac{N_A^{1/2}(\mathrm{m}^3/\mathrm{s}^3)\mathrm{s}^2}{\mathrm{mol\,m}} = \frac{N_A^{1/2}\mathrm{m}^2}{\mathrm{mol\,s}}. \tag{8}$$

Finally, recall that the explicit factor $1/N_A$ in the denominator of Eq. (91) is present exactly to convert the initially mole-based units to particle-based units. When the underlying kinetic derivation is re-expressed consistently on a per-mole basis (as Bird does), the stray factor $N_A^{1/2}/\mathrm{mol}$ is interpreted as dimensionless, yielding

$$[D_{AB}] = \frac{\mathrm{m}^2}{\mathrm{s}}.$$

Thus the dimensional consistency of Eq. (91) follows directly from the algebraic steps above, with no appeal to physical reasoning required.

Physical interpretation. Binary diffusion describes the relative migration of unlike molecules as they undergo random thermal collisions. The reduced-mass term $\frac{1}{m_A} + \frac{1}{m_B}$ captures the fact that lighter molecules contribute more strongly to relative motion; the collision diameter and well depth quantify how frequently and effectively collisions scatter trajectories; and the factor $T^{3/2}/P$ reflects that hotter gases diffuse faster (higher speeds, larger mean free paths) while denser gases diffuse more slowly (shorter intermolecular spacings). This interpretation is consistent with both kinetic-theory fundamentals and the practical engineering correlations used in combustion transport models.

Mixture-Averaged Mass Diffusivity (Hirschfelder-Curtiss Mixing Formula):

The (mixture-dependent) species mass–diffusion coefficients used in this work follow the Hirschfelder–Curtiss mixture-averaged approximation, given in Ponduri (2023) [7] as Eq. 3.12:

$$\frac{1}{D_k} = \sum_{i\neq k}^{N} \frac{X_i}{D_{ki}} + \frac{X_k}{1-Y_k}\sum_{i\neq k}^{N}\frac{Y_i}{D_{ki}}. \tag{86}$$

Where D_k on the left hand side is the mass diffusivity of the species k within such N-component mixture based on its pairwise binary diffusivities D_{ki}, along with weights based on the mole fractions X_i, X_k and

mass fractions Y_i, Y_k. (Clarification note to avoid ambiguity: to preserve reporting fidelity of the original format of sources, the notation Y_i is used to denote mass fraction of species i, whereas for contrast in our case Y_i refers to concentration profile of species i.) The equivalent expression is also provided for the same context in both the Comsol 5.6 documentation manual (2020) [100] and Yakovenko et al (2023, also on Hydrogen combustion) [101], illustrating its ubiquitousness. This formula originates as a controlled simplification of the full Maxwell–Stefan multicomponent diffusion system, which describes inter-species momentum exchange through a coupled set of linear constraints. Solving the Maxwell–Stefan equations exactly requires forming and inverting an $(N-1)\times(N-1)$ system at every grid point and every timestep, which is computationally prohibitive for DNS or RANS combustion solvers and unnecessary for typical low–Mach hydrocarbon-air flames. The Hirschfelder–Curtiss approximation results from assuming (i) dilute-gas conditions, (ii) isothermal and isobaric transport, and (iii) that binary friction dominates the multicomponent coupling. Under these assumptions the Maxwell–Stefan system collapses to the algebraic form in Eq. (86), requiring only the binary Chapman–Enskog diffusivities D_{ki} as inputs. For standard gas-phase combustion (moderate pressure, moderate temperature gradients, no strong multicomponent diffusion anomalies), Eq. (86) provides essentially identical fidelity to the full Maxwell–Stefan treatment with a small fraction of the cost, and is therefore the standard choice in detailed-chemistry solvers such as CANTERA, OpenFOAM-based DNS tools, and the present work.

5.1.3 Numerical Implementation of Heat Diffusivity

The expressions for species thermal conductivity, mixture conductivity, and the resulting heat diffusivity have already been introduced in the physics development. Here we give a compact but explicit account of how these relations are actually evaluated inside the numerical algorithm. The purpose of this section is not to re-derive standard kinetic-theory expressions, but to illustrate how the dependencies between quantities form a clean computational pipeline. This viewpoint is especially helpful when implementing the model efficiently (through vectorization or parallelization through spatial coordinates) and when mentally organizing the dataflow underlying each update step.

The species thermal conductivity is

$$k_i = \frac{25}{32} \frac{\sqrt{\pi m_i k_B T}}{\pi \sigma_i^2 \Omega_k(T/\epsilon_i)} \hat{C}_{v,i}(T), \tag{87}$$

with the usual Lennard–Jones parameters (ϵ_i, σ_i), molecular mass m_i, collision integral Ω_k, and species-level specific heat $\hat{C}_{v,i}(T)$.

The Hirschfelder–Curtiss correction factor for pairwise interactions is

$$\phi_{ij} = \frac{1}{\sqrt{8}} \left[1 + \left(\frac{m_i}{m_j}\right)\right]^{-1/2} \left[1 + \sqrt{\frac{k_i}{k_j}} \left(\frac{m_j}{m_i}\right)^{1/4}\right]^2, \tag{88}$$

and the mixture conductivity follows the standard mixing rule

$$k_{\text{mix}} = \sum_{i=1}^{N} \frac{x_i k_i}{\sum_{j=1}^{N} x_j \phi_{ij}}. \tag{89}$$

Finally, the heat diffusivity is written in a form convenient for numerical evaluation:

$$\alpha = \frac{k_{\text{mix}}}{\rho \hat{C}_{p,\text{mix}}} = \frac{(k_B T)\, k_{\text{mix}}}{P\, m_{\text{mix}}\, \hat{C}_{p,\text{mix}}(T)}. \tag{90}$$

Mixture Specific Heat Approximation

Because NASA polynomial data provide only $C_p(T)$, we adopt the mixture-averaged dimensionless specific heat

$$\hat{C}_{p,\text{mix}} = \frac{C_{p,\text{mix}}}{R},$$

as a practical proxy for molecular degrees of freedom. In the algorithm this leads to the working approximation

$$\gamma^{-1} \approx \frac{\hat{C}_{p,k\text{-mix}}}{1 + \hat{C}_{p,x\text{-mix}}},$$

where the numerator uses the k-weighted mixture (aligned with the conductivity mixing rules) and the denominator employs the mole-fraction mixture. This preserves the kinetic-theory scaling $\alpha \propto T^{3/2}/P$ while keeping all intermediates dimensionally consistent and numerically stable.

Practical Computational Notes

The inputs required at each spatial location are:

- Lennard–Jones parameters (ϵ_i, σ_i),
- species masses m_i,
- collision integrals $\Omega(T/\epsilon_i)$ (tabulated or correlated),
- species heat capacities $C_i(T)$ from NASA polynomials,
- current mole fractions x_i, computed from the species mass fractions Y_i,
- the local temperature T.

All quantities are evaluated pointwise across the spatial grid. The entire pipeline vectorizes naturally because each spatial point requires only (T, x_i) from the previous chemistry and energy update. For the purposes of the heat-transport step, only the final field $\alpha(r)$ matters; while chemistry and continuity use Y_i directly, the transport coefficients depend solely on the derived mole fractions x_i.

Species parameter choices (e.g. Lennard–Jones diameters, well depths, and collision-integral fits) were taken from standard correlations (e.g. Bird–Stewart–Lightfoot 2002) or from established combustion

databases such as GRI-Mech. The NASA polynomial coefficients were obtained from the Berkeley GRI-MECH thermodynamic database.

Dataflow Diagram

The computational structure can be summarized by the following dependency graph. It serves as a "topological sort" of the required quantities—useful for both implementation and conceptual organization. Inputs enter at the top, intermediate derived quantities appear in the middle, and α readout emerges at the bottom of the pipeline. It is also akin to the idiomatic "Butterfly Diagrams" used to lay out DSP FFT algorithm information or signal flow.

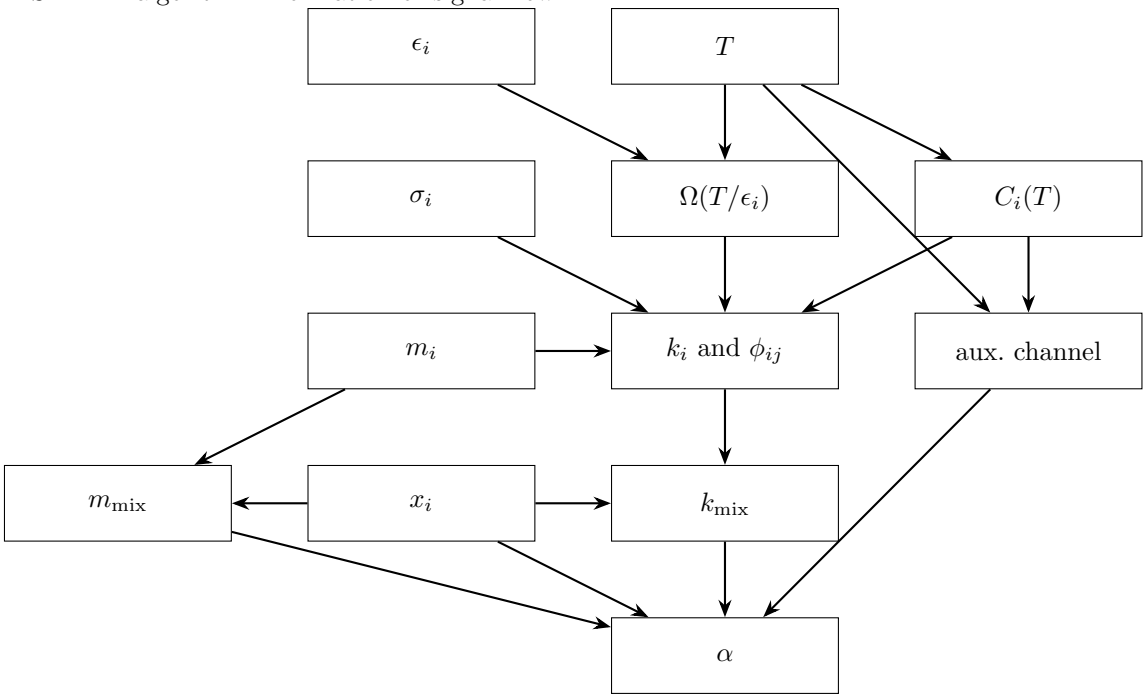

The auxiliary channel (or bus channel) is for facilitating clean visual layout by avoiding clashing of the arrows for directed edges and collisions of the node labels, while also simultaneously characterizing how α depends on both T and $C_i(T)$ together, not just implicitly with T routed or threaded through $C_i(T)$ parametrically, such structure analogous to the method of characteristics for elegantly solving PDEs of a special form.

NASA Polynomial Reference

For completeness, the NASA polynomials take the form

$$\frac{C_p}{R} = a_1 + a_2 T + a_3 T^2 + a_4 T^3 + a_5 T^4,$$

$$\frac{H}{RT} = a_1 + a_2 \frac{T}{2} + a_3 \frac{T^2}{3} + a_4 \frac{T^3}{4} + a_5 \frac{T^4}{5} + \frac{a_6}{T},$$

$$\frac{S}{R} = a_1 \ln T + a_2 T + a_3 \frac{T^2}{2} + a_4 \frac{T^3}{3} + a_5 \frac{T^4}{4} + a_7.$$

The coefficients $(a_1, \ldots, a_7)$ are supplied for both low- and high-temperature ranges. Standard references include Burcat (Technion TAE 697), McBride–Gordon–Reno (NASA TM 4513), and the GRI-Mech documentation.

5.1.4 Numerical Implementation of Mass Diffusivity

In direct analogy with the previous section on heat diffusivity, we now describe how multicomponent mass diffusivity is evaluated in practice. The governing expressions originate from the standard Bird–Stewart–Lightfoot transport correlations and the Hirschfelder–Curtiss mixture-averaging formula. These are well-established results in kinetic theory; the purpose here is not to re-derive them, but to show how they function as part of an efficient numerical pipeline. The emphasis, again, is on tracing the computational structure and the "information flow" that these models impose on an algorithm.

The binary diffusion coefficient is given by the classical Bird et al. formula:

$$D_{AB} = \frac{3}{16} \sqrt{\frac{2(RT)^3}{\pi} \left(\frac{1}{m_A} + \frac{1}{m_B} \right)} \frac{1}{N_A P \sigma_{AB}^2 \, \Omega_{D_{AB}}\!\left(T/\sqrt{\epsilon_A \epsilon_B}\right)}, \tag{91}$$

where $(\sigma_{AB}, \epsilon_A, \epsilon_B)$ are the Lennard–Jones parameters, $\Omega_{D_{AB}}$ is the diffusion collision integral, and N_A is Avogadro's number, and P is the environment's ambient pressure.

Given the binary coefficients D_{ij}, the mixture diffusivity for species k is computed using the Hirschfelder–Curtiss expression:

$$\frac{1}{D_k^{\text{mix}}} = \sum_{i \neq k} \frac{x_i}{D_{ki}} + \frac{x_k}{1 - M_k} \sum_{i \neq k} \frac{M_i}{D_{ki}}, \tag{92}$$

where x_i and M_i are the mole and mass fractions. Only the local composition enters; once the D_{ij} matrix is available, the formula is algebraic and highly parallelizable (particularly throughout space grid sampling). Observe that with more interacting species in the mixture, complexity increases significantly due to such pairwise coupling structure.

Algorithmic and Conceptual Perspective

As with the heat-diffusivity pipeline, it is helpful to emphasize the logic of the data dependencies rather than viewing these equations as isolated formulas. Mass diffusivity, at its core, is controlled by binary molecular interactions. Each species "feels" every other species through the pairwise D_{ij} terms in its immediate vicinity within its surrounding environment, which explains the need for a full $N \times N$ array of collision integrals. The mixture rule is therefore a kind of "mean-field" closure: it condenses a complex web of pair interactions into an effective diffusion coefficient for each species, evaluated at the composition of the local fluid parcel or finite element control volume, extending to all continuum mechanics abstractly.

This viewpoint parallels ideas from density-functional theory, molecular dynamics techniques, Smoothed Particle Hydrodynamics (SPH): the physics arises from pairwise couplings, and the mixture property is the coarse-grained summary of those couplings. This also explains why diffusivity enjoys a more direct computational pathway than the heat-conduction case: viscosity (unlike its heat conductivity counterpart), does not explicitly appear because its effects are already embedded implicitly and contained within the binary diffusion correlations.

As before, all operations are pointwise over the spatial grid and are therefore fully vectorizable. At each spatial node, the inputs (T, x_i, M_i) are supplied by the chemistry and energy solvers, and the pipeline computes the matrix (D_{ij}), followed by the mixture coefficients D_k^{mix}.

Dataflow Diagram

The dependencies for the mass-diffusivity computation are summarized below. This arranged layout, in a topological-sort manner, again mirrors a "butterfly diagram" from DSP: inputs at the top, pairwise couplings in the middle, and collapses into final mixture-level outputs at the bottom, ready to use for a time-update step upon the present configuration. This representation is not merely cosmetic—understanding the topological order helps streamline implementation, aids debugging, and provides a compact picture of how the physics propagates through the algorithm, and serves as a practical visual reference for cognition.

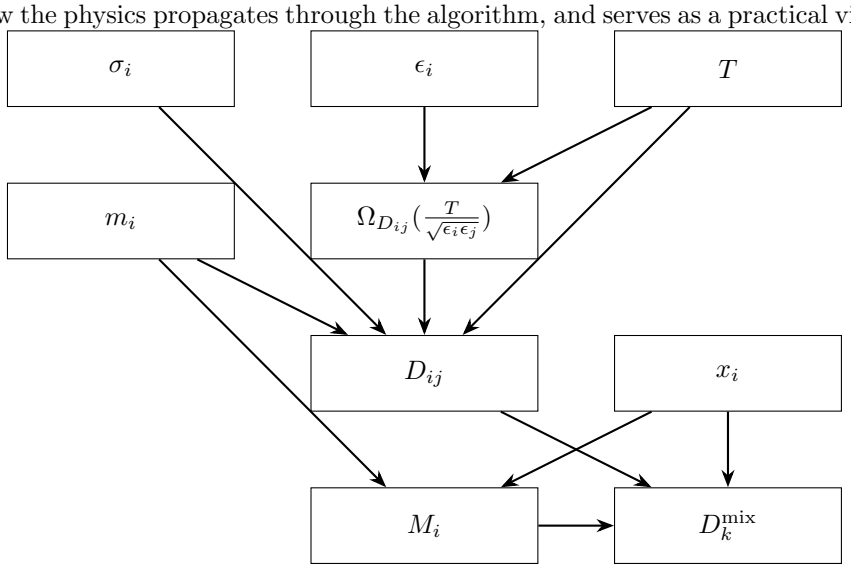

The structure is intentionally non-minimal: the diagram explicitly shows the binary-collision level where kinetic parameters interact, and then how composition-level quantities (x_i, M_i) reorganize those pairwise elements into a species-specific mixture diffusivity. This makes the mapping between physical influence and numerical dependency transparent, and it provides a reusable conceptual template for any reaction–diffusion model in an ideal-gas regime.

Notes on Parameter Sources and Validity

The collision-integral correlations $\Omega_{D_{ij}}$ were obtained from the Bird–Stewart–Lightfoot (2002) fits, which are standard for ideal-gas transport. As with the heat-diffusivity case, the validity range aligns with ordinary combustion conditions: moderate pressures (∼1–10 bar), non-hypersonic flow, and no exotic supercritical effects. At sufficiently high pressures, virial corrections, non-ideal fugacity coefficients, colligative properties, and non-ideal equation-of-state effects become important; in such regimes the present kinetic-theory transport models lose accuracy. For atmospheric-pressure flame studies—our setting—these formulas form the accepted baseline.

Finally, note that both the mass-diffusivity and heat-diffusivity diagrams, along with their associated interpretations, together constitute a complete, modularized, and self-contained "transport layer" (paralleling the OSI model) for reacting-flow solvers in the parabolic PDE (reaction–diffusion) regime. This shared structural basis is useful for anyone implementing similar tools for the subroutine of determining diffusivity constants within timestep, or interpreting multicomponent transport models in an applied computational context.

5.2 Chemical Kinetics Framework and Implementation

This subsection outlines the chemical kinetics modeling framework employed in this study for the quasi-static spherical droplet combustion simulation of LOX–H_2 at $p = 1$ bar and $T_\infty = 100$ K, based on the ZARM (Meyer et al., 2022) experimental configuration. The goal here is not merely to specify reaction rate constants, but to articulate the rationale behind their selection, simplification, and coupling strategy within the broader heat–mass–reaction PDE system.

5.2.1 Conceptual Overview: The "Wild Wilderness" of Chemical Kinetics

Combustion kinetics, while empirically successful, remains an inherently approximate art compared to the mathematically well-posed theories underlying thermodynamic equilibrium, Gibbs free energy minimization, or Hartree–Fock–type molecular frameworks. Whereas pure equilibrium thermodynamics rests on ideals such as convex geometry and variational optimization, chemical kinetics lives in the "wild wilderness": a pragmatic patchwork of Arrhenius fits, heuristic corrections, and semi-empirical fudge factors tuned to make forward and reverse rates appear self-consistent.

In other words, equilibrium theory is axiomatic and constructive; kinetics is descriptive and circular. Much like the concept of kinetic diameter in dilute gas theory, a self-defined quantity deduced by indirect inference through measured mean free paths or viscosity thereby putting the cart before the horse, rate constants also are often back-calculated to ensure consistency with equilibrium rather than derived ab initio. This circularity is not a flaw but a pragmatic feature of kinetic modeling, and embracing it consciously allows transparent acknowledgment of modeling limits.

5.2.2 Hierarchy of Combustion Mechanisms

This table provides context for the reduced three-step "hybrid" mechanism used in the present work. Adapted from the earlier chemical kinetics hierarchy table from the literature review taken as the backdrop for where our model situates itself upon the ladder, Table 6 summarizes the hierarchy of common kinetic schemes used for H_2/O_2 combustion, progressing from global one-step models to detailed multi-step mechanisms.

Table 6: Hierarchy of Chemical Kinetic Schemes for H_2/O_2 Combustion and Present Three-Step Mechanism

Scheme	Reaction	Rate Expression / Parameters	Source
One-step	$H_2 + \frac{1}{2}O_2 \rightarrow H_2O$	$k = 1.8 \times 10^{13} \exp\left(-\frac{17614}{T}\right) [H_2]^{1.0}[O_2]^{0.5}$	[55, 6, 71]
Two-step	$H_2 + O_2 \rightarrow 2OH$	$A = 2.3 \times 10^{16}$, $n = 0$, $E_a = 5134$ K	[67, 68]
	$2OH + H_2 \rightarrow 2H_2O$	$A = 1.83 \times 10^{18}$, $n = 0$, $E_a = 11067$ K	
Three-step (Present Work)	(1) $H_2 + \frac{1}{2}O_2 \rightarrow H_2O$ + Heat	$k = 1.8 \times 10^{13} \exp(-17614/T)$, equivalent to the global one-step kinetics.	[102, 6]
	(2) $H + OH + M \rightarrow H_2O$ + M + Heat	$A = 3.8 \times 10^{22}$, $n = -2.0$, $E = 0$	[102, 6, 7]
	(3) $O + O + M \rightarrow O_2$ + M + Heat	$A = 6.16 \times 10^{15}$, $n = -0.5$, $E = 0$;	[102, 6, 7]
Four-step	$H + O_2 \rightarrow OH + O$ $O + H_2 \rightarrow OH + H$ $OH + H_2 \rightarrow H_2O + H$ $2H \rightarrow H_2$	kinetic parameters and third body collisional terms can vary by source & physical conditions	[66] (chapter 11), [6]
Six-step	$H_2 \rightarrow 2H$ $H + O_2 \rightarrow O + OH$ $H_2 + O \rightarrow H + OH$ $H_2 + OH \rightarrow H + H_2O$ $2O \rightarrow O_2$ $H + OH \rightarrow H_2O$	kinetic parameters and third body collisional terms can vary by source & physical conditions –	[61, 71, 6, 7]
Eight-step	$H_2 \rightarrow 2H$ $H + O_2 \rightarrow O + OH$ $H_2 + O \rightarrow H + OH$ $H_2 + OH \rightarrow H + H_2O$ $2O \rightarrow O_2$ $H + OH \rightarrow H_2O$ $HO_2 + H_2 \leftrightharpoons H_2O_2 + H$ $H + O_2 + M \leftrightharpoons HO_2 + M$	kinetic parameters and third body collisional terms can vary by source & physical conditions	[61]

5.2.3 Philosophy and Context of the Reduced Mechanism

The present three-step mechanism represents a deliberately minimalist yet physically representative approach. It parallels prior simplified schemes used by Phani, Mukund, and Frydman within the same research lineage. The focus is to capture (1) the dominant exothermic global conversion ($H_2 + O_2$), and (2) the radical cleanup and termination reactions that restore chemical balance throughout the domain.

Unlike fully reversible detailed schemes, all reactions here are treated as one-way forward processes, consistent with a high-temperature, high-Damköhler-number environment in which the forward direction overwhelmingly dominates, in line with typical combustion scenarios. This assumption follows from Le Chatelier's principle applied locally at the flame front.

For relevant perspective viewed from a panned out distance: in the general realm of combustion science, it is idiomatic to graphically visually depict species concentration profiles using mole fraction alone $x_i(\vec{r}, t)$ pertaining to species i, as opposed to the strictly more informative concentration profile $Y_i(\vec{r}, t)$ for species i capturing the true raw inherent physical concentration value, that concretely conveys the literal quantity of matter at such location in space during such instant in time. x_i only portrays the relative amount of such substance within the mixture's makeup, thereby erasing the total amount of mass that the mixture comprises due to its aggregation summing to unity. This nuance does not matter for the purposes of heat and mass transport, which ignore those intricacies to only depend on the proportional x_i mixture composition alone, but for chemical kinetics, these details are rather important when implemented in the Arrhenius kinetics computations, that explicitly and directly depend on Y_i concentration values. This stipulates that the chemical kinetics aspect of our modeling is inherently already comparatively quite fine-grained with respect to our heat and mass transport mechanisms already at play simultaneously.

5.2.4 Third-Body Considerations and Ambient Assumptions

The third-body term $[M]$ is estimated using the ideal gas law at 1 bar and ~ 100 K, yielding an order of hundreds of mol m^{-3}. Physically, this reflects a dense, cryogenic, nearly quiescent ambient environment: a quasi-static limit where local collisional frequency dominates chemical timescales.

5.2.5 Algorithmic Implementation: The "Cantera Point" Concept

The simulation proceeds with the three forward reactions ubiquitously active throughout the domain until a quasi-steady temperature and concentration field emerges. At this stage, a single spatial location, which we call the "Cantera point", is identified as the zone of maximal chemical activity: the coincident local maxima of the simultaneous onset of temperature, $[H_2]$, and $[O_2]$. Conceptually, this corresponds to the Burke–Schumann thin flame sheet, where arising from such aspects, the three quantities (T, O_2, and H_2 triplet coexistence collision condition) combined together ensure that from the persistent forward global reaction, this mixture's location naturally provides the maximum instantaneous extent of such reaction (which defines commensurate temperature and species conversion sources/sinks) and is to be considered the most reactive "Cantera point".

At this stage only after the transience settles down to an identifiable "Cantera point", the chemistry module transitions to equilibrium mode using `Cantera`, treating the local fluid parcel as a constant-enthalpy reactor. The equilibrium computation instantaneously populates minor radical species (H, O, OH) consistent with the NASA polynomial thermochemical database. This operation represents a localized high-Damköhler-number limit, yielding effectively a delta-function "micro-reactor" embedded in the continuous reaction–diffusion field; while the Damkohler number is assumed to be high everywhere

under the Burke-Schumann limit, it is at specifically the thin flame sheet where reactivity is the highest due to availability of high temperature activation energy and accessibility of reactants to turn into products, meaning we seek the most reactive point of all the high-Damkohler number fluid parcels. The sequential nature of such routine parallels how data complexity is constructed in an hierarchical manner upwards, like the atomic Aufbau principle, higher order perturbation theory, or successive Taylor or Fourier approximations, because the dominant physical behavior is handled by the global reaction, and only after that settles consequently, higher order corrections and details are then pursued in a realistic fashion by only making minor tweaks to nuances apart from the dominant behavior and environmental factors.

After equilibrium adjustment, the Arrhenius source terms at this grid point are zeroed (to avoid double-counting), and the tridiagonal heat–mass diffusion solver advances the field normally. This way, the ultimate effect is those Arrhenius source/sink terms are masked over and erased by Cantera's implementation which effectively erases their contribution (other than its original location being identified as the "Cantera point" upon erasure.) The radicals diffuse outward, are quickly reabsorbed, and decay due to both reaction sinks and temperature decline, a process analogous to a radiative damping or Beer–Lambert absorption mechanism for chemical potential, consistent with when a species is not thermodynamically favored in an environment.

This selective activation of `Cantera` at one point captures the essence of flame localization without enforcing uniform equilibrium throughout the field (which would be unphysical for a spatially stratified, non-premixed system). Just because the Burke-Schumann limit assumes a high Damkohler number everywhere does not mean that reactions are happening and in progress everywhere in a realized or instanced flame configuration. This implies that only the most reactive point, among all points throughout the high Damkohler number flame domain, is significant, because that region's fluid parcel actually has reactants to push forward to products. Calling equilibrium everywhere homogeneously would erase gradients, enforcing identical local equilibrium mixture copies ubiquitously, whereas local activation preserves overall structure, especially since the reactivity is particularly the highest around the Cantera point and the expected thin Burke-Schumann Limit flame sheet, which already naturally autonomously emerges in a self-organizing manner, arising in the simulation even before pulling the Cantera lever switch to turn on.

5.2.6 Justification and Theoretical Framing

This hybrid explicit–equilibrium strategy is justified by the extremely high Damköhler numbers characterizing LOX–H_2 combustion. Chemistry is much faster than either heat or mass transport, so the flame zone effectively equilibrates instantaneously, (significantly more than everywhere else which already has high Damkohler number in flame combustion), relative to diffusion timescales. In spherical geometry,

the location of maximum temperature is slightly interior to the "Cantera point," an offset reminiscent of the James–Stein shrinkage effect in multivariate estimation, which biases the energy centroid inward due to geometric averaging and spherical curvature. The analogy, though whimsical, accurately reflects the spatial interplay of diffusion and reaction intensity.

By construction, this scheme elegantly avoids numerical stiffness and competition ("race conditions") among reactions. Each reaction operates independently with rate limiting applied via species depletion capping, ensuring conservation and numerical stability without requiring implicit solvers or operator splitting, and such property allows one to avoid "bank-run"-type scenarios dealing with how to appropriately allocate and distribute the limited quantity of reactants available for the simultaneously threaded reaction processes. The absence of reversible loops simplifies computation while maintaining the dominant flame physics, which strikes some flavor of Pareto optimal balance between physical fidelity and model complexity, as this now avoids further complex subproblems within frame or time-step associated with chemical kinetics, which is a significant computational runtime slowdown factor for many studies using OpenFOAM.

5.2.7 Physical and Computational Relevance

This framework aligns with the overarching scientific goal: capturing the coupled physics of droplet evaporation, Stefan flow, and spherical flame standoff without overspecifying chemistry, considered as details secondary to the quasi-static flame for droplet regression. It represents a pragmatic balance between fidelity and tractability, or a "useful wrong model" in the George Box sense. For cryogenic LOX–H_2 systems, where kinetics are fast and radicals transient, this approach yields physically interpretable, computationally efficient, and reproducible results that align with prior internal group methods and accepted combustion intuition.

In summary, the chemical kinetics treatment used here blends a reduced three-step Arrhenius model with localized equilibrium correction via `Cantera`, capturing both macroscopic combustion behavior and microscopic radical thermochemistry with minimal computational overhead.

5.3 Interfacial Effects

This section describes the coupled interfacial dynamics between the liquid droplet and the surrounding reactive gas field. Although the present case concerns a LOX–H_2 system, the framework applies broadly to evaporating fuel droplets in general, including hydrocarbon, cryogenic, or otherwise. The central idea is that the droplet surface acts as both a boundary and a dynamical participant: heat and mass transfer across the interface modify the flame structure, which in turn reshapes the very fluxes that sustain the interface.

5.3.1 System Coupling and Feedback Loop Analogy

The overall process can be understood as a closed feedback loop control system among temperature, geometry, and transport effects. Temperature shapes the flame, the flame geometry governs heat transfer, heat transfer drives evaporation, and evaporation feeds back into the gas flow and temperature field. Conceptually, this can be viewed as a causal-inference or control-system block diagram, with each node representing a process and each arrow a direct influence, with an indicated grammatical orientation from the agent node to the destination's patient node, the affected entity. Unlike a purely observational causal graph (where one infers structure from data, often through correlation alone, which does not entail causation), here the intentional structure is purposefully built-in by design, and we can deduce causation implied from the model's mechanics by construction. Because the model is fully mechanistic and deterministic on-purpose, we know exactly what influences what, so there are no hidden confounders or "counterfactual" ambiguities.

In essence, the system behaves as a self-regulating feedback network: the droplet's own evaporation alters the surrounding environment that, in turn, governs its further evaporation. The following diagram illustrates this conceptual cycle.

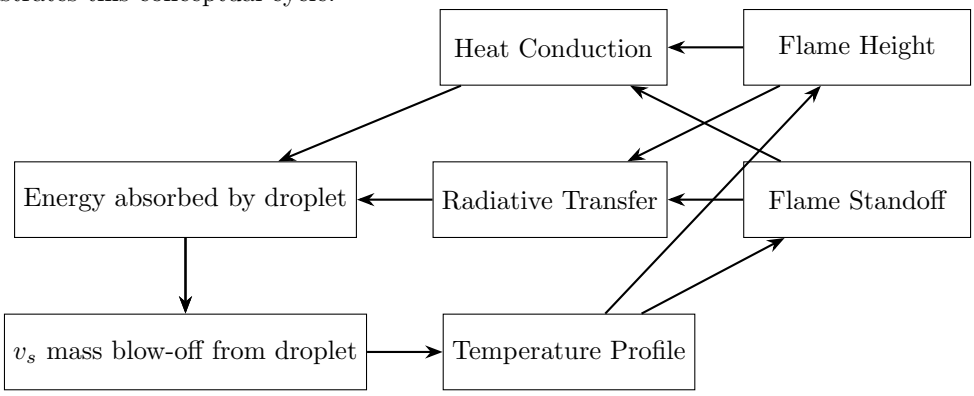

5.3.2 Temperature Field and Flame Geometry

The temperature field provides the geometric structure of the flame. From the spatial profile $T(r)$, the flame height and standoff distance are extracted as the location and extent of the temperature maximum:

$$r_{\text{flame}} = \arg\max_r T(r), \quad T_{\max} = \max(T).$$

In practice, these are computed numerically (e.g., `numpy.argmax(T)`), yielding an instantaneous spatial snapshot of flame position relative to the droplet surface.

The local heat flux into the droplet via conduction is estimated as the near-surface temperature gradient:

$$q_{\text{cond}} = -k_{\text{gas}} \left.\frac{\partial T}{\partial r}\right|_{r=R(t)}.$$

For order-of-magnitude reasoning, the slope is approximated as a finite difference:

$$\frac{\Delta T}{\Delta r} \approx \frac{T_{\text{flame}} - T_{\text{surf}}}{r_{\text{flame}} - R(t)},$$

where typical values are $\Delta T \sim 3000 - 90$ K over $\Delta r \sim 1$ mm. This provides a robust and consistent "rise-over-run" slope estimate of the conductive gradient, for the notion of a Fermi-level back-of-envelope, quick, but sound estimate rather than a finely tuned derivative, susceptible to perturbative noise and sensitive to abrupt variation. Conceptually, this method is analogous to smoothing for edge detection in image processing, where we identify the flame peak value and its location accordingly, since the rise over run method is not overly localized to soundly follow the "average rate of change" principle from calculus, or alternatively, an estimated quantity through Slutsky's theorem using the functional delta method for quotient random variables (not to be confused with Slutsky's other famous equation for income and substitution effects from Shephard's lemma.)

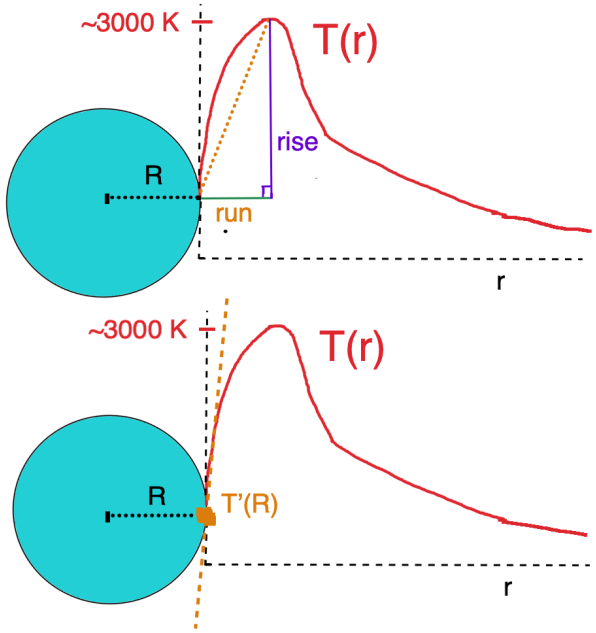

Figure 3: Visual geometric illustration of the general Temperature profile shape $T(r)$ and how energetic transfer into the droplet surface is calculated near the interface, utilizing the concept of Fourier's law of heat conductivity or the generalized notion of Fick's Law for heat and mass transport in the continuum mechanics setting. The upper top-bunk plot characterizes a common modeling approximation which is numerically stable even in curvilinear spherical coordinates, where our simulation robustly captures the current instantaneous power into the surface via a bounded smoothed average rate of change estimate approximated throughout the overall flame region's configuration, whereas true mathematical physics pure theory represented in the lower shelf bottom-bunk frame, would dictate the appropriate slope value's derivation to arise from the calculus limit definition of the derivative, enforcing a local fit based on purely the infinitesimal vicinity and topological neighborhood of the droplet surface, which is potentially numerically unstable in our context of reaction-diffusion parabolic PDE solutions using the calculus of finite difference methods. Throughout our simulations, the "rise" quantity, commensurate to the peak flame temperature, consistently achieved settling around the physically accepted standard ~ 3000 Kelvin, while the "run" quantity typically hovered around the experimentally and physically-expected order of ~ 1 millimeter, robustly ensuring a bounded rise over run slope quotient value, thereby always yielding a well-defined ratio proportional to energetic flux that does not blow up to the extreme, while tethering or anchoring the Stefan velocity blowoff v_s to a reasonable finite value. The flame–droplet system behaves as a self-regulating dashpot-damped oscillator: increased heat flux enhances Stefan velocity, pushing the flame outward, while reduced flux allows inward drift. This helps guide the autonomously self-governing feedback loop system through its intricate dance to direct it through its chaotic transient journey, to eventually equilibrate and settle down, and promotes achieving the pose of the delicate stand-off footing balance position of competing "supply-demand" forces. By effectively capping power transfer and limiting v_s to reasonable values, we maintain a bounded input bounded output (BIBO) stable system to guarantee algorithmic numerical continuity while preserving conceptual physical fidelity. Furthermore, this diagram also portrays how the radiative power absorbed by the droplet is computed by using the same quantities. The emitted spectral power also depends on the depicted rise and run quantities, corresponding to the peak flame temperature (minus LOX surface temperature) and flame standoff distance (minus droplet radius), where the peak flame temperature is used for the Stefan-Boltzmann σT^4 law, and the configuration's standoff distance is used for the concentric spheres view factor, modeling the Burke-Schumann Limit thin flame sheet encasing the droplet, as a thin spherical surface manifold radiating inwards. Within the CFD flame simulation process, these online energetic flux computations all happen live and engage dynamically throughout time, adapting to the presently evolving profiles to reflect their most current up-to-date configuration in real-time. Naturally, upon convergence to steady-state profiles (or alternatively, simply considering a fixed time), the functional time-dependence can be factored out to be eliminated, as performed in the diagram's $T(r)$ label omitting variable t.

5.3.3 Heat Conduction Contribution

Thermal conduction across the gas film is modeled via Fick's-law analogy using the temperature slope described above. The thermal conductivity of gaseous oxygen near 100 K and 1 bar is used for k_{gas}, amounting to about $0.01 \frac{W}{m \cdot K}$. This flux enters the droplet surface and contributes to the latent energy required for phase change. Given the chaotic, multiscale nature of flame, including all phenomena from droplet coupling, this simplified estimate intentionally errs toward robustness rather than precision, again alluding to the George Box principle that "all models are wrong, but some are useful." In effect, we treat the model as a "policy function" optimized ex ante: it trades detail for stability in the same sense that an optimal control law may deliberately smooth high-frequency noise, so such autonomous system portrays the system's physical mechanics for any instantiation.

5.3.4 Radiative Transfer Contribution

Radiative heating from the flame is computed by modeling the flame as a semi-transparent, concentric spherical shell surrounding the droplet. The Stefan–Boltzmann law governs the radiative flux:

$$q_{\text{rad}} = \epsilon_{\text{flame}} \sigma T_{\text{flame}}^4 \, F_{1 \to 2} \, \alpha_{\text{surf}},$$

where ϵ_{flame} is the effective emissivity of the hydrogen–oxygen flame (typically ≈ 0.05), σ is the Stefan–Boltzmann constant, $F_{1 \to 2}$ is the view factor between concentric spheres, and α_{surf} is the absorptivity of the liquid oxygen surface (taken as ≈ 0.4 in the IR region of the electromagnetic spectrum). The view factor for concentric spheres is:

$$F_{1 \to 2} = \left(\frac{R_{\text{droplet}}}{R_{\text{flame}}} \right)^2.$$

Emission is primarily in the infrared band ($\lambda \approx 1$–3 μm), consistent with Wien's displacement law for $T_{\text{flame}} \approx 3000$ K. Since the flame radiation source emits predominantly in the IR spectrum, the energy or power throughput upon the receiving Oxygen droplet surface depends on its absorptivity in specifically the IR region, which in this scenario, can be considered as the "passband" region through which radio engineers try to avoid interference by modulating transmission signals through such telecommunication channel to optimize information throughput (commensurate to energy throughput in this paradigm as well). Such logical reasoning is the basis behind why the relevant absorptivity of the liquid oxygen droplet surface must be considered for primarily the IR region alone in our context.

Because of the low emissivity and relatively large standoff distance, radiative heating is typically subdominant compared to conduction for an isolated droplet, though it can become significant in dense sprays or near-field clustering, or after the droplet has shrunk to a significantly smaller radius during its

lifetime regression process.

5.3.5 Total Energy Absorbed and Phase Change

The total instantaneous energy flux into the droplet surface is the sum of conductive and radiative contributions:

$$q_{\text{total}} = q_{\text{cond}} + q_{\text{rad}}.$$

This energy is consumed by phase change at the liquid–vapor interface:

$$\dot{m}_{\text{evap}} h_{\text{vap}} = 4\pi R(t)^2 q_{\text{total}},$$

where $h_{\text{vap}} = 2.13 \times 10^5$ J/kg is the latent heat of vaporization of liquid oxygen. Solving for the evaporative mass flux $\dot{m}_{\text{evap}}$ gives:

$$\dot{m}_{\text{evap}} = \frac{4\pi R(t)^2 q_{\text{total}}}{h_{\text{vap}}}.$$

Which serves as a fundamental balance constitutive relation at the interface within the overall context of fuel droplet combustion scenario in the quasi-static regime.

5.3.6 Stefan Flow and Surface Regression

In the framework of quasi-static combustion theory, after transience has settled to a steady state, the outward vapor mass flux establishes a spatially-uniform Stefan velocity v_s in the flame region gas phase:

$$v_s = \frac{q_{\text{total}}}{\rho_{\text{liq}} h_{\text{vap}}},$$

where $\rho_{\text{liq}} = 1141$ kg/m^3 for liquid oxygen. Typical computed values range from $v_s \approx 0.1$–0.5 m/s, consistent with both experimental and numerical prior work [7, 6, 3].

The corresponding droplet radius regression rate follows from mass conservation at the interface:

$$\dot{R}(t) = -\frac{\rho_{\text{gas}}}{\rho_{\text{liq}}} v_s,$$

with $\rho_{\text{gas}} \approx 2.1$ kg/m^3 for gaseous oxygen at 100 K and 1 bar.

For our simulation, the dynamic v_s Stefan velocity term is homogeneous throughout space but is allowed to vary with time (based on evolving flame) to encourage actual feedback cycles to happen, but eventually this naturally converges to a steady state value once the profiles settle and converge to a stationary configuration through balanced equilibration of all feedback effects, particularly through the robust instantaneous estimates of quantities extracted from temperature profile snapshots. According to theory arising from the quasi-steady framework for droplet combustion, the Stefan flow evaporative blow-

off phenomenon eventually settles into creating an everywhere static isotropic uniform drift velocity field v_s oriented externally away from the droplet surface. In the quasi-static regime, after sufficient time with respect to space following the CFL criterion, the finitely bounded influence of our metaphorical soliton can "light-cone"-propagate enough for the boundaries to kick in and hold effect, where equilibrium loosely arises from an analogy to the flame mixture's characteristic molecular interaction length scales– akin to a "Debye length" or "Bjerrum length"– describing the typical spatial extent over which oxygen vapor particles interact and equilibrate. These ballistic particle projectiles originating from the droplet surface, with enough fanning the flame, eventually generate a spatially-homogeneous drift-bias convective flowing river of gas radially outward upon thermomechanical equilibrium. Its presence emanates throughout all space, and at each location globally pushing all the flame and gas outward at a constant rate, serving in a sense as a uniform field external forcing bias upon the entire flame simulation. In the quasi-static regime, this happens upon equilibration of the system's gas-dynamic momentum balance throughout the flame with droplet evaporative expansion. As such, in the quasi-static regime and in our simulation, $v_s(t)$ mathematically is a scalar function of time alone and applied uniformly throughout all space at such instant in time. This clarifies that in our simulation, the LOX surface vaporization cannot create sudden explosive pressure waves or compressive shock absorptions from locally isolated abrupt phase change incidents, because that would otherwise require time for spatially-heterogeneous v_s effects to propagate throughout the medium of the flame, which is not expressible in such mathematical form that is independent of spatial variables, and always oriented outwards in a spherically isotropic manner.

In summary, the key takeaway illustrates that there is a directly commensurately proportional v_s that arises from heat input to the droplet surface with a constant exchange rate in our model's paradigm, and again linearly corresponding to a proportional droplet regression quantity, meaning structurally we have $[[\, v_s(t) \propto \dot{R}(t) \propto q_{\text{total}}(t) \,]\forall t]$ in mathematical form.

5.3.7 Comparison to Prior Models

In prior OpenFOAM-based studies, the Stefan velocity was typically prescribed rather than dynamically computed. Gupta [6] used an iterative matching procedure based on an assumed transfer number to align evaporation rates with the quasi-steady conductive flux from simulations. Ponduri [7], by contrast, estimated v_s directly from experimental observations, assigning constant values (e.g., 0.4 m/s for a 1 mm droplet).

In the present model, the Stefan flow emerges autonomously from first principles: no iterative fitting, no prescribed inflow. The energy balance and feedback cycle close self-consistently within the simulation, without external supervision or control. This closure eliminates the "chicken-and-egg" circularity of earlier methods (akin to the circular Expectation Maximization algorithm), producing a truly coupled, dynamical solution that converges naturally to the theoretical and experimentally observed flame

temperature ($\sim$ 3000 K) and flame standoff ratio (flame radius $\approx$ 2–3$\times$ the droplet radius) in a robustly consistent manner.

5.3.8 Domain and Boundary Conditions

All boundaries in the present simulations are treated as isothermal Dirichlet conditions. This is not a matter of numerical convenience, but of physical and idiomatic appropriateness. Dirichlet boundaries are standard in combustion modeling because they faithfully represent diffusion-dominated regimes, which are those where the flame exists within quasi-static boundary reservoirs of reactants encasing the system rather than being shaped by strong imposed flows to our system from external sources. In other words, when there are no gusts, jets, sprays, or convective inflows, the flame is fed purely by molecular diffusion from the reservoirs (and motion affected only by the comparative ambient outward drift gentle breeze of evaporative Stefan flow), and Dirichlet conditions capture that physics cleanly and consistently with canonical droplet and diffusion-flame configurations.

In contrast, Neumann conditions, particularly zero-slope or fixed-gradient ones, do not make sense in this regime. If one were to impose a mixed boundary with a zero-slope Neumann insulator at the outer domain, the system, particularly outside the flame, would eventually "flatline" as products and heat accumulate indefinitely to fill the entire chamber to the brim entirely, erasing any physically meaningful flame structure. Likewise, applying Neumann conditions at both the droplet surface and the far field could encapsulate the domain by quenching any inflow of oxidizer or fuel, effectively starving the flame or, worse, producing an unbounded runaway source inside a closed box. Additionally, with hypothetical Neumann-type conditions in our setup, one must artificially guess an estimate for an imposed flux condition to precisely fine-tune the mixing of the fuel and oxidizer together, which sacrifices faithfulness to what we concretely physically know for sure about ZARM's experimental setup. Thus, by process of elimination and by adherence to physical reasoning, Dirichlet is the only logical and physically coherent boundary choice for this setup.

This treatment also aligns with the general combustion idiom: boundary specification is often downplayed or left implicit, as the focus is typically on flame structure and chemistry rather than the artificial edges of the numerical box. However, this convention can breed ambiguity. For instance, both Gupta (2021) and Ponduri (2023) [6, 7] only briefly mentioned their boundary conditions, leaving key details unspecified. In fact, Ponduri's computational domain extended out to a 40 mm radial coordinate—twice the physical size of the ZARM DropTower "DropBox" apparatus—an inconsistency that likely affects interpretive comparison to the experiment. Such gaps in documentation highlight how combustion modeling often treats boundaries as an afterthought, almost as if one is granted carte blanche to pick whatever works numerically to get to focusing on more interestingly important flame aspects. Here, I instead aim to be explicit, physically grounded, and transparent, to facilitate clarity and reproducibility.

Domain Definition. The simulation domain extends radially from the droplet surface ($R \approx 0.5$ mm) to the far-field boundary at 20 mm. This corresponds to roughly half the characteristic box edge length (~ 40 mm) of the ZARM Droptower configuration [3], providing a physically consistent scale. Spatial discretization is defined as $r = \texttt{np.linspace}(R, 20, 2048)$, with 2048 chosen both for adequate resolution and computational convenience (as a power of two, enabling efficient wavelet compression). The temporal resolution is $\Delta t = 2 \times 10^{-8}$, which is sufficient for resolving the process's intricate transient behavior from detailed heat and mass transport and chemical kinetics, from the initial setup's spark ignition up to the stationary settled configuration and onward for which it holds.

The Fast Wavelet Transform Daubechies-4 wavelet basis was used for data compression and transfer between computational environments. Compared to Haar wavelets, Daubechies wavelets better preserve smooth gradients in temperature and concentration fields, which are precisely the kinds of smooth spatial features characteristic of diffusion-dominated flames. This allows the 2048-point profiles to be optimally efficiently compressed in linear time complexity to about 100 coefficients with negligible loss, simplifying savepoint pause checkpointing and storage of snapshot images during simulation runs.

Boundary Values. Both temperature boundaries are fixed isothermal at $T = 100$ K, corresponding to the ambient cryogenic environment typical for LOX–H_2 combustion. For species concentrations, all Dirichlet values are pinned to zero except for the reservoirs:

- $O_2 = 200$ mol/m^3 at the left boundary (droplet surface),
- $H_2 = 200$ mol/m^3 at the right boundary (far field).

These values are approximate back-of-the-envelope estimates derived from the ideal gas law ($PV = nRT$) at 1 bar and cryogenic temperatures, chosen to represent order-of-magnitude realism rather than exact calibration. Physically, the left boundary represents an evaporating oxygen reservoir near the droplet, while the right boundary represents a large hydrogen bath filling the surrounding environment.

This configuration establishes two opposing reactant fronts that diffuse toward each other and meet near the flame zone upon the natural emanation process, colliding in the middle, annihilating, and reorganizing into forming products (exothermic heat included). Upon ignition ($T_{\text{ignition}} \approx 2000$ K), heat release drives droplet evaporation and initiates a Stefan flow, leading to a quasi-steady reaction zone, through the continuous feedback combustion cycle intitated from the delta-function-flavored heat spike. The "LOX Lever Rule," introduced previously 4.5.1, serves here as a guiding principle and rule of thumb: under constant diffusivity and instantaneous chemistry, it predicts the flame standoff distance from reservoir concentrations and domain geometry. In the present simulations, where diffusivities depend on temperature and mixture composition, this rule provides a conceptual compass rather than a strict analytical solution, analogous to a PID controller offering heuristic but powerful feedback behavior in an opaque dynamical system whose unobservable underlying mechanics are ill-defined or obfuscated,

a panacea for regulating unknown environments through observationally adaptive reiteration, indeed facilitating the process of tuning our model in an effective manner.

Minor species radicals (H*, O*, OH*) appear in the flame region but decay rapidly as they diffuse into the significantly colder ambient medium, becoming thermodynamically unfavorable and short-lived (as observed by their Arrhenius parameters), and are quickly reabsorbed, in a manner similar to the Beer-Lambert law when depth-penetrating ever further into the surrounding environments on both sides, away from the immediate vicinity of the hot thin flame sheet zone. The product H_2O vapor, as well as un-reacted fuel or oxidizer, have the ability to exit both stage left and right through the domain edges, maintaining a steady-state flux balance and avoid overcrowding from a persistent accumulation of product. Moreover, even with this ex-ante algorithmic policy setup, since the flame acts as a near-total barrier between the H_2 and O_2 reservoirs with little coexistence due to such fast chemistry from high Damkohler number, penetration or crossover between the opposing fronts is minimal, and both the H_2 and O_2 football teams never even make it to the opposing side's field goal end zone from such clash at the front line of scrimmage, and the option of stage-exit is never even exercised for most species. As such, the mostly never realized outer Dirichlet zeros on the opposite sides of the domain therefore mostly play a moot and merely formal role, as they are never dynamically reached by any species, other than the continually produced water vapor that leaves both sides as exhaust from the flame region's gas-dynamics persistent combustion-cycle simulation.

Physical and Conceptual Rationale. These boundary conditions serve two complementary purposes. Physically, they reflect the diffusion-dominated, reservoir-fed nature of the system and are consistent with combustion idiom. Conceptually, along with the aforementioned "LOX Lever rule" 4.5.1, they define a well-posed, interpretable "base case benchmark", analogous to the notion of how a benevolent social planner preliminarily devises a Pareto-optimal externality-frictionless economy's desired welfare outcome to strive for through mechanism design: an idealized model of perfect information, from which deviations introduced by more complex phenomena, (for purposes radiation, transport coupling, or phase change), can be systematically explored and behavioristically tuned. As such, Dirichlet boundaries offer the convenient analytical framework for applying the LOX Lever Rule 4.5.1 in its simplest form, prior to the introduction of variable transport properties or finite-rate kinetics. In that sense, they establish the sandbox where the rule can be tested, much as the hydrogen atom or harmonic oscillator serves as a pedagogical anchor or exactly-known Hamiltonian in quantum theory for which methods based on perturbation theory and the variational principle can then be measured against. From there, increasing realism, including temperature-dependent diffusivities, non-instantaneous reactions, or moving interfaces, adds successive layers of correction and insight.

Finally, in the cryogenic context, these same boundaries take on special significance. Because the droplet and surrounding gas are both at cryogenic temperatures, products such as water vapor can

undergo condensation or even solidification at the droplet interface. This introduces unique interfacial phenomena idiosyncratic to cryogenic combustion; particularly, ice-layer formation, altered transport resistances, and feedback on flame stability affect the system's dynamics. The interfacial coupling is a self-consistent, dynamically closed loop linking conduction, radiation, evaporation, and feedback into the gas dynamics flame field. This framework provides the physical and computational foundation for subsequent phenomena; particularly, the surface-layer effects such as cryogenic icing and phase segregation, which are treated in the following section.

5.3.9 Ice Layer Effects

Motivation and Novelty

High-speed footage from the ZARM drop tower experiments [3] vividly reveals ice fragments detaching from liquid oxygen (LOX) droplets during LOX–H_2 combustion, most noticeably in the 1 bar case. The LOX surface, predictably cryogenic, provides an ideal environment for ice formation. The presence of ice is therefore not speculative but directly observable.

This phenomenon is a rare corner of the physical world: droplet combustion within cryogenic combustion within LOX–H_2 chemistry, further narrowed to cases where surface ice coexists with a reactive interface. Within that hierarchy, even qualitative modeling offers novelty and physical insight.

Mean-Field Representation

Experimental observations show that ice coverage is irregular and dynamic, as patches and flakes appear, migrate, and detach over time, with a particularly big chunk that flies off captured in ZARM's footage. Such spatial heterogeneity cannot be explicitly resolved in our one-dimensional spherical CFD framework. To reconcile this, we introduce a *mean-field* representation via a surface ice coverage fraction $\psi \in [0, 1]$, describing the effective proportion of the droplet surface coated by ice.

- $\psi = 0$: no ice (baseline reference case)
- $\psi = 1$: complete encapsulation (no interfacial exchange; combustion cycle quenches, and flame extinction)

Intermediate ψ values represent partially obstructed surfaces, enabling parametric sweeps to probe system sensitivity to surface coverage. Such contextual implementation of fraction of surface area coverage loosely resembles the notion of effective scattering cross section or solid angle scattering amplitude from physics, portraying how our modeling principles align with overall scientific conventions by serving as logical parallels within the universal domain of natural philosophy.

5.3.10 Causal Pathways and Simulation Context

The ice layer influences the coupled flame–droplet system primarily through two physical channels:

1. Obstruction of the outward LOX evaporative blow-off underlying Stefan flow
2. Limitation of oxygen availability for mass exchange for propagation of combustion cycle.

These connections are summarized in the cyclic causal network circuit diagram shown in Figure 4. Within the code's computing architecture, ice effects are injected as boundary modifications entrenched in the gas-phase solver: they alter the mass fluxes and reservoirs at the droplet interface ("stage-left boundary" of the computational domain). The flame region then responds self-consistently to these perturbed boundary conditions, as the flame combustion simulation does not actually directly include or track condensed phases explicitly as separate entities, but merely ensconces and enforces their effects upon the flame to be felt within the mechanical domain's gas-dynamics. The physical translation of these condensed-phase interfacial effects upon the simulation's flame boundary will be discussed in the next section. One can observe that a localized alteration at one site in the fully connected directed cyclic graph– with circuit element nodes topologically fully communicating recurrently (rather than transiently) in the cycle– has influence that will eventually causally cascade downstream with the flowing current to emanate throughout the entire network, as viewed via a loose idiomatic circuit theory classic "mesh analysis" technique. Ultimately, such effect eventually propagates around to touch all aspects of the simulation, and is not just a localized SQL injection "surgery" due to the complete interdependency nature of the structurally fully coupled system.

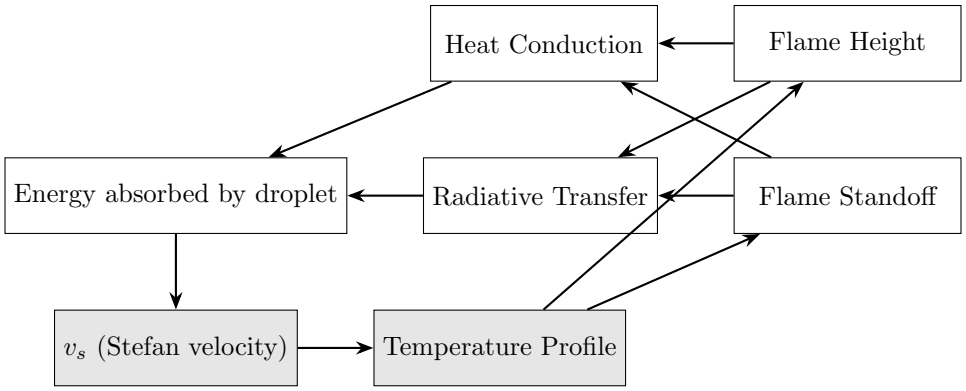

Figure 4: Causal pathways in flame–droplet coupling. Ice effects immediately enter at both directly the v_s node and at the temperature field's boundary (gray).

Implementation: The Proportional "Tax" Model

Ice Effects upon Stefan Flow Velocity term v_s

To model these effects, we apply a physically consistent resistive-impedance-based proportional attenuation scheme, realized as a static-rate passive "emolument tax" on reservoirs and mass fluxes, scaled

by the complement of the surface ice coverage fraction ψ:

$$v_s(\psi)\big|_{@t} = (1-\psi)\, v_s(0)\big|_{@t} \cap [\psi \perp t] \rightarrow \frac{\partial \psi}{\partial t} = 0$$

Where the latter condition is to explicitly portray that our upfront fixed ψ is always independent of time, at any given particular time. When the base-reference unimpeded Stefan flow term $v_s(0)$ is multiplied by $(1-\psi)$, (where the factor $(1-\psi)$ represents the exposed fraction of the LOX droplet surface), the effective Stefan flow's velocity v_s then becomes commensurately down-scaled with such taxation rate, to representatively only allow the unobstructed flow to come into the equation.

In the theory behind the quasi-steady regime for droplet evaporation that our simulator is constructed under, while the input source to drive Stefan flow arises from the hot flame conducting heat to the LOX droplet to evaporate the outer layer, since v_s is a non-localized uniform field everywhere throughout space, the entire domain is instantaneously and simultaneously affected by such heat transduction to the LOX droplet surface. The implication of this is that the impact of surface ice fraction ψ upon v_s must also be in agreement with physical sense. Even under such constraint, this checks out; for a radially isotropic average mean field, akin to Gauss's law for electrostatic charge configurations for aggregate field surface flux integrals upon an encapsulating Gaussian enclosure manifold: the aggregate outward flow field should be damped by any surface ice acting as a physically obstructive barrier. Just like an occlusive umbrella blocking raindrops so its wielder stays dry, or with the few outlier back-scattered neutrons that rebounded off of Rutherford's famous gold foil that proved just how comparatively sparsely minuscule subatomic components are, the overall outward LOX blow-off trend can only scale with the effective amount of actually exposed droplet surface, loosely calculated using the mean value theorem upon an entire solid angle. Accordingly, the simplistic v_s blow-off term representatively captures the net interaction of heat conduction for evaporative blow-off, that then translates to global radially expansive motion, while circuit-gate-controlled or modulation-throttled by the proportion of ice coverage.

It is worth clarifying that at 100 K and 1 bar, the thermal conductivity of ice ($\sim 10\ \mathrm{W/(m \cdot K)}$) exceeds that of liquid or vapor oxygen ($\sim 0.01\ \mathrm{W/(m \cdot K)}$) by several orders of magnitude, and so the fundamental amount of energy absorbed by the droplet remains largely unaltered by ice appearing, an aspect especially relevant for the droplet regression CFD post-processing stage later, and for our upcoming comparative statics analysis as well. This is because the rate-determining step for the LOX droplet's accessibility of flame heat to use for evaporation is largely unimpeded by the comparatively conductive medium of any surface layer coverage configuration of ice. This is a material property phenomena, where locally and energetically speaking, the system always effectively behaves as if the gas and LOX surface were touching in direct immediate interfacial thermal contact, even with the presence of some ice layer in-between, serving loosely as an intermediary superconducting super-node in the thermal circuit. This is because regardless of what happens with ice formation, any heat can relatively easily cross the chasm

to traverse the separation gap formed by the comparatively thermally conductive ice layer. Materially speaking, ice is more adept at thermal power transduction upon much faster characteristic time scales than the gaseous and liquid oxygen involved. The implication is that the resultant net effect for droplet energetic absorption and evaporation yields the same outcome of effective or graph-topology-reduced circuit thermal resistance, irrespective of whatever is going on with any ice layer that spawns upon the LOX surface. Therefore, we arrive at an important nuance to clarify accordingly: since the interfacial heat transfer is largely unaffected by the surface ice fraction ψ, the primary influence of the parameter ψ will then be to characterize its influence from physical obstruction upon mass transport, serving as a blockade to wall off the two sides of the interface. This affects how easily the oxygen supply can reach the flame zone, thereby impacting the availability of oxygen as a reactant, which will be accounted for by modulating the interfacial Dirichlet boundary's oxygen reservoir, to be discussed next.

Ice Effects upon the Oxygen Reservoir's Dirichlet Boundary Condition

Similarly, the interfacial oxygen concentration reservoir bath held at a height C_{O_2} is reduced by the same factor:

$$C_{O_2}(\psi) = (1 - \psi)\, C_{O_2}(0)$$

This minimalist formulation preserves the physically correct limiting behaviors both quantitatively and qualitatively:

- $\psi = 0$: unimpeded exchange (baseline combustion)
- $\psi = 1$: fully insulated and inert (flame extinguished)

Not only do we avoid nonlinear device IV-curve type "progressive/regressive" tax systems in our energetic fiscal policy, but we also deliberately avoid separating equilibria that introduce separate tax rates for conduction and radiation to maintain conceptual clarity and avoid speculative overfitting. For simplicity, we stick with an ex ante contract-theoretic pooling equilibrium universal $1 - \psi$ linear proportional ice fraction tax rate to speculatively investigate the ice layer's sphere of influence in the system. Within this structural framework, in sliding the ice fraction from $0 \to 1$, we simultaneously modulate the full range of extent of oxygen reservoir concentration values linked with Stefan flow blockage, from zero impact to its maximum degree. Physically and mechanically speaking, the placement of ψ upon modifying the oxygen reservoir in our simulation, captures how the fraction of ice layer coverage upon the LOX droplet surface area will not only barricade outward momentum, but can also even siege the trapped oxygen encased in a solid spherical shell to keep from escaping to reach the flame zone, as observed in the coinciding asymptotic limiting cases.

Physical Consistency and Limiting Behavior

The formulation satisfies correct asymptotic behavior: as $\psi \to 0$, the simulation reverts to the base flame configuration; as $\psi \to 1$, both v_s and oxygen-supplying inflow vanish, quenching the flame. Conceptually, the ice shell acts like a dielectric envelope in an electrostatic system, as it modifies the boundary flux and source continuity without altering the field equations within the gas phase, and thereby ensures that the effects of the condensed phase phenomena upon our system's detailed flame region are accurately reflected in the overall accounting books, without directly including condensed phases to explicitly dynamically track in the simulation, (for the within-frame CFD subroutine upon fixed droplet radius).

Dynamic Steady-State Structure

At a fixed droplet radius, the flame–droplet system reaches a quasi-stationary configuration governed by feedback between heat transfer and Stefan-driven mass flux blow-off outwards to the exterior. The interaction behaves like a self-balancing oscillator: if the flame approaches the surface, enhanced heat flux increases v_s, pushing the flame outward; if the flame retreats, reduced flux weakens v_s, allowing the flame to drift inward. The equilibrium standoff distance thus autonomously self-emerges from opposing monotonic tendencies, from an energetic balance akin to the equilibrium point of a supply–demand curve, or a hydrogen-like atom potential minimum dependent on the atomic number to Bohr orbit radius quotient Z/a_0. The 3000 K steady flame temperature peak remains nearly invariant with ψ, droplet radius R, and arbitrary initial configuration (upon sustained combustion, post-startup transience from ignition temperature delta-spike), highlighting the intrinsic stoichiometric stability of LOX–H_2 flame combustion.

Comparative Statics: Coverage vs. Thickness Dimensional Analysis

For completeness momentarily, it is scientific procedurally important to consider how ice layer thickness across the droplet surface could play any potentially relevant impact for the purposes of our simulation's methods. Ultimately, the physical influence of ice coverage fraction upon heat conduction ψ likely dominates over ice layer thickness; conceptually, a heating radiator boxed in cardboard (maybe its shipping transport packaging container), considered in a short-term small-room setting, loses heating efficiency primarily due to the complement-"scattering amplitude" solid angle of blocked area, and not so much due to the thickness of the cardboard box shell layer. Another way to characterize this phenomenon is for the purpose of carrying many apples home from the grocery store, a large paper bag will perform better than a water bottle would for the task; even if the flimsy paper bag can easily get wet, as for this particular logistics scenario, the large volume capacity suffices as the dominant factor, especially compared to less relevant aspects such as being waterproof and air-tight as a carrying-container. This illustrates how in our setting, the unobstructed view factor plays a bigger role than aspects of the material

itself that such obstruction comprises. Likewise, along this line of thinking, at 100 K and 1 bar, the thermal conductivity of ice (~ 10 W/(m $\cdot$ K)) exceeds that of liquid or vapor oxygen (~ 0.01 W/(m $\cdot$ K)) by several orders of magnitude. Thus, it is the solid-angle obstruction, namely, the surface coverage, that governs the energy coupling, not the ice thickness itself, which cannot marginally contribute that much given such drastically contrasting material property comparison. This is especially compounded when facing head to head with our extensive parameter sweep investigating from 0 to 100 % ice fraction.

It is difficult to optically inspect the detailed happenings at the droplet interface due to limited resolution of the ZARM camera footage zooming into the LOX surface (reportedly about 16.1 micrometers per pixel), not to mention the overall technical difficulty of precision instrumentation setup for such an experimental environment, so for now we can only speculate about this topic. While it is obfuscated what is really fundamentally going on at the surface with the ice structural configuration's thickness, from our present assessment with respect to the flame and droplet evaporation, the actual thickness of such ice layer is likely moot for our purposes. Furthermore, thermal conduction coupling effects from ice likely pale in comparison to the dominant important factor that the surface ice structurally acts as a surrounding concretely solid physical barrier, obstructing the flowing exchange of matter and momentum from crossing the interfacial border.

For interdisciplinary perspective, in quantum chemistry and molecular physics, often times the molecular orbitals are considered more significant than the spin orbitals, as the aspect of the approximate location of where the electron could end up being found, tends to be more relevant for such material's electronic structure than any particular notion of its "orientation" or internal-angular-momentum-flavored intrinsic intricacies regarding spin (outside of Pauli exclusion principle which determines orbital occupancy capacity, loosely akin to the depletion force and overlap or excluded volume of particles in a colloidal suspension.) Similarly in our situation, the LOX droplet surface coverage is the dominant aspect compared to ice layer thickness.

Modeling Decision Philosophy

This approach favors interpretability for the combustion community over micrometric realism. The single parameter ψ spans the continuum from unimpeded to fully encapsulated conditions, while preserving asymptotic consistency and physical plausibility. It would be mathematically more insightful (as strictly more information would be accessible) to provide a type of two-dimensional eutectic phase diagram (flavor perhaps normalized like for a dimensionless MD Lennard-Jones substance) image for our physical system's model, such map which portrays specifically what happens with modulation by independently altering the orthogonal aspects of effective oxygen reservoir depression versus Stefan flow reduction. Furthermore, this could even be stratified further by radiative transfer versus heat conductive transfer, all mapped upon a multi-dimensional hypercube response surface for factorial analysis in experimental

design to capture the entire combinatorial space. This allows one to potentially speculate about and test any generalized arbitrary hypothesis modulation trajectory via ψ by performing bilinear or trilinear interpolation upon the reported and tabulated pixels or voxels in such space, but such freedom and flexibility follows the curse of dimensionality and thus suffers accordingly as it is becomes harder to parse and interpret.

5.4 CFD Postprocessing and Droplet Regression Overview

Following completion of the CFD simulations, the postprocessing phase begins once the transient flow field reaches a quasi-steady configuration. This section describes the workflow used to extract, organize, and interpret the converged data, and the subsequent droplet regression reconstruction that yields lifetime and flame evolution statistical quantities for resultant data analysis.

At convergence, the CFD results can be regarded as a stationary snapshot of the mechanical setup and thermochemical state for a given droplet radius R, such flavor of interpretation characterized in a loose sense as a statistical "regression" of profiles estimates and best predictors based on variable R throughout a range of values that run the gamut. Each snapshot represents a "frozen freeze-frame" state capturing all dominant transport and chemical processes at play and in progress, sufficient to reconstruct the time evolution of droplet regression shrinkage in postprocessing. By connecting these disjoint and spatially-sampled equilibrium configurations corresponding to different R values, the full droplet lifetime and dynamic flame behavior can be reconstructed deterministically from these "minimal complete sufficient statistics data," and conveniently efficiently recalled from the lined up aggregation of simulations, tabularly rounded up in sequential order and ready to use. This ultimate manner of arrangement of converged species concentration and temperature profiles similarly parallels an optimized SQL query selection table, that efficiently filters and methodically fetches only the relevant information from a search library's database, such ground-set of values always structurally organized for the quickest of call-up accessibility. As such, the terminally extracted CFD still-frames provide enough information for all succeeding relevant purposes, and the overall simulation structure of the numerical computation pipeline behind such process will be laid out and explained in its entirety in the following sections.

5.5 Physical Framework and Quasi-Steady Approximation

The quasi-steady assumption forms the foundational setup of both the CFD modeling and postprocessing. In this framework, chemical kinetics are assumed to equilibrate much faster than hydrodynamic or evaporative timescales. Physically, this is justified by the large Damkoehler number regime of LOX–H_2 combustion, where reaction rates and high temperatures vastly exceed the characteristic diffusion and droplet shrinkage times, and indeed usually the case for the majority of combustion scenarios involving standard flame gas-dynamics. This is also particularly the case for cryogenic combustion, which is why

Gupta (2021) [6], (before EBI-DNS with Ponduri (2023) [7]), injected inert Helium to simulations in the OpenFOAM environment to ensure stability for its in-house solvers that are catered toward hydrocarbon flames of lower temperatures. Consequently, our combustion flame simulations stabilize (from an initial spark or starting configuration using the steady state of the previous neighboring larger radius simulation run) on millisecond scales as a typical generous upper bound, while droplet radius evolution occurs over hundreds of milliseconds or longer, as exhibited by both the ZARM experiments [3] and our simulations included.

This comparative hierarchy of timescales–extremely fast chemistry, slower gas-phase transport, and slowest condensed-phase motion and regression– supports treating the CFD stage's final instantaneous stationary solution output, as a quasi-steady state destination at which it ultimately arrives, stratified by each R value as pre-computations to be scanned and passed through in succession for postprocessing. Empirically, for each R value, simulations directly confirm, that explicit droplet shrinkage during the transient ignition settling phase is actually negligible (e.g., R decreases from 0.500 mm to $\sim$0.499 mm during flame stabilization), reinforcing the validity of the quasi-steady treatment. This allows the avoidance of dealing with the intricacies of a dynamic but slowly moving boundary at the droplet's surface at radius R throughout the CFD phase, and in our case, conveniently allows for the flame domain's spatial resolution to have a discrete sampled coordinate mesh-grid scaffolding, setup initialized simply as r=np.linspace(R, 20 millimeters, 2048 sample size numpy vector length) in our Python computational environment.

The physical justification connectedly aligns with classical droplet combustion theory involving the Spalding mass transfer number, Clausius–Clapeyron vapor–liquid equilibrium, Stefan flow velocity, Burke–Schumann flame sheet limit, and high Damkohler asymptotics, all as interlaced entities and jointly interwoven concepts within the unified overarching quasi-static evaporation framework. Under these near-ideal conditions (low Mach number, negligible turbulence, moderate pressure $\sim$1 bar, $T \sim 100$ K ambient), these assumptions provide an accurate and computationally efficient representation of the dominant physics at play for droplet vaporization and droplet combustion scenarios.

5.6 Computational Workflow Pipeline

The postprocessing pipeline proceeds sequentially yet is parallelizable across all droplet radii. Each radius value R is simulated independently under quasi-steady assumptions, as their interactions are entirely decoupled until finally linking their hands up together during the droplet regression postprocessing period, forming an animation of evolving profiles along the chain of still-frames. For each R, the following stages occur:

1. **CFD Stage (Global Reaction Phase):** The CFD simulation is advanced until the startup transient ignition stabilizes into a stationary flame configuration. This captures the dominant global

$H_2 + \frac{1}{2}\ O_2 \rightarrow H_2O$ + heat reaction field, and serves as the asymptotically stagnant stationary measure distribution of such underlying adapted process.

2. **Extended Cantera Stage (Minor Species Refinement):** Upon convergence of the global field but still with CFD in play, the Cantera lever is pulled by a Heaviside step function in time to abruptly switch the tool's protocol on, which thereby finds and masks the location of the most reactive region with the highest Arrhenius rate in progress (among all flame fluid parcels with high Damkohler number), identifying the Burke-Schumann limiting thin flame sheet, where Cantera chemistry is activated to introduce radical intermediates (OH, O, H). Subsequently, injection of the minor species allows incorporation of recombination effects as a corollary, since those minor species emanate around the flame vicinity via ongoing diffusion, then quickly recombine and become mopped up in cooler regions away from the flame where radicals are thermodynamically and kinetically unfavored, implemented in silico with the now-responsive omnipresent secondary and tertiary reaction multi-threads that always continuously and ubiquitously happen throughout the entire flame domain. They persistently seek radicals to recombine, and now at this point, they have the opportunity to actually do so with radicals in-hand. This comparatively smaller aspect represents a higher-order perturbative correction analogous to first-order terms in a Taylor expansion or in perturbation theory from an already known Hamiltonian, capturing minor but physically relevant effects on the stationary fields as an addendum to the dominant physics already at play.

3. **Steady-State Verification and Storage:** Once all species and temperature fields settle into smooth equilibrium profiles, the simulation is halted, and the iteratively converged upon final fields ($T_R(r)$, $Y_{i,R}(r)$) are saved for postprocessing, terminating the CFD portion of the workflow.

This process is repeated for a range of droplet radii (0.500 mm down to 0.050 mm). Each configuration is independent and may be computed in parallel since coupling between different R states occurs only during postprocessing, and the avenue for such linkage is primarily for cumulatively stacking the computed interstitial inter-arrival hit times separating two juxtaposed radii values throughout the droplet regression lifetime.

5.7 Data Handling and Wavelet Compression

Each stored stationary solution comprises dense spatial profiles over a sampling scheme of 2048 radial grid points. To optimize our data handling, storage, and transfer between various workspace environments, Daubechies-4 (Daub4) wavelet transforms are employed for fast compression. The grid size (a power of 2) enables optimal application of the fast wavelet transform (FWT) using the standard efficient lifting scheme arising from the two-scale relation and Riesz representation theorem's multi-resolution analysis. Daub4 is selected over Haar wavelets due to its superior smoothness representation properties

for continuously differentiable profiles, such as temperature and species concentration fields, whose shape and likeness are more akin to gentle rolling undulatory waves as opposed to craggy peaks or jagged precipices, nuisance parameter qualities in our context as exhibited by the classic infamous Weierstrass function.

The FWT, using such aforementioned pyramid scheme lifting algorithm, operates in linear time $\mathcal{O}(N)$, analogous to the tridiagonal solver complexity, but by exploiting Mandelbrot's notion of fractal self-similarity in the manner of Hausdorff measure within the wavelet basis for computational efficiency. Such self-similarity is even more symmetric than the Fourier basis of the Discrete Fourier Transform Vandermonde matrix, beating out the famous Gauss-Cooley-Tukey Fast Fourier Transform's $\mathcal{O}(N \log N)$ complexity. As can be seen from the labyrinthine simulation procedure layout diagram, wavelet compression computational efficiency that yet still preserves numerical precision, makes the wavelet-based compression approach particularly advantageous for our purposes; our workflow pipeline requires repeatedly intermittent save-point pauses, checkpoint continuation data transfers, and adaptively iterative fine-tuning manipulations for parameter tweaking, which must happen within the computational workstation, so wavelet compression significantly facilitates navigating those processes for merging copious results between various workbench Python Notebooks.

5.8 Droplet Regression Reconstruction and Temporal Backtracking

After all stationary frames are stored, the droplet regression sequence is reconstructed through post-processing. The method involves sequentially "stitching" the steady-state snapshots corresponding to descending droplet radii R_n. The heat flux into the droplet at each R_n is computed once from the static profile (which inherently contains all underlying fluxes geometrically self-encoded, extractable using a one-time call-up of the CFD timestep update routine's hard-coded flux subroutine), yielding the rate of regression $\dot{R}$. Using a simple Euler method for ODE time-stepping via slope field tracking,

$$\Delta t = \frac{\Delta R}{\dot{R}},$$

the time increments between successive radii are determined. This allows reconstruction of the temporal trajectory $R(t)$, i.e., the droplet lifetime survival curve, and corresponding derived quantities such as flame standoff distance evolution and dynamic energetic transactions.

This postprocessing stage effectively transforms the collection of static CFD frames into a dynamic droplet regression sequence that can be sewn into a visual graphic animation or motion picture, capturing both the physical and temporal evolution without re-solving the precomputed PDEs.

5.8.1 Visual Summary and Interpretation

The entire computational procedure can be represented as a directed acyclic graph for the whole information and dataflow pipeline, that pushes through to the end at the bottom-right corner. The structure highlights the modular parallelism over droplet radii, sequential chemical refinement stages, and the final seamless weaving into a continuous regression timeline tapestry. The approach ensures computational efficiency, physical consistency, and interpretability across the entire droplet combustion lifetime.

Schematic representation of the CFD–Cantera–Postprocessing dataflow pipeline for droplet regression reconstruction.

5.9 Details within the CFD Postprocessing Stage: Handling Interfacial Effects

5.9.1 Inspiration behind Parameterization and Motivation Behind Temporal Mapping

Building upon the ice-layer modeling introduced earlier, the postprocessing framework translates surface phenomena into their effects on temporal evolution and regression rate. At this stage, we have ultimately already accounted for the effective impedance stemming from the ice layer surface area coverage

fraction of the LOX droplet surface within the previous CFD phase, in which it only affects the final resting configuration of the flame, determined upon the settled balance arising from the ice-modified Stefan flow blow-off and oxygen reservoir height governing the dynamics. While the in-simulation CFD captures steady-state flame-droplet interactions under modified boundary fluxes, the postprocessing analysis interprets how such interfacial conductivity and resistivity affect the temporal progression of droplet shrinkage.

5.9.2 Geometric Interpretation

Conceptually, using comparative statics upon the effects of any ice presence, this can be viewed as a differential geometry transformative mapping, reparameterizing the droplet evolution curve with respect to a slowed or accelerated race-car "speed of traversal" through the race-track of pre-defined physical arrival "time-attack" checkpoints in state space. Since the checkpoints are already fixed along the way at specific particular points throughout the circuit, the inter-arrival times are established upon the velocity of driving through the race course and tracing along the entire route. Since no momentum carries over at the interstice between subsequent legs of the race, accounting for the aggregate time elapsed becomes a simple cumulative Riemann sum or integral. In particular, due to the PID-control-flavor "proportional tax/amplification" scheme upon all energetic transfer at the interface, the warping of the curve's propagation arises from simply a scale-factor, which steepens or flattens the underlying slope field that is being tracked via the Euler time-step method for first-order ODE numerical solutions.

5.9.3 Generating Response Signal Function of Droplet Regression throughout Time

A standard equidistant lattice of R radii values was chosen for the "checkpoints", because it follows from the principle of Maximum Entropy from E.T. Jaynes's school of thought. This is because with a uniform prior among all variables, without upfront information about the R process, Lloyd-Max type optimal quantization conditions propose that we should not bias our limited resolution toward any particular R regions, which is why characteristically sampling at the Nyquist rate is typically performed upon a uniformly spaced grid for universal contexts.

Producing a time series-type signal for the response variable of the droplet's dynamic evolution requires numerically solving such our invertible and separable-then-integrable autonomous ODE system. At each successive stepping stone in the staircase, one accumulates the time elapsed until it reaches the next successive rung on the ladder. While we already know the spatial radii values, we need to access the associated times corresponding to each droplet radius value. As we traverse the path accumulating time lapses after passing each sequential notch, we'll eventually end up with an ordered list of coordinate pairs of radii values with their attached arrival times. This method of backtracking in our context, parallels aspects of dynamic programming's typical second pass phase, a standard method identifying

the relevant update increments upon the successive terminal optimal value grid, to actually explicitly reconstruct the underlying optimal trajectory that inherently generated such final optimal value, all satisfying the Hamilton-Jacobi-Bellman equation.

Since the heat transfer from the flame is always non-negative throughout the entire droplet's lifetime, the survival curve of the droplet is thus monotonically decreasing from constant shrinkage (or at least non-increasing), akin to the inverse CDF probability measure for a longitudinal survival analysis curve. As an aside corollary on this note, this metric also facilitates the analysis of a statistical ensemble of droplets of varying size, the entire population cluster heterogenously undergoing evaporation at different stages of life at any given time. Since we know from the monotonic behavior of the survival function, we can invert the implicit function, which yields the desired relevant quantity for us to extract and plot. This result can be viewed as borrowed from the continuous mapping theorem applied to probability measures, allowing invertability of any CDF or survival curve, by preserving the classic "vertical-line-test" property of mathematically well-defined functions, even in mapped image space under involution.

The core idea of this analysis demonstrates that algorithmically using some integral image, (but for feeding the rope to thread the needle of our 1D vector signal), to stitch together the neighboring checkpoint relative time lapse differences into an explicit absolute arrival time value assigned and tacked onto such droplet radial coordinate in sequence, conveniently guarantees that the final result samples an invertible function signal (by mathematical standards.)

5.9.4 Rate of Droplet Regression from Interfacial Effects in Postprocessing

In the numerical implementation, droplet evolution is represented as a trajectory through a sequence of quasi-stationary configurations (checkpoints along the route) corresponding to a discrete grid of radii. These points are predetermined and equidistant in radius space. The effective temporal mapping arises from successively integrating the instantaneous energy flux into the droplet as previously described, i.e.

$$\frac{dR}{dt} \propto -q_{\text{in}}(t),$$

where q_{in} represents the total current heat flux incident upon the droplet surface at the present configuration.

Associated arrival times en route govern what the regression curve's shape graphically looks like, marked by each instance passing by a grid-point. This can also be viewed as the underlying autonomous ODE system's Euler slope field locally becoming either steepened or flattened accordingly, which means it takes shorter, or longer, respectively, to cruise and coast at such fixed rate to the next notch R-value in descent.

An alternative but equivalent viewpoint can be provided as follows: any dynamic scaling factor upon

this survival curve's proportional-hazards-type relationship can be viewed as an expansion-or-contraction modification that operates primarily as a temporal reparameterization, rather than a fundamental alteration of the inherent geometric trajectory on the fixed-radius grid. This loosely parallels the Theorema Egregium's point about intrinsic curvature in embedded space: the droplet-regression grid-points at fixed R remain inherently identical, while only the parameterized rate of traversal through them with respect to physical time changes. This simple scaling relationship effectively dilates the temporal evolution, thereby either pulling the breaks or stepping on the gas upon the road's traversal, as in our earlier race-car vehicle analogy as it drives along the route. The result is a time-warp that reschedules the arrival moments at each checkpoint, with those timeline record-logs determining when each stationary point is overtaken, whose integrated action can either elongate the time coordinates with respect to space to become expansively stretched, or squeeze those time coordinates to become compressed, of the same flavor of light-cone coordinate Lorentz transformation from Einstein's relativity.

As an analogy in our discussion, while the underlying optimization objective function mathematically remains the same, all of statistical elastic net, LASSO, and ridge regression methods can be equivalently interpreted in both a frequentist viewpoint and Bayesian standpoint, whose respective frameworks usefully and uniquely apply among various idiomatic settings. Similarly, while this section may pedantically belabor the various descriptions behind the mechanics of post-processing, those diverse perspectives characterize valuable hints regarding the intuitive insight behind generating regression curves. Furthermore, these notions are universally applicable to any situation involving quasi-static droplet combustion, whose geometric aspect will be visually apparent in shapes from the results section plots.

5.9.5 Postprocessing LOX Surface Area Ice Layer Coverage Fraction ψ

In the absence of ice, q_{in} follows directly from conductive and radiative transfer terms. When surface ice coverage ψ is present, the flux is attenuated by a proportionately-scaling "tax" factor $(1 - \psi)$:

$$q_{\text{in}}(\psi) = (1 - \psi)\, q_{\text{in}}(0).$$

The retention of the proportional "ice tax" $(1 - \psi)$ term (originally from CFD earlier) again here in postprocessing, reflects the fact that, even though solid ice efficiently conducts heat as discussed in earlier sections, the energy entering the droplet under partial surface encapsulation is not utilized with the same evaporative efficiency as in the fully liquid case without ice crystal obtrusion. When ice coverage limits the outflow of gaseous oxygen through the surface, local vapor becomes trapped beneath the solid patches, elevating the near-surface partial pressure in accordance with Henry's law and diminishing the net Stefan outflux. In this quasi-sealed configuration, additional heat input preferentially increases internal temperature and vapor pressure rather than sustaining steady evaporation. The effective consequence

is a reduction in the fraction of incident thermal energy actually contributing to the droplet regression process, which is represented here as a proportional attenuation $(1 - \psi)$ upon q_{in} which applies to the spherical-shell-shaped receding radial interface. Thus, the ice tax captures the reduced thermodynamic efficiency of heat-to-mass conversion within the droplet system, within the ultimately obfuscated mechanistic pipeline of mystically transmogrifying heat into LOX vapor blow-off. This process is primarily influenced by the configurationally-extrinsic surrounding ice crystals serving as a concrete mass barrier that induces physical obstruction, independent of the intrinsic material heat conductivity of such model-proposed solid ice phase upon the droplet surface. Our study which focuses purely on the gas-dynamics flame region, does not simulate the LOX droplet's inner liquid phase heat and mass transport dynamics, and so our coarse-grained approximation renders such attenuated "noisy-side-lobe" exogenous mysteries moot for the endogenous "main-lobe pass-band" purposes of our modeling interests.

To provide the general characterizing intuition behind this phenomena: for a condensed phase to convert into a more rarefied gaseous phase via evaporative boiling or sublimation, such condensed phase requires actual ambiently surrounding room to expand into a more spacious dilute phase of less density, the enthalpy of such process typically requiring heat intake. This can also be viewed through the lens of smoothed particle hydrodynamics. While the amount of molecular motion– commensurate to system temperature by constructive definition in statistical thermodynamics– may be sufficient for some outer particles to break off from the conglomerated collective cluster of potential-pair-wise sticky particles of which the aggregated condensed phase comprises, those thermally-excited particles may struggle to totally break free when a concrete physically obstructive barrier is in the way of its escape route. For a rarefied gaseous phase to form, the flock of escapee particles must take flight to make it sufficiently far enough away, so that the juggernaut adhesive pack does not round them up to become assimilated back into the herd. Path-evasion is particularly difficult when confined to a small playground arena region for playing hide-and-go-seek tag, where the surrounding boundary obstacle blocks passage to the external environment. If a significant population of runners decides to flee, overcrowding leads to increased pressure, lessening the chance of elusion to make it easier for the "Amoeba" condensed-phase blob to progress with accumulative consumption of the stragglers in such metaphorical game, microscopically aligning with Henry's law in the context of kinetic theory. Furthermore, the situation of runners trying to escape, but colliding against the wall, is consistent with the quantum statistical mechanics version of pressure arising from kinetic theory, using the translation partition function of the particle in a box energy levels, explaining where the "ice-tax revenue" went, and further characterizing it as not merely a "lump-sum tax".

5.9.6 Introducing the Ruffle-Factor Parameter $\phi(R)$

The postprocessing stage incorporates a *Ruffle Factor* $\phi(R)$ to account for non-spherical deformation (while its fast marching method's surface topology remains unaffected), observed experimentally as seen in the ZARM droptower experiments. [3]. As the droplet evolves, deviations from sphericity increase the effective interfacial surface area available for exchange of heat and mass transfer. This deformation acts as an amplifying gain on flux, because of such effective surface area augmentation. To illustrate why under the assumptions that non-sphericity must serve as an amplification factor, here is a quick calculus of variations proof that verifies a sphere-shaped object configuration indeed minimizes its surface area for any given fixed volume of 3D spatial occupancy:

- In cylindrical coordinates: $A[r] = 2\pi \int r\sqrt{1+(r')^2}dz$, $V[r] = \pi \int r^2 dz$ Lagrange multiplier λ constraint: $J[r] = 2\pi \int (r\sqrt{1+(r')^2} - \frac{\lambda}{2}r^2)dz$
- Invoke Beltrami Identity upon Euler-Lagrange: $\frac{r}{\sqrt{1+(r')^2}} - \frac{\lambda}{2}r^2 = C$
- First-Order Condition arises from Integration Constant: $r^2 + z^2 = R^2$✓
- Second-Order Condition also satisfied via the Legendre-Clebsch condition: $F(r, r') = r\sqrt{1+(r')^2} - \frac{\lambda}{2}r^2 \rightarrow \frac{\partial^2 F}{\partial (r')^2} = \frac{r}{(1+(r')^2)^{\frac{3}{2}}} > 0$✓
- This demonstrates that both the necessary and sufficient conditions for optimality hold for this solution that represents a sphere. ✓

Empirically, the inception of $\phi(R)$ is modeled as a radius-dependent gain that increases sharply once the droplet shrinks past approximately half of its initial size, consistent with the onset of strong non-sphericity observed in ZARM's footage and imagery analysis, particularly evident in both Figure 7a and Figure 4 from Meyer et al. (2022). [3] Since the effect of the ruffling-factor $\phi(R)$ enhances heat transfer to the droplet, a gain factor of $\phi(R) = 1$ implies parsing the heat calculations for the case of an unperturbed perfect sphere baseline reference from the variational principle/variational method, and anything larger provides purely augmentative effects. Increasing $\phi(R)$ means the droplet evaporates faster, speeding up the process of descending from one R value its immediate neighbor, thereby lessening the separative interstitial time gaps. This geometrically compresses the time-axis to yield shrunken time-coordinates for the droplet regression, but still upon the same original R samples, akin to the boosting Lorentz-transform's length contraction and time dilation from Einstein's relativity, such aspect to be visually apparent in our results section plots.

Physical Underpinnings

Physically speaking, this phenomenon parallels the classic Coke-and-Mentos experiment, which demonstrates an example of a physical reaction. The submerged Mentos candy has such intricate microstructure

upon its rough surface that it provides an ample supply of nucleation sites for the carbonated beverage's dissolved carbon dioxide to rapidly form gaseous bubbles. Normally, over longer periods of time at atmospheric pressure, an unsealed carbonated beverage gradually goes flat because the drop in external pressure shifts the equilibrium described by Henry's law, causing dissolved carbon dioxide to bubble out of the now supersaturated solution. Immersing such a Mentos as a physical catalyst so severely accelerates the kinetic rate of nucleation that the entire contents of the can or bottle spurt out through the nozzle in a steady stream of rapid gaseous expansion, similar to turbulent river rapids. Similarly, a gecko has upon its sticky feet countless micro-structural adhesion setae, each forking into even finer spatulae, which are highly branched fibers that produce enormous interfacial surface contact area. This configuration enables strong Van der Waals adhesion, characterized by a high Hamaker constant, allowing the gecko to support its own weight to climb a vertical wall.

These examples parallel our case, with a ruffled-surface LOX droplet blob that possesses strictly more surface area than a sphere for interaction, thereby amplifying all effects that penetrate the interface.

Thus, the combined modified flux is expressed as:

$$q_{\text{modified}} = \left[\phi(R)\,(1-\psi)\right]\, q_{\text{original}}.$$

Here, $\phi(R) \geq 1$ amplifies due to ruffling, while $(1-\psi) \in [0,1]$ attenuates due to ice coverage, forming a composite quantity based on both parameters $\phi(R)$ and ψ.

5.9.7 Leidenfrost-Type Correction to Decouple Effects

Motivation and Inspiration behind Introducing the Leidenfrost Correction Factor

During parameter sweeps, an unintended interaction emerged: increasing ice coverage ψ altered the final flame standoff distance and ratio generated by the earlier CFD by tugging it in, thereby amplifying (from such geometric effects alone) the heat transfer to the LOX surface throughout CFD postproduction for droplet regression. This phenomenon is loosely similar to the shielding effect of outer valence shell electrons becoming blockaded by inner orbital electrons by "steric hindrance", expanding the Bohr atomic radius compared to the baseline for hydrogen-like atoms proportional to α_0/Z for non-interacting independent electrons– except we're now accounting for the flame radius becoming diminished (instead of augmented) by the inner "shielding" boundary layer of surface ice coverage. The CFD geometric impact of the ice coverage ψ upon the resting flame configuration to magnify power, then ultimately cancels out any postprocessing evaporative impedance delay from such ice fraction ψ, thereby negating its influence and nullifying any measurable observables upon aspects of the droplet's lifetime; in other words, the droplet lifetime remains mostly constant with any choice of ice fraction. From a causal-inference analysis perspective, this creates a type of multi-collinear or confounding effect in the droplet

regression rate response variable, and to resolve such discrepancy, we need to counteract its adverse effects appropriately in post-processing. To be able to peer at what might happen with the counterfactual case: Had ice coverage not affected the flame's geometric shape, thereby only diminutively impacting the postprocessing rate of evaporation, such droplet's lifetime would then be expanded to persist longer via protective slower consumption. Therefore, the counterfactual claim from such causal intervention would isolate the direct effect of postprocessing impedance upon lifespans from just ice coverage itself, avoiding postprocessing disturbance from the flame's geometric distortion. As a heuristic estimate of such ballast counterbalance obtained through observation of the simulation's behavior throughout the tinkering process, an ad hoc corrective denominator "fudge factor" was introduced:

$$q_{\text{modified}} = \left[\phi(R)\,\frac{1-\psi}{1+3\psi}\right] q_{\text{original}}.$$

The $(1 + 3\psi)$ term heuristically and empirically "partials out" the spatial geometric compression effect on flame position—akin to a Frisch–Waugh–Lovell (FWL) partial regression adjustment—allowing analysis of the pure causal impact of ice coverage alone on regression speed. By factoring out extreme surface gradients in rate-postprocessing, using causal inference lexicon, we can loosely isolate out the "average treatment effect" from the ice layer's influence, while still respecting the unknown details of the chaotically messy interfacial behavior.

Of note, due to the mathematical form of a product that preserves the ability to independently factorize into a product of ψ and $\phi(R)$ terms, the nature of aspects with respect to causal inference upon the ice coverage ψ remains irrespectively orthogonal to the direct immediate impact of any non-spherical behavior.

The Actual Leidenfrost Effect

This nomenclature treatment parallels the conceptual logic of a Leidenfrost layer: the ice, or possible Kolmogorov micro-scale turbulent vapor cushion, introduces a resistive boundary that insulates the liquid surface and impedes direct energy coupling. To clarify, the actual denotation of the Leidenfrost effect refers to how an interstitial gaseous pocket cushion region of separation can form through an extreme temperature conduction gradient between a hot solid and cold liquid contact interface, such as a cool droplet of water upon a sizzling stove frying pan or a hot potato dunked in frigid liquid nitrogen. The vaporized-fluid thin-film or bubbling boundary layer that forms between the liquid and solid interface, (by material physical contact as opposed to within the phase-diagram abstraction upon the solidus and liquidus boundary lines), temporarily serves as a thermodynamically insulating layer to shield the liquid from further boiling from continued heat transfer. This contrasting phenomenon parallels the windchill effect, where gaseous motion continually replaces the skin's contact layer of stagnant air already warmed by body temperature, with freshly new untouched air from the ambient external atmospheric temperature, portraying how wetsuits mitigate such effect to keep divers warm while swimming in chilly

lakes.

While the true microphysical process may differ from the actual strict denotation of the Leidenfrost effect, the analogy's captured essence succinctly conveys the emergent macroscopic effect, while cognitively concisely and linguistically soundly expressing the modeling intent.

5.9.8 Summary of Ad Hoc Interfacial Parameters

For numerical implementation, two pure phenomenological parameters govern all postprocessing interfacial effects:

- **Ice Fraction** $\psi \in [0, 1]$: proportional LOX-droplet outer layer surface area coverage by ice crystals, imposing a multiplicative flux attenuation $(1 - \psi)$ in postprocessing
- **Ruffle Factor** $\phi(R) \geq 1$: empirical gain function encoding enhanced interfacial area due to non-sphericity, usage entirely in editing effects for CFD postproduction

On their own, in postprocessing, the combined action of the non-spherical deformation ruffle-factor $\phi(R)$ with LOX surface area layer proportional ice coverage fraction ψ is as follows:

$$q_{\text{modified}} = [\phi(R)(1 - \psi)]\, q_{\text{original}}.$$

If we choose to incorporate the "Leidenfrost-Type" corrective factor, their combined action modulates the total effective energy transfer signified as:

$$q_{\text{modified}} = \left[\phi(R)\frac{1 - \psi}{1 + 3\psi}\right] q_{\text{original}}.$$

Where the afterthought ad hoc bottom bunk "fudge factor" $(1 + 3\psi)$ dampening term is heuristically shoved into the quotient's lower shelf denominator. This quantity was tinker-tuned experimentally in silico, by roughly empirically "eyeballing" a thumbnail sketch of the exhibited behavioral tendencies of the droplet surface ice coverage fraction ψ's "pulling force" (as a simile) upon the settled flame standoff distance.

This compact formulation preserves the correct limiting cases:

$$\psi = 0 \Rightarrow q_{\text{modified}} = \phi(R) q_{\text{original}}, \quad \psi = 1 \Rightarrow q_{\text{modified}} \approx 0, (\text{and CFD flame extinction})$$

and maintains physical plausibility while empirically aligning simulated droplet lifetimes with experimental results and physical intuition.

5.9.9 Recapitulation and Outlook of Interfacial Phenomena during Postprocessing

This phenomenological but physically consistent treatment allows the simulation to span a realistic envelope of possible interfacial conditions, ranging from pristine spherical droplets to ice-encapsulated, ruffled, quasi-chaotic configurations, without overwhelming the model with explicit microphysics complications.

The method also ensures consistency between the bridge connecting the earlier CFD stage to postprocessing; after a fixed ice fraction value ψ is chosen upfront and locked in for all CFD frames, we must commit to following through with this established ψ value, to continue to carry out the rest of the entire postprocessing stage with using such ψ value, for completeness and continuity. Anything otherwise would imply a dynamically-evolving surface-ice-fraction parameter that changes with time, e.g. $\psi(t) \rightarrow \frac{\partial \psi}{\partial t} \neq 0$, which is not what we're modeling in this study. Furthermore, doing so would require completely restructuring the conjoined CFD and postprocessing protocols, and may sacrifice structural independencies of underlying intermediate processes. This structural dependency is akin to backwards induction or dynamic programming, where the next move is forced, a preconditioned decision in sequence that is recursively stuck given previous steps, until the whole trajectory becomes fixed and entirely revealed once a boundary condition is imposed, structurally "overcoming the unknown entropy" as is said in cybersecurity contexts. In our model, since constant ψ is not supposed to be changing, it recursively demands that it continue to be fixed throughout. To avoid unnecessary complexity for our purposes, our method's simplicity preserves interpretability while enabling controlled exploration of coupled interfacial phenomena.

6 Results

6.1 Comparison of Baseline Model with Theory and Experiment

6.1.1 Classic D-Square Law Validation

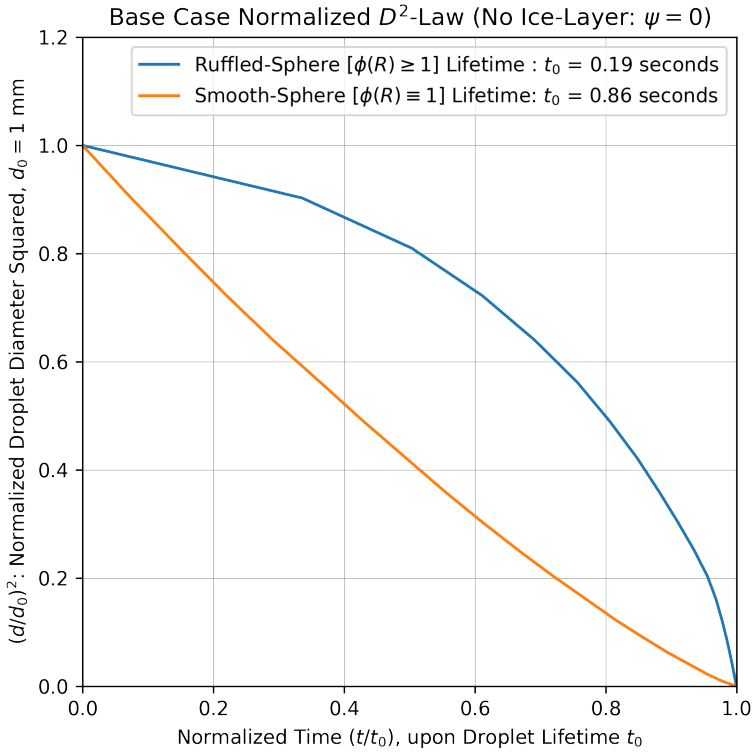

Figure 5: Normalized comparison against the theoretical ideal-case D^2-law that assumes a perfect sphere. While the ZARM droptower experiments showed near-spherical D^2 behavior for high-pressure (supercritical) cases, at our computationally investigative focus of 1 bar (subcritical), the experimentally observed droplet lifetime was approximately 0.13 s, a much shorter lifespan than analytical theory would predict. Our baseline smooth-sphere simulation, which indeed diagnostically respects the theoretically presumed idealized D^2-law behavior, yields a lifetime of 0.86 s, consistent with prior numerical spherical lifetime estimates on the order of $\sim$ 1 s from Gupta (2021) and Ponduri (2023) [6, 7]. Only by applying a ruffle-factor correction throughout the droplet regression's CFD post-processing, can we consistently and simultaneously match: 1. the short experimental lifetime's order of magnitude, 2. the experimentally measured curve's concavity deviation from the idealized linear D^2-Law, and 3. the plot tracking the dynamic non-sphericity metric (via regression footage's image-processing), all observed in Figure 7a of Meyer (2022) [3], and also presently concurrently exhibited together here in the above figure.

The smooth-sphere baseline simulation reproduces the classical D^2-law with high fidelity, yielding a droplet lifetime of approximately 0.86 s. The empirically introduced *ruffle factor* $\phi(R)$ was fitted ad hoc and heuristically, specifically fine-tuned to empirically match the ZARM Figure 7a [3] subcritical case, introducing curvature consistent with experimentally observed non-sphericity that becomes pronounced during the second later half of droplet lifetime (loosely around when $t/t_0, R/R_0 \approx 0.5$). This non-spherocity effectively increases the surface area, enhancing heat transfer and thus shortening the

lifetime. The ruffle factor therefore acts as a geometric correction to approximate the influence of surface deformation, maintaining physical consistency by matching both lifetime magnitude and curvature trends observed experimentally. In contrast, the simulated ideal smooth-sphere case follows a nearly linear D^2 decay, as expected for diffusion-limited evaporation. Further details will be expounded upon afterwards in the discussion section.

6.1.2 Flame Standoff and Droplet Diameter Evolution

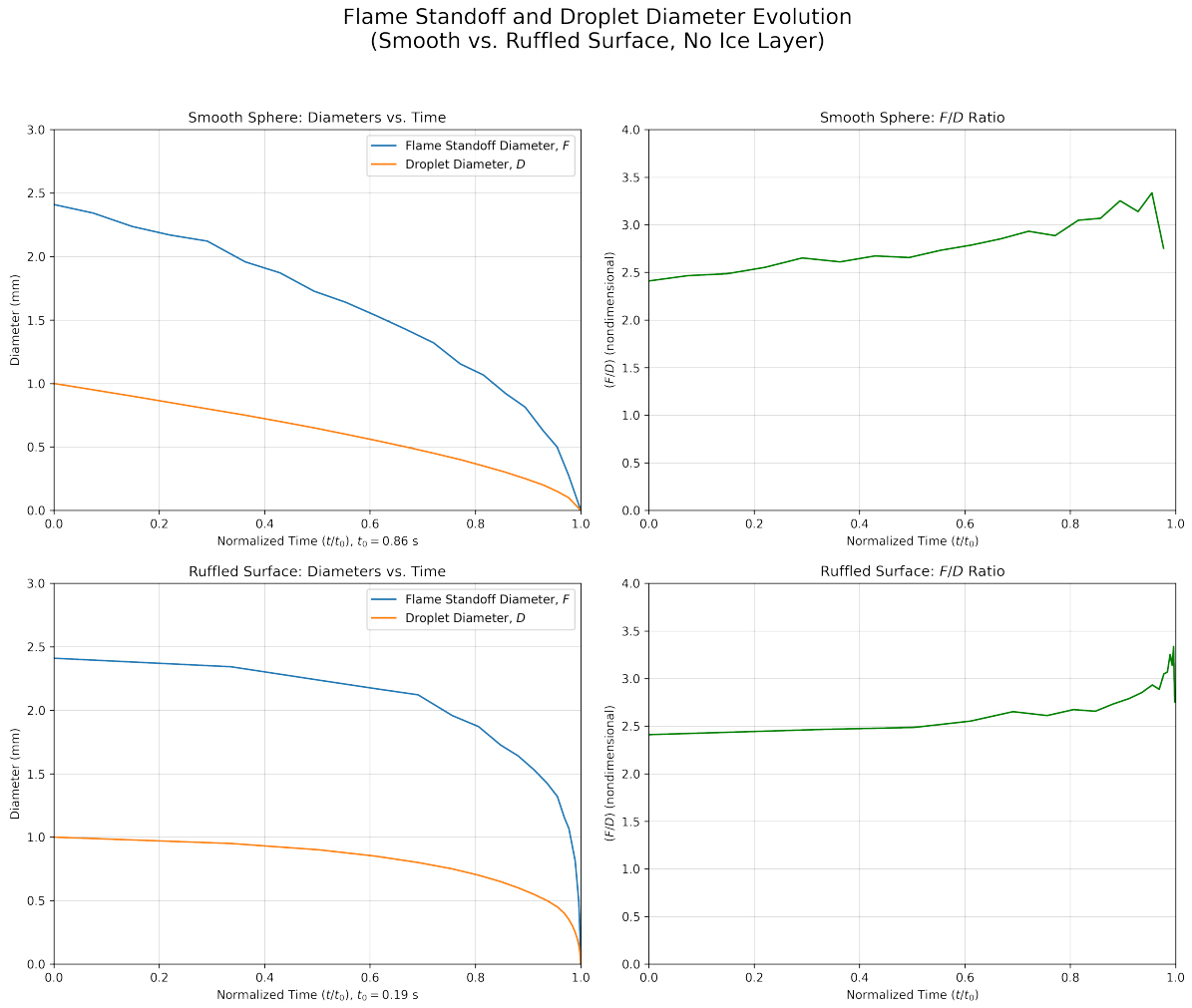

Figure 6: Evolution of flame standoff and droplet diameter for smooth and ruffled surfaces (no ice layer $\psi = 0$). The flame diameter recedingly tracks the droplet diameter as it shrinks, reasonably maintaining distance of a relatively constant standoff ratio ($F/D \approx 2$–3.5), matchingly consistent with ZARM's 1 bar subcritical case measurements observed in Figure 8a from Meyer (2022). [3]

Figure 6 compares both the smooth-sphere and ruffled-surface cases, of the dynamic flame standoff diameter and droplet diameter, in normalized space throughout the droplet regression process. The lower panels represent the ruffled-surface runs, which show similar qualitative behavior to the smooth-sphere case, but as expected, with slight warping of the regression trajectories due to geometric distortion effects described in the earlier methods section. The standoff ratio remains nearly constant throughout

the burn, supporting a quasi-steady diffusion-limited regime, in concert with theory and faithful to the experimental trends observed by ZARM in Figure 8a from Meyer (2022) [3].

6.1.3 Flame Field Visualization: Stationary Temperature and Species Profiles of Various Droplet Radii

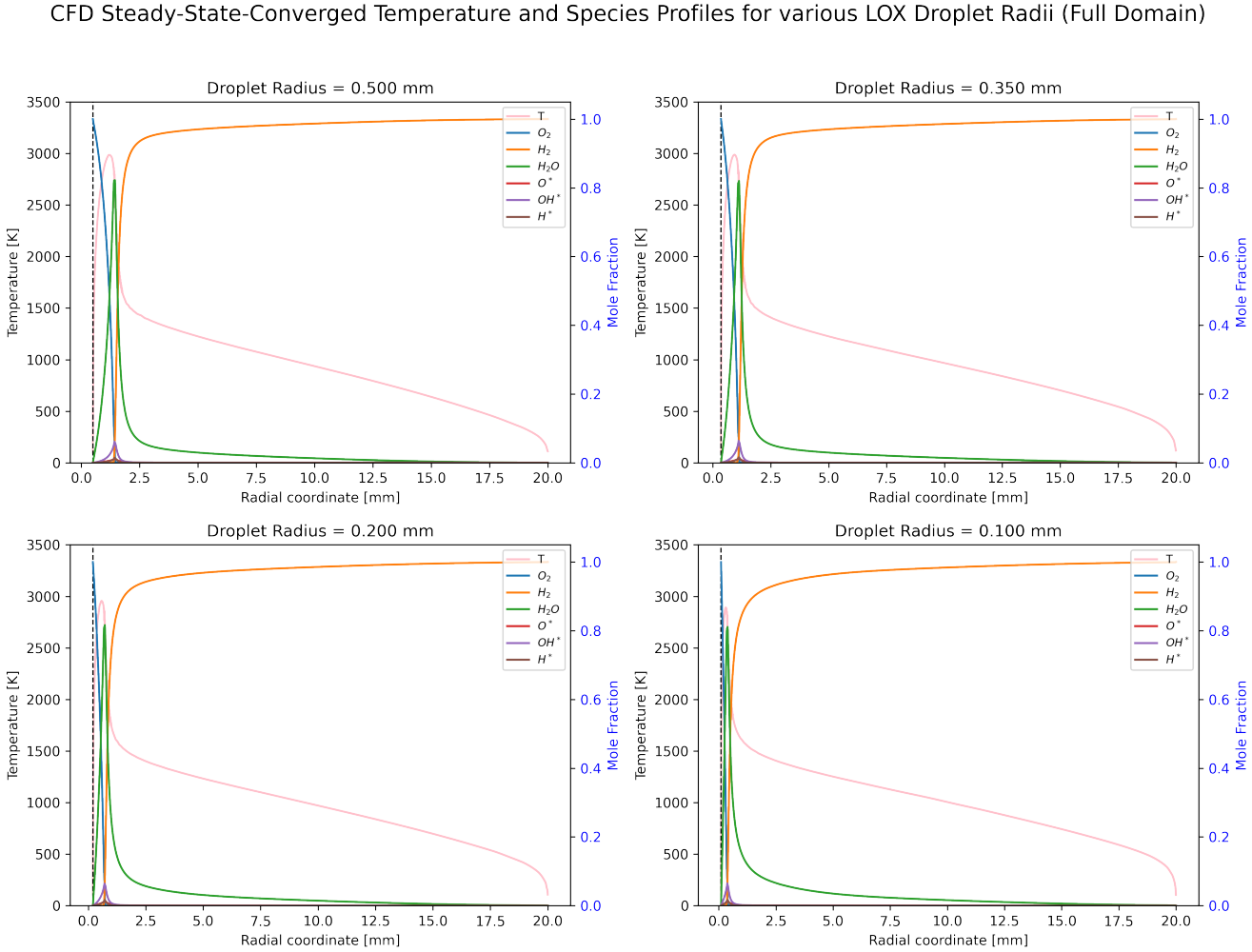

Figure 7: Full-domain steady-state temperature and species fields obtained from the CFD flame simulation surrounding the evaporating LOX droplet. Shown are representative snapshots of the converged profiles later used for the evaporative regression post-processing. The dashed vertical line marks the droplet surface.

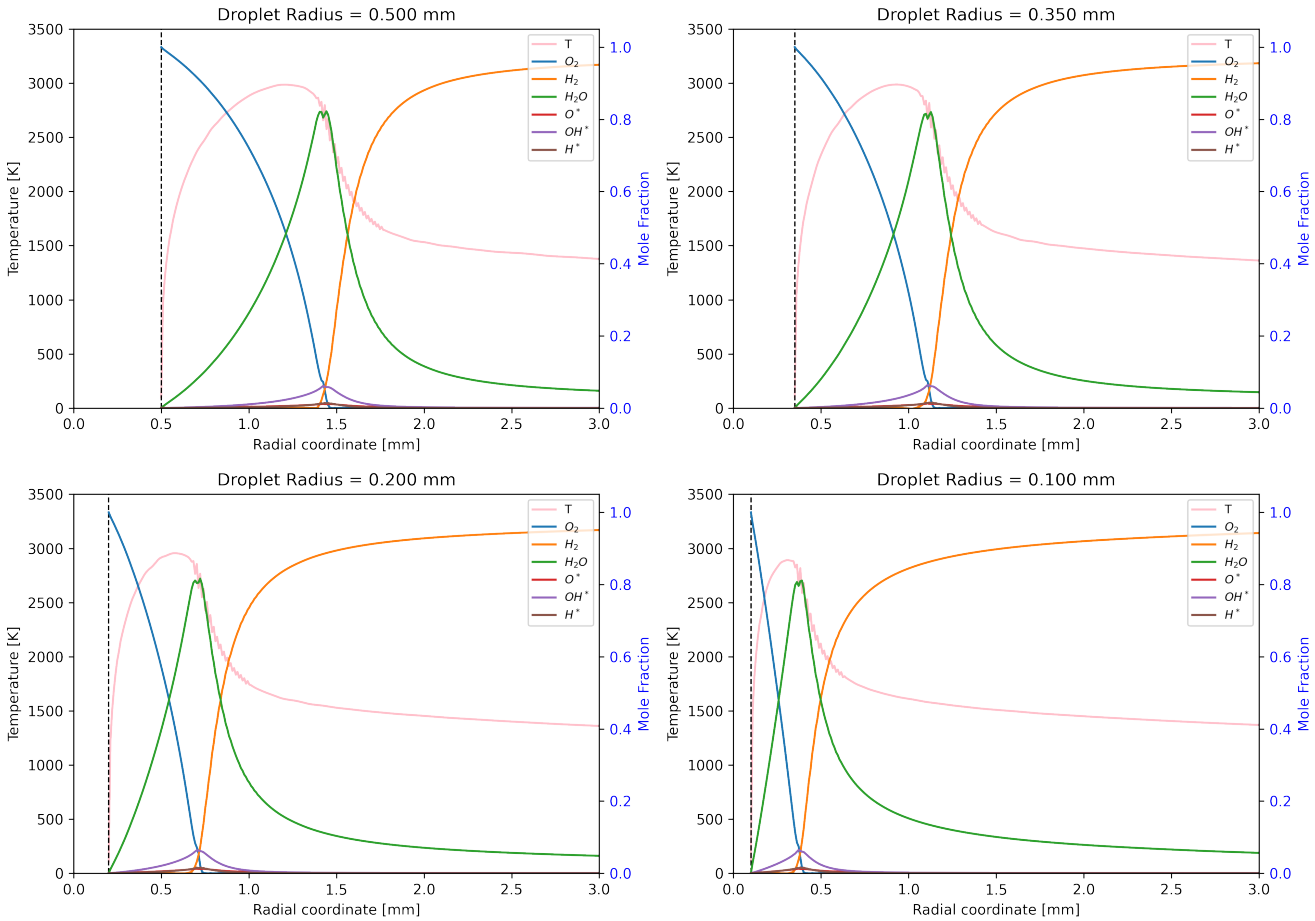

Figure 8: Near-field view (0–3 mm) of the steady-state CFD temperature and species profiles around the LOX droplet. This zoomed representation highlights the flame structure and species stratification close to the droplet surface. The dashed line indicates the droplet interfacial boundary.

The steady-state temperature and species fields shown in Figure 7 and Figure 8 illustrate representative snapshots of the flame structure surrounding LOX droplets of varying radii. Across all cases, the peak flame temperature consistently reaches approximately 3000 K peak flame temperature near the flame standoff region, independent of droplet size, consistent with standard accepted values. Minor species, including radicals OH^*, O^*, and H^*, are observed to form primarily within and around this high-temperature zone and diffuse outward before being reabsorbed and rapidly quenched in the cooler surrounding gas. The oxygen and hydrogen profiles exhibit minimal spatial overlap, consistent with the asymptotically near-instantaneous chemistry or high Damkohler number limit of the system and the thin, Burke–Schumann-like flame sheet that forms under these quasi-steady conditions, as can be seen by the most reactive "Cantera point", observably apparent by visual inspection. These visualizations provide a complementary perspective to the temporal flame tracking and droplet regression analyses presented elsewhere, offering insight into the local species stratification and temperature distribution that underpins the evaporative regression process. While an aphorism says a picture is worth a thousand

words, a GIF-type animation is usually around a thousand pictures, which characterizes the multimodal insight garnered by stitching the frames together in CFD postproduction for motion picture animation postprocessing, vaguely implied in this laid-out series of still-frames, as stillshots arranged chronologically successively in the four panel figures of panned out figure 7 and zoomed-in closeup shot of figure 8.

6.1.4 Ruffle-Factor $\phi(R)$ Visualization

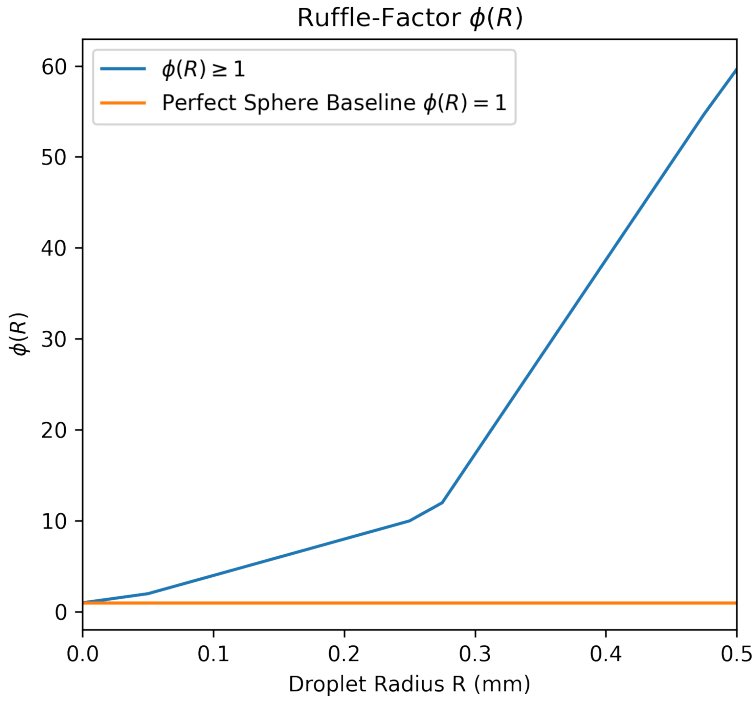

Figure 9: Ruffle-factor $\phi(R)$ showing deviation from ideal spherical geometry.

The "ruffle-factor" $\phi(R)$, serving as a "fudge-factor" implemented ad hoc in CFD post-processing for the evaporative-shrinkage numerical routine, quantifies deviations from perfect sphericity as the droplet regresses. Empirically, $\phi(R)$ remains low during early stages, rising significantly in the latter half of the droplet lifetime, consistent with experimental non-sphericity trends inferred from the experimental ZARM footage's image analysis, as explicitly depicted in the bottom-bunk basement plot from Figure 7a of Meyer (2022) [3], generated using the methodology depicted in Figure 4 of Meyer (2022) [3]. This correspondence holds both graphically qualitatively, and loosely point-wise mathematically, for mollifier-smoothed and convex functions.

6.2 Influence of Surface Ice Fraction ψ on Droplet-Regression

We next consider cases with surface ice coverage fractions $\psi = 0\%$, 30%, and 75%, to focus on the effect of varying ice fraction on regression dynamics.

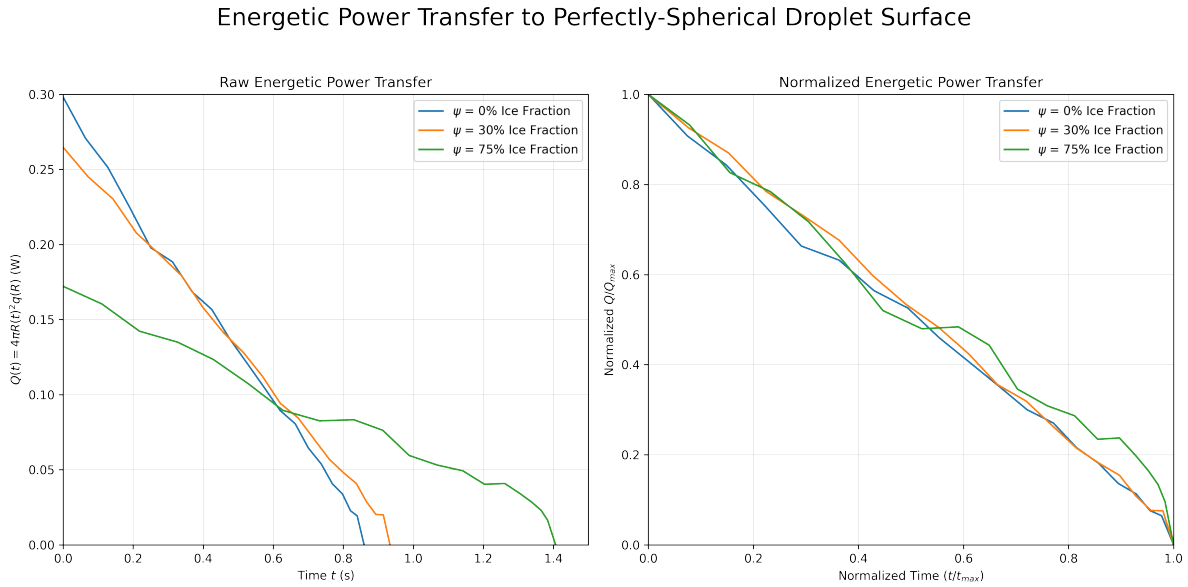

Figure 10: Dynamic, interfacial energetic power transfer to a perfectly-smooth-sphere-shaped LOX–H_2 droplet surface for varying ice fraction values ψ. (**Left**) Raw power-transfer rate $Q(t) = 4\pi R(t)^2 q(R)$. The droplet lifespans are depicted upon the survival curves' various collision point intersections upon the zeroes of the horizontal time axis, along with disparate heights of power absorption curves that vary with surface ice coverage fraction ψ. (**Right**) Same data projectively depicted in normalized space $Q/Q_{\max}$ and $t/t_{\max}$, where curves collapse to a nearly linear decay throughout the droplet's entire lifetime, diagnostically consistent with diffusion-limited D^2-law behavior.

The normalized energetic-transfer plot (right panel) shows approximate linearity across all ice fractions, confirming that $Q(t) \propto R(t)^2$, indicating that quasi-steady diffusion-limited regression persists, satisfying a heat and mass transport behavior diagnostic check. As an additional diagnostic check, the energetic order of magnitude is consistent with previous estimates of around 0.3-0.5 Watts from Ponduri (2023). [7], ensuring that relevant quantities remain physically reasonable.

6.2.1 Dataflow Schematic for $Q(t)$ and $D^2(t)$ Computation

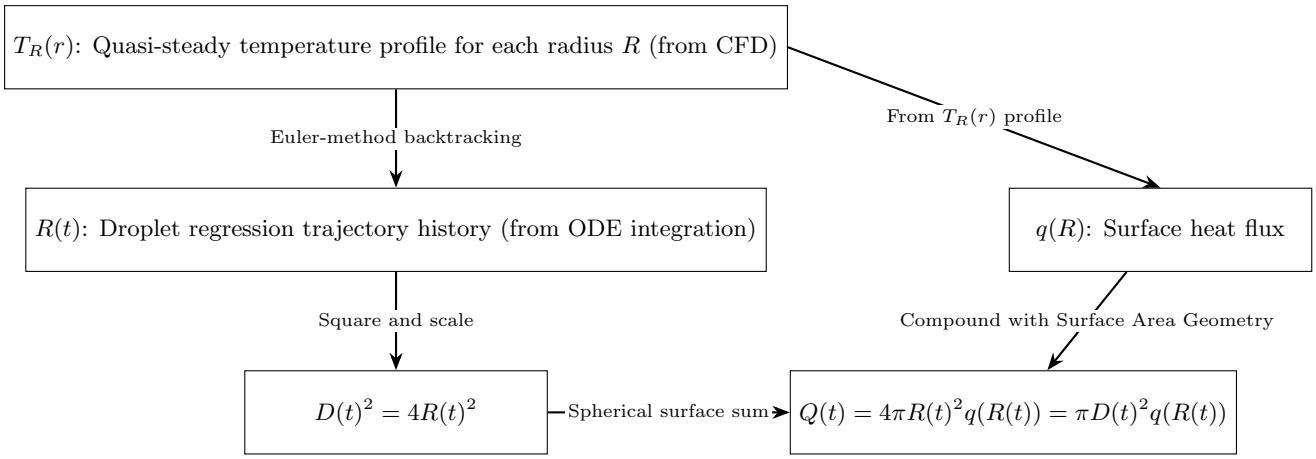

This schematic summarizes how CFD flame data and regression models combine to yield $Q(t)$ and $D^2(t)$. The quasi-steady temperature field provides the local heat flux $q(R)$, which drives the ODE-based regression $R(t)$. While $D^2(t)$ depends purely on geometric shrinkage, $Q(t)$ incorporates full flame–droplet coupling physics. Their normalized similarity arises because $q(R)$ remains approximately constant across the trajectory, arising from the property that the flame standoff ratio doesn't drastically waver too much throughout the droplet's lifetime.

6.2.2 Interpretation: Why Different Diagnostic Plots $Q(t)$ and $D^2(t)$ Behave Similarly

In a diffusion-limited regime with roughly constant flame standoff ratio behind the reasonably steady surface heat flux $q(R)$:

$$Q(t) = 4\pi R(t)^2 q(R) \approx C \cdot R(t)^2.$$

Since the D^2-law implies $R(t)^2$ decreases linearly in time, both $D^2(t)$ and normalized $Q(t)$ collapse onto a linear trajectory. However, while $D^2(t)$ encodes only the droplet geometry, $Q(t)$ captures full thermal–chemical coupling expressed with true real-life display values. Deviations in raw $Q(t)$ thus directly expose the influence of ice obstruction and flame pull-in, revealing underlying non-idealities not evident from scaled normalized geometric regression alone.

6.3 Effect of Ice Coverage ψ and Leidenfrost Adjustment upon Flame Standoff Radius throughout Droplet Lifetime

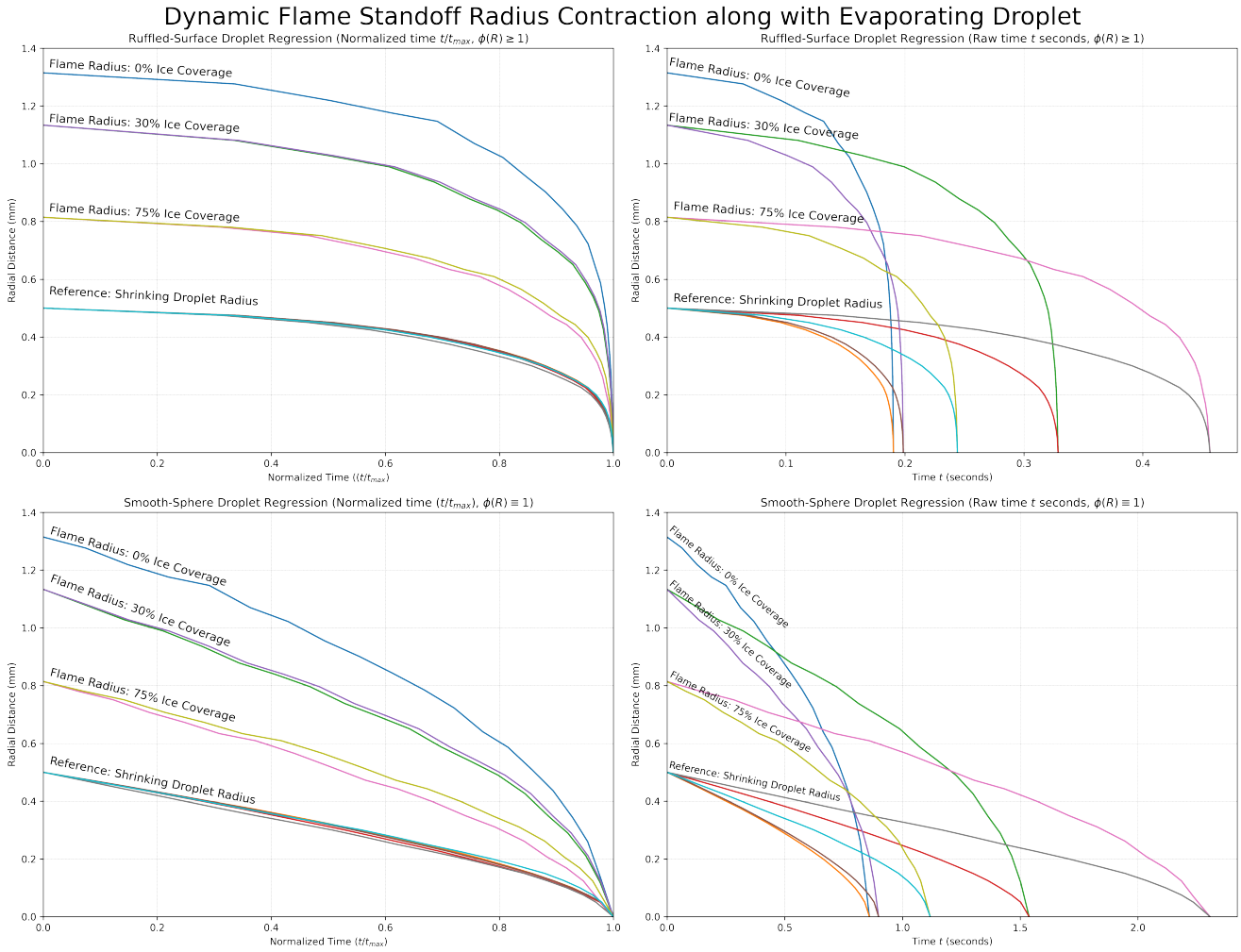

Figure 11: **(Upper Left)** Ruffled-surface droplet evaporation process ($\phi(R) \geq 1$) tracking the flame that retreats together with the droplet's edge. As can be seen with respect to the corresponding shrinking droplet radius reference underneath, for a given ψ ice coverage fraction, the flame standoff ratio remains mostly statically constant throughout the regression. **(Upper Right)** The same data plotted in the space of raw values instead of normalized coordinates. Now the discrepancy underlying the Leidenfrost-adjusted curves can be seen. Since droplet regression can only be retarded by the Leidenfrost corrective denominator, it is easy to distinguish that the longer-lifespan survival curve (of the two initially conjoined) corresponds to such. **(Bottom Left and Right)** The same process's information matched, but for the case of a perfectly smooth sphere ($\phi(R) \equiv 1$).

Figure 11 was generated by simulating trajectories of a plethora of droplet evaporation processes of various ψ values for surface ice coverage, both smooth-sphere and ruffled-surface droplet geometries of $\phi(R)$, and stratified on the account of the Leidenfrost corrective adjustment factor, visually depicted dynamically across each droplet's normalized lifespan. The two plots on the right-hand side, as observed by the monotonically decreasing behavior of all curves, can be loosely interpreted as various characteristic reliability functions of the underlying adapted supermartingale stochastic process (e.g. Cox regression)

that governs the associated failure times, idiomatically used throughout renewal queuing theory operations research in the context of reliability engineering. Such analogous rendition elucidates why the Leidenfrost-insulated trajectories must survive longer than their counterparts, as the slower rate of consumption allows the outlasting droplet's mass to remain for a longer duration before vanishing. Through a similar mechanism naturally, higher surface ice coverage leads to an increase in droplet lifespan as well, while also pulling the flame in closer to the droplet surface everywhere.

6.4 Comparing Relative Effects of Radiation versus Conduction

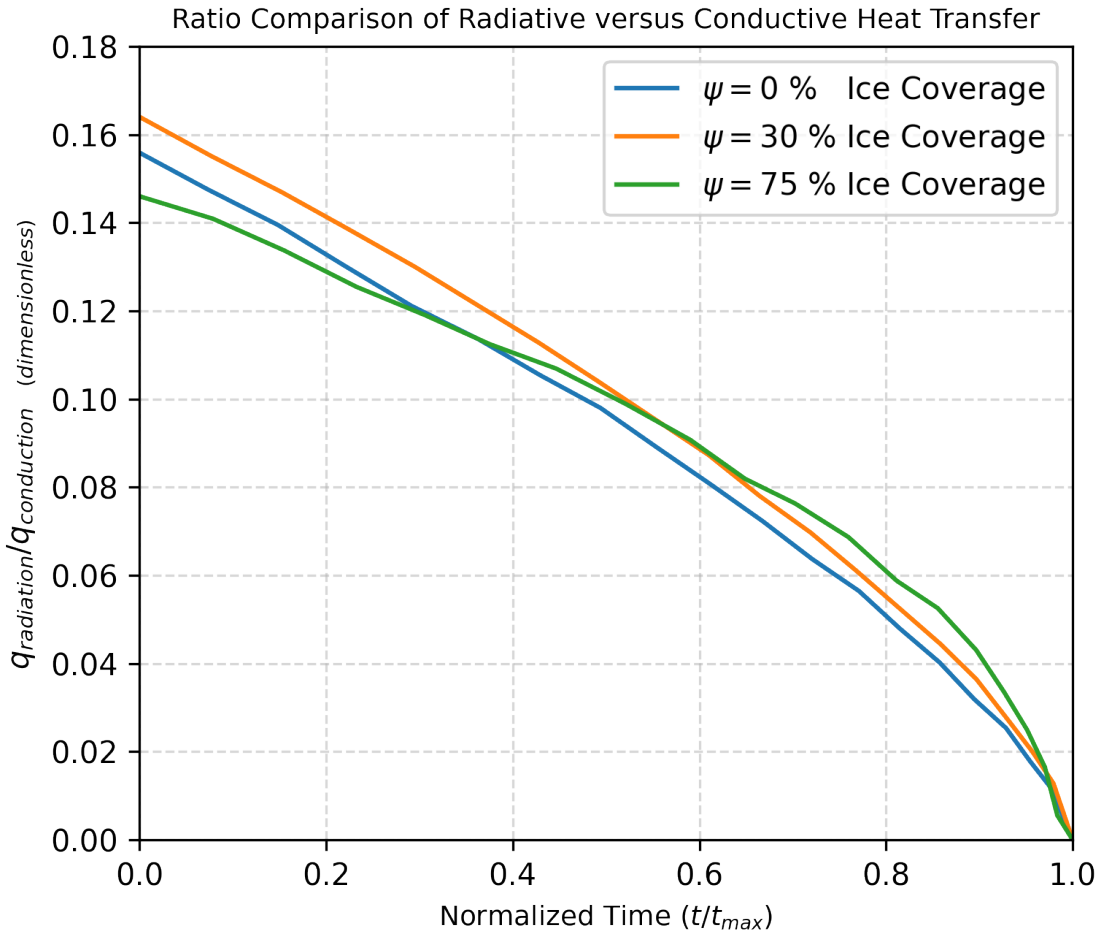

Figure 12: The quotient of radiative energetic transfer over conductive energetic transfer throughout the droplet's normalized lifetime. This dimensionless ratio indicates the relative strengths of each physical phenomenon's contribution to interfacial heat transport aspects throughout the droplet regression process.

As applied to all simulations, the globally low, uniformly bounded values of $q_{\text{radiation}}/q_{\text{conduction}} \leq 0.2$ throughout all ice coverage fractions ψ, portray how conductive effects dominate radiative effects throughout the simulations, hinting that conductive energetic transfer consistently has a comparative advantage

in efficiency over radiative energetic transfer to the droplet surface. Furthermore, as seen through the descending behavior of the curves as the droplet ages, heat conduction increasingly becomes the primary factor correspondingly against the proportionally weaker effects of radiation. This efficacy disparity arises primarily because the tiny Stefan-Boltzmann constant is of a minuscule order of magnitude, while the view factor, proportional to flame standoff ratio, remains mostly statically constant throughout, limiting the power from radiative aspects to a small threshold. Meanwhile, the mostly stationary peak flame temperature, consistently fixed to around 3000 K, forming the vertical rise numerator of our "rise-over-run" quotient formulating the derivative slope $\frac{\partial T}{\partial r}$ estimate involved with calculating conductive power, ends up becoming divided by an ever smaller horizontal "run" quantity from the flame standoff encroaching upon the droplet surface as it ages. Since the peak flame temperature's location becomes ever nearer while it continually approaches the droplet interface, compared to the peak flame temperature value remaining mostly constant, the flame's rising heat conductive contribution to the droplet grows over time. This aspect eventually further dominates the already mostly static radiative contribution of quite limited capability, explaining the downward trend of the monotonically decreasing behavior of the concave curves.

6.5 Droplet Lifetime Trends among all Parameters

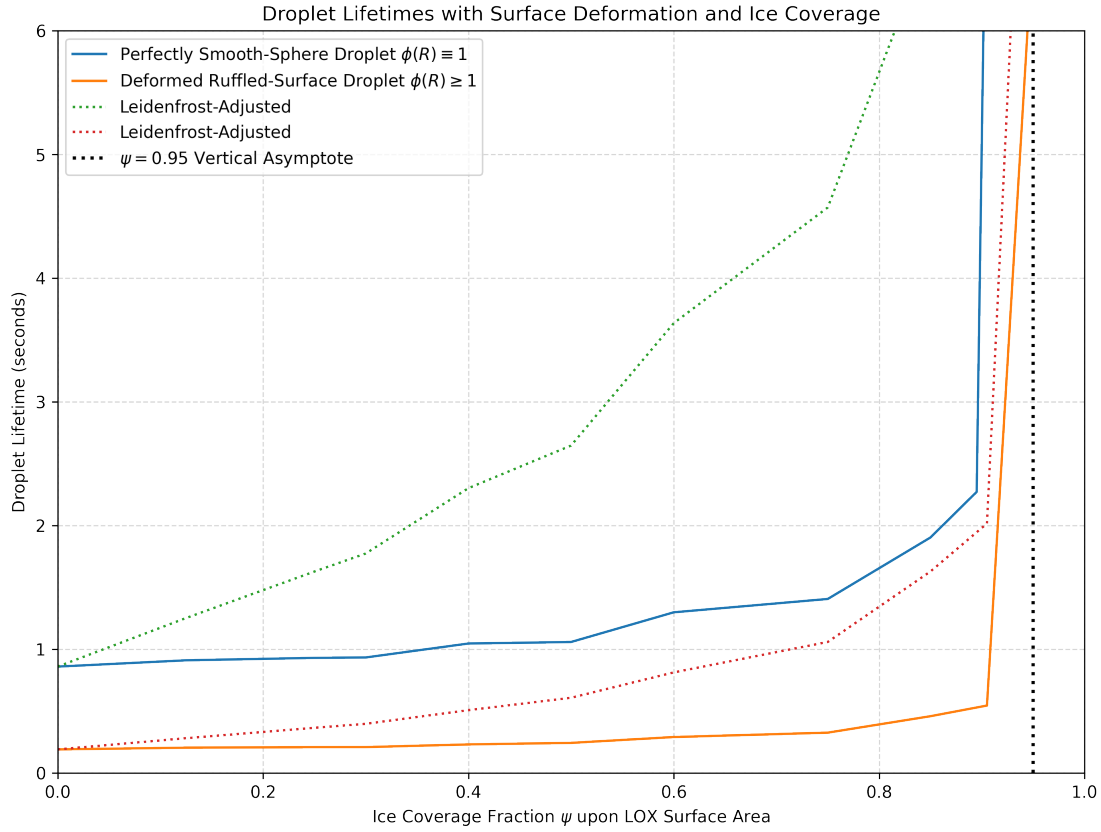

Figure 13: Response variable of droplet lifetime tendencies, with respect to varying LOX droplet surface area ice coverage fraction parameter $\psi \in [0, 1)$, stratified separately by the two distinctly contrasting geometric cases of a perfectly smooth spherical droplet $\psi(R) \equiv 1$ versus a deformed-shape ruffled-surface droplet with $\psi(R) \geq 1$, along with each's correspondingly-paired Leidenfrost-factor adjustment.

Figure 13 shows how droplet lifetime is influenced by the various aspects of our modeling endeavors, akin to a factorial analysis of a balanced experimental design. Throughout the space of increasing ice fraction ψ, the response curves represent droplet lifespan values resulting from various evaporative postprocessing routines for droplet regression. The smooth-sphere case intersects with its Leidenfrost-adjusted counterpart upon the corresponding $\psi = 0$ vertical axis with associated vertical intercept of lifetime $t_0 = 0.86s$, where they both stem from such fork in the road to each branch off on its own individual response curve trajectory. Likewise, the ruffled-surface case intersects with its Leidenfrost-adjusted counterpart upon the corresponding $\psi = 0$ vertical axis with associated vertical intercept of lifetime $t_0 = 0.19s$, where they both stem from such fork in the road to each branch off on its own individual response curve trajectory.

The key takeaway tendencies, quite intuitively, are as follows:

- Overall, increasing ice fraction slows droplet regression from evaporative resistance, and thus increases droplet lifetime.
- The Leidenfrost-factor adjustment also relatively impedes the temporal backtracking process for evaporation, its intent to counterbalance the effects from the increased vicinity of the flame induced by ice coverage, thereby also increasing droplet lifetime.
- As visually evident, non-spherical geometry by far has the largest impact on droplet regression during combustion, yielding the most sizable disparity between the response surfaces. This is because ruffled deformation most significantly accelerates the evaporation rate associated with the CFD post-processing, and ultimately results in comparatively severely reduced droplet lifetimes.

Furthermore, as physical intuition expects, there is indeed a vertical asymptote near $\psi = 1$ delineating 100 % complete surface coverage, occurring numerically in silico when the computationally simulated flame for $\psi = 0.95$ extinguishes in the simulation's elderly stages near the end of such droplet's lifetime. When that happens, the evaporative process stagnates and the flame combustion cycle quenches, rendering it difficult for such feedback loop to persist, subsequently making it challenging to continue shrinking the droplet in the absence of a proper flame. This yields lengthy outlier lifespans, erroneously orders of magnitude larger than relevance. As such, though these extreme values are not explicitly visually shown in the plot, the hinted notion is still indicatively implied, specifically depicted by the dotted vertical line denoting an asymptote at the location $\psi = 0.95$.

7 Discussion

7.1 Non-Spherical Deformation of LOX Droplet

7.1.1 The Anisotropic Mechanisms Underlying Non-Spherical Deformation

Non-spherical behavior likely exerts one of the most dominant influences upon the entire droplet regression process. Understanding its potential causes, and what physical mechanisms conspire to induce such anisotropy is therefore paramount, both for interpreting simulation outcomes and for extrapolating to real-world microgravity combustion environments.

At its core, the LOX droplet, as a simile, is not merely a rigid marble but rather a living, breathing interface; it can be elastic and reactive, trembling under the combined orchestration of surface tension, heat flux, and vapor recoil. Even when initialized as an idealized perfect sphere, the coupled interplay between internal and external fields from the underlying physical phenomena, ensures that such geometric perfection is only fleeting. The droplet soon dances into asymmetry with anisotropic behavior.

Internal liquid-phase motion. Although our numerical framework does not directly resolve liquid-phase hydrodynamics, one plausible culprit for anisotropy stems from internal convective motion and temperature gradients which are not explicitly simulated. Localized heating near the interface can spawn internal eddies and swirling vortices within the liquid oxygen phase, loosely conceptually akin to thermo-capillary Marangoni convection as opposed to the Boussinesq approximation in higher-g environments. These convective circulations drive uneven temperature distributions and, consequently, spatially varying evaporation rates, a feedback loop of inhomogeneity. The droplet's interior, in essence, behaves like a slow-breathing lung, with its own gentle weather system of miniature thermals, whose invisible churn subtly bulges and dents the outer surface.

Surface instability and modal oscillations. Another route to asymmetry emerges from the surface itself. The interface acts as a tense membrane supporting oscillatory modes describable by spherical harmonics, each representing a possible standing-wave vibration upon the droplet's surface. Minute perturbations–thermal, acoustic, or convective– can seed growth in these modes, and once initiated, the engendered coupling between vapor recoil and capillary forces may amplify the higher-order distortions. In a complex-valued representation of such disturbances, the real and imaginary components correspond to spatial and phase offsets across the interface, forming a kind of harmonic interference pattern that manifests as anisotropy. Even starting from an ideal mathematical sphere, nonlinear coupling through this dynamic phase space tends naturally toward ruffling, interpretively invoking the same ergodic hierarchies and cascade mixing behavior that Kolmogorov's theory attributes to turbulence, of the same flavor of Boltzmann's famous *Stosszahlansatz* underlying the molecular chaos description of statistical mechanics.

Porous meniscus regions and vapor recoil jets. As the surface continues to deform, localized thinning and puncturing can create a porous meniscus or micro-holes through which vapor effuses. These transient pores behave analogously to the microthrusters of a maneuvering spacecraft– the escaping gaseous oxygen blows off to exert reactive impulses upon the droplet, sometimes inducing translational motion. The phenomenon of vapor recoil has been well documented in literature: when the escaping flux is sufficiently strong and asymmetric, the recoil momentum can deform or even propel the droplet itself. The effect resembles an astronaut using a punctured suit as a makeshift jetpack, or a balloon releasing air through a small nozzle, resembling the same qualitative principle, now operating in cryogenic miniature.

Microgravity and chamber environment. Unlike pure zero-gravity, in microgravity conditions such as those of the ZARM drop tower experiments, the absence of a dominant gravitational field reduces buoyancy-driven convection but does not eliminate motion entirely. The LOX droplet effectively free-floats within the surrounding gaseous hydrogen, its dynamics governed primarily by local flow distur-

bances and vapor recoil impulses. With such motion, residual gas drag and chamber pressure (typically near one atmosphere) introduce a weak aerodynamic coupling. At higher pressures approaching supercritical conditions, the standard theoretic D^2-law paradigm's conventional treatment may approximately hold, preserving quasi-static regression as observed in the high-pressure ZARM droptower experiments [3]; yet at lower, subcritical pressures, experimental lifetimes from ZARM's experiments shorten dramatically, signaling the onset of enhanced non-spherical and translational behaviors, in conjunction with visual evidence from comparing the experimental footage of the droplet combustion processes at various pressures. While in spray-injection situations for fuel combustion, droplets behave as ballistic projectiles– in a microgravity environment, the droplet becomes more like a drifting ember than a stationary torch.

Surface roughness, ice morphology, and feedback. Further complicating this picture is the surface ice layer that intermittently forms upon the droplet during oxygen-hydrogen combustion. The speckled nucleation of ice crystals is inherently stochastic, leading to freckled irregular patchwork coverage and roughness that feed back into the local heat and mass transfer balance. This is akin to randomized pixels corrupted with "salt-and-pepper" noise encountered in image processing. Each crystallite grain that randomly forms upon the surface, acts as a minute protrusion or micro-lens altering the local radiative field and modifying vapor escape pathways. This chaotic texture further promotes anisotropy, creating a dynamic feedback loop between surface roughness, local flux concentration, and ruffling evolution.

Ignition asymmetry and transient turbulence. Even at the very beginning of the experiment, asymmetry is inevitable. The ignition spark—typically triggered from below the droplet in the ZARM configuration– is itself spatially biased upon initiation. The ignition plume momentarily engulfs the droplet in a violently nonuniform thermal field, inducing steep gradients before any quasi-static regime can be established. The turbulent field's instantaneous extreme variation generates transient turbulence and shear that leave lasting geometric fingerprints on the droplet's shape evolution, making it difficult for the system to maintain isotropy, characterized as an inverted pendulum, such unstable fixed point in Floquet theory that can only be maintained through extreme external drives with high frequency excitation. Spherical symmetry, in this light, is more of a convenient fiction than a physical reality.

Summary. In summary, since the details of the entire process are obfuscated by the limited resolution of the experimental apparati at ZARM, many of these notions are primarily speculative. It is likely that the non-spherical deformation of the LOX droplet is not a singular phenomenon but rather a messy, cacophonous symphony of interacting effects– surface oscillations, internal convection, vapor recoil, ice roughness, and ignition turbulence– all entangled within a microgravity choreography. Each mechanism contributes a stanza to the droplet's evolving geometry, expanding its surface area and, in doing so, amplifying the effective interfacial coupling that governs regression rate. The droplet's path through

time is probably therefore less a smooth fade than a fluttering unraveling, where its geometry is sculpted by chaos, yet governed by the deterministic whisper of physics underneath.

7.1.2 Zooming into the Surface Ice

Clearly, ice fraction and nonsphericity interact quite intimately, and almost inseparably, as seen in previous sections. Yet due to the limited resolution (reportedly ~ 16 μm/pixel) of the ZARM drop tower experimental footage [3], the true microscopic choreography at the liquid–solid–gas interface, especially during subcritical pressure operation, remains an unresolved mystery. The camera sees the macroscopic ballet, not the finesse of the subtle molecular whisper. Hence, only through computational modeling can physically grounded speculation begin to fill the observational gaps.

We know ice is present: it visibly manifests as discrete blotches, occasionally shedding chunks that fling off dramatically, deforming the droplet as it nears its terminal stage. The footage suggests fragmentation, nonuniform solidification, and asymmetric recoil. In our work, however, the primary focus remains on spherical-symmetry quasi-static regression and lifetime behavior, analogous to studies of various complex public health effects upon longitudinal population longevity analyses. Thus, we employ radial averaging as a statistical act of mercy, to compress the chaotic, anisotropic truth into a single representative geometric abstraction, that hopefully, with minimal Kullback-Leibler divergence, captures the most meaningful aspects. Within that abstraction, we can extract meaningful quantities, though we remain aware of the epistemic humility required: the molecular-scale complexity at the interface (and especially within the triple point critical regime) exceeds our continuum-scale reach.

Nevertheless, discussing what we *cannot* observe is vital. It sets the ambient backdrop for the modeling decisions that follow, particularly motivating the etiological genesis and conceptual birth of the "ruffle-factor" formulation discussed next. The surface ice, with all its enigmatic feedback loops and stochastic nucleation dynamics, must be acknowledged not just as a nuisance but as a generative uncertainty: one that motivates parameterization, not paralysis, to provide inspiration for investigative curiosity, with room for alternative approaches. Our shrouded realm of exploration could be considered "antifragile" as Taleb famously describes in his book with such title. [103] In short, the unchartered territory of ice may be a mystery, but it is a productive one upon the frontier of cryogenic combustion.

7.1.3 Ice Fraction and Its Modeling Implications

In the simulation framework, the ice interface directly couples into the gas–dynamics boundary conditions. Specifically, we modulate the Dirichlet oxygen boundary reservoir at the droplet surface from an initial 200 mol/m^3 down to zero, scaled proportionally by the ice surface coverage fraction ψ, while also together with ψ simultaneously levying a resistive "tax" upon Stefan flow velocity within the CFD domain. Post-processing then imposes an additional, phenomenological impedance, which functions as

another tax on the effective regression rate using such ψ.

Why apply such a penalty, if ice, as a material, is more thermally conductive than liquid oxygen or its vapor? The answer lies not in conductivity but in obstruction: the ice physically impedes mass flux and local evaporation, echoing a Henry's law–like throttling effect on gaseous oxygen escape. A contrapositive viewpoint and various counterfactual computational experiments illustrate the issue's core: ignoring the ice parameter ψ altogether during the droplet regression CFD postprocessing, produces unrealistically short lifetimes with respect to the D^2-law due to the flame pull-in effect, with increasing ice coverage paradoxically *accelerating* droplet demise. That would be physically absurd: a blockage should not act as an accelerator. Even when we correctively account for such flame pull-in effect using our Leidenfrost adjustment to cancel its impact out, the model's droplet lifetime still remains constant independent of whatever ice value ψ is chosen, which contradicts experimental observations that illustrate that ice is clearly at play to appear somewhere along the droplet lifetime pipeline. In other words, even if the causal effect of ice upon droplet lifetime is merely through the confounding variable of contributing to mechanistic avenues of non-spherical deformation, we can still reject the "null hypothesis" that ice is completely irrelevant, implying that it is meaningful to incorporate ice into our model somewhere such that it integrates with droplet lifetime trends in some noticeable manner. In postprocessing mathematically speaking, we really only have rate of evaporation to play with, meaning a one dimensional parameter space with only one limited degree of freedom to tinker with (like a statistical curved exponential family), and so as long as ψ shows up in such expression, whatever underlying structural causal relationships are at play in the directed graph, can all be moralized to in a sense be "swept under the rug" for our modeling purposes upon implementation.

To illustrate this intuition, imagine a Brownian walker within nested boundaries: the walker must hit the inner boundary before the outer one. Geometrically, smaller enclosures correspond to faster hitting times. Analogously, a droplet's evaporative flux cannot "escape" faster when encased in an additional barrier; such behavior would violate fundamental geometric reasoning akin to first-passage principles in stochastic calculus. Thus, the model enforces a physically consistent impedance behavior: increased ψ lengthens lifetime.

This principle reconciles with experiment. The ZARM subcritical (1 bar) tests show drastically shorter lifetimes than those predicted by idealized, D^2-law behavior, which the supercritical experiments exhibited. Hence, while ice alone slows the process, the *dominant* acceleration likely arises from non-spherical "ruffling" dynamics. The model must therefore combine both effects, namely ice impedance and geometric amplification together, to reconcile simulation and experiment.

7.1.4 Modeling Logic Behind the Ruffle Factor $\phi(R)$

Having established the physical role of ice, we turn to the ruffle factor $\phi(R)$, serving as the mathematical avatar of non-sphericity. In the simplest possible terms– of the flavor of standard model dimensionality reduction techniques such as SVD-PCA, k-means clustering, or t-distributed stochastic neighbor embedding– our simulation collapses the messy multi-dimensional chaos of surface deformation into two distinctly disjoint scalar parameters:

$$\phi(R) \in [1, \infty), \quad \psi \in [0, 1].$$

Here, ψ governs interfacial obstruction, while $\phi(R)$ amplifies flux through enhanced effective surface area. Both act multiplicatively within the postprocessing stage of the model, applied to the nominal quasi-static spherical flux q_{original}:

$$q_{\text{modified}} = [\phi(R)\,(1 - \psi)]\, q_{\text{original}}.$$

The rationale is straightforward yet subtle: the ice coverage reduces available exposed-skin active surface (and/or the efficacy of such available interface), while non-spherical shape-wise deformation directly expands it geometrically. Together they describe the tug-of-war between insulation and exposure, between impediment and amplification. Even if they are not exact quantities, akin to the notions of effective kinetic collision diameter or effective scattering cross section from physics, they still serve as physically meaningful quantities for analysis. Similarly, even if the cardinal nominal value of Von-Neumann-Morgenstern expected lifetime utility is in and of itself somewhat meaningless in isolation, the utility function's ordinal and comparative relations encode, in a complete and self-consistently ranked manner, consumer preferences in dynamic stochastic optimal control settings, and formulate the axiomatic foundation of decision theory, serving as intuitively informative quantities for similar modeling in the formal philosophy analog of natural philosophy.

The ruffle factor embodies the notion that any deviation from spherical symmetry—rippling, folding, dimple formation, or full chaotic deformation—inevitably increases surface area. By the earlier calculus of variations demonstration, the sphere minimizes surface area for a given volume, so any departure must therefore amplify flux by geometry alone. Hence, $\phi(R)$ begins at unity (perfect sphere) and rises monotonically with deformation severity.

In implementation, $\phi(R)$ was empirically constructed as a piecewise-linear ramp:

$$\phi(R) = \begin{cases} 1 + 22(1 - R/R_0), & R > 0.5R_0, \\ 10 + 100(0.5 - R/R_0), & R \leq 0.5R_0, \end{cases}$$

loosely approximating the visual ruffling observed in ZARM's Figure 7(a) [3] calculated using the image processing processing methodology from Figure 4 in Meyer (2022) [3]. In our code, this corresponded to a concatenated NumPy array:

```
np.concatenate((np.linspace(1,12,10), np.linspace(10,60,10)))
```

to provide an empirical sketch of how ruffling ramps as the droplet shrinks.

There is also, conveniently, another more purely geometric or physics-based interpretation of the coupling between the ruffle factor $\phi(R)$ and the ice coverage fraction ψ using the lens of vector calculus and physics. Quite akin to the notions of surface integral flux and solid angle scattering amplitude, the ruffle factor $\phi(R)$ characterizes the relative effective interfacial surface area gain with respect to the normalized baseline of a perfect sphere of radius R, upon which the surface integral flux is to be calculated. As a simile to help characterize, after zooming into a miniature surface area element contact patch upon the lipid bilayer of a cell's semipermeable membrane, one will observe a certain density of follicles to facilitate exchange– typically ATP-driven ion pumps for the osmosis of nutrients, or HVAC-flavored management of the regulated internal environment of the cell body with respect to the exterior. Rather than through ion channel pores, heat and mass transfer happens upon the solid-liquid-gaseous interface, where the amount of flux directly scales with the interfacial contact area, where the loose "vector field" in consideration is now the efficacy or speed of exchange, oriented orthogonally to such surface element, aggregated per unit area upon such surface integral upon the membrane manifold. In spherical coordinate geometry, the vector field is assumed to always be oriented in the direction of $\hat{\vec{\mathbf{r}}}$, which is a reasonable approximation for the situation, akin to the configurational geometric modeling behind the Derjaguin approximation. In a similar light, in accounting for the reflectivity of the Earth in environmental geo-science or satellite remote sensing, it is customary to primarily consider optical characteristics pertaining to the ocean, of which about 70 % of the Earth's surface comprises. From this geometric picture, this sort of loose multiplication of base area times field-strength-height (independent of the Cavalieri principle) yields a loose volume-based quantity, thereby characterizing the multiplicative nature of the two parameters in question.

Occam's razor and the art of parameterization. As George Box famously wrote, "All models are wrong, but some are useful." Following this ethos– and echoed by Page's *The Model Thinker* [104]– our $\phi(R)$ is not meant to fully "capture reality," but rather to encode the perceived essence of what actually matters for our modeling portrayal of reality. This concept also enormously parallels Richard Hamming's famous book *The Art and Science of doing Engineering* [105], especially considering how we perceive nature to corrupt every Shannon communication channel with seemingly some sort of additive white Gaussian noise, a foundational axiomatic assumption behind telecommunications engineering. The analogy to micro-founded econometrics is also apt: just as the gist of education correlates with income

not due to intrinsic virtue but through signaling equilibria (à la Akerlof's "lemons" or Spence's signaling model, both Nobel Prize economists), [87, 106] our $\phi(R)$ captures the effective outcome of countless hidden mechanisms: recoil, turbulence, asymmetry, and instability.

We could, of course, invoke higher-dimensional formulations (e.g. $\phi\big(R, \psi(t), \psi'(t), t\big)$), or shape-dependent PDEs, or explicit coupling to curvature tensors, but doing so would overfit physics with metaphysics. Occam's razor slices cleanly here: $\phi(R)$, as a one-dimensional function (and easily tuned), suffices to encode the net ruffling gain in a quasi-static radial framework.

An extremely useful property of deliberate simplicity in modeling context is the evasion of the quagmire of combinatorial mixtures between effects, a morass of complexity arising from the curse of dimensionality, attributed to the realm of fuzzy logic pioneered by Zadeh (1988) [107], entering a swamp of submodular set functions exhibiting returns to scale serving as a cognate for the economic network effect, Shapley value analyses, and treatment mixture effects upon regression adjustments. To characterize this notion: while dipping potato fries in ketchup is a natural pairing with likely a desirable positive "eutectic" mixture effect, and the same likely applies to drizzling chocolate sauce with ice cream, it is on the other hand, likely an unfavorable pairing to pour chocolate sauce on potato fries and cover ice cream with ketchup, implying estimating the realized popularity of each individual edible-entity on its own, as a standalone consumable in isolation, becomes garbled when the combinatorial statistical treatment mixtures are involved upon the incidence and design matrix. Fortunately, a panacea to the situation is by considering that if pizza is now the new craze of food-court concessions customers, and is so popular in demand compared to both ice cream and fries sales combined, that their interactions with their associated condiments are negligible. Analogously in our situation with modeling the process of the LOX droplet's regression, while it is possible that the surface ice coverage ψ and the non-spherical deformation $\phi(R)$ mix effects and causally interact, at some point not too far along the way as the droplet progressively shrinks, the droplet already "on its way out", can be functionally considered deceased, especially when the flame engulfs the comparatively small droplet and it checks out completely. Sweating chump-change pennies on the dollar among the minute and last-minute interactions in this "lame-duck" droplet scenario is largely as insignificant as small potatoes, providing further justification for preserving simplicity in our modeling setting.

The geometry of amplification. The multiplicative structure $\phi(R)(1-\psi)$ is not arbitrary– it echoes the physical logic of combined attenuation and exposure, as previously intuited. In essence:

- $\phi(R)$ scales with the fractal-like expansion of surface area, analogous to the classic coastline paradox.
- $(1-\psi)$ scales with the fraction (or efficacy) of that area actually active for evaporation.

This product encapsulates the effective interacting geometry: ruffled yet partially frozen. The metaphor extends to Mandelbrot's fractal mathematics– Gabriel's Horn, the Koch curve, Sierpinski Triangular gaskets– where increasing "ruffledness" yields a loose unresolvable paradox arising from infinite perimeter or surface area within finite bounds, giving rise to the seminal mathematical concepts of (Box-Counting) Hausdorff measure and fractal dimension as used in ergodic chaos theory. In similar spirit, the $\phi(R)$ term theoretically approaches infinity as roughness tends toward unbounded microstructure; physically, it just means vastly enhanced local gradients and exchange rates, especially when translated or projected onto the subspace of what is directly relevant to droplet regression. In the spirit of the Gauss–Bonnet theorem, where the total integral of curvature over a manifold yields a topological invariant, $\phi(R)$ represents the integrated measure of geometric distortion condensed into one scalar descriptor. It is the "Euler characteristic" of chaos, expressed as a gain factor.

This primordial idea of summarizing a measure-theoretic distributional configuration of mass density is the central bedrock of all of probabilistic statistics and data informatics, and is sometimes referred to as "Law of the Unconscious Statistician" which defines expectation operator with respect to a probability measure. The fundamental abstraction pertaining to its essence is to convey a central summarizing scalar value of a statistical quantity arising from a random variable, which in practice turns into the flavor of the field of "data analytics" that has become popular in modern times, a term coined by visionary John Tukey at Bell Labs, along with the terms "bit" for "binary digit" and "software", all in the middle of the 20th century. Common practical techniques for data visualization and summarization for assessing pattern-theoretic information trends in data sets can include generating "Box and Whisker plots" or "Stem and Leaf plots", both of which Tukey originally proposed in his seminal book "Exploratory Data Analysis" [84]. Alternatively, one can creatively encode information in the likeness of facial structural profile features to succinctly depict information and interleave their associated trends using "Chernoff Faces", which nicely make use of the innately hard-coded human psychological visual cognitive ability to immediately recognize the visages of people they know in their community. This idea is also not unique to data science; it is very much used in physical sciences as well, just under a slightly different format. While probability distributions must be normalized to unity by the Born rule or the axioms of Kolmogorov, physical distributions on the other hand explicitly characterize the mass distribution profile and are normalized to the nominal total quantity of mass, which can alternatively be viewed as non-normalized signal processing filters that have a gain that's not necessarily zero Decibels, commensurately scaled to the physical quantity of interest. Viewed through this lens, physical quantities such as moment of inertia and center of mass are merely summarizing quantities of the mass density distribution and geometry, mathematically akin to the expectation operator but scaled to the total cumulative aggregate mass.

In this light, not only is it acceptable for our modeling purposes to portray the complex boundary

of the LOX surface layer's mechanics with only a handful of summarizing parameters, but also, since investigators of various interdisciplinary fields have already been doing this type of analysis for quite a while now, it has almost become tantamount scientific convention.

Heuristic justification and empirical grounding. The function $\phi(R)$ was chosen because it bridges idealized spherical models (droplet lifetime $\sim 1\,\mathrm{s}$) with ZARM data (lifetimes $\sim 130\,\mathrm{ms}$) [6, 7]. Without such amplification, the discrepancy remained irreconcilable. With careful choice of heuristic tuning, the $\phi(R)$ function allowed the intersectional simultaneous matching of 1. the experimental droplet's lifetime while still respecting the D^2 law from idealized theory, 2. actually account for non-spherical deformation within our radially-symmetric model, and 3. empirically reasonably match the experimental trajectories from figures 7 and 8 in Meyer (2022) [3]. The tuned parameter acts like a dynamic compressor or expander in signal processing: it modulates flux amplitude as a function of droplet radius, akin to a "knee" in a logarithmic dynamic range curve, ensuring the modeled decay behaves plausibly across regimes.

Synthesis. Ultimately, $\phi(R)$ and ψ function as orthogonal explanatory components, which can be viewed as a PCA-like decomposition of physical causes. One modulates availability (ice impedance), the other modulates intensity (geometric amplification), a common modeling technique in surface science deposition and adsorption models. The conjoined product $\phi(R)(1-\psi)$ thus summarizes the effective heat and mass transfer state at any given droplet radius, reconciling the model's spherical constraints with the physical system's chaotic truth:

$$q_{\text{modified}} = [\phi(R)(1-\psi)]\, q_{\text{original}}, \tag{93}$$

This imparts a deceptively simple equation hiding within it the full entanglement of morphology, thermodynamics, and geometry.

In summary, we cannot capture every ripple, every icy ridge, or every fleeting asymmetry, but we can encode their collective consequence for tractability, just as physicists have long entertained with back-of-the-envelope Fermi-number analyses using the famous "Spherical-Cow" modeling. The "ruffle factor" is not a correction; it is an homage to complexity, distilled through the art of modeling.

7.1.5 Leidenfrost-Type Adjustment Factor

Motivation: the problem in the modeling chain. During parameter sweeps, an unintended artifact emerged within the CFD–postprocessing loop: increasing the ice surface coverage fraction ψ pulled the flame standoff distance inward toward the droplet. This geometric contraction, when fed into post-processing, inadvertently amplified the local heat flux back onto the droplet surface, thereby offsetting the intended impedance tax that ψ was designed to impose.

In effect, the model accidentally created a feedback loop: more ice ⇒ flame settles closer ⇒ higher heat flux in postprocessing ⇒ faster regression. The result was an almost total cancellation of ψ's supposed physical slowdown effect in postproduction for droplet shrinkage. Droplet lifetime remained roughly constant regardless of ψ, an outcome both numerically stable yet physically absurd. A barrier should not act as an accelerator in any aspect of the pipeline.

This subtle self-negation arose because the CFD field solution for flame position dynamically responds to boundary conditions, whereas the subsequent postprocessing assumes those geometries are exogenous and static after settling down. The combination thus violates the independence assumption implicit in the quasi-static framework.

Diagnosing the source. The root of the issue lies in how the interfacial heat flux was originally computed: as a "rise-over-run" ratio, the peak flame temperature (rise, ~ 3000 K) divided by the spatial gap between the flame standoff radius and droplet radius (run). This is a common and numerically stable approximation that works particularly well for spherical coordinates, ensuring the system quickly equilibrates and maintains a realistic flame temperature plateau.

However, when ψ increases, the flame standoff distance decreases. Since the numerator (temperature difference) is fixed, the denominator shrinks, inflating the computed flux, which is exactly the opposite of the desired physical effect. The "rise" stays constant, but the "run" collapses. Thus, the presence of ice paradoxically enhances heating through purely geometric arithmetic, not through real physics.

Physical interpretation and limits. In reality, the formation of a surface ice or vapor film should impede both heat and mass transfer– akin to the Leidenfrost effect, where a thin vapor cushion thermally insulates a droplet from a hot surface. Similarly, in cryogenic combustion, the ice layer and associated vapor recoil can produce a quasi-insulating barrier that decouples the flame from direct conductive heat flux.

Such interfacial effects likely exist below the CFD grid resolution (and ZARM's experimental footage pixel-resolution): within micron-scale boundary layers where turbulence, recoil, and local saturation hysteresis dominate. The phenomena are reminiscent of Fickian transport saturation or "overdriven" media responses, analogous to a blowing out an audio transducer loudspeaker driven beyond its linear range, where the system no longer transmits incremental input proportionally, but instead dissipating it into turbulent micro-motions. This scenario is also reminiscent of stress-strain curves to determine the thresholds for strain hardening, necking, and plasticity fracture mechanics failure, past the linear Young's modulus region. In silico when handling such steep gradients, this manifests as an additional effective insulation layer after passing an extreme threshold, further impeding transport.

The heuristic ad hoc fix. To counteract the artificial coupling between ψ and flame standoff geometry, we introduced a phenomenological correction– a multiplicative "Leidenfrost-type" attenuation factor in the postprocessing expression:

$$q_{\text{modified}} = \left[\phi(R)\frac{1-\psi}{1+3\psi}\right] q_{\text{original}}.$$

The denominator $(1 + 3\psi)$ heuristically attenuates the artificially amplified flux arising from flame pull-in effects. In conceptual terms, it "partials out" the spurious geometric dependence on ψ introduced by the CFD's self-adjusting flame geometry. The coefficient 3 was chosen empirically from simulation trends– an order-one tuning constant yielding physically plausible monotonic lifetimes across the ψ sweep, consistently in reasonable coinciding agreement with both experiment and quasi-steady theory.

Interpretation and justification. This term effectively isolates the direct, causal effect of surface ice impedance from the indirect, geometric effect of flame contraction. In causal-inference language, it performs an adjustment analogous to the Frisch–Waugh–Lovell (FWL) theorem: removing a confounding regressor to reveal the pure treatment effect of interest.

Physically, the correction can be viewed as increasing the effective "run" in the rise-over-run flux calculation, which compensates for the artificial proximity of the flame front caused by increased ψ. In doing so, the postprocessed evaporation rate better reflects interfacial transport physics rather than geometric artifacts.

On the limits of quasi-static approximation. Naturally, this ad hoc adjustment does not resolve deeper limitations: the lack of detailed interfacial resolution, the absence of molecular dynamics in our modeling framework, and the grid-scale averaging of transport properties. These factors are endemic to continuum CFD operating in regimes where phase-change processes occur near or below the grid spacing, especially under subcritical conditions.

Nevertheless, the corrective factor provides a pragmatic bridge, to maintain consistency with physical intuition, while preserving the model's numerical stability and tractability. The Leidenfrost-type adjustment therefore functions less as a correction and more as a calibration lens, allowing us to view the simulation results through the appropriate causal framing: one that respects the multiscale insulation effects of the ice layer, without being deceived by numerical geometry artifacts.

Summary. In summary, the $(1+3\psi)$ denominator restores physical sensibility to the model's treatment of ice by counteracting the flame-pull-in feedback. It reestablishes the intuitive monotonic relationship between increasing ice coverage and increasing droplet lifetime, aligning the simulated behavior with experimental observation. While heuristic in construction, it remains faithful to the spirit of physical modeling– transparent, adjustable, and grounded in observed simulation behavior.

7.1.6 Strong Semblance of an Interpretable and Plausible Model

***Medial Caesura* on the Natural and Formal Philosophical Validity of our Model**

Who truly knows what is going on beneath the LOX-droplet's interface? Perhaps no one fully– but the quasi-static framework gives us a convincing language and a compass. Within the quasistatic evaporation regime for droplet regression, we assume (at least initially) spatially uniform pressure, steady Stefan flow, and only minor spatial variation in transport properties. These are, of course, conditional premises, which are standard yet idealized. It is worth acknowledging explicitly that these premises may not be universally satisfied. The symbolic logical framework we construct is thus founded upon contingent truths: internally consistent, complete, and sufficient within the formal calculus of its assumptions confines, which aligns with the axiomatic foundations of mathematics forming the bedrock of all subsequent theorems.

Yet, as with a broken clock that is right twice a day, even a noisily imperfect model may align precisely with nature under specific configurations. The fact that our structural framework mechanically reproduces key physical observables, both qualitatively and quantitatively, aligned with these two zero-measure conditions from the Dirac measure atomic clock hand configurations, is not coincidence but evidence that the model captures something fundamentally correct– at least within its domain of validity.

Empirical alignment: subcritical vs. supercritical regimes. At high pressure, droplets tend to remain spherical and supercritical, consistent with the diffusion-limited D^2 law. By contrast, at subcritical conditions, erratic nonsphericity emerges and the D^2 law is experimentally violated. The model reproduces this bifurcation robustly, with the conditional ability to capture both behaviors based on parameter inputs. It is therefore improbable that agreement arises from mere coincidence or numerical "bogosort luck." This is the same line of reasoning, (a type of *reductio ad absurdum* proof technique), behind the common practice of using extreme p-values to reject the null hypothesis in the statistical hypothesis testing procedure, implying that it is unlikely to have hit the target purely by blind happenstance among the sigma algebra's gigantic event space of all potential modeling decisions, hinting that our model's information content cannot be utterly zero. By the Holmesian principle– when the impossible alternatives are eliminated, the remaining improbable explanation must be the one-single truth– the only plausible explanation is that the model is capturing the essential causal mechanism: geometric deformation drives deviation from ideality.

Logical structure of the modeling argument. All physical modeling is, at its heart, a structured argument. We begin with premises (boundary conditions, material laws, closure assumptions), apply a logical calculus (the governing equations and constitutive relations), and derive conclusions that are true within the world defined by those premises, implementing unique antecedents to generate interesting consequences. In that sense, the model operates analogously to a formal proof: sound and complete within its own axiomatic system. This reflects the broader philosophical lineage of physics modeling–

from the symbolic logic of Hilbert systems to the computational generativity of Chomskyan grammars and the Church–Turing paradigm of constructibility.

Just as Newton's law of gravitation elegantly described planetary motion but failed for Mercury's orbit until Einstein's relativistic corrections arrived, our model's partial deviations from experiment may not be failures, but rather signposts of the next layer of theory awaiting inclusion. Techniques from computational modeling simulation can powerfully shed novel insight by expanding what is already known, such as how computational astronomers have expanded our solar system through mechanical simulation of physical laws to reveal significant clues about the location of a hypothetical "Planet X" past the Kuiper belt that is invisible to sunlight. A simulation that can explain counterintuitive phenomena– such as flame standoff contraction under partial icing– already demonstrates interpretive power. Unlike a black-box neural net with unexplainable AI, this framework remains transparent, causal, and classically computable, built from first-principles thermofluid reasoning.

Current Model Accuracy Compared to Hypothetical Alternatives The timekeeping chronometry of postprocessed regression employs a "plug-in estimator" for surface heat flux $q(R)$ based on sufficient statistics derived from the temperature field—namely, argmax(T) and max(T)—modulated by ice fraction and surface roughness factors. Beyond these, few parameters remain that could meaningfully improve explanatory power. In other words, the model already occupies a kind of logical local pareto optimum: parsimonious yet sufficient.

The analogy to a Q–Q plot in exploratory data analysis [84] is instructive: by plotting model outputs against theoretical expectations, one can visually assess normality, ANOVA variance structure, and heteroskedasticity, on the path of ascertaining whether any problematic deviations from idealized assumptions occurred. As seen in 10 for combustion science, the near-linear collapse across cases substantiates the quasi-steady diffusion-limited assumption; deviations quantify ice-induced obstruction and flame-geometry distortion.

Synthesis and interpretive argument. Taken holistically, the model meets three coinciding criteria: (1) it aligns with both theoretical limiting cases and experimental observations; (2) it is grounded in first-principles physics yet retains interpretability and tunability; and (3) it captures a range of phenomena inaccessible to prior open-source OpenFOAM CFD efforts [6, 7], such as full coupling of flame, Stefan flow, and postprocessed regression under varying ice morphology, due to inherent efficient construction and design of the current lean-machine simulator.

It is particularly challenging to simultaneously satisfy these three factors together due to their distinct dimensions upon different inherent aspects: 1. quantitative agreement, 2. qualitatively interpretable and physical, and 3. system complexity requirements. In sum, the model is not merely numerically accurate but philosophically coherent. It is a self-consistent argument in the language of physics: internally valid, externally plausible, and empirically corroborated. To borrow from the spirit of constructive logic: given

the premises, the consequent follows necessarily. The decisive evidence, both qualitative and quantitative, conclusively indicates that this framework is indeed doing something *right*, consummating a compellingly convincing model of our conception.

8 Conclusion

8.1 Recapitulation, Novelty, and Significance

This work investigated LOX–H_2 droplet combustion phenomena as exhibited in the ZARM drop-tower experiments of Meyer (2022) [3], by employing a custom-built, lean numerical simulator specifically designed to probe and reproduce key interfacial behaviors. The overarching motivation was to construct a tractable yet physically faithful model capable of exploring the coupled physics, including flame dynamics, Stefan flow, and droplet regression, that proved computationally or structurally inaccessible in prior high-overhead expenditure CFD frameworks such as OpenFOAM.

Summary of approach and rationale. The "lean-machine numerical simulator" developed here embodies a deliberately minimalist philosophy: it implements the essential physics without the heavy abstractions or black-box opacity of legacy packages. This simplicity afforded direct control over each modeling component, enabling iterative tinkering, high interpretability, and efficient parallel and adaptive experimentation. The model integrates all previously fragmented effects– including flame coupling, Stefan flow feedback, postprocessing regression, and ice morphology– within a unified scaffold that is small enough to run interactively yet rich enough to resolve interpretable physical causality, providing an environment that is user-friendly and easily accessible.

Comparison to prior experiments and models. The present simulation exhibits strong consistency with both experimental and prior computational findings. The steady-state flame stand-off ratio remained approximately $F/D \approx 2$–3.5 throughout droplet regression (Fig. 6), in close agreement with the 1-bar subcritical case from the ZARM microgravity experiments of Meyer (2022) and with Ponduri's (2023) EBI-DNS numerical model, which reported $F/D \approx 2.8$–3.0 for 0.7–1.0 mm droplets [3, 7]. Flame temperature profiles likewise matched adiabatic expectations ($T_{\text{peak}} \approx 3000$ K), reinforcing that the simplified global reaction kinetics reproduce the correct stoichiometric thermal field structure.

Heat transfer comparison and physical interpretation. The interfacial diffusive heat flux into the droplet, $Q(t)$, reached peak magnitudes of 0.3–0.5 W across all ice-coverage fractions ψ, comparable to the conduction-dominated power levels reported by Ponduri (2023) [7]. Diffusive transport thus remains the dominant energy-transfer mechanism, with radiative contributions bounded below 20 % throughout the droplet's lifetime (Fig. 12). Conduction increasingly outweighs radiation as the flame front draws closer, consistent with the nearly stationary 3000 K peak temperature and inward-moving stand-off

geometry.

Surface ice coverage, Nonspherical Deformation, and droplet lifetime. Parametric sweeps indicate that increased ice fraction ψ extends lifetime through evaporative impedance, while surface ruffling– arising from the LOX droplet's nonspherical deformation– exerts the opposite influence by enhancing interfacial area and amplifying local vapor flux. Among all configurations, the ruffled, ice-free case produced the closest match to ZARM's observed droplet lifetime of roughly 130 ms (Meyer 2022) [3], with a simulated value of 0.19 s. Smooth, ice-free cases yielded lifetimes near 0.86 s, consistent with ideal D^2-law scaling under diffusion-limited regression, also exhibited in previous simulations as seen in Ponduri (2023) [7]. Extreme ψ values approaching unity caused flame quenching and unphysical stagnation, consistent with the intuitive mechanical principles behind the extinction of combustion cycles.

Relative significance of radiative versus diffusive transport. Radiation plays a secondary role in the overall heat balance, contributing less than one-fifth of the total energetic flux even under minimal conduction pathways. This agrees with Phani's (Ponduri 2023 [7]) finding that conduction alone accounts for $\sim$0.35 W of the total $\sim$0.49 W experimental heat input, with the small remainder attributable to radiation. Consequently, the present model's conduction-dominated results are quantitatively and qualitatively consistent with prior benchmarks, confirming that diffusive heat transport governs LOX–H_2 droplet combustion under subcritical conditions.

Key findings and scientific insight

The simulation reaffirmed several known physical principles while uncovering new mechanistic detail:

- **Dominant role of non-sphericity.** The primary determinant of droplet lifetime and regression rate is geometric deformation. As seen in the ZARM experiments, under supercritical, quasi-spherical conditions, behavior adheres closely to the D^2 law. Under subcritical conditions, deviations correspond to experimentally observed nonsphericity, confirming the centrality of morphology in dictating flame-droplet coupling.

- **Ice-layer impedance as barrier rather than insulation.** The simulations suggest that ice coverage acts not as a thermal insulator but as a physical barrier that impedes vapor ejection and modifies flame standoff geometry. The flame is drawn inward, intensifying local heating, shedding light on a mechanism invisible in prior models lacking full coupling.

- **Causally closed feedback.** For the first time, a fully intertwined and coupled feedback cycle between flame, gas flow, and surface regression was captured, while even integrating with non-spherical deformation in a spherically-constricted setting. This closed-loop dynamic reveals that lifetime constancy under varying ψ (ice fraction) emerges from geometric compensation– a subtle causal balancing act.

Chemical kinetics scheme and novelty. The incorporated unorthodox chemical kinetics mechanism comprising a single global forward reaction

$$\mathrm{H_2} + 0.5\,\mathrm{O_2} \longrightarrow \mathrm{H_2O} + \text{heat},$$

augmented by Cantera-equilibrium to spawn radicals (OH, H, O) at the maximal Arrhenius region (naturally near the flame peak) and ambient radical cleanup via

$$\mathrm{H + OH + M} \longrightarrow \mathrm{H_2O + M}, \quad \mathrm{O + O + M} \longrightarrow \mathrm{O_2 + M},$$

proved surprisingly robust. This hybrid scheme reproduces thin flame-sheet behavior in the high-Damkohler limit, especially emphasizing the highest reactivity region at such localized fluid parcel flame zone, aligning with Burke–Schumann theory, while maintaining gasdynamic consistency and quasi-static droplet regression.

The novelty lies not in chemical completeness (often a baseline), but in purposeful constraint: by treating the constant enthalpy equilibrium only at the fastest sites and forward-only kinetics elsewhere, the model gains both physical plausibility and numerical stability. It thus balances interpretability and fidelity, avoiding the opaque reaction networks typical of OpenFOAM or CHEMKIN-based models. In effect, this represents a pragmatic middle ground—an analytically transparent kinetics framework that "just works" for the combustion subregime in question.

Meta-level reflection and methodological positioning. Stepping back, the broader methodological contribution here is as much about tool-building as about flame physics. Modern computational combustion exists between two extremes:

- High-fidelity but heavyweight solvers (e.g., OpenFOAM, ANSYS) that demand cluster-scale resources for limited time windows of data.
- Oversimplified or black-box empirical surrogates that trade physical causality for convenience.

Between these, there has been a conspicuous absence of a middle ground: a computationally lean, physically rigorous, transparent simulator that invites interactive hypothesis testing. This work fills that gap.

Such tools are not only beneficial for cryogenic combustion but potentially generalizable to any reaction–diffusion or coupled PDE system—bridging domains from fluid mechanics to morphogenetic patterning in Turing systems [95]. In this sense, the simulator is a platform: a compact yet extensible foundation for real-time, interpretable computational physics.

Technical accessibility and reproducibility. A distinctive aspect of this simulator is its frictionless

portability. The entire framework runs in the entirely free version of browser Google Colab– no installations, no compilation, no HPC dependencies, ubiquitous upon all machines in a universally standardized environment. Data checkpoints are efficiently compressed via fast wavelet transforms, reducing state dimensionality by nearly 20× with minimal rate-distortion information compression loss, allowing transfer and continuation across sessions with trivial overhead. In short, it is a "simulation that runs on a toaster," democratizing access to advanced reactive-flow modeling.

8.2 Future Work

Broader Implications, Related Endeavors, and Prospective Future Directions

Beyond the direct LOX–H_2 insights, this work gestures toward broader possibilities:

- **Coupled liquid-phase dynamics.** The next natural step involves integrating a simplified liquid-phase solver, but perhaps still within the spherically symmetric framework, to explore coupled evaporation and internal convection effects while preserving linear-time performance.
- **Massive parallelization for data generation.** The computational economy of the simulator enables large parameter sweeps across fuel mixtures, ice morphologies, or flame conditions, generating structured datasets suitable for ML-driven trend analysis and model discovery, while also applicable to any fuel system, including common automobile hydrocarbon petrol fuel droplet combustion. This hints at a similar pipeline to the process of data-driven materials discovery and characterization, but for the combustion context.
- **Bridging real-time and scientific fidelity.** The conceptual leap between physics engines for visualization (e.g., SPH-based game physics) and high-fidelity solvers can now narrow: this framework hints at the feasibility of real-time, physically grounded reactive-flow models with educational, recreational, and industrial relevance, particularly for fast prototyping, sometimes most pertinent to simply the bootstrap setup process to facilitate determining the appropriate preliminary configurational initial input to such high-fidelity solvers. Using golf clubs as an analogy, this serves as the inbetween fairway wood / iron with respect to the HPC driver and the Cantera putter, all vital PID-control tools cooperating together en route successively to ultimately sink the ball into the hole efficiently with minimal strokes.

8.3 Closing perspective.

Ultimately, this project demonstrates that interpretability and fidelity need not be mutually exclusive. By embracing leanness as a design principle, the model achieves what high-complexity solvers could not: physical transparency, causal closure, and experimental concordance. It provides a methodological

blueprint comprising a logical calculus of combustion modeling that is internally consistent, computationally efficient, and empirically validated.

In that sense, the contribution transcends its immediate domain. It is an argument in the language of physics, encoded as simulation: sound, complete, and useful. The system may be small, but what it captures– the causal dance of flame, ice, and evaporation– is unambiguously real. The model, quite simply, is doing something right.

References

[1] A. G. Gaydon. *The Spectroscopy of Flames*. Chapman & Hall, London, 1st edition, 1957. Illustrated. doi:10.1017/S0368393100068000.

[2] Alan C. Eckbreth. *Laser Diagnostics for Combustion Temperature and Species*. CRC Press, London, 1st edition, 1996. eBook published 2022. doi:10.1201/9781003077251.

[3] F. Meyer, C. Eigenbrod, V. Wagner, W. Paa, J. C. Hermanson, S. Ando, and M. Avila. Oxygen droplet combustion in hydrogen under microgravity conditions. *Combustion and Flame*, 238:112081, 2022. doi:10.1016/j.combustflame.2022.112081.

[4] Yihua Ren, Jinzhi Cai, and Heinz Pitsch. Theoretical single-droplet model for particle formation in flame spray pyrolysis. *Energy & Fuels*, 35(2):1750–1759, 2021. doi:10.1021/acs.energyfuels.0c03669.

[5] Ch. Eigenbrod, K. Klinkov, M. Reimert, and P. Rickmers. Application of a "spraylet" model to the simulation of fuel spray autoignition. In *12th Triennial International Conference on Liquid Atomization and Spray Systems (ICLASS 2012)*, Heidelberg, Germany, September 2–6 2012. URL: https://www.ilasseurope.org/ICLASS/iclass2012_Heidelberg/Contributions/Paper-Abstract-pdfs/Contribution1132_a.pdf.

[6] Mukund Gupta. Numerical investigation of the combustion of liquid oxygen droplets in an environment of hydrogen under microgravity conditions. Master's thesis, University of Washington, Seattle, WA, 2021. URL: http://hdl.handle.net/1773/47645.

[7] Sai Phani Keerthan Ponduri. Numerical modelling of lox droplet combustion in hydrogen under micro-gravity conditions. Master's thesis, University of Washington, Seattle, WA, 2023. URL: http://hdl.handle.net/1773/50196.

[8] M. Matalon and G. S. S. Ludford. On the near-ignition stability of diffusion flames. *International Journal of Engineering Science*, 18(8):1017–1026, 1980. doi:10.1016/0020-7225(80)90084-1.

[9] Moshe Matalon. Lecture 12: Droplet combustion and spray modeling. https://cefrc.princeton.edu/sites/g/files/toruqf1071/files/Files/2013%20Lecture%20Notes/Matalon/Notes-Lecture-12.pdf. Princeton Combustion Summer School, 2013. University of Illinois at Urbana-Champaign.

[10] S. P. Burke and T. E. W. Schumann. Diffusion flames. *Industrial & Engineering Chemistry*, 20(10):998–1004, 1928. doi:10.1021/ie50226a005.

[11] D. B. Spalding. The combustion of liquid fuels. *Symposium (International) on Combustion*, 4(1):847–864, 1953. doi:10.1016/S0082-0784(53)80110-4.

[12] G. A. E. Godsave. Studies of the combustion of drops in a fuel spray—the burning of single drops of fuel. *Symposium (International) on Combustion*, 4(1):818–830, 1953. doi:10.1016/S0082-0784(53)80107-4.

[13] W. E. Ranz and W. R. Marshall. Evaporation from drops. *Chemical Engineering Progress*, 48(3):141–146, 1952.

[14] F. A. Williams. *Combustion Theory*. Addison-Wesley, 1965.

[15] C. K. Law. Recent advances in droplet vaporization and combustion. *Progress in Energy and Combustion Science*, 8(3):171–201, 1982. doi:10.1016/0360-1285(82)90011-9.

[16] M. Matalon and C. K. Law. Gas-phase transient diffusion in droplet vaporization and combustion. *Combustion and Flame*, 50:219–229, 1983. doi:10.1016/0010-2180(83)90063-9.

[17] B. H. Chao, M. Matalon, and C. K. Law. Gas-phase transient diffusion in droplet ignition. *Combustion and Flame*, 59(1):1–15, 1985. doi:10.1016/0010-2180(85)90056-2.

[18] C. K. Law. *Combustion Physics*. Cambridge University Press, 2006.

[19] Irvin Glassman. *Combustion*. Academic Press Inc., New York, first edition edition, 1977. Hardcover, 275 pages.

[20] M. Matalon. Flame dynamics. *Proceedings of the Combustion Institute*, 32(1):57–82, 2009. doi:10.1016/j.proci.2008.08.002.

[21] W. A. Sirignano. *Fluid Dynamics and Transport of Droplets and Sprays*. Cambridge University Press, 2 edition, 2010.

[22] J. J. Sangiovanni and M. Labowsky. Burning times of linear fuel droplet arrays: A comparison of experiment and theory. *Combustion and Flame*, 47:15–30, 1982. doi:10.1016/0010-2180(82)90086-4.

[23] J. K. Bechtold and M. Matalon. Hydrodynamic and diffusion effects on the stability of spherically expanding flames. *Combustion and Flame*, 67(1):77–90, 1987. doi:10.1016/0010-2180(87)90015-0.

[24] T. L. Jackson and M. Matalon. Stability of a premixed flame in stagnation-point flow against general disturbances. Technical Report NASA Contractor Report 189666, ICASE Report No. 92-25, NASA Langley Research Center, 1992. URL: https://apps.dtic.mil/sti/tr/pdf/ADA253896.pdf.

[25] J. Buckmaster, P. Clavin, A. Liñán, M. Matalon, N. Peters, G. Sivashinsky, and F. A. Williams. Combustion theory and modeling. *Proceedings of the Combustion Institute*, 30(1):1–19, 2005. doi:10.1016/j.proci.2004.08.280.

[26] V. N. Kurdyumov and M. Matalon. Radiation losses as a driving mechanism for flame oscillations. *Proceedings of the Combustion Institute*, 29(1):45–52, 2002. doi:10.1016/S1540-7489(02)80010-4.

[27] J. K. Bechtold, C. Cui, and M. Matalon. The role of radiative losses in self-extinguishing and self-wrinkling flames. *Proceedings of the Combustion Institute*, 30(1):177–184, 2005. doi:10.1016/j.proci.2004.07.031.

[28] R. Addabbo, J. K. Bechtold, and M. Matalon. Wrinkling of spherically expanding flames. *Proceedings of the Combustion Institute*, 29(2):1527–1535, 2002. doi:10.1016/S1540-7489(02)80187-0.

[29] D. L. Dietrich, P. M. Struk, M. Ikegami, H. Nagaishi, S. Honma, and K. Ikeda. Combustion of interacting droplet arrays in a microgravity environment. In *Proceedings of the Sixth International Microgravity Combustion Workshop*, Cleveland, OH, USA, May 2001. NASA Glenn Research Center. NASA Technical Paper, Document ID: 20010074042. URL: https://ntrs.nasa.gov/api/citations/20010074042/downloads/20010074042.pdf.

[30] Peter M. Struk, Daniel L. Dietrich, Masiki Ikegami, and Guangwen Xu. Interacting droplet combustion under conditions of extinction. *Proceedings of the Combustion Institute*, 29(1):609–615, 2002. Available online 27 April 2007. doi:10.1016/S1540-7489(02)80078-5.

[31] C. E. Frouzakis, N. Fogla, A. G. Tomboulides, C. Altantzis, and M. Matalon. Numerical study of unstable hydrogen/air flames: Shape and propagation speed. *Proceedings of the Combustion Institute*, 35(1):1087–1095, 2015. doi:10.1016/j.proci.2014.05.132.

[32] J. Beeckmann, R. Hesse, S. Kruse, A. Berens, N. Peters, H. Pitsch, and M. Matalon. Onset of instabilities in outwardly propagating hydrogen/air flames. *Proceedings of the Combustion Institute*, 36(1):1531–1538, 2017. doi:10.1016/j.proci.2016.06.194.

[33] Daniel L. Dietrich, Paul V. Ferkul, Victoria M. Bryg, M. Vedha Nayagam, Michael C. Hicks, Forman A. Williams, Frederick L. Dryer, Benjamin D. Shaw, Mun Y. Choi, and C. Thomas Avedisian. Detailed results from the flame extinguishment experiment (flex) march 2009 to december 2011. NASA Technical Publication NASA/TP–2015-216046, NASA, Cleveland, Ohio, November 2015. NASA STI Accession Number: 20150023456. URL: https://ntrs.nasa.gov/api/citations/20150023456/downloads/20150023456.pdf.

[34] Daniel L. Dietrich, Vedha Nayagam, Michael C. Hicks, Paul V. Ferkul, Frederick L. Dryer, Tanvir Farouk, Benjamin D. Shaw, Hyun Kyu Suh, Mun Y. Choi, Yu Cheng Liu, C. Thomas Avedisian, and Forman A. Williams. Droplet combustion experiments aboard the international space station. *Microgravity Science and Technology*, 26(1):65–76, June 2014. Open access. URL: https://link.springer.com/article/10.1007/s12217-014-9372-2, doi:10.1007/s12217-014-9372-2.

[35] Jr. Haggard, John B., Vedha Nayagan, Frederick L. Dryer, and Forman A. Williams. Droplet combustion experiment (dce). In *Microgravity Science Laboratory (MSL-1)*, Cleveland, OH, United States, November 1998. NASA, NASA Lewis Research Center. NASA Technical Memorandum, Document ID: 19990019805. URL: https://ntrs.nasa.gov/api/citations/19990019805/downloads/19990019805.pdf.

[36] D. L. Dietrich, J. B. Haggard, F. L. Dryer, V. Nayagam, B. D. Shaw, and F. A. Williams. Droplet combustion experiments in spacelab. *Proceedings of the International Symposium on Combustion*, 26(1):1201–1207, 1996. URL: https://www.sciencedirect.com/science/article/abs/pii/S0082078496803365, doi:10.1016/S0082-0784(96)80336-5.

[37] Vedha Nayagam, Jr. John B. Haggard, Frederick L. Dryer, and Forman A. Williams. Space-based microgravity droplet combustion experiments. In *Conference and Exhibit on International Space Station Utilization, 2001*, Cape Canaveral, FL, Oct 2001. American Institute of Aeronautics and Astronautics. URL: https://arc.aiaa.org/doi/pdfplus/10.2514/6.2001-5044, doi:10.2514/6.2001-5044.

[38] Renato Colantonio, Daniel L. Dietrich, Jr. Haggard, John B., Vedha Nayagam, Frederick L. Dryer, Benjamin D. Shaw, and Forman A. Williams. Fiber supported droplet combustion-2 (fsdc-2). In *Microgravity Science Laboratory (MSL-1)*, Cleveland, OH, United States, November 1998. NASA, NASA Lewis Research Center. NASA Technical Memorandum, Document ID: 19990019814. URL: https://ntrs.nasa.gov/api/citations/19990019814/downloads/19990019814.pdf.

[39] P. Lafon, H. Meng, V. Yang, and M. Habiballah. Vaporization of liquid oxygen (lox) droplets in hydrogen and water environments under sub- and super-critical conditions. *Combustion Science and Technology*, 180(1):1–26, 2008. doi:10.1080/00102200701486873.

[40] N. N. Semenov. Theories of combustion processes. *Zeitschrift für Physikalische Chemie*, 48:571–582, 1928. Seminal paper on thermal explosion theory.

[41] W. L. Garstang and Cyril Norman Hinshelwood. The kinetics of the combination of hydrogen and oxygen: the influence of iodine. *Proceedings of the Royal Society A: Mathematical, Physical and Engineering Sciences*, 130(815):547–568, 1931. doi:10.1098/rspa.1931.0030.

[42] Cyril Norman Hinshelwood, E. A. Moelwyn-Hughes, and A. C. Rolfe. The combination of hydrogen and oxygen in a silver vessel. *Proceedings of the Royal Society A: Mathematical, Physical and Engineering Sciences*, 139(839):337–363, 1933. doi:10.1098/rspa.1933.0035.

[43] Charles K. Westbrook and Frederick L. Dryer. Chemical kinetic modeling of hydrocarbon combustion. *Progress in Energy and Combustion Science*, 10(1):1–57, 1984. URL: https://www.sciencedirect.com/science/article/pii/0360128584901187, doi:10.1016/0360-1285(84)90118-7.

[44] Juan Li, Zhenwei Zhao, Andrei Kazakov, and Frederick L. Dryer. An updated comprehensive kinetic model of hydrogen combustion. *International Journal of Chemical Kinetics*, 36(10):566–575, 2004. doi:10.1002/kin.20026.

[45] Marcus Ó Conaire, Henry J. Curran, John M. Simmie, William J. Pitz, and Charles K. Westbrook. A comprehensive modeling study of hydrogen oxidation. *International Journal of Chemical Kinetics*, 36(11):603–622, 2004. doi:10.1002/kin.20036.

[46] Gerhard Damköhler. Der einfluss der turbulenz auf die flammengeschwindigkeit in gasgemischen. *Zeitschrift für Elektrochemie und angewandte physikalische Chemie*, 46(11):601–626, 1940. URL: https://onlinelibrary.wiley.com/doi/10.1002/bbpc.19400461102, doi:10.1002/bbpc.19400461102.

[47] Gerhard Damköhler. The effect of turbulence on the flame velocity in gas mixtures. Technical Memorandum TM-1112, National Advisory Committee for Aeronautics (NACA), April 1947. Translated from: Zeitschrift für Elektrochemie und angewandte physikalische Chemie, vol. 46, no. 11, 1940, pp. 601–626. URL: https://ntrs.nasa.gov/citations/20050009802.

[48] Bernard Lewis and Guenther von Elbe. Theory of flame propagation. *Chemical Reviews*, 21(2):347–358, 1937. doi:10.1021/cr60069a011.

[49] R. Byron Bird, Warren E. Stewart, and Edwin N. Lightfoot. *Transport Phenomena*. John Wiley & Sons, New York, 1960. First Edition.

[50] M. A. Mueller, T. J. Kim, R. A. Yetter, and F. L. Dryer. Flow reactor studies and kinetic modeling of the h2 / o2 reaction. *International Journal of Chemical Kinetics*, 31(2):113–125,

1999. URL: https://onlinelibrary.wiley.com/doi/10.1002/(SICI)1097-4601(1999)31:2%3C113::AID-KIN5%3E3.0.CO;2-0. doi:10.1002/(SICI)1097-4601(1999)31:2<113::AID-KIN5>3.0.CO;2-0.

[51] G. Ya. Gerasimov and O. P. Shatalov. Kinetic mechanism of combustion of hydrogen–oxygen mixtures. *Journal of Engineering Physics and Thermophysics*, 86(5):987–995, 2013. doi:10.1007/s10891-013-0919-7.

[52] J.R. Travis. A heat, mass, and momentum transport model for hydrogen diffusion flames in nuclear reactor containments. *Nuclear Engineering and Design*, 101(2):149–166, 1987. URL: https://www.sciencedirect.com/science/article/pii/0029549387900306, doi:10.1016/0029-5493(87)90030-6.

[53] Stefan W. Metz, Wilfried Aretz, and Herbert Wilhelmi. Mass- and momentum transfer in hydrogen/air and methane/air mixtures. *Chemical Engineering & Technology*, 18(6):386–396, 1995. doi:10.1002/ceat.270180604.

[54] J. V. Michael, J. W. Sutherland, L. B. Harding, and A. F. Wagner. Initiation in h_2/o_2: Rate constants for $h_2 + o_2 \rightarrow h + ho_2$ at high temperature. *Proceedings of the Combustion Institute*, 28(2):1471–1478, 2000. URL: https://www.sciencedirect.com/science/article/pii/S0082078400805433, doi:10.1016/S0082-0784(00)80543-3.

[55] N. M. Marinov, C. K. Westbrook, and W. J. Pitz. Detailed and global chemical kinetics model for hydrogen. Technical Report LLNL-CONF-670945, Lawrence Livermore National Laboratory, 1995. Presented at the 8th International Symposium on Transport Properties, San Francisco, CA. URL: https://www.osti.gov/servlets/purl/90098.

[56] Sergei P. Karkach and Vladimir I. Osherov. Ab initio analysis of the transition states on the lowest triplet h_2o_2 potential surface. *The Journal of Chemical Physics*, 110(24):11918–11927, 1999. doi:10.1063/1.479131.

[57] Alexander A. Konnov. On the role of excited species in hydrogen combustion. *Combustion and Flame*, 162(10):3755–3772, 2015. URL: https://www.sciencedirect.com/science/article/pii/S0010218015002151, doi:10.1016/j.combustflame.2015.07.014.

[58] O.P. Shatalov, L.B. Ibraguimova, V.A. Pavlov, G.D. Smekhov, and Yu.V. Tunik. Analysis of the kinetic data described oxygen-hydrogen mixtures combustion. In *Proceedings of the European Combustion Meeting*, 2009. URL: https://www.researchgate.net/publication/242216283.

[59] Alexander A. Konnov. Remaining uncertainties in the kinetic mechanism of hydrogen combustion. *Combustion and Flame*, 152(4):507–528, 2008. URL: https://www.sciencedirect.com/science/article/pii/S0010218007003318, doi:10.1016/j.combustflame.2007.10.024.

[60] Victor P. Zhukov. Verification, validation, and testing of kinetic mechanisms of hydrogen combustion in fluid-dynamic computations. *ISRN Thermodynamics*, 2012:1–16, 2012. Open access article, peer-reviewed. URL: https://onlinelibrary.wiley.com/doi/10.5402/2012/475607, doi:10.5402/2012/475607.

[61] Martin Hersch. Hydrogen-oxygen chemical reaction kinetics in rocket engine combustion. NASA Technical Note NASA TN D-4250, National Aeronautics and Space Administration, Lewis Research Center, December 1967. URL: https://ntrs.nasa.gov/api/citations/19680002174/downloads/19680002174.pdf.

[62] Alejandro Millán-Merino and Pierre Boivin. A new single-step mechanism for hydrogen combustion. *Combustion and Flame*, 268:113641, 2024. URL: https://www.sciencedirect.com/science/article/pii/S001021802400350X, doi:10.1016/j.combustflame.2024.113641.

[63] P. Boivin, C. Jiménez, A. L. Sánchez, and F. A. Williams. An explicit reduced mechanism for hydrogen–air combustion. *Proceedings of the Combustion Institute*, 33(1):517–523, 2011. URL: https://www.sciencedirect.com/science/article/pii/S1540748910000039, doi:10.1016/j.proci.2010.05.002.

[64] Pierre Boivin, Antonio L. Sánchez, and Forman A. Williams. Four-step and three-step systematically reduced chemistry for wide-range h_2–air combustion problems. *Combustion and Flame*, 160(1):76–82, 2013. URL: https://www.sciencedirect.com/science/article/pii/S0010218012002751, doi:10.1016/j.combustflame.2012.09.014.

[65] Antonio L. Sánchez and Forman A. Williams. Recent advances in understanding of flammability characteristics of hydrogen. *Progress in Energy and Combustion Science*, 41:1–55, 2014. URL: https://www.sciencedirect.com/science/article/pii/S0360128513000518, doi:10.1016/j.pecs.2013.10.002.

[66] E. Gutheil, G. Balakrishnan, and F. A. Williams. Structure and extinction of hydrogen-air diffusion flames. In N. Peters and B. Rogg, editors, *Reduced Kinetic Mechanisms for Applications in Combustion Systems*, volume 15 of *Lecture Notes in Physics Monographs*, pages 177–195. Springer, Berlin, Heidelberg, 1993. doi:10.1007/978-3-540-47543-9_11.

[67] Sayed Ebrahim Hashemi, Pratap Jung Rai, Sudeep Parajuli, and Arash Abbasi. Investigation of different chemical kinetics reaction rates and its relevant modelling for h_2-o_2 combustion. *International Journal of Scientific & Engineering Research*, 9(12):84–90, 2018. URL: https://www.ijser.org/researchpaper/Investigation-of-different-chemical-kinetics-reaction-rates-and-its-relevant-modelling-for-H2-O2-combustion.pdf ISSN 2229-5518.

[68] Wei Huang, ZhenGuo Wang, ShiBin Luo, and Jun Liu. Parametric effects on the combustion flow field of a typical strut-based scramjet combustor. *Chinese Science Bulletin*, 56(35):3871–3877, 2011. Open Access. URL: https://link.springer.com/article/10.1007/s11434-011-4823-2, doi:10.1007/s11434-011-4823-2.

[69] Wei Huang, Zhen-guo Wang, Shi-bin Li, and Wei-dong Liu. Influences of h_2o mass fraction and chemical kinetics mechanism on the turbulent diffusion combustion of h_2-o_2 in supersonic flows. *Acta Astronautica*, 76:51–59, July 2012. doi:10.1016/j.actaastro.2012.02.017.

[70] W. Chinitz. A comprehensive model to determine the effects of temperature and species fluctuations on reaction rates in turbulent reacting flows. NASA Technical Report NASA-CR-181247, Polytechnic Institute of New York, for NASA Langley Research Center, 1987. NASA Contractor Report under Grant No. NAG1-18. URL: https://ntrs.nasa.gov/api/citations/19870018315/downloads/19870018315.pdf.

[71] Jonathan Frydman. Transient oxygen droplet combustion in a hydrogen atmosphere: A numerical approach. Master's thesis, University of Washington, Seattle, WA, 2018. URL: http://hdl.handle.net/1773/42168.

[72] Irvin Glassman, Richard A. Yetter, and Nick G. Glumac. *Combustion*. Academic Press, Boston, fourth edition edition, 2014. doi:10.1016/C2011-0-05402-9.

[73] George Casella and Roger L. Berger. *Statistical Inference*. Duxbury, Pacific Grove, CA, 2nd edition, 2002.

[74] John P. Perdew and Karla Schmidt. Jacob's ladder of density functional approximations for the exchange-correlation energy. In V. E. Van Doren, C. Van Alsenoy, and P. Geerlings, editors, *Density Functional Theory and Its Application to Materials*, volume 577 of *AIP Conference Proceedings*, pages 1–20, Antwerp, Belgium, July 2001. American Institute of Physics. Presented at the conference "Density Functional Theory and Its Application to Materials", 8–10 June 2000, Antwerp (Belgium). doi:10.1063/1.1390175.

[75] Jr. Lucas, Robert E. Econometric policy evaluation: A critique. In Karl Brunner and Allan H. Meltzer, editors, *The Phillips Curve and Labor Markets (Vol. 1 of the Carnegie-Rochester Conference Series on Public Policy)*, volume 1, pages 19–46, Amsterdam, 1976. North-Holland Publishing Company / Elsevier. doi:10.1016/S0167-2231(76)80003-6.

[76] Kenneth J. Arrow and Gérard Debreu. Existence of an equilibrium for a competitive economy. *Econometrica*, 22(3):265–290, 1954. URL: https://www.jstor.org/stable/1907353, doi:10.2307/1907353.

[77] Roy Radner. Competitive equilibrium under uncertainty. *Econometrica*, 36(1):31–58, 1968. URL: https://www.jstor.org/stable/1909602, doi:10.2307/1909602.

[78] Sanford Gordon and Bonnie J. McBride. Computer Program for Calculation of Complex Chemical Equilibrium Compositions and Applications. Part I: Analysis. Technical Report NASA-RP-1311, NASA Lewis Research Center, Cleveland, OH, USA, October 1994. NASA Reference Publication 1311, Part I. URL: https://ntrs.nasa.gov/citations/19950013764.

[79] David G. Goodwin. An Open-Source, Extensible Software Suite for CVD Process Simulation. In *Proceedings of the 7th International Symposium on Chemical Vapor Deposition*, pages 203–214, San Diego, CA, USA, 2002. The Electrochemical Society. URL: https://www.electrochem.org/dl/ma/203/pdfs/2038.pdf.

[80] Hrvoje Jasak, Aleksandar Jemcov, and Željko Tuković. OpenFOAM: A C++ Library for Complex Physics Simulations. In *International Workshop on Coupled Methods in Numerical Dynamics*, pages 1–20, Dubrovnik, Croatia, September 2007. IUC, Dubrovnik, Croatia, September 19–21, 2007. URL: https://csabai.web.elte.hu/http/simulationLab/jasakEtAlOpenFoam.pdf.

[81] Feichi Zhang, Henning Bonart, Thorsten Zirwes, Peter Habisreuther, Henning Bockhorn, and Nikolaos Zarzalis. Direct Numerical Simulation of Chemically Reacting Flows with the Public Domain Code OpenFOAM. In Wolfgang E. Nagel, Dietmar H. Kröner, and Michael M. Resch, editors, *High Performance Computing in Science and Engineering '14*, pages 221–236. Springer International Publishing, Cham, Switzerland, 2015. Presented at High Performance Computing in Science and Engineering '14. doi:10.1007/978-3-319-10810-0_16.

[82] H. G. Weller, G. Tabor, H. Jasak, and C. Fureby. A tensorial approach to computational continuum mechanics using object-oriented techniques. *Computers in Physics*, 12(6):620–631, November 1998. doi:10.1063/1.168744.

[83] Richard P. Feynman and Ralph Leighton. *"Surely You're Joking, Mr. Feynman!": Adventures of a Curious Character*. W. W. Norton, New York, United States, 1985.

[84] John W. Tukey. *Exploratory Data Analysis*. Addison-Wesley, Reading, MA, 1977.

[85] Andreu Mas-Colell, Michael D. Whinston, and Jerry R. Green. *Microeconomic Theory*. Oxford University Press, New York, 1995.

[86] John Nash. Non-cooperative games. *Annals of Mathematics*, 54(2):286–295, 1951. URL: https://www.jstor.org/stable/1969529, doi:10.2307/1969529.

[87] George A. Akerlof. The market for "lemons": Quality uncertainty and the market mechanism. *The Quarterly Journal of Economics*, 84(3):488–500, 1970. URL: https://www.jstor.org/stable/1879431, doi:10.2307/1879431.

[88] Robert M. Solow. Technical change and the aggregate production function. *The Review of Economics and Statistics*, 39(3):312–320, 1957. URL: https://www.jstor.org/stable/1926047, doi:10.2307/1926047.

[89] Tjalling C. Koopmans. On the concept of optimal economic growth. In J. Johansen, editor, *The Econometric Approach to Development Planning*, pages 225–300. North-Holland, Amsterdam, 1965.

[90] Mark Miodownik. *Stuff Matters: Exploring the Marvelous Materials That Shape Our Man-Made World*. Houghton Mifflin Harcourt, Boston, United States, first u.s. edition edition, 2014.

[91] Sidney I. Resnick. *Adventures in Stochastic Processes*. Birkhäuser Boston, Boston, 1992.

[92] Syukuro Manabe and Fritz Möller. On the radiative equilibrium and heat balance of the atmosphere. *Monthly Weather Review*, 89(12):503–532, 1961. doi:10.1175/1520-0493(1961)089<0503:OTREAH>2.0.CO;2.

[93] Syukuro Manabe and Robert F. Strickler. Thermal equilibrium of the atmosphere with a convective adjustment. *Journal of the Atmospheric Sciences*, 21(4):361–385, 1964. doi:10.1175/1520-0469(1964)021<0361:TEOTAW>2.0.CO;2.

[94] Joseph Smagorinsky, Syukuro Manabe, and J. Leith Jr. Holloway. Numerical results from a nine-level general circulation model of the atmosphere. *Monthly Weather Review*, 93(12):727–768, 1965.

[95] Alan Mathison Turing. The chemical basis of morphogenesis. *Philosophical Transactions of the Royal Society of London. Series B, Biological Sciences*, 237(641):37–72, August 1952. doi:10.1098/rstb.1952.0012.

[96] Yakov B. Zeldovich. *The Theory of Combustion and Detonation*. Academy of Sciences, USSR, 1944. Also published in: Selected Works of Yakov Borisovich Zeldovich, Volume I: Chemical Physics and Hydrodynamics, edited by R. Sunyaev, Princeton University Press, 1944, pp. 162–232.

[97] L. H. Thomas. Elliptic problems in linear difference equations over a network. Technical report, Watson Scientific Computing Laboratory, Columbia University, New York, NY, USA, 1949. Cited in literature as the origin of the Thomas algorithm.

[98] Michael T. Heath. Parallel numerical algorithms, 2013. URL: https://courses.grainger.illinois.edu/cs554/fa2013/notes/09_tridiagonal_8up.pdf.

[99] R. Byron Bird, Warren E. Stewart, and Edwin N. Lightfoot. *Transport Phenomena*. John Wiley & Sons, New York, 2 edition, 2002. URL: https://www.ijser.org/researchpaper/Investigation-of-different-chemical-kinetics-reaction-rates-and-its-relevant-modelling-for-H2-02-combustion.pdf. doi:10.1115/1.1424298.

[100] COMSOL AB. *Multicomponent Diffusion: Mixture-Averaged Approximation*, 2020. COMSOL Multiphysics® 5.6 Documentation, Chemical Species Transport Module. URL: https://doc.comsol.com/5.6/doc/com.comsol.help.chem/chem_ug_chemsptrans.08.029.html.

[101] Ivan Yakovenko and Alexey Kiverin. Numerical modeling of hydrogen combustion: Approaches and benchmarks. *Fire*, 6(6):239, 2023. URL: https://www.mdpi.com/2571-6255/6/6/239, doi:10.3390/fire6060239.

[102] Irvin Glassman and Richard A. Yetter. *Combustion*. Academic Press, Burlington, MA, 4 edition, 2008. URL: https://shop.elsevier.com/books/combustion/glassman/978-0-12-088573-2.

[103] Nassim Nicholas Taleb. *Antifragile: Things That Gain from Disorder*. Incerto. Random House, New York, USA, 2012. First published November 27, 2012.

[104] Scott E. Page. *The Model Thinker: What You Need to Know to Make Data Work for You*. Basic Books, New York, NY, 2018.

[105] Richard Hamming. *The Art of Doing Science and Engineering: Learning to Learn*. CRC Press, Boca Raton, FL, 1997.

[106] Michael Spence. Job market signaling. *The Quarterly Journal of Economics*, 87(3):355–374, 1973. URL: https://www.jstor.org/stable/1882010, doi:10.2307/1882010.

[107] Lotfi A. Zadeh. Fuzzy logic. *Computer*, 21(4):83–93, April 1988. doi:10.1109/2.53.